

2017-04-19

# Towards Closed-loop, Robot Assisted Percutaneous Interventions under MRI Guidance

Niravkumar Amrutlal Patel  
*Worcester Polytechnic Institute*

Follow this and additional works at: <https://digitalcommons.wpi.edu/etd-dissertations>

---

## Repository Citation

Patel, N. A. (2017). *Towards Closed-loop, Robot Assisted Percutaneous Interventions under MRI Guidance*. Retrieved from <https://digitalcommons.wpi.edu/etd-dissertations/130>

This dissertation is brought to you for free and open access by [Digital WPI](#). It has been accepted for inclusion in Doctoral Dissertations (All Dissertations, All Years) by an authorized administrator of Digital WPI. For more information, please contact [wpi-etd@wpi.edu](mailto:wpi-etd@wpi.edu).

# Towards Closed-loop, Robot Assisted Percutaneous Interventions under MRI Guidance

by

Niravkumar Patel

A Dissertation

Submitted to the Faculty

of the

WORCESTER POLYTECHNIC INSTITUTE

In partial fulfillment of the requirements for the

Degree of Doctor of Philosophy

in

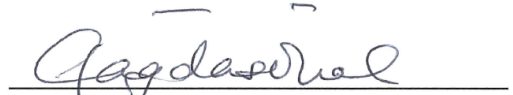
Robotics Engineering

April 2017

APPROVED BY:



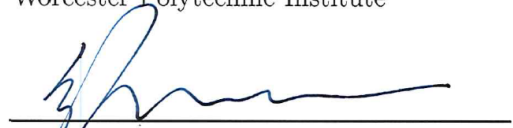
Prof. Gregory S. Fischer, Advisor  
Worcester Polytechnic Institute



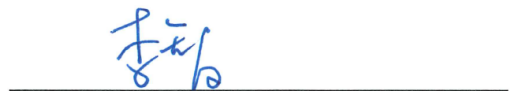
Prof. Cagdas D. Onal, Committee Member  
Worcester Polytechnic Institute



Prof. Michael Gennert, Head of the Department  
Worcester Polytechnic Institute



Prof. Junichi Tokuda, Committee Member  
Harvard Medical School



Prof. Zhi Li, Committee Member  
Worcester Polytechnic Institute

## **Abstract**

Image Guided Therapy (IGT) and surgery systems have been a focused research area for over two decades. Outcome of various surgical procedures in terms of quality of treatment, patient recovery and post treatment quality of life has improved by use of various imaging modalities such as Ultrasound (US), Computed Tomography (CT) and Magnetic Resonance Imaging (MRI). Though, MRI has primarily been a diagnostic imaging modality, in recent years various MRI guided procedures are being performed in both research and clinical settings. Also, over the last decade, various MRI guided robotic devices have been developed and used clinically for percutaneous interventions such as prostate biopsy, brachytherapy and tissue ablation. Though, MRI provides better soft tissue contrast compared to CT and US, it poses various challenges such as constrained space, less ergonomic patient access and limited material choices due to its high magnetic field. Even after advancements in MRI compatible actuation methods and robotic devices using them, as acquisition of multi-slice or 3D MR images typically take more than 30 seconds, most MRI guided interventions still rely on preoperative images acquired a few days prior the treatment and in some cases intraoperative images acquired during the surgical procedure. This thesis presents an intraoperative MRI guided robotic system for transperineal prostate biopsy with open-loop image guidance, system architecture for closed-loop robotic interventions, closed-loop needle steering under real-time MRI guidance and an integrated system for conformal brain tumor ablation under real-time MR-thermometry monitoring.

An intraoperative MRI guided robotic system for prostate biopsy comprising of an MRI compatible 4-Degrees of Freedom (DOF) robotic manipulator, robot

controller and control application with Clinical User Interface (CUI) and surgical planning applications (3DSlicer and RadVision) is described. This system utilizes intraoperative images acquired after each full or partial needle insertion for needle tip localization. Presented system was approved by Institutional Review Board (IRB) at Brigham and Women’s Hospital (BWH) and has been used in 30 patient trials. Successful translation of such a system utilizing intraoperative MR images motivated development of system architecture for closed-loop, robot assisted, real-time MRI guided percutaneous interventions.

Robot assisted, closed-loop intervention could improve positioning and localization of the therapy delivery instrument, improve physician and patient comfort and provide safer surgical workflow. Also, utilizing real-time MR images could allow correction of surgical instrument trajectory and controlled therapy delivery. This thesis, presents an architecture for closed-loop percutaneous interventions under real-time MRI guidance. Two of the applications validating the presented architecture: closed-loop needle steering and MRI guided brain tumor ablation are demonstrated under real-time MRI guidance.

A steerable needle could be beneficial in percutaneous interventions where it might be necessary to avoid certain critical tissue structures while accessing desired lesion, which might not be accessible with a strain insertion. Steerable needle controlled by an MRI compatible robot and real-time MR image based needle tracking could allow closed-loop needle insertion with dynamic needle trajectory planning to hit a desired target location. In this thesis, an integrated system comprising of an MRI-compatible robot, robot controller, real-time MRI based needle tracking and three different steering approaches are presented.

Stereotactic neurosurgery system comprising of an MRI compatible robot, real-time Linux based embedded robot controller, interstitial high intensity focused ul-



trasound ablation system, active tracking coil based ablation probe localization and real-time MRI based thermal dose monitoring is presented. Presented system has been validated with gelatin phantom studies and has been approved by Institutional Animal Care and Use Committee (IACUC) for animal trials.

## Acknowledgements

I would first like to express my gratitude to my advisor Prof. Gregory S. Fischer for his guidance, mentoring and support throughout my PhD. His knowledge in all aspects of medical robotics has been an incredible support whenever I needed an advice. He has been an incredible supervisor, especially his enthusiasm for research and openness for exploring new research possibilities have been an inspiration for me. Whenever I needed an intellectual support, academic guidance or career advice, support from Prof. Fischer has been invaluable. I would also like to thank Prof. Cagdas Onal, Prof. Zhi Li and Prof. Junichi Tokuda for serving on my thesis committee as committee members. Their insightful reviews have improved the content throughout the dissertation. I would also like to acknowledge our collaborators who provide valuable engineering and clinical contributions for this dissertation: Prof. Clare Tempany, Prof. Nobuhiko Hata and Prof. Junichi Tokuda from Brigham and Women's Hospital, Harvard Medical School; Prof. Iulian Iordachita and Dr. Sohrab Eslami from Johns Hopkins University; Prof. Julie Pilitsis from Albany Medical College; Prof. Matt Gounis and Dr. Shaokuan Zheng from Umass Medical School; Prof. Reinhold Ludwig and Prof. Gene Bogdanov from WPI; Dr. Clif Burdette, Emery Williams, Tamas Heffter, Goutam Ghoshal and Paul Neubauer from Acoustic MedSystems Inc.; Prof. Sarthak Misra, Dr. Pedro Moreira, and Tim van Katwijk from University of Twente. I would also like to thank my lab mates from Automation and Interventional Medicine (AIM) Robotics Research Laboratory for collaborative work and friendship: Gang Li, Weijian Shang, Chris Nycz, Radian Gondokaryono, Marek Wartenberg, Paulo Carvalho, Adnan Munawar, Alex Camilo, Kevin Harrington, Zhixian Zhang, Michael Delph, and Satya Janga. It has been exciting and very supportive working with you all. I would like to thank robotics and mechanical engineering staff: Deborah Baron, Katherine Crighton, Tracey Coetzee,

Barbara Edilberti, Barbara Furhman, Randy Robinson, Erica Stults, and Shannon Cotter for their patient and timely help whenever I needed.

This work was supported by NIH R01CA166379, NIH BRP RO1-CA111288, which have provided indispensable financial support for this dissertation.

Finally, I am deeply thankful to my family and my wife, for their love, understanding, encouragement and support. I could never have come this far without their support. This work would not have been possible without the help and support of my family, advisor, colleagues and friends. I would like to expressly thank everyone who has helped me over the past 5 years of my PhD life.

# Dedication

I would like to dedicate my dissertation to my family.

# Contents

<b>Abstract</b>	<b>ii</b>
<b>Acknowledgement</b>	<b>iv</b>
<b>List of Figures</b>	<b>xiv</b>
<b>List of Tables</b>	<b>xv</b>
<b>1 Introduction</b>	<b>1</b>
1.1 Background and Motivation . . . . .	2
1.1.1 Motivation for Intraoperative MRI Guided Prostate Interventions . . . . .	3
1.1.2 Motivation for MRI Guided Robot Assisted Percutaneous Interventions . . . . .	3
1.1.3 Motivation for Closed-loop Interventions . . . . .	5
1.1.4 Motivation for Steerable Needle Interventions . . . . .	5
1.1.5 Motivation for MRI-guided Stereotactic Neurosurgery Interventions . . . . .	7
1.2 Literature Review . . . . .	8
1.2.1 MRI Guided Percutaneous Prostate Interventions . . . . .	8
1.2.2 Asymmetric-tip Needle Steering Interventions . . . . .	12

1.2.3	Robot Assisted Stereotactic Neurosurgery . . . . .	14
1.3	Dissertation Overview . . . . .	17
1.4	Dissertation Contributions . . . . .	19
1.4.1	Intraoperative MRI guided Prostate Biopsy . . . . .	19
1.4.2	Architecture for Closed-loop MRI Guided Interventions . . . .	20
1.4.3	Closed-loop Needle Steering under MRI Guidance . . . . .	20
1.4.4	Closed-loop Brain Tumor Ablation Under Real-time MRI Guid- ance . . . . .	20

## **2 Intraoperative MRI Guided Robotic System For Prostate Biopsy with Open-loop Image Guidance 22**

2.1	Contributions . . . . .	22
2.2	Introduction . . . . .	23
2.3	System Architecture and Clinical Workflow . . . . .	24
2.3.1	System Architecture . . . . .	24
2.3.2	Clinical Workflow . . . . .	27
2.4	Electromechanical System Design . . . . .	29
2.4.1	Needle Placement Parallel Manipulator . . . . .	29
2.4.2	Ultrasonic Piezoelectric Actuators . . . . .	31
2.4.3	MRI Robot Controller . . . . .	33
2.5	Navigation and Robot Control Software . . . . .	35
2.5.1	Robot Registration and Surgical Navigation . . . . .	35
2.5.2	Robot Control Software . . . . .	37
2.6	Experiments and Results . . . . .	40
2.6.1	Preclinical Evaluation: Phantom Studies under MRI Guidance	42
2.6.2	Preliminary Clinical Patient Study . . . . .	43
2.7	Discussion and Conclusion . . . . .	45

<b>3</b>	<b>System Architecture for Closed-loop MRI Guided Percutaneous Interventions</b>	<b>51</b>
3.1	Contributions . . . . .	51
3.2	Proposed System Architecture . . . . .	52
3.3	Unified Imaging Device Interface . . . . .	52
3.4	Real-time Image Processing . . . . .	53
3.4.1	Therapy Device Tracking . . . . .	54
3.4.2	Therapy Monitoring . . . . .	55
3.5	Surgical Planning and Navigation . . . . .	55
3.6	Robot Control Application . . . . .	55
3.7	Conclusions . . . . .	56
<b>4</b>	<b>Closed-loop Needle Steering under MRI Guidance</b>	<b>57</b>
4.1	Contributions . . . . .	57
4.2	Introduction . . . . .	58
4.3	Asymmetric-tip Needle Kinematic Model . . . . .	60
4.4	Gaussian-based Continuous Rotation and Variable (CURV) Curvature Steering Model . . . . .	62
4.5	System Architecture . . . . .	63
4.6	Real-time needle tracking with MRI . . . . .	67
4.6.1	Continuous MR Image Acquisition . . . . .	68
4.6.2	Autonomous Scan Geometry Control . . . . .	68
4.6.3	Autonomous Needle Tracking . . . . .	69
4.7	Closed-loop Steering Methodology . . . . .	71
4.8	Steering Approaches . . . . .	75
4.8.1	Autonomous Steering with Bevel Angle Control . . . . .	76
4.8.2	Autonomous Needle Insertion with CURV Steering Model . . . . .	76

4.8.3	Teleoperated Needle Insertion with CURV Steering Model . .	76
4.9	Experiments and Results . . . . .	77
4.9.1	Experiment Setup . . . . .	77
4.9.2	Results for Bevel Angle Controlled Steering . . . . .	78
4.9.3	Results from Autonomous CURV steering . . . . .	78
4.9.4	Results from Teleoperated Insertion with CURV steering . . .	79
4.10	Discussion and Conclusions . . . . .	80

## 5 Closed-loop Conformal Brain Tumor Ablation under Real-time MRI

<b>Guidance</b>		<b>82</b>
5.1	Contributions . . . . .	82
5.2	Introduction . . . . .	83
5.3	System Architecture . . . . .	85
5.4	MRI Compatible Neurosurgery Robot . . . . .	88
5.5	Embedded Robot Controller . . . . .	89
5.6	Robot Control Application . . . . .	91
5.7	Surgical Navigation System . . . . .	92
5.7.1	Robot Workspace Analysis . . . . .	95
5.7.2	TheraVision . . . . .	95
5.7.3	3DSlicer . . . . .	97
5.8	Ablation Probe Tracking Using Active Coils . . . . .	99
5.8.1	Probe Construction . . . . .	99
5.8.2	Probe Localization Algorithm . . . . .	100
5.9	MRI Based Thermal Dose Monitoring . . . . .	102
5.9.1	MatMR-TD Monitor Application . . . . .	106
5.10	Experiments and Results . . . . .	108
5.10.1	Accuracy Assessment in MRI . . . . .	108



5.10.2	Active Tracking Based Probe Localization . . . . .	109
5.10.3	Results from a Preliminary Animal Study . . . . .	111
5.11	Discussion and Conclusion . . . . .	114
<b>6</b>	<b>Conclusions</b>	<b>117</b>
6.1	Dissertation Contributions . . . . .	117
6.1.1	Intraoperative MRI guided Prostate Biopsy . . . . .	117
6.1.2	Closed-loop Needle Steering under MRI Guidance . . . . .	118
6.1.3	Closed-loop Brain Tumor Ablation under Real-time MRI Guid- ance . . . . .	118
6.2	Impact of Presented Work . . . . .	119
6.3	Future Work . . . . .	120
	<b>Appendix</b>	<b>121</b>
<b>A</b>	<b>Prostate Robot Work-flow and User Manual</b>	<b>122</b>

# List of Figures

1.1	Motivation for needle steering interventions . . . . .	6
1.2	Using needle steering for accessing multiple lesion sites using single entry-point . . . . .	7
1.3	Prototype MRI-compatible robotic systems for percutaneous prostate interventions . . . . .	9
1.4	Clinically used MRI-compatible robotic systems for prostate inter- ventions . . . . .	10
1.5	Duty cycling approaches for needle steering . . . . .	12
1.6	Image-guided robotic needle steering systems . . . . .	13
1.7	Prototype MRI-compatible robots for stereotactic neurosurgery . . .	15
1.8	Clinically used MRI-compatible robotic systems for stereotactic neu- rosurgery procedures . . . . .	16
2.1	Typical prostate biopsy robot system setup . . . . .	25
2.2	Prostate robot system architecture and data flow . . . . .	28
2.3	Clinical workflow for robot assisted prostate biopsy . . . . .	30
2.4	Prostate robot CAD model . . . . .	32
2.5	Prostate robot control system block diagram . . . . .	35
2.6	Prostate robot kinematics transformation chain . . . . .	37
2.7	Surgical planning interface: RadVision . . . . .	38

2.8	Prostate robot Clinical User Interface(CUI)	40
2.9	Prostate robot restricted control and maintenance user interface	41
2.10	Prostate robot accuracy assessment	43
2.11	Prostate robot patient setup	46
2.12	Analysis of patient trial	47
3.1	Closed-loop system architecture	53
3.2	Unified imaging device interface	54
4.1	Needle steering system setup	60
4.2	Nonholonomic needle model	61
4.3	CURV needle steering model	63
4.4	CURV needle steering model: effect of changing steering effort	64
4.5	CURV needle steering model: effect of changing gaussian width	64
4.6	Closed-loop needle steering system architecture	65
4.7	Needle tracking flowchart	66
4.8	Scan geometry control for needle steering	67
4.9	Autonomous needle tracking in realtime MRI	69
4.10	Autonomous needle tracking application	70
4.11	Maximum needle deflection Vs needle curvature	71
4.12	Needle steering parameter calculation	73
4.13	Needle steering workflow	75
5.1	Stereotactic neurosurgery frames	84
5.2	NeuroBlate and ClaerPoint systems	85
5.3	NeuroAblation robot closed-loop system architecture	86
5.4	Typical NeuroAblation robot system setup	87
5.5	MRI compatible neurosurgery robots	89

5.6	Custom developed encoder interface and breakup board . . . . .	90
5.7	Custom cable design . . . . .	91
5.8	Current generation controller block diagram . . . . .	92
5.9	NeuroAblation robot Clinical User Interface (CUI) . . . . .	93
5.10	Slicer communication interface . . . . .	94
5.11	TheraVision workflow . . . . .	94
5.12	Entry point based workspace and navigation . . . . .	96
5.13	TheraVision modules for tumor ablation . . . . .	97
5.14	Slicer user interface . . . . .	98
5.15	Ablation patters for ACOUSTx <sup>TM</sup> ultrasound applicators . . . . .	100
5.16	Ablation probe construction . . . . .	101
5.17	Tracking coil localization image processing steps . . . . .	103
5.18	Ablation probe localization process . . . . .	104
5.19	MatMR-TD Monitor Application . . . . .	107
5.20	Probe localization experiment setup . . . . .	110
5.21	Probe localization results and overlay . . . . .	110
5.22	3DSlicer scene for animal study accuracy assessment . . . . .	113
5.23	Comparison of calculated versus achieved thermal dosage . . . . .	114

# List of Tables

2.1	Experimental Results of Prostate Robot MRI Phantom Study . . . .	43
2.2	Imaging Protocols for the Patient Study . . . . .	45
2.3	Accuracy Assessment of Preliminary Patient Study . . . . .	45
4.1	Accuracy Assessment Bevel Angle Controlled Steering to 5 Targets .	78
4.2	Autonomous CURV Steering Results . . . . .	79
4.3	Teleoperated Insertion CURV Steering Results . . . . .	80
5.1	NeuroAblation Robot Imaging Protocols for MRI Phantom Studies and an Animal Study . . . . .	108
5.2	Experimental Results of NeuroAblation Robot MRI Phantom Study .	109
5.3	Accuracy Assessment for One of The Animal Studies . . . . .	111

# Acronyms

**IGT** Image Guided Therapy.

**US** Ultrasound.

**CT** Computed Tomography.

**MRI** Magnetic Resonance Imaging.

**DOF** Degrees of Freedom.

**CUI** Clinical User Interface.

**IRB** Institutional Review Board.

**IACUC** Institutional Animal Care and Use Committee.

**TRUS** Transrectal Ultrasound.

**DBS** Deep Brain Stimulation.

**RCM** Remote Center Motion.

**PRF** Proton Resonance Frequency.

**TD** Thermal Dose.

# Chapter 1

## Introduction

IGT systems have become a popular clinical use-case for various surgical procedures. IGT has improved quality of the surgical procedures by leveraging enhanced visualization of surgical plan overlaid on anatomical structures of interest, using software tools such as 3DSlicer [1]. Also during the surgical procedure, three dimensional visualization of the anatomical structures, location of the surgical tools and previously prepared surgical plan assists the physician for making a better informed decision. Use of imaging for interventions such as Transrectal Ultrasound (TRUS) guided prostate cancer detection [2] and CT guided Deep Brain Stimulation (DBS) electrode placement [3] has resulted in improved procedural outcome. Though CT and US guided procedures had been common for past few decades, in recent years MRI has become a choice of imaging modality due to its superior soft tissue contrast. But, MRI poses various challenges such as constrained space, less ergonomic patient access and high magnetic field strength, limiting choice of materials suitable for the operating environment. In past decade various MRI guided robotic systems have shown promising improvements for various percutaneous interventions [4, 5]. Though such systems have made advancements, most systems still rely on preoper-

ative or in some cases intraoperative images and lack real-time imaging feedback. This thesis addresses the challenges posed to perform closed-loop, robot assisted percutaneous interventions under real-time MRI guidance.

## 1.1 Background and Motivation

MRI provides superior soft tissue image quality compared to CT and US, making it an ideal choice for image guided surgical procedures. Until recently, MRI has been in use only for diagnostic purposes, but for past decade MRI guided percutaneous interventions such as prostate biopsy, brachytherapy and tumor ablation has been studied extensively [6, 7]. Also, in recent years, various robotic devices have been developed for MRI guided percutaneous interventions. Using robotic device coupled with image guidance could improve quality of the diagnosis or treatment which relies on accurate placement of a needle like device such as a biopsy gun [8]. Presence of such a robotic device could help reduce human errors by software based surgical workflow management and 3D visualization of desired anatomical structures. Intra-operative MRI guidance has been utilized by various research groups to demonstrate that the quality of treatment could be improved. Though, MRI guided interventions could provide better treatment quality, it poses challenges such as stringent operating room environment due to strong magnetic fields, electromagnetic interference due to use of metallic objects and electronic components which are essential for functioning of a robotic device. Along with such challenges, utilizing real-time MRI brings new challenges of system integration and closed-loop control of the robotic device for trajectory correction and treatment monitoring.



### **1.1.1 Motivation for Intraoperative MRI Guided Prostate Interventions**

Prostate cancer is the second most common cancer and the second leading cause of cancer death in American men. According to the American Cancer Society, about 1 in 7 men will be diagnosed with prostate cancer and 1 in 38 will die of prostate cancer [9]. The outcome of prostate biopsy procedure for diagnosis and brachytherapy procedure for treatment depends greatly on accurate placement of the biopsy needle or radioactive seed respectively. IGT offers to improve diagnosis and therapy for prostate cancer, thanks to its capabilities for providing intraoperative image-based feedback enabling greater procedural accuracy. TRUS is the current standard imaging modality for guiding prostate biopsy and brachytherapy seed placement, but the relatively low image quality can only offer minimal specific information of the prostate tumor, which limits its ability to precisely localize suspicious focal lesions [10, 11]. MRI is an alternative and ideal modality for surgical guidance due to its ability to perform multi-parametric and high resolution soft tissue imaging without ionizing radiation [12]. However, the tightly confined scanner bore (typically 60 – 70cm in diameter) restricts the accessible space and results in awkward ergonomics for manually placing needles inside the MRI machine. To address this issue, robotic devices could be introduced for assisting needle placement, under intraoperative MR image guidance.

### **1.1.2 Motivation for MRI Guided Robot Assisted Percutaneous Interventions**

Superior image quality of MRI coupled with robotic precision has potential to improve outcome of various percutaneous interventions relying on accurate placement

of the surgical tools such as biopsy needle or ablation probe. Combining the image guidance with robotic device could bring following advantages to existing manual procedures.

1. Better surgical planning and navigation: with image guidance and robotic assistance, surgical plan could be better visualized with overlay of desired lesion, desired target location and workspace of the robotic device [13]. Such visualization ensures the reachability of the surgical site using the robotic device and hence the physician doesn't have to do tedious and sometime erogenous manual registration of the surgical scene.
2. Improved feedback: with robotic control and imaging feedback, the physician gets better overall understanding of the treatment progress. The robotic device provides accurate positioning of the surgical device, while the imaging feedback provides better visualization of the anatomical structures.
3. Safer surgical workflow: with robotic device, the surgical workflow could be improved as the physical access to the patient in a tightly constrained MRI bore is reduced only to a small portion of the procedure and in case of fully actuated robotic systems it might not be needed at all. Also, the safety could be ensured by utilizing a software application enforcing surgical workflow defined by a state machine.
4. Realtime treatment monitoring: for surgical procedures such as tumor ablation, MRI could be utilized to monitor the treatment progress using MR-thermometry providing real-time monitoring of the thermal dosage delivered to the lesion.

### 1.1.3 Motivation for Closed-loop Interventions

Most MRI guided percutaneous procedures have been utilizing intraoperative MR images to locate surgical tool during the procedure, while some procedures do utilize real-time imaging, such as tumor ablation. The next step towards improving the procedure would naturally be using the real-time feedback for improving the needle or probe placement accuracy and treatment monitoring. This inspired development of a system architecture desired to advance such percutaneous interventions towards closed-loop procedures. Closing this control loop allows real-time instrument tracking and trajectory correction. Also for procedures such as tumor ablation, it allows closed-loop monitoring and control of thermal dosage being delivered to the lesion. This thesis demonstrates two closed-loop procedures under MRI guidance: (1) closed-loop needle steering under real-time imaging and (2) closed-loop brain tumor ablation with real-time MRI based thermal dosage monitoring.

### 1.1.4 Motivation for Steerable Needle Interventions

Needle based percutaneous interventions are most common minimally invasive procedures. For procedures such as DBS electrode placement or tissue ablation, strain needle trajectories are desired. But, for procedures such as tissue biopsy or brachytherapy, sometimes it is not feasible to access the lesion with straight needle insertion. Also, tissue deformation and movement are common issues affecting the procedural accuracy. For such procedures, precurved or bevel tipped needle could be used to steer it towards the target lesion while avoiding the critical structures and compensating the tissue deformation and movement. As shown in Fig. 1.1 a steerable needle could allow access to target locations while avoiding the obstacle which would not be feasible with straight insertion trajectory [14]. Also, steerable needle could allow

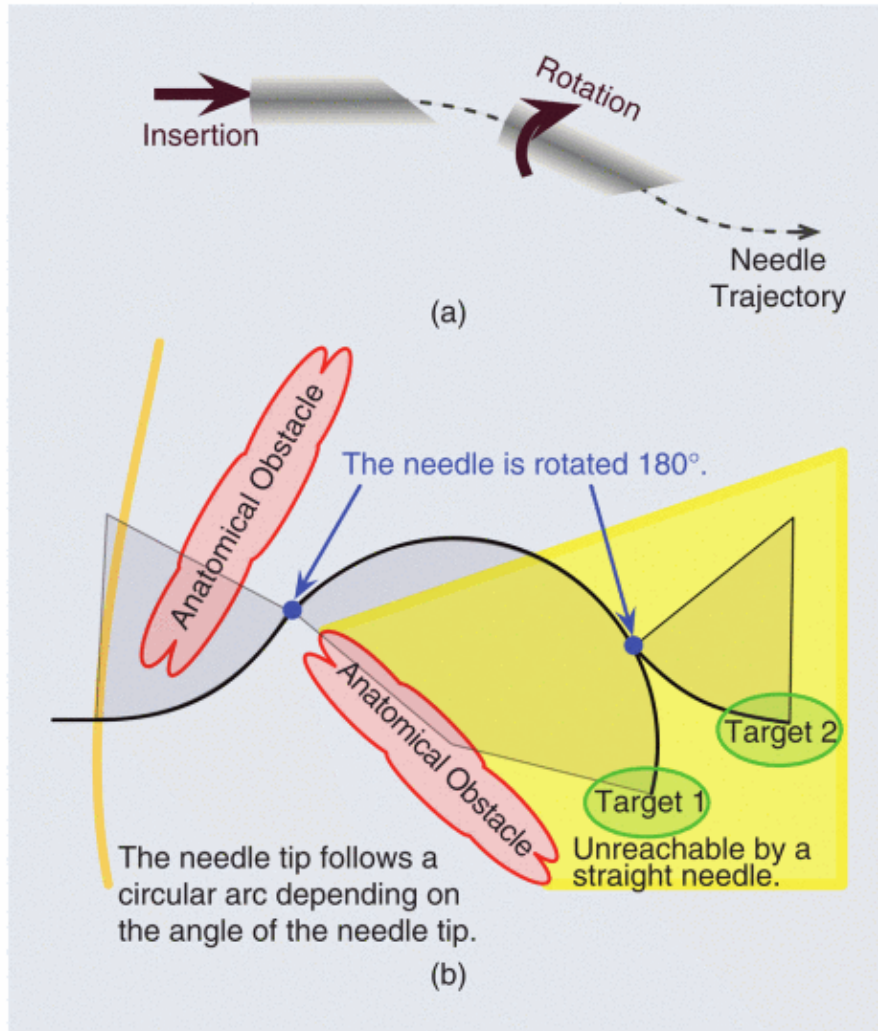


Figure 1.1: Needle steering for avoiding an obstacle while accessing a target location [14]©2008 IEEE

access to multiple lesion sites through single point of entry [15] as shown in Fig. 1.2. It is not feasible to model the tissue properties on the needle path and hence the needle curvature could not be estimated precisely. To overcome this limitation, performing such interventions with real-time image guidance could allow to reduce any modeling errors and potentially correct the trajectory of the needle as it is being inserted.

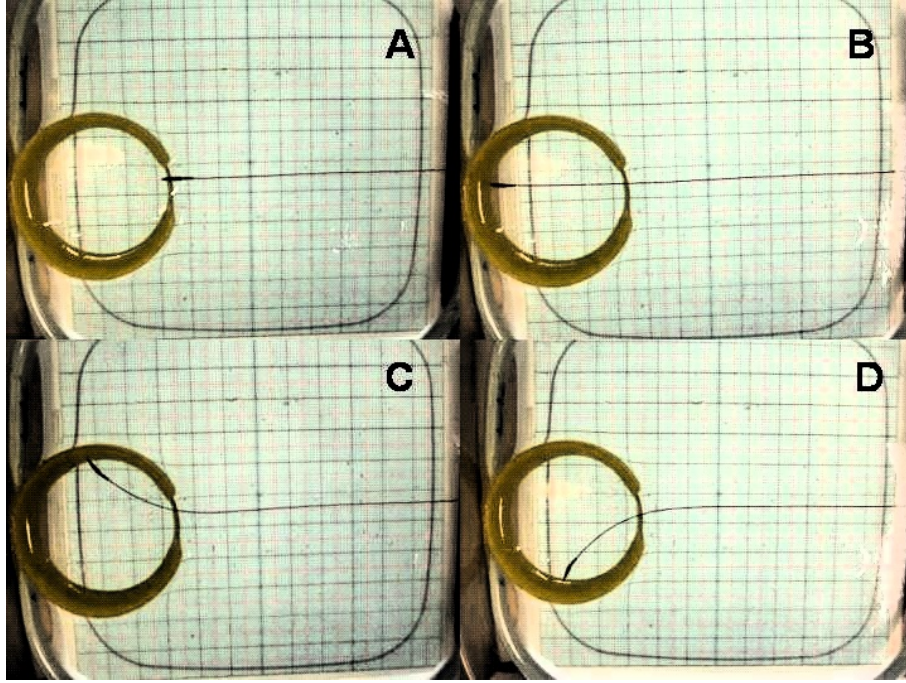


Figure 1.2: Needle steering for accessing multiple lesion sites through single entry point [15]©2006 IEEE

### 1.1.5 Motivation for MRI-guided Stereotactic Neurosurgery Interventions

Stereotactic neurosurgery is among the most common image guided surgical procedures. X-ray and CT has been in use for surgical procedures such as DBS electrode placement [3]. Compared to X-ray and CT, MRI provides better soft tissue contrast

without any ionizing radiation, making it more suitable for brain interventions. MRI guided robotic system for stereotactic neurosurgery was first conceptualized by Masamune et.al in 1995 [16]. Over last twenty years, MRI guided neurosurgery systems have advanced in terms of improved surgical planning, better procedural precision and real-time therapy monitoring. But, due to challenges posed by MRI environment, there are very few robotic systems utilizing true potential of MR imaging such as active tracking coil based therapy device localization and real-time imaging based therapy monitoring. Also, most existing robotic systems are either semi-actuated or utilizes only intraoperative MR images, which requires moving patient in and out of the bore. Developing MRI-compatible robotic system for in-bore surgical procedure could improve procedural accuracy, provide better surgical navigation and reduce patient movement in and out of the bore. Also, utilizing real-time imaging could allow therapy monitoring for surgical procedures such as tumor ablation. This thesis presents an integrated system for MRI-guided, closed-loop conformal brain tumor ablation under real-time MR imaging.

## **1.2 Literature Review**

### **1.2.1 MRI Guided Percutaneous Prostate Interventions**

Percutaneous prostate interventions are among the most common surgical procedures performed under MRI guidance. As MRI environment does not allow use of traditional electromagnetic actuators such as AC or DC motors, various research groups have developed MRI compatible actuators using pneumatic, hydraulic and piezoelectric principles. Also, many robotic device prototypes using such actuators have been developed for prostate biopsy and brachytherapy procedures. Though, MRI compatible robotic devices have been used for prostate biopsy and brachyther-

apy procedures in both research and clinical setups, most systems are still in early clinical trials.

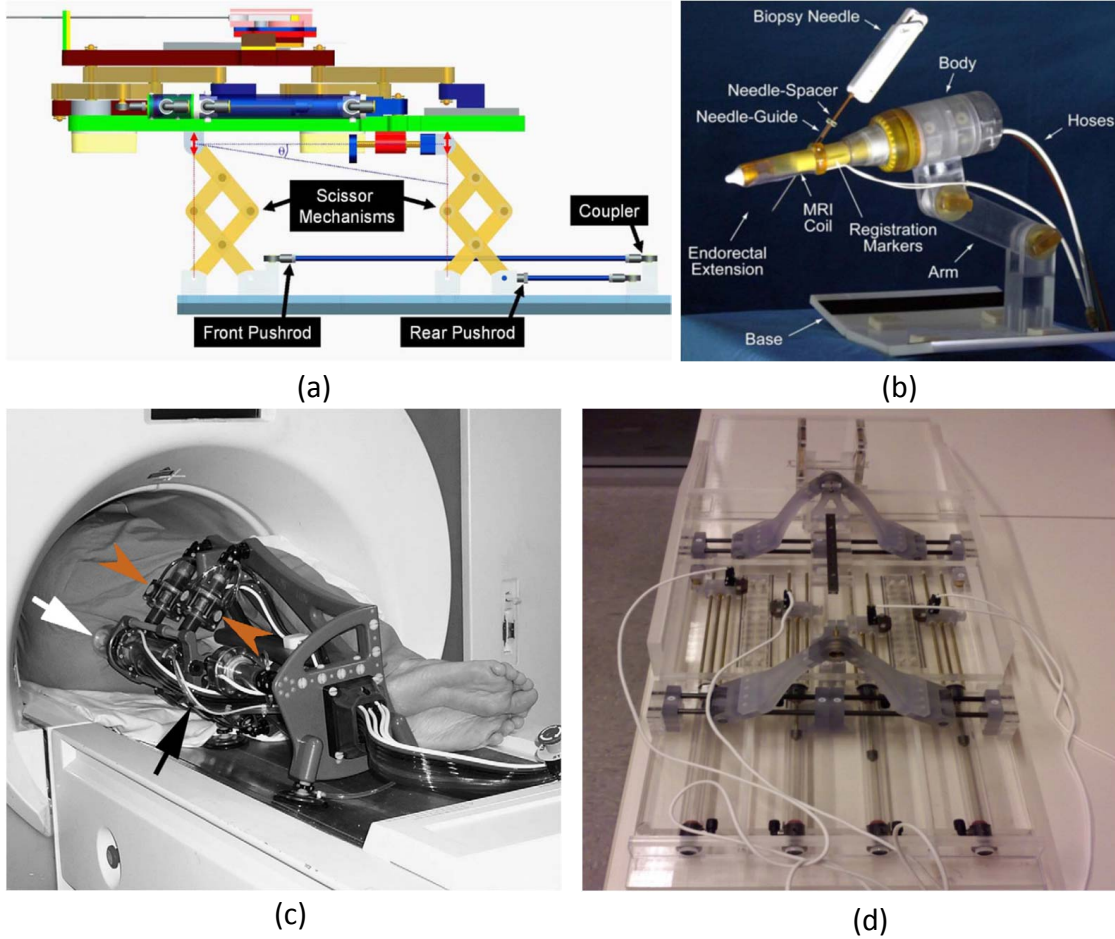


Figure 1.3: prototype systems for MRI guided percutaneous prostate interventions: (a) pneumatic robot for transperineal prostate needle placement [17]©2008 IEEE (b) PneuStep motor actuated MRI-safe robot for endorectal prostate biopsy [18]©2013 IEEE (c) MRI Stealth robot for transrectal prostate interventions [19]©2007 Taylor & Francis and (d) robot for MRI-guided transperineal prostate intervention using pneumatic cylinders [20]©2013 Wiley Online Library

Hydraulic actuation potentially could be MRI-safe, but it is seldom employed in MRI robots because of the potential for fluid leakage and cavitation [25] as well as the inconvenience of having to reset a closed hydraulic system for each use if not permanently installed. Pneumatic actuation fundamentally can be designed MRI-safe,



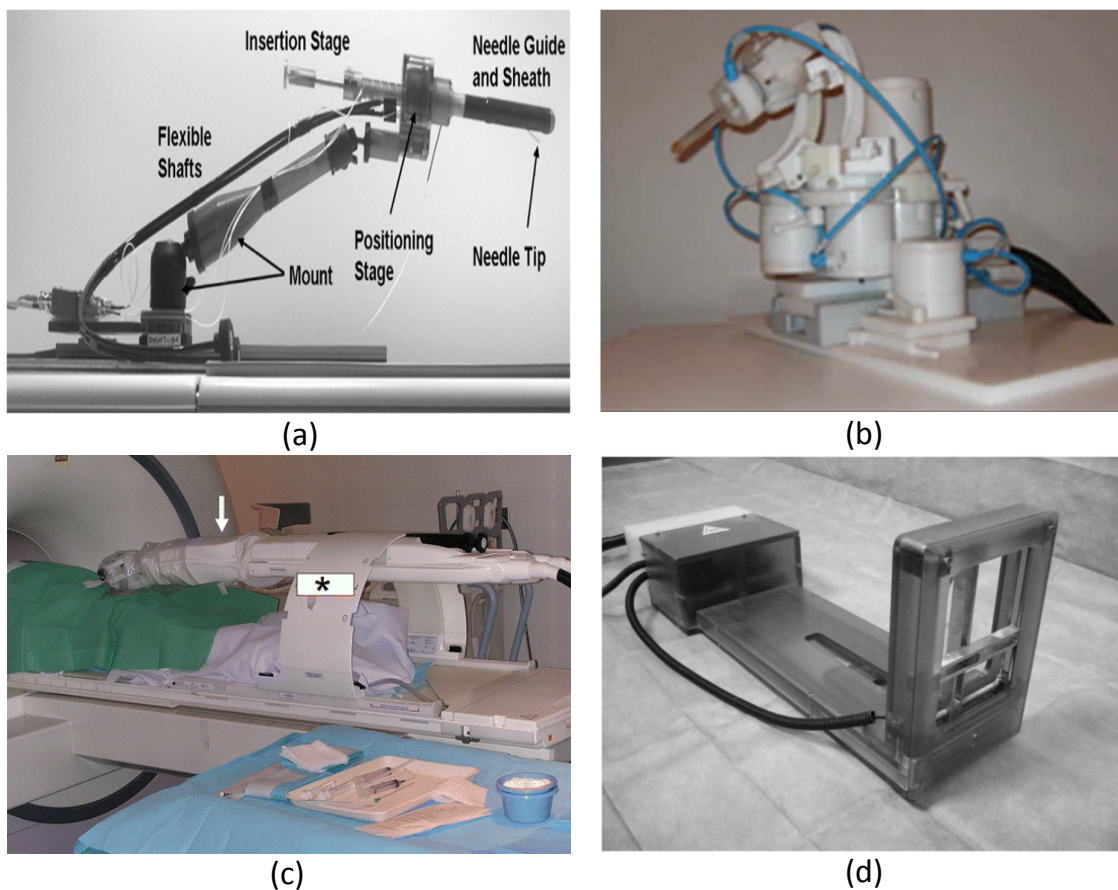


Figure 1.4: Clinically used, MRI-compatible robotic systems for prostate biopsy: (a) transrectal prostate biopsy robot using piezoelectric actuator [21]©2013 IEEE (b) Pneumatically actuated robot for transrectal prostate biopsy [22]©2011 Radiological Society of North America Inc. (c) pneumatically driven robotic system for transgluteal prostate biopsy [23]©2011 Radiological Society of North America Inc. (d) robotic needle-guidance template device for in-bore transperineal prostate biopsy [24]©2014 Wiley Online Library



and pneumatically actuated MRI robotic systems based on pneumatic cylinders include [17, 20, 26]. Also custom pneumatic actuators have been developed [27], PneuStep pneumatic step motor were developed by Stoianovici et al. [28], and have been adopted for prostate interventions [18, 19]. Schouten et al. presented a pneumatic turbine-based actuator [29] and tested it clinically for MRI-guided transrectal prostate biopsy [22]. A servo-pneumatic drive system developed by Innomotion (Innomedic, Herxheim, Germany) was applied to the first cadaver study of transgluteal biopsies [30], and then tested clinically in patients [23]. Nonmagnetic piezoelectric actuators can provide high precision positioning (submicron) with excellent dynamic performance in compact size. Song et al. presented a 2-DOF motorized needle guide template with ultrasonic motors to resemble the conventional TRUS-guided prostate intervention [31]. Krieger et al. designed a compact prototype of piezoelectrically actuated robot for transrectal MRI-guided needle intervention with 2-DOF motorized needle driver mounted on a 6-DOF passive arm [21]. Although several MRI-guided robotic systems have demonstrated feasibility of performing interventional procedures in phantom studies, only very few of them have been tested clinically including [23, 24, 32, 33]. Further development and thorough clinical certification are required to advance for clinical use, especially from the perspective of targeting accuracy, clinical workflow, safety mechanisms and sterilization. A comprehensive review of MRI-guided robotics and corresponding actuation methods are depicted in [34–36]. Fig. 1.3 shows some of the prototype systems for prostate biopsy while Fig. 1.4 shows some of the robotics systems used clinically. Though these systems have been used clinically, they utilize intraoperative MR images and lack real-time image based needle localization and closed-loop control of the robotic device based on imaging feedback.

### 1.2.2 Asymmetric-tip Needle Steering Interventions

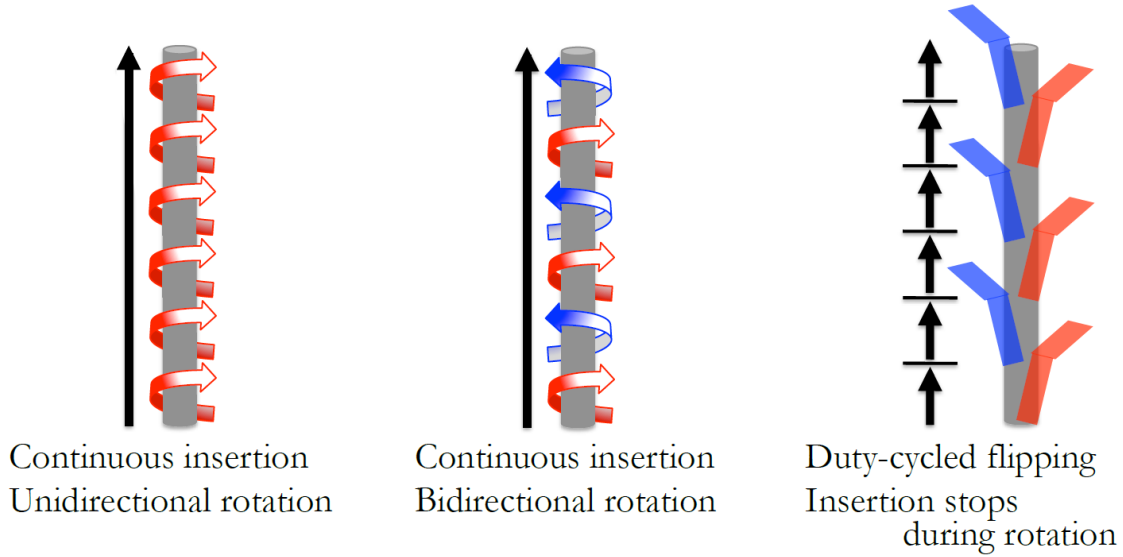
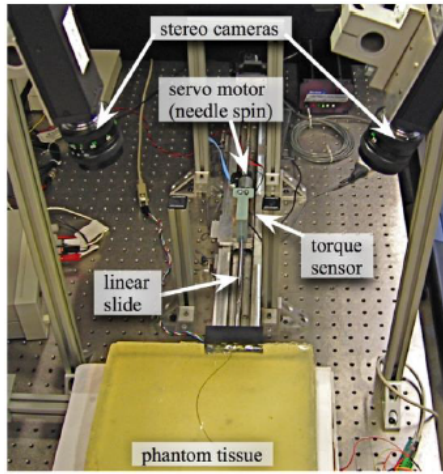


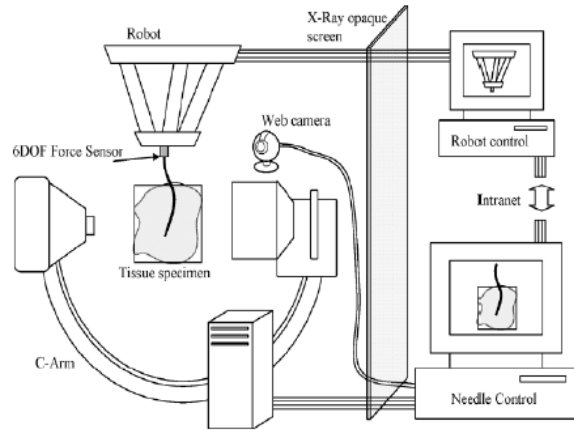
Figure 1.5: Needle steering approaches using duty cycling [37]©2014 IEEE

Needle based percutaneous interventions are among the most popular minimally invasive procedures. Needle steering approaches such as manipulation of concentric continuum tubes [42–44], precurved [45] and tip-based needle steering [14, 46] has been studied extensively. This section focuses on bevel-tipped needle steering approaches.

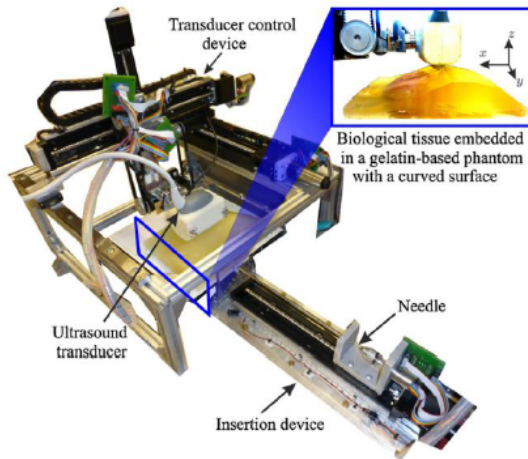
Bevel-tipped needle experiences asymmetric forces at the needle tip and results in curved path, this phenomenon could be utilized to create non-straight needle insertion trajectories. A bevel tipped needle could be used to steer the needle away from the critical tissue structure or obstacles, for example it can be used to access certain part of prostate while avoiding collision to the pubic arch. Bevel-tipped needle steering has been studied extensively and various steering approaches have been explored. Needle steering under various imaging modalities has been studied extensively. Glozman et.al [39] presented a robotic system for needle steering under real-time fluoroscopic image guidance. Minhas et.al [47] presented needle steering



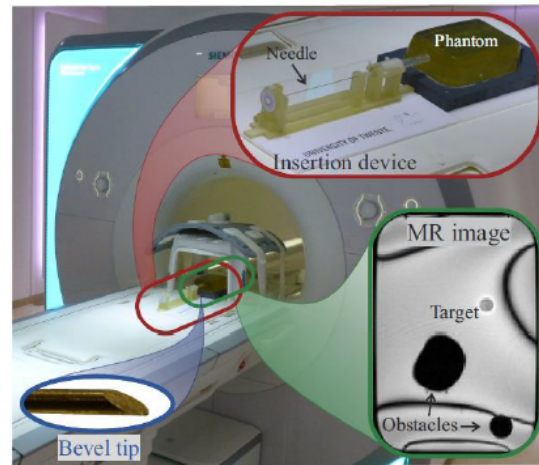
(a)



(b)



(c)



(d)

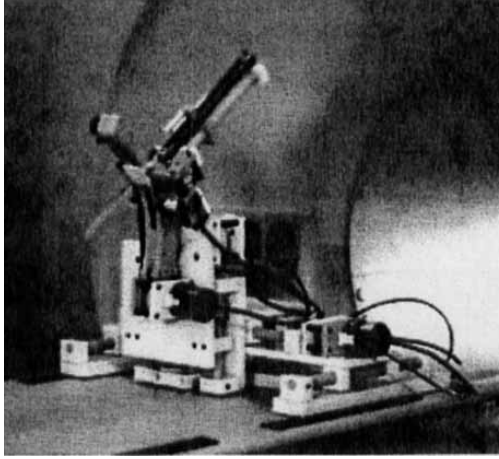
Figure 1.6: Robotic systems for image guided needle steering: (a) system with integrated planning and image-guided control for planar needle steering [38]©2008 IEEE (b) robotic flexible needle steering using virtual springs model under X-ray guidance [39]©2007 IEEE (c) robotic system for ultrasound-guided three-dimensional needle steering in biological tissue [40]©2015 Elsevier (d) intraoperative MRI guided needle steering system [41]©2014 IEEE

using duty cycled needle rotation and insertion using digital camera images, while three different needle steering approaches duty-cycled spinning (DCS), bidirectional duty-cycled spinning (BDCS), and duty-cycled bevel flipping (DCF) are presented in [37], Fig. 1.5 shows the needle insertion procedure for those approaches. Also, motion planning for image guided needle steering has been explored [48, 49].

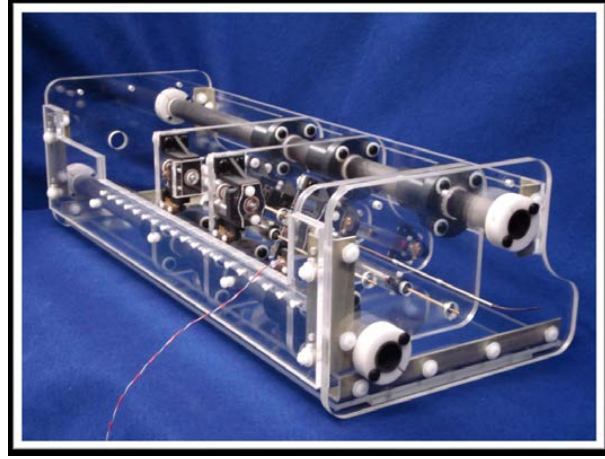
Ultrasound has been one of the most widely used imaging modality for guiding the needle steering procedures. Though ultrasound guided robotic needle steering has been studied extensively, including real-time image guidance [50–55], there are a very few works dealing with MRI guided needle steering. Hao et.al [56] presented robotic system for brachytherapy seed placement, Seifabadi et.al [57] presented tele-operated system for needle steering under MRI guidance while, Moreira et.al [41] used intraoperative MR images for feedback for performing needle steering. But, there is no work dealing with real-time MRI guided robotic needle steering till date, due to the challenges such as real-time needle tracking, scanner control and closed-loop robot control using imaging feedback. Fig. 1.6 shows some of the robotic system for image guided needle steering.

### **1.2.3 Robot Assisted Stereotactic Neurosurgery**

Stereo-tactic neurosurgery is one of the most common procedures performed under image guidance. CT has been the choice of imaging modality for past decades due to its low cost and small space requirements. But, due to better soft tissue contrast and no ionizing radiation like CT, MRI has become a better choice for brain interventions. Various MRI guided systems for tumor ablation have reached to clinical trials and have even become marketed product [5, 58, 59]. Though, some of the systems are partially automated, there is a need for fully actuated robotic assistant to reduce patient movement in and out of the MRI bore. Such a sys-



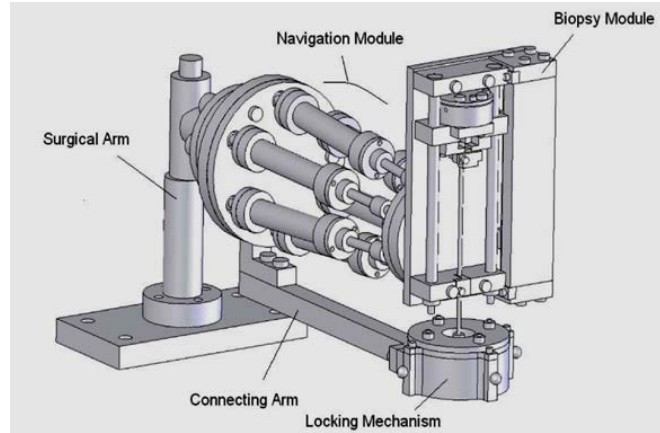
(a)



(b)



(c)



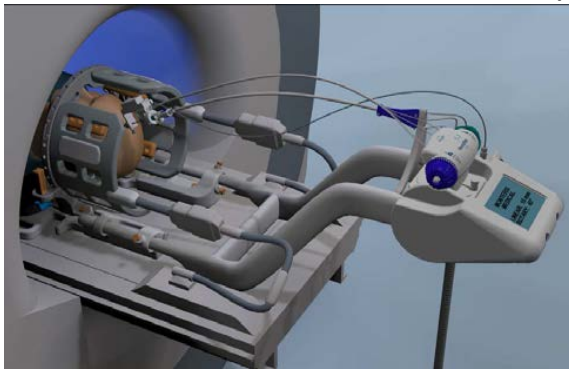
(d)

Figure 1.7: MRI compatible robots for stereotactic neurosurgery: (a) ultrasonic motors actuated needle insertion manipulator for stereotactic neurosurgery [16]©1995 Taylor & Francis (b) pneumatic robot for MRI-guided thermal ablation [60]©2012 ASME (c) meso-scale SMA-actuated MRI-compatible neurosurgical robot [61]©2012 IEEE (d) modular hydraulic/pneumatic actuated tele-robotic system for closed-bore MRI-guided neurosurgery [62]©2008 IEEE





(a)



(b)



(c)

Figure 1.8: Clinically used, MRI guided robots for stereotactic neurosurgery: (a) intraoperative MRI guided NeuroArm system [5]©2008 IEEE (b) the neuroBlate system for laser interstitial thermal therapy of brain tumors [58]©2014 Taylor & Francis (c) the ClearPoint system for interventional MRI guided stereotactic surgery [59]©2012 NIH

tem could potentially reduce overall procedure time and improve tool placement accuracy. Some commonly used robotic systems utilizing preoperative CT and/or MR images for neurosurgery are the neuromate (Renishaw Mayfield, Lyon, France), Pathfinder (Prosurge, High Wycombe, United Kingdom), the NeuroArm (University of Calgary, Calgary, Alberta, Canada) and Renaissance (MAZOR Robotics). Though these system utilizes preoperative images for surgical planning they do not consider intraoperative images. Fig. 1.7 shows of the prototype systems for stereotactic neurosurgery under MRI guidance. ClearPoint and NeuroBlate are completely MRI guided semi-robotic systems for laser based tumor ablation, but they are semi-actuated and manually operated, also they do not have a precise ablation device localization capability. Fig. 1.8 shows some of the clinically used systems for MRI guided stereotactic neurosurgery procedures. Developing a fully actuated robotic system with active tracking coil based ablation device localization and real-time thermal dosage monitoring could potentially improve overall quality of the procedure. Chapter 5 describes development of an integrated neurosurgery system for conformal brain tumor ablation under real-time MRI guidance.

### 1.3 Dissertation Overview

This dissertation discusses MRI guided, robot assisted percutaneous interventions under intraoperative and real-time image guidance. A robotic system for intraoperative MR image guided prostate biopsy, system for real-time needle steering and an integrated system for conformal brain tumor ablation under real-time MRI guidance are presented.

Chapter 2 describes development and validation of a robotic system for intraoperative MRI guided transperineal prostate biopsy. Development of a 4-DOF robotic

manipulator, low noise embedded robot control system capable of driving ultrasonic motors, surgical planning and navigation applications RadVision and 3DSlicer and a clinically usable robot control application are described. Thorough validation of the system in form of MR compatibility, targeting analysis and surgical workflow management are presented. This system has been used for 30 patient trials. During the clinical trials, we observed that the patient movement, tissue deformation and needle deflection has been some of the factors affecting the needle placement accuracy, which could potentially be improved by utilizing continuously acquired MR images in closed-loop fashion to correct the needle trajectory as needle is being inserted towards the desired target lesion.

Chapter 3 describes an architecture for closed-loop percutaneous interventions under MRI guidance. The development of intraoperative MR guided prostate biopsy system motivated development of such an architecture, which could be adopted for various procedures. Various essential components for closed-loop interventions are described and their desired functionalities are presented. This architecture is validated by closed-loop needle steering and brain tumor ablation procedures under real-time MRI guidance.

Chapter 4 presents an integrated system for closed-loop needle steering under real-time MRI guidance. A 2-DOF robotic manipulator, inserting and rotating a bevel-tipped needle is used for steering the needle towards a predefined target. To achieve fully closed-loop steering, real-time needle tracking, scanner control and needle steering algorithm are integrated. Experiments are performed in gelatin phantom, using three different steering methodologies. This system adopted the closed-loop system architecture presented in Chapter 3. Development of various system components is described and results achieved from phantom studies are presented.



Chapter 5 presents an integrated system for conformal brain tumor ablation under real-time MRI guidance. Various system modules such as: 7-DOF MRI compatible robotic manipulator, real-time Linux based embedded robot controller, custom developed encoder and robot interfaces, FDA approved ablation control system and an ablation device, surgical planning and navigation applications (TheraVision and 3DSlicer), MR thermometry and ablation probe localization using active tracking coil are presented. Development of various hardware and software components is described. Results achieved from experiments for ablation probe localization, accuracy assessment in MRI and a preliminary animal study are presented.

Finally, Chapter 6 reports dissertation contributions, impact of presented work and future work.

## **1.4 Dissertation Contributions**

This dissertation explores feasibility of performing closed-loop, robot assisted percutaneous interventions under real-time MRI guidance. A system architecture describing various system components required to perform such interventions is developed and validated. Presented work is motivated from development of an intraoperative MRI guided robotic system for prostate biopsy with open-loop image guidance, which has been used for 30 patient trials. The presented architecture is validated by performing real-time MRI guided needle steering and conformal brain tumor ablation.

### **1.4.1 Intraoperative MRI guided Prostate Biopsy**

Developed and integrated an intraoperative MRI guided robotic system for transperineal prostate biopsy. Evaluated needle placement accuracy in gelatin phantom stud-

ies, optimized surgical workflow and developed patient safety mechanisms necessary for clinical trials. Supported 30 patient trials at Brigham and Womens' hospital.

### **1.4.2 Architecture for Closed-loop MRI Guided Interventions**

Proposed an architecture for performing closed-loop percutaneous interventions under MRI guidance. Described various system components and desired functionalities necessary to develop and validate such a system. Validated proposed architecture by performing closed-loop needle steering and conformal brain tumor ablation under real-time MRI guidance.

### **1.4.3 Closed-loop Needle Steering under MRI Guidance**

Developed real-time needle tracking and MRI scanner control system components, and integrated them with an MRI compatible robot and needle steering algorithm to perform closed-loop needle steering under real-time MRI guidance. Validated autonomous bevel angle controlled, Gaussian-based Continuous Rotation and Variable (CURV) Curvature Steering Model based and teleoperated insertion based needle steering approaches.

### **1.4.4 Closed-loop Brain Tumor Ablation Under Real-time MRI Guidance**

Developed robot controller, robot control application, surgical planning and navigation interfaces, active tracking coil based ablation probe localization algorithm and real-time MRI based thermal dose monitoring application needed for performing MRI guided conformal brain tumor ablation. Developed communication interfaces

between these system components to delivery an integrated system. Also, validated the integrated system accuracy in gelatin phantom and preliminary animal studies.

## Chapter 2

# Intraoperative MRI Guided Robotic System For Prostate Biopsy with Open-loop Image Guidance

### 2.1 Contributions

This chapter describes development of a robotic system for MRI guided prostate biopsy. MRI Compatible robotic manipulator was developed by our collaborator at Johns Hopkins University, while me and my colleagues at AIMLab designed and developed robot controller compatible with the MRI environment ensuring least interference with the MRI system. I developed low level motion control firmware and added safety and reliability features needed to ensure patient safety, including surgical workflow management ensuring that the user induced errors are detected and feedback is provided to the system operator and physician. Also, Clinical User In-

terface (CUI) was developed to assist surgeon with all necessary information in the operating room during the surgical procedure. I played an instrumental role in integrating various system components such as robot, embedded robot controller, robot control application and surgical planning and navigation applications (RadVision and 3DSlicer). Though, I have participated at every stage in system development, my contributions come from software development and system integration leading to translation of a prototype system to an operating room. Also, I along with my colleagues designed and performed system accuracy and MRI compatibility experiment needed for validation of integrated system before using it in clinical settings. The final version of clinically optimizes system has been used at Brigham and Womens' hospital for 30 patient trials after obtaining an IRB approval(#2000P001520, PI: Kemal Tuncali, M.D).

## **2.2 Introduction**

Percutaneous prostate intervention are among the most common surgical procedures performed under MRI guidance. The outcome of prostate biopsy procedure is closely coupled to accurate placement of the biopsy needle. Robotic device under intraoperative MR image guidance could improve the needle placement accuracy. But, development of robotic systems in the MRI environment poses challenges such as the strong magnetic (usually 1.5T to 3T) and radio frequency (RF) fields. Ferromagnetic materials can be exposed to extremely strong magnetic force and may be a fatal safety hazard. Hence, electromagnetic actuators (e.g. typical DC motors), are contraindicated for use in the MRI room. Further, electric signals may cause significant image degradation due to electromagnetic interference. The American Society for Testing and Materials (ASTM) classified the devices for the MRI environment

as MRI-safe, MRI-Conditional and MRI-Unsafe (ASTM F2503). Significant efforts have been investigated to overcome these critical issues for MRI-compatible robotic systems. In terms of actuation principles, MRI-guided robotic assistants for prostate interventions may be classified as hydraulic, pneumatic, and piezoelectric actuation.

Although the pneumatic actuation has the intrinsic features of being MRI-safe, its major limitations are the difficulty of precise and stable servo control, especially when long pneumatic transmission line is utilized, and relatively bulky profile compared to piezoelectric actuators.

Nevertheless, significant image degradation is a major problem for piezoelectric actuators utilizing off-the-self drivers. MR image signal-to-noise ratio (SNR) may be reduced by as much as 80% without RF shielding, and even with RF shielding the SNR may still be degraded by 40% - 60% [21,63]. In our previous work, we have developed a custom MRI robot controller to drive piezoelectric actuators [64]. With this, we developed a prototype of fully actuated MRI-guided prostate intervention robot, which demonstrates that SNR reduction can be limited to 15% [65,66].

Prostate biopsy procedure could be performed with four different approaches: (1) transrectal, (2) transperineal, (3) endorectal and (4) transgluteal. This chapter presents the integrated system for robot assisted transperineal prostate biopsy and its components.

## **2.3 System Architecture and Clinical Workflow**

### **2.3.1 System Architecture**

This system is developed to optimize a typical prostate biopsy procedure under MRI guidance by assisting the manual procedure using a robotic needle alignment device. Though optimized for prostate biopsy procedures, it adopts a modular design ap-

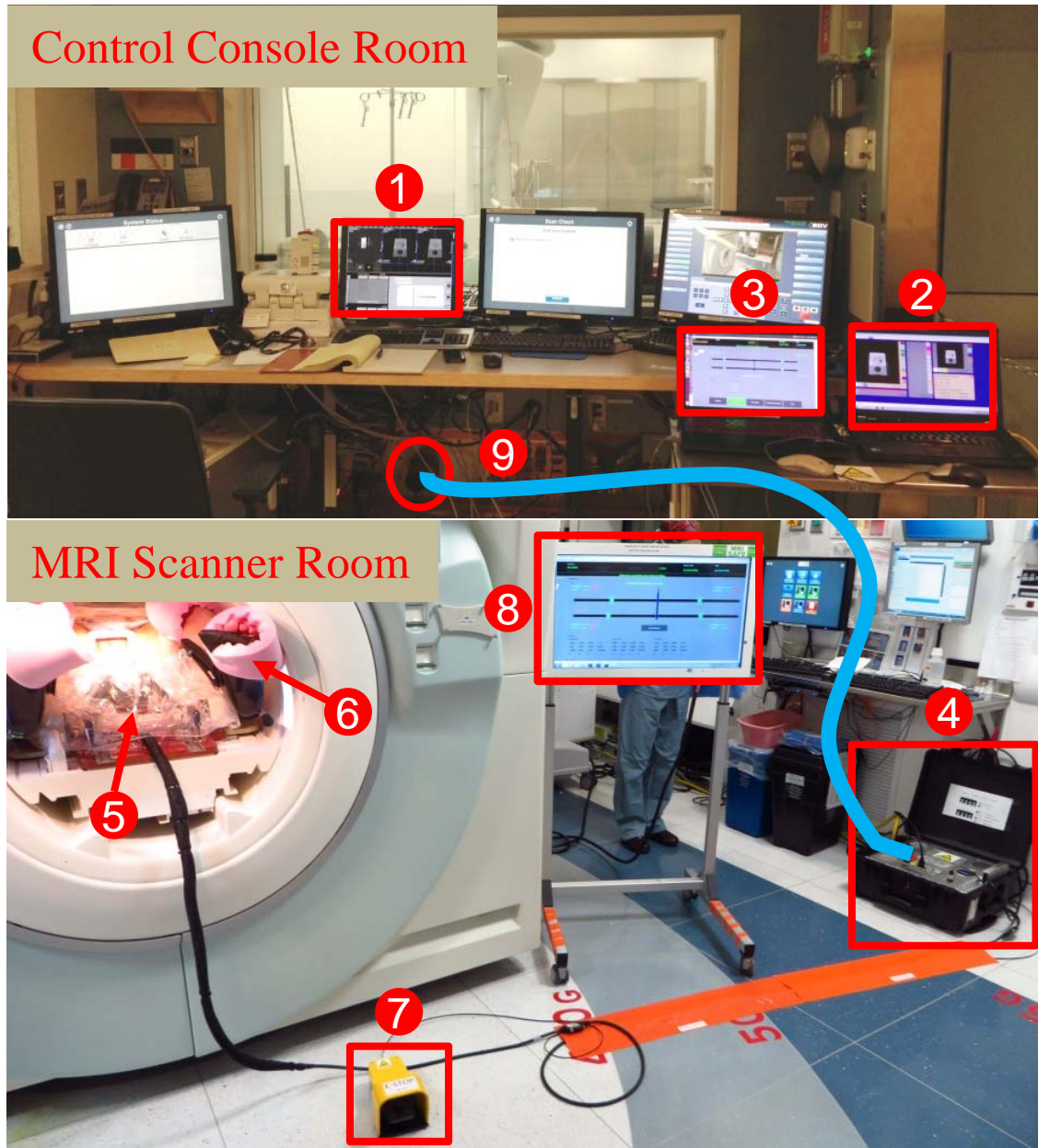


Figure 2.1: Clinical system configuration. In the control console room: (1) MRI control console, (2) surgical navigation user interface, and (3) robot control software. Inside the scanner room: (4) MRI compatible robot controller, (5) robotic manipulator inside the scanner bore covered with sterile drape, (6) patient lying inside the scanner bore in semi-lithotomy position, (7) foot-pedal, and (8) MRI-compatible display showing robot status to the clinician. Communication between the control room and scanner room is through (9) fiber optic cable.

proach making the architecture capable of supporting various needle-based interventional procedures. The system comprises four major modules: 1) surgical planning and navigation user interface, 2) robot control software, 3) MRI-compatible robot controller, and 4) needle placement manipulator. In the beginning of the procedure, 3D-Slicer [1] is used to prepare the surgical plan by registering the intraoperative images to the preoperative planning images based on the deformable registration method [67]. Targets now defined in the intraoperative images are transferred to the surgical navigation user interface RadVision<sup>TM</sup>, a brachytherapy treatment planning system that has received FDA 510(k) clearance (Acoustic MedSystems Inc., IL, USA). RadVision visualizes the targets in image space, registers the robot's coordinate frame to the MR images, and forwards the registered targets to the robot control software via OpenIGTLink communication protocol [68].

The robot control software computes the robot kinematics and motion control plan, resolving the targets from task space (patient coordinates) to joint space (robot motions). The custom MRI robot controller is developed to provide high precision and low noise closed-loop control of the ultrasonic piezoelectric motors. Fiber optic Ethernet, running through the patch panel of MRI scanner room, establishes the connection between the robot control software (running on a computer in the console room) and robot controller (residing beside the MRI scanner), to eliminate the transmission of any electrical signals into the scanner room that may introduce noise during imaging. Fig. 2.1 illustrates the clinical system configuration, distinguishing the components inside the MRI scanner room and the control console room. Fig. 2.2 further depicts the system architecture and data flow between various modules of the system.

Communication between all of the modules is through network-based media (except between robot controller and physical manipulator which is shielded cable with



differential signaling). This implies that not only each module's operating platforms (e.g. Windows, Linux, and OS X), but also the programming languages (e.g. C++, C, Java) are independent. Moreover, each module of this system could be potentially replaced with other modules of equivalent functionality (e.g. the robot manipulator designed for prostate biopsy in this study could be replaced with another manipulator designed for stereotactic neurosurgery [64]) or a simulation at any level to aid in development and validation.

### **2.3.2 Clinical Workflow**

The clinical robot-assisted workflow is intended to mimic that of the traditional template-based prostate interventions [69], allowing similar location of surgical personnel and use of standard equipment. The primary workflow steps are as follows:

1. Place patient board inside MRI scanner bore, position patient on the board in semi-lithotomy position.
2. Image the fiducial frame (attached to patient board) and the prostate of patient.
3. Register the robot to image space (i.e. patient coordinates) based upon fiducial frame images.
4. Register intraoperative images to preoperative images and define/confirm the targets.
5. Initialize the robot outside the scanner bore.
6. Cover the robot with sterile drape and attach the sterile needle guide.
7. Slide the robot into the patient board and lock in place.

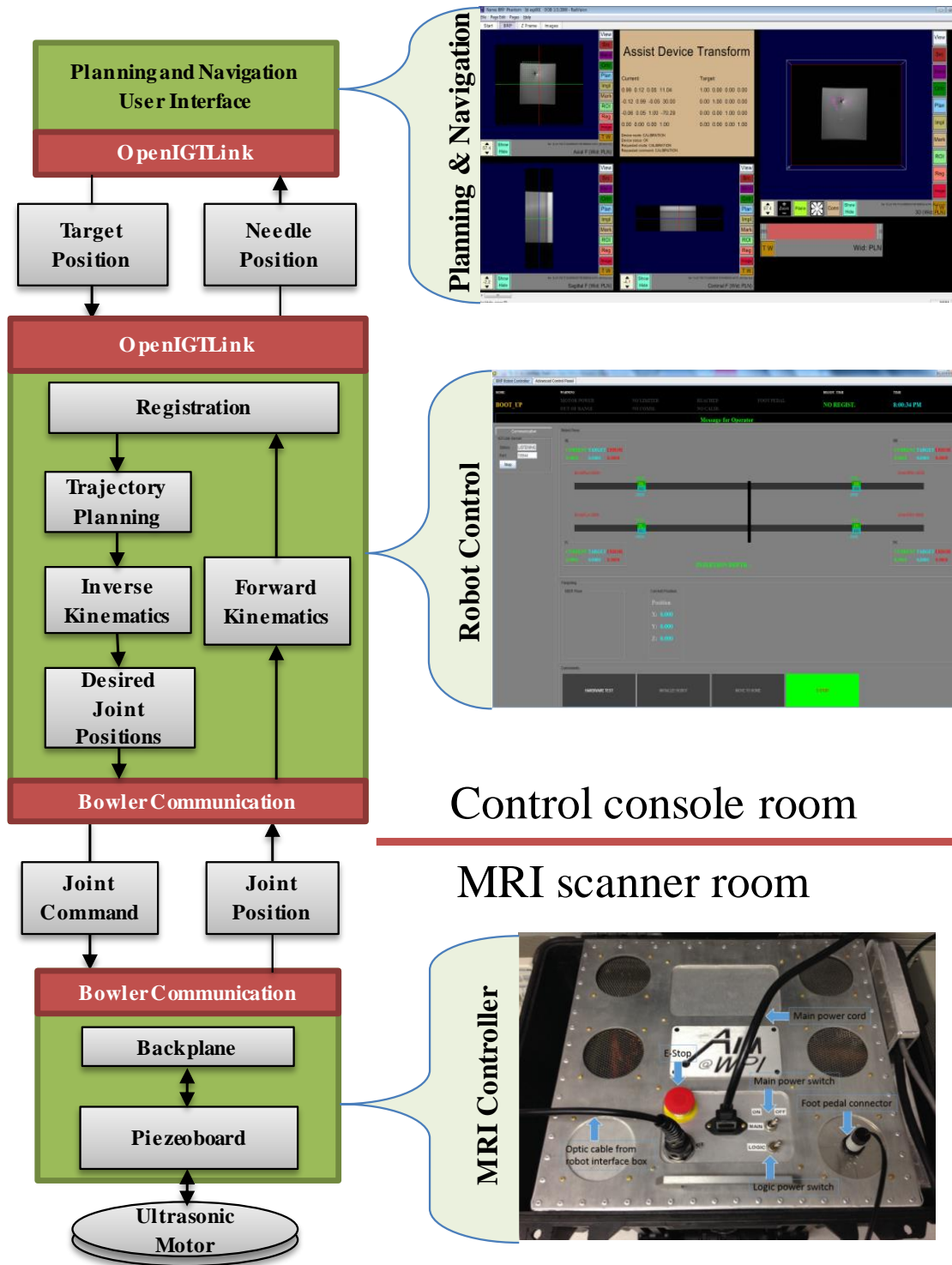


Figure 2.2: System architecture and data flow: Left) Primary system modules and data flow among them using OpenIGTLink and Bowler communication protocols, Right) Corresponding software and hardware components.

8. Set a target in image space using navigation user interface.
9. Align the robot automatically and insert the needle manually.
10. Take confirmation images to verify needle tip position.
11. Collect biopsy sample and retract the needle manually.
12. Repeat steps 8 – 11 for each suspected lesion.

Patient preparation including patient positing, anesthesia, and configuring the sterile field matches the conventional template-based procedures, helping ensure a level of comfort among the clinical team with the use of the robotic device. For aligning the robot manipulator and inserting the needle, the workflow is managed and enforced by the robot control software. Fig. 2.3 illustrates the robot control workflow and corresponding stages of the clinical procedure. The well-defined steps of the finite state machine are ensured in both the user interface and robot control software, guiding the user. The system ensures that the workflow transitions are enforced, allowing only validated state transitions to pass through. Invalid transitions (e.g. sending target without a valid registration) are abandoned and reported to the user. Once the robot manipulator is aligned (with motion only occurring while a foot-pedal is asserted), the actuators are locked to prevent any unintentional motion during the needle insertion stage.

## **2.4 Electromechanical System Design**

### **2.4.1 Needle Placement Parallel Manipulator**

The robot manipulator is designed to perform in-bore prostate transperineal interventions with the patient lying in the supine position and legs in the semi-lithotomy

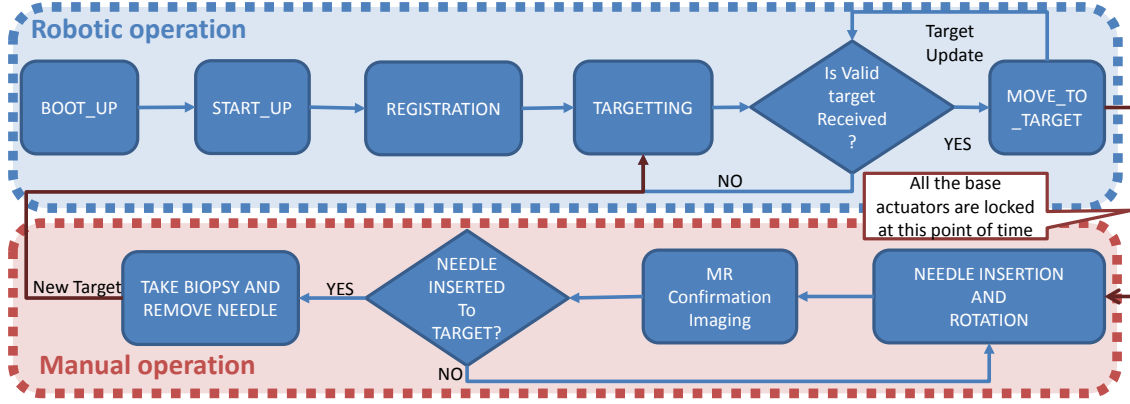


Figure 2.3: Flowchart of the robot control workflow and robot operation modes, showing only valid transitions from one state to another.

configuration. To cover the entire volume of prostate and accommodate patient variability, the manipulator is designed to provide 4-DOF actuated motion (2-DOF translation and 2-DOF angulation) for aligning the needle with two trapezoid stages, as shown in Fig. 2.4. Each trapezoid stage is constructed of a U-shape frame supported by two parallelogram linkage mechanisms on linear sliders. The sliders are actuated by a lead-screw mechanism driven by an ultrasonic piezoelectric motor (USR60-S4N, Shinsei Corp., Tokyo, Japan) via a pulley-belt mechanism. The two trapezoid stages are connected through two rigid bars with ball-socket joints at the front and spherical joints at the rear to allow angulation. A needle guide is attached on top of the trapezoid stages via spherical joints on the rigid bars for guiding the needle insertion trajectory. Two guide holes are incorporated into the needle guide with a vertical spacing of  $35mm$  to enhance the reachable workspace and account for patient anatomy and placement variability. The robot manipulator platform slides into the patient board on two linear rails and is repeatably locked in place with locking screws. The sterile fiducial frame comprises nine embedded MRI-visible fluid tubes (MR-Spots, Beekley Corp., Bristol, CT) is repeatably fixed on the centerline of the patient board. The fiducial tubes are configured in three sets of “Z” shapes

in three orthogonal planes, as described in Section IV-A. The fiducial frame is also used to help constrain the skin of the patient’s perineum and maintain the robot’s workspace between the patient’s legs.

In terms of the materials, three main factors are considered: MRI compatibility, stiffness, and sterilizability. The manipulator is made of non-ferrous materials to be compatible with MRI environment. The body of the robot, including the trapezoid stages, is machined with high strength Polycarbonate filled with 20% fiberglass to maintain high stiffness of the mechanism. The needle guide and fiducial frame, which have direct contact with patient, are 3D printed with biocompatible Ultem (Polyetherimide) and Polycarbonate, respectively. The sterile components have been certified by Nelson Labs (Salt Lake City, UT) for sterilization using Sterrad 100S system (Advanced Sterilization Products, Irvine, CA). All the other components of the manipulator are covered with a disposable, pre-sterilized clinical plastic drape to create the sterile environment. Detailed descriptions of mechanism design, robot kinematics, and workspace analysis were presented in our previous work [70].

## 2.4.2 Ultrasonic Piezoelectric Actuators

Piezoelectric actuators are driven by the controlled oscillation of ceramic crystals based on the piezoelectric effect. Magnetism utilized by typical electromagnetic motors and clearly contraindicated for use with MRI is therefore not required, making piezoelectric actuators a popular class of actuators in the MRI environment. In terms of driving signal, piezoelectric actuators can be classified into two main categories: harmonic and non-harmonic. Harmonic actuators, such as Shinsei, Nanomotion (Nanomotion Ltd., Yokneam, Israel), and DTI (Discovery Technology International, Inc., Sarasota, FL) are driven by sinusoidal waveform on two channels at high frequency (typically  $20kHz - 200kHz$ ). Non-harmonic actuators, such as

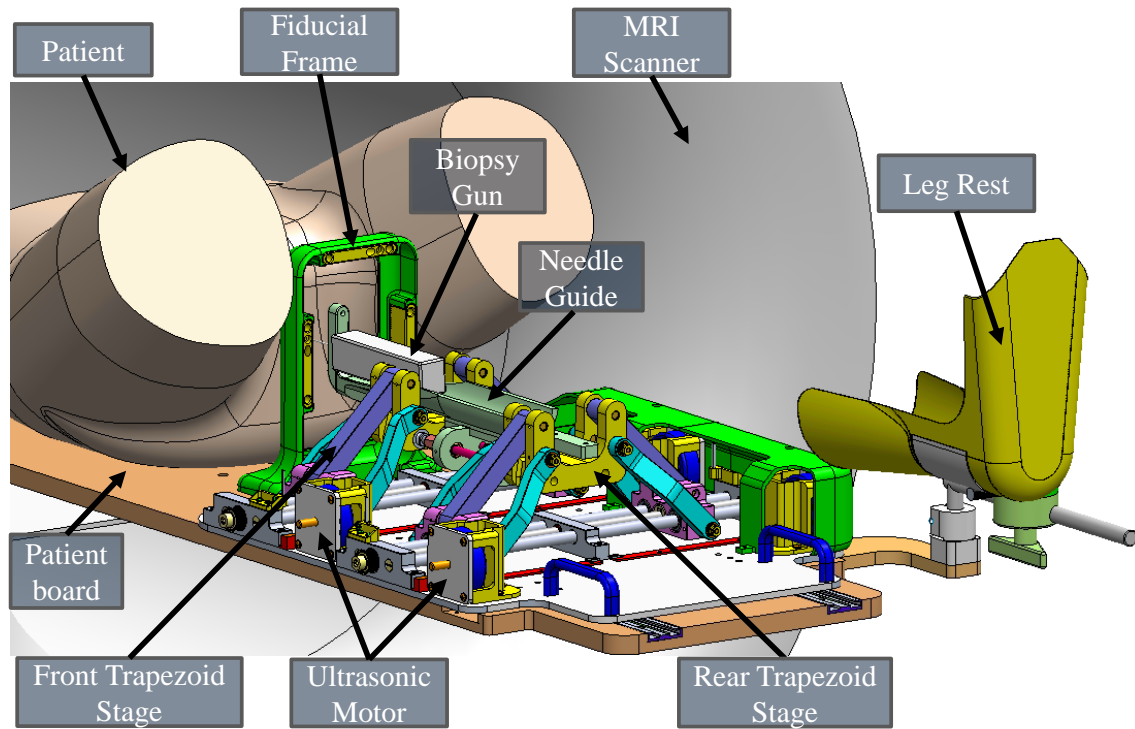


Figure 2.4: Annotated CAD model of the parallel manipulator for transperineal prostate intervention inside the MRI scanner bore. The patient lies in the supine position, the robotic manipulator is placed between the legs, and a biopsy gun targets the prostate through the perineum. Note that the leg rest and motor covers are hidden on the left side to visualize the internal structure of the manipulator.

PiezoLegs (PiezoMotor, Uppsala, Sweden), are generally driven by more complex shaped waveform on four channels at lower frequency ( $750Hz - 3kHz$ ). The Shinsei harmonic ultrasonic actuator is adopted in this robotic system, due to its unique characteristics of high torque output, self-retention, and compactness.

The Shinsei actuator is comprised of a rotor and a stator. The stator is made of elastic body and piezoelectric ceramic unit. Two sinusoidal high frequency waveforms with  $90^\circ$  phase shift are applied to the piezoelectric ceramic unit to generate two standing waves on the elastic body, combining to generate a traveling wave that provides ultrasonic vibration to move the rotor and thus drive the motor. The two sinusoidal driving waveforms are generated by the corresponding Shinsei D6060 motor driver, which requires two channel input signals to control the driver output. A previously developed custom MRI robot controller [65] was adapted for this robotic system with appropriated modifications and improvements to interface with Shinsei motor drivers and control the robot.

### 2.4.3 MRI Robot Controller

The MRI robot controller consists of two primary components within a shielded enclosure: 1) The backplane which includes an embedded controller that coordinates the motion control information from the planning level with the device level and 2) piezoelectric driver cards which generate control signals and perform closed loop motion control of the ultrasonic motors. The block diagram of the controller system is depicted in Fig. 2.5. The backplane exchanges control data with high level control PC via fiber optic Ethernet, and then forwards the data to each driver card via the serial peripheral interface (SPI) bus. The drivers process a proportional-integral-derivative (PID) control loop with data acquired from high level motion information and low level robot sensor feedback to generate control commands through a

direct digital synthesizer (DDS), based on a microcontroller (PIC32MX460F512L, Microchip Technology Inc., Chandler, AZ, USA) and field-programmable gate array (FPGA) (Cyclone EP2C8Q208C8, Altera Corp., San Jose, CA, USA). The output digital command is converted to analog signal through high-speed digital-to-analog converters (DACs) (DAC2904, Texas Instruments Inc., Dallas, TX, USA) and passes from linear amplifier out to the Shinsei motor driver through  $\pi$  filters. Optical encoders with differential drivers (EM1-1-1250-I and PC4, US Digital, Vancouver, WA, USA) are used for position feedback, which has been proved to be compatible with MRI environment. The incorporation of precise DDS, high performance DACs, linear amplifiers, and  $\pi$  filters enables precise waveform shape control while precluding electrical noise. A further technique to reduce the electrical noise is enclosing all electronics including power regulation in an electromagnetic interference (EMI) shielded aluminum enclosure acting as a Faraday cage.

Safety and reliability are crucial design considerations for a robotic system used in a clinical environment. To this end, several safety mechanisms are introduced into the controller design. A non-metallic foot pedal equipped with a fiberoptic photoelectric sensor is utilized by the clinician as an interlock for enabling motion only when engaged. Custom optical limit switches are installed on both ends of the four sliders to prevent the robot from reaching hard stops at the edge of the mechanism and damaging the robot. Stall detection based on the encoder feedback is used to monitor the robot motion status. In case of malfunction detected (i.e. encoder reading lost, jumped, or updated incorrectly), the stall detection mechanism automatically triggers a solid state relay that disconnects motor power and thus stops the robot motion. An emergency-stop switch installed in the power chain between the 24V regulator and the motor driver can directly shut down the motor power manually by the users, independent of any software components, in case of any



urgent robot failure. LED indicators mounted on the upper surface of the controller box indicate the status of each piezoelectric driver board with varying color codes for the clinician.

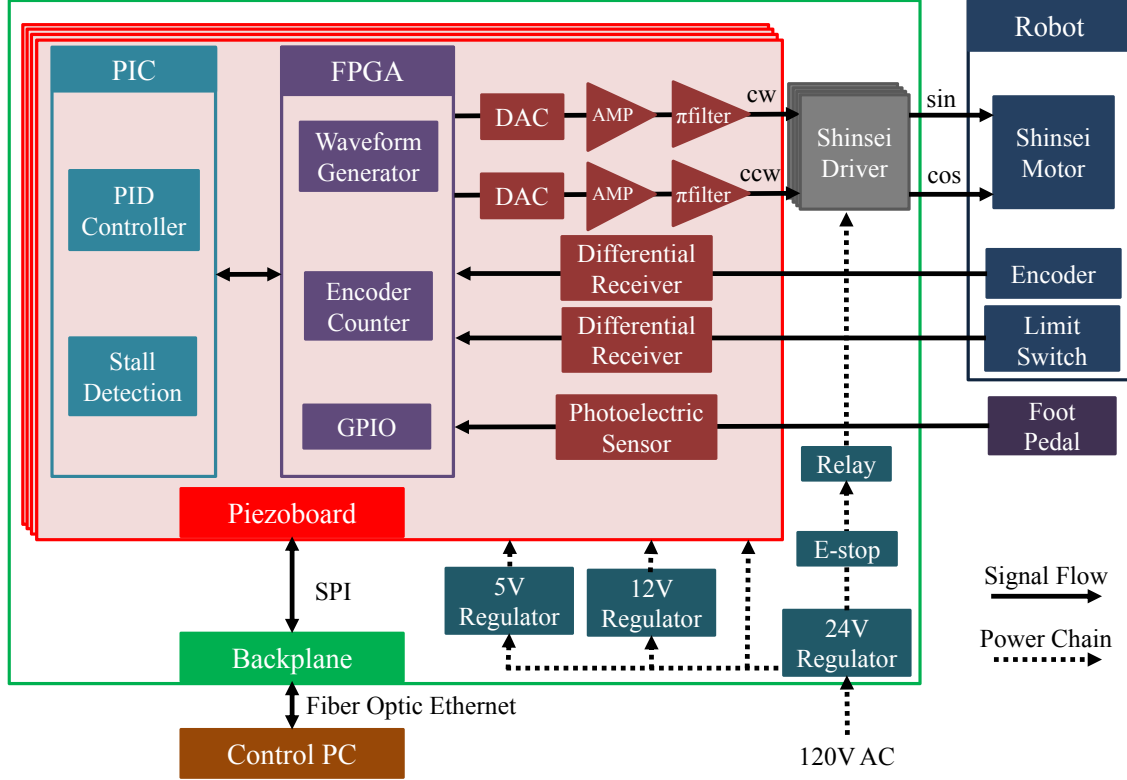


Figure 2.5: Block diagram depicting major components of the controller system. The controller is powered by the isolated, grounded 120V AC supply in the MR scanner room. All the power, control, and driver electronics are encased in an EMI shielded enclosure while communicating with the control PC through fiber optic Ethernet.

## 2.5 Navigation and Robot Control Software

### 2.5.1 Robot Registration and Surgical Navigation

3D Slicer and RadVision are used for surgical planning and navigation. The surgical plan is prepared using multi-parametric images, based on which targets are

defined in suspected lesions on preoperative digital imaging and communications in medicine (DICOM) format images which are pushed to the 3D Slicer workstation. In the beginning of the procedure, intraoperative images are acquired and deformable registration is performed using 3D Slicer to relate the surgical plan from preoperative images to intraoperative images. The registered surgical plan (i.e. targets in patient coordinates) are transferred to the navigation software RadVision over a network via OpenIGTLink and shown to the clinician for the visual confirmation.

Fiducial frame based registration is performed to register the robot to the patient coordinate system (i.e. MRI image space in right-anterior-superior (RAS) coordinates). Images of the fiducial frame are acquired and the DICOM images are pushed to RadVision, which then calculates the robot registration transform using line marker registration which has reported registration accuracy of  $1.00 \pm 0.73mm$  and  $1.41 \pm 1.06^\circ$  [71]. The calculated registration transform is sent over a network via OpenIGTLink to the robot control application, where it is used to calculate the 6-DOF needle tip pose in patient coordinates through the transformation chain as shown in Fig. 2.6.

The patient anatomy may be visualized in RadVision in the perspective of axial, sagittal, coronal as well as combined 3D view for monitoring the needle track and confirming actual target positions. During the procedure, targets defined in patient coordinates at the time of surgical planning are selected in RadVision, and then sent to the robot control software described in Section 2.5.2 using the OpenIGTLink protocol. On receiving the desired target transform, the robot control application calculates desired joint positions using robot registration transform and inverse kinematics. Desired joint positions are sent to the robot controller via the Bowler communication protocol [72] and the robot awaits foot pedal engagement by the clinician to initiate motion.

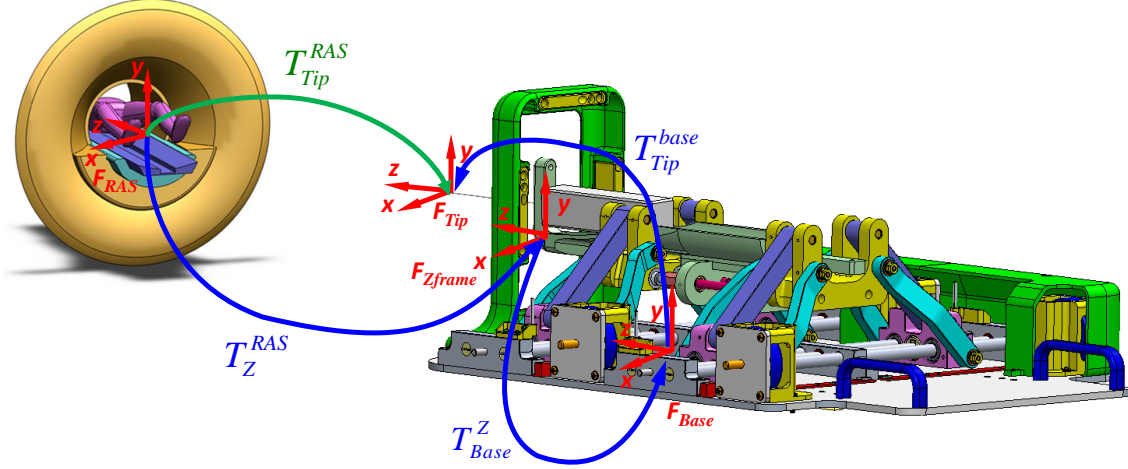


Figure 2.6: Kinematic transformation chain for registering the robotic system to the MR scanner coordinate system (RAS coordinates) based on imaging of the fiducial frame (Z-frame).

### 2.5.2 Robot Control Software

The robot control software is developed in Java with the capability to: define robot description using extensible markup language (XML), compute forward and inverse kinematics, generated coordinated motion commands, communicate via OpenIGTLink, and provide user interfaces for clinicians and system operating engineers. The robot control application ensures the clinical workflow by coordinated communication with robot controller and the navigation software. Two user interfaces, (1) CUI (clinician user interface) : minimalistic interface for clinicians and (2) CMUI (control and maintenance user interface) : restricted access low level interface for engineers to troubleshoot and maintain the robot controller are part of the robot control application as shown in Fig. 2.8 and Fig. 2.9, respectively.

The CUI panel is displayed during the intervention as identified by #8 in Fig. 2.1 illustrates, and is composed of five modules: 1) The controller status module indicates the control mode, target range warning, hardware errors, and target status. 2) Communication status shows the server port number and connection status.

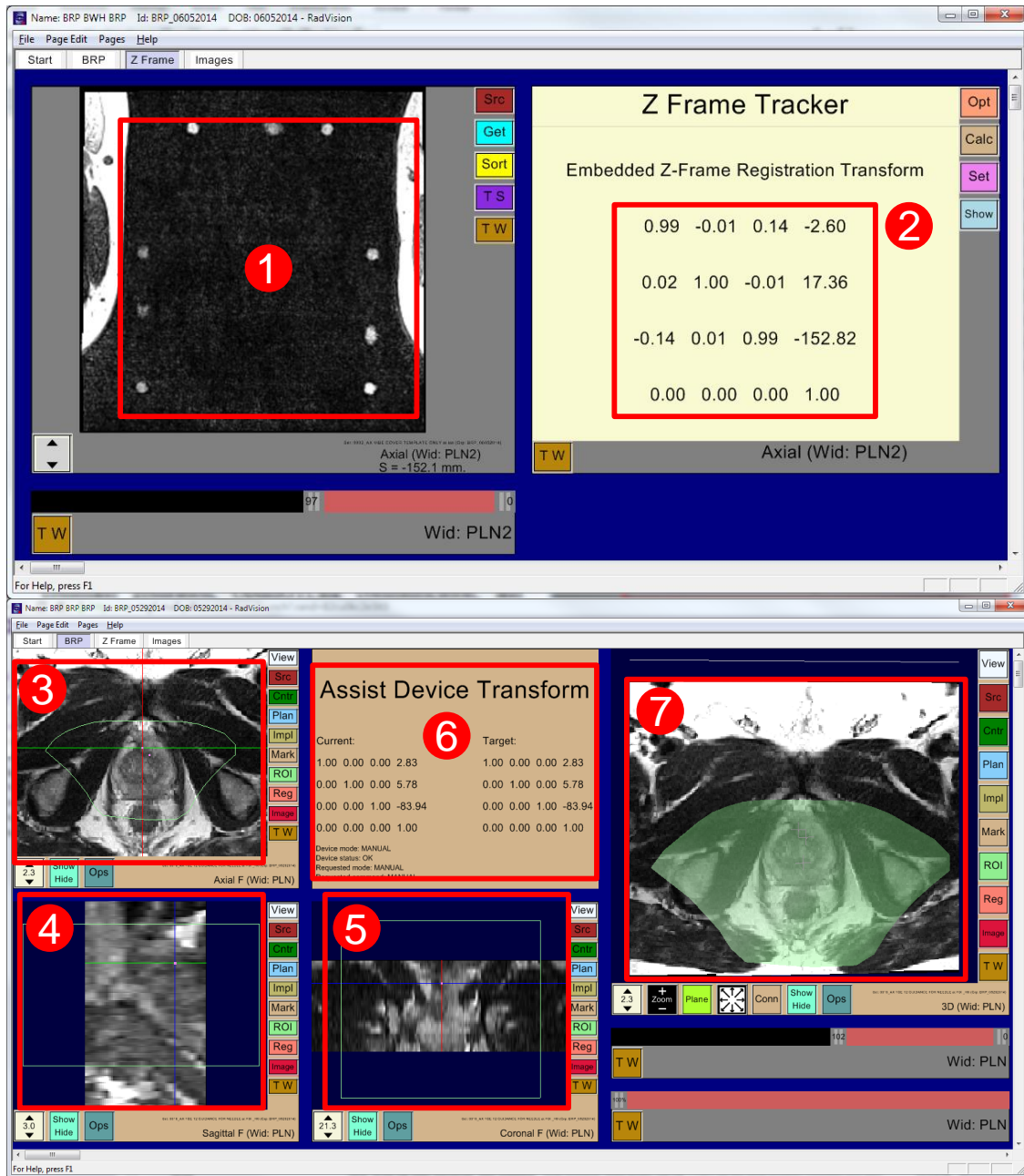


Figure 2.7: RadVision user interface showing (1) acquired MR images of fiducial frame, (2) calculated robot registration transform, (3) axial view, (4) sagittal view, (5) coronal view, (6) robot status, current robot pose, and desired target pose, and (7) 3D view with overlaid reachable robot workspace shown in light green. Also in all image views (3, 4, 5) light green boundary indicates reachable robot workspace.

3) Robot pose reports the current and target position as well as the error for each slider in joint space. Needle insertion depth shows the required depth to be inserted manually to reach the target. Green and cyan blocks demonstrate the current and target position of each slider of mechanism in a graphical fashion to facilitate reporting the slider positions and checking the motion range, which helps the physician for a visual confirmation of the robot position. 4) Targeting panel reports the 6-DOF robot registration, current and target robot positions in RAS coordinate system. 5) The control command module is operable to send commands to robot controller to initialize, home, and stop the robot.

The primary functionality of the CMUI is to edit control command parameters that are used for system debugging purpose and are transparent to clinicians. The CMUI includes five primary modules: 1) Robot registration module shows the fiducial frame registration matrix and robot base offset matrix with respect to fiducial frame. The registration matrices could be sent from RadVision via OpenIGTLink or typed manually. 2) Robot poses module reports the 6-DOF current target and current actual robot position in the image space. 3) Target operation module represents new target pose that could be set in RadVision via OpenIGTLink or typed manually. Additional buttons are intended for control of needle insertion in a future automatic version. 4) Robot control commands are editable to set and indicate robot status as well as initialize the robot to home position. 5) Joint control module is used to set control command for individual axis in joint space. The values could be generated automatically from homogeneous transformation of the target matrix based on inverse kinematics or entered manually for each axis individually.

Both control panels are configurable for any desired robot mechanism. The robot is configured through the XML files containing axis names, PID controller parameters, motion range, scale factors from raw encoder ticks to engineering units

and driving frequency ranges. Each node, i.e. joint axis, is editable, addable and removable according to specific robot mechanism. It is extensible and flexible to be applied to varying robotic systems with different mechanism configurations and control parameters.

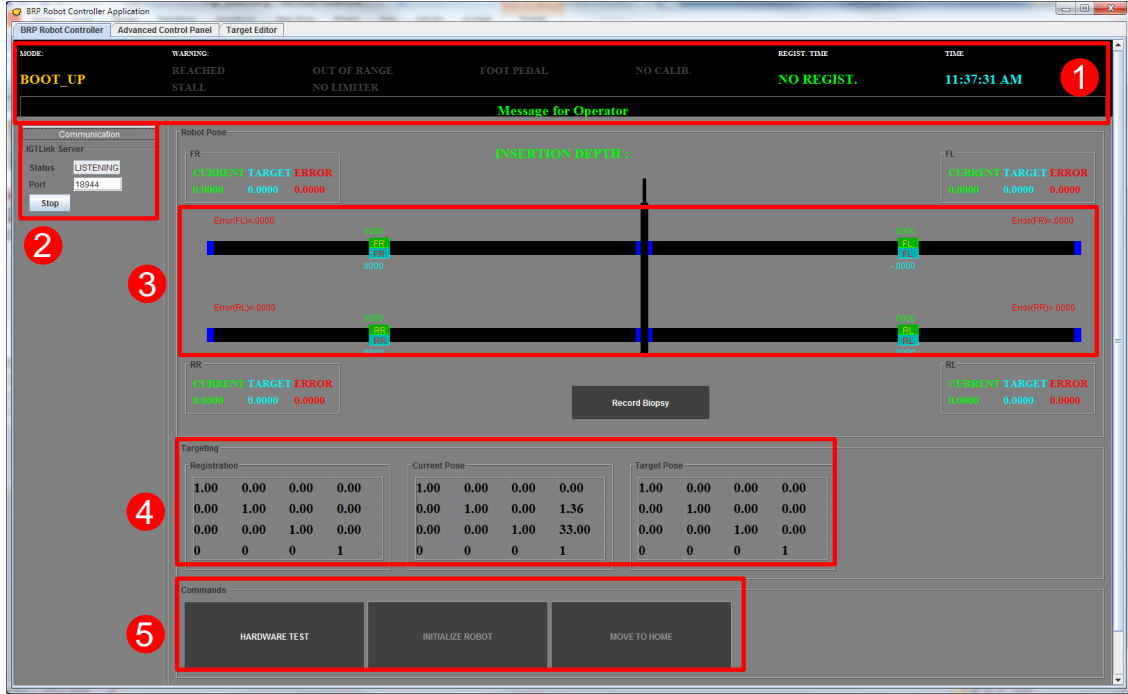


Figure 2.8: Clinical robot control application (CUI) showing: (1) robot status information, (2) OpenIGTLink connection status with the navigation application, (3) current and target robot joint positions, (4) robot pose, registration transform and target transform and (5) control buttons for robot hardware test and initialization.

## 2.6 Experiments and Results

Results from preclinical evaluation of the system with validation in phantom studies under MRI guidance and a clinical feasibility with a preliminary patient study are presented.

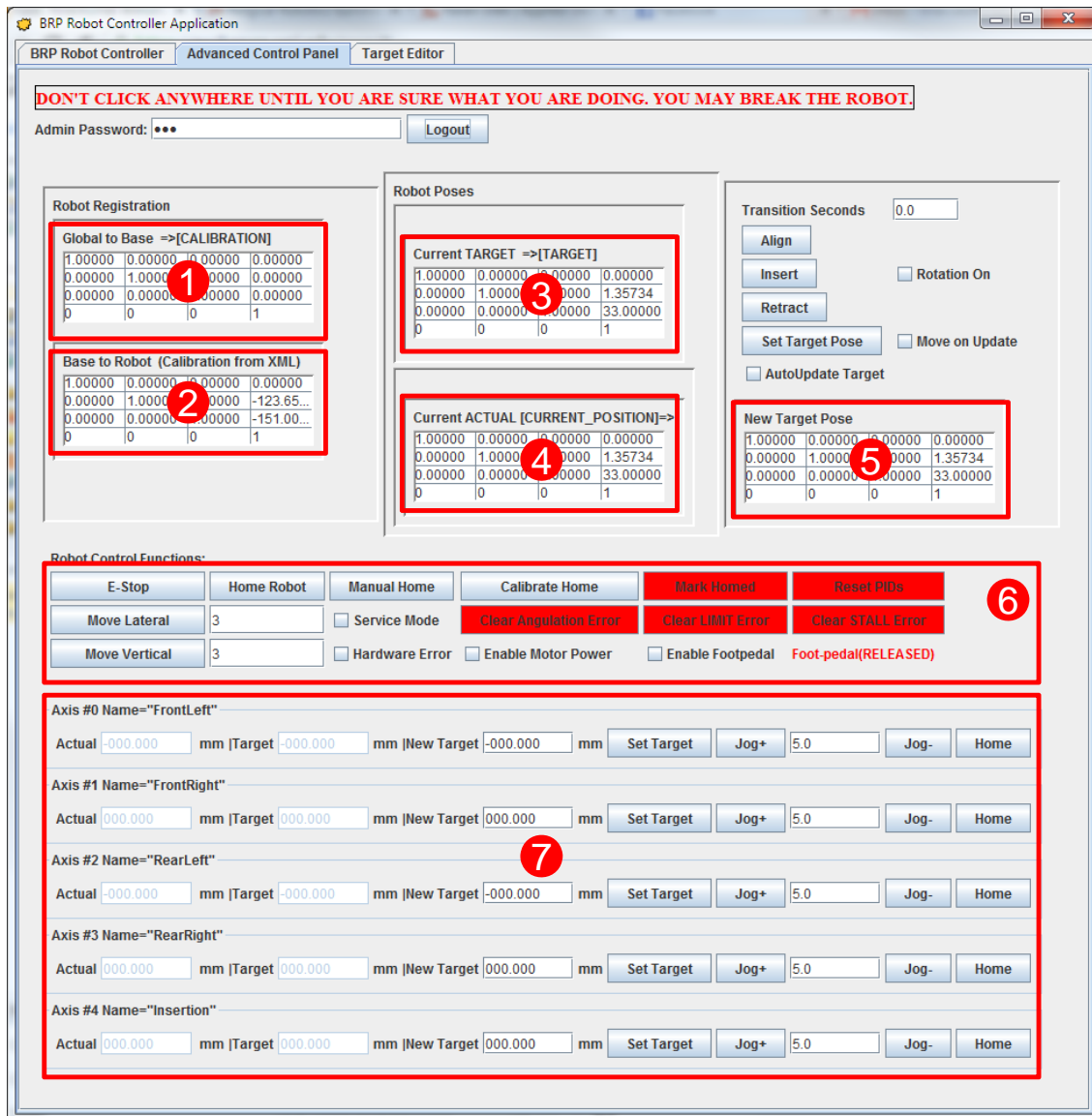


Figure 2.9: Restricted control and maintenance user interface (CMUI) showing: (1) robot registration transform, (2) fiducial frame to robot origin transform, (3) desired target pose, (4) current robot pose, (5) interface for manually entering target pose, (6) control buttons for robot maintenance, and (7) individual axis control interfaces.

### 2.6.1 Preclinical Evaluation: Phantom Studies under MRI Guidance

Phantom studies were performed under live MRI guidance to evaluate the targeting accuracy of the system inside a 3T MAGNETOM Verio scanner (Siemens AG, Erlangen, Germany). The phantom used in this study is a mixture of gelatin and water with 22% concentration. An 18-gauge MRI-compatible biopsy needle was manually inserted into the phantom and imaged with diagnostic T2-weighted turbo spin echo (T2W-TSE) imaging protocol (imaging parameters are listed in Table 2.2: Needle Confirmation). The experiment was conducted in five independent sessions. For each session, new registration of the fiducial frame and initialization of the robot were performed, and five targets were randomly selected in RadVision covering typical focal region of prostate biopsy. Hence, 25 targets in total were collected to assess the system accuracy. The experimental setup was designed as a mock up of typical clinical procedures, which commonly include 1 – 5 targets and require only one registration for each patient. The experiment was conducted with the clinical team and strictly followed the proposed clinical workflow, as described in Section II-B.

The desired target positions defined in RadVision were compared with actual needle tip positions (manually segmented from MRI volume images) to assess targeting accuracy. For the clinical procedures, the in-plane (RA-plane) error plays more significant role than the error along needle insertion axis (S-axis), since the insertion depth along S-axis is adjusted manually by the clinician to the desired depth via interactively updated imaging. Therefore, in-plane error is the metric assessed in this study, with results depicted in Fig. 2.10. The experiments results are summarized for each of the five session in Table 2.1, with RMS error in the



R-axis (signed lateral), A-axis (signed vertical), and RA-plane (total magnitude) of  $1.1mm$ ,  $1.0mm$ , and  $1.5mm$ , respectively.

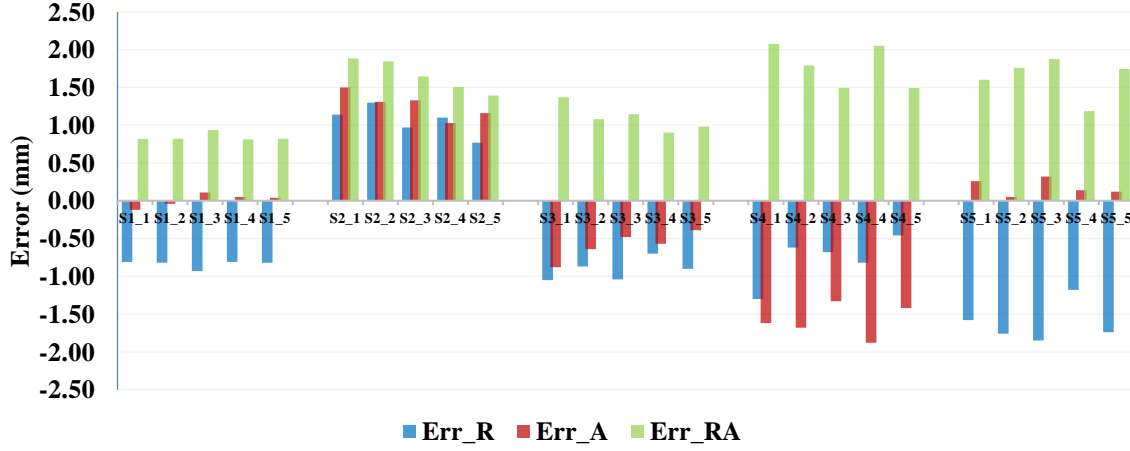


Figure 2.10: Plot of measured needle placement accuracy in each of the five trials in each of the five sessions. Data is shown with errors in the lateral R-L direction ( $Err_R$ ), vertical A-P direction ( $Err_A$ ), and total in-plane error magnitude ( $Err_{RA}$ ).

Table 2.1: Experimental Results of Prostate Robot MRI Phantom Study

Session #	Error_R(mm)			Error_A(mm)			Error_RA(mm)		
	Max	Min	RMS	Max	Min	RMS	Max	Min	RMS
1	-0.9	-0.8	0.8	-0.1	0.1	0.1	0.9	0.8	0.8
2	1.3	0.8	1.1	1.5	1.0	1.3	1.9	1.4	1.7
3	-1.1	-0.7	0.9	-0.9	-0.4	0.6	1.4	0.9	1.1
4	-1.3	-0.5	0.8	-1.9	-1.3	1.6	2.1	1.5	1.8
5	-1.9	-1.2	1.6	0.3	0.1	0.2	1.9	1.2	1.7
Total	1.1			1.0			1.5		

## 2.6.2 Preliminary Clinical Patient Study

Viability of the intraoperative image guided robot assisted procedure is presented through an initial clinical procedure of prostate biopsy performed on a 60 year old

male patient inside a 3T MAGNETOM Verio scanner with IRB approval and patient consent, abiding by the aforementioned clinical workflow. Under IV conscious sedation, the patient was placed on the patient board in the semi-lithotomy position with legs rested on the support. Fig. 2.11 illustrates the system configuration for this patient study, and the imaging protocols used in this study are listed in Table 2.2. After patient positioning, the sterilized fiducial frame was attached on the patient board and registration was performed by acquiring MRI images with the *Localizer* protocol. After registration of the fiducial frame, a new set of images of the prostate region were acquired using the *Intraoperative* protocol with Body Matrix and Spine Matrix coils (Siemens AG, Erlangen, Germany), and then registered to the preoperative planning images. Based on the registered images, two suspicious sites were selected in RadVision and sent to the controller for aligning the robot manipulator. Once the robot was aligned in place, the radiologist manually inserted an 18-gauge MRI-compatible core biopsy needle (Fully Automatic Biopsy Gun, InVivo Corporation) into the prostate gland through the robotically aligned needle guide. A confirmation image was used to validate the actual needle tip location with *Needle Confirmation* protocol. If the needle was not within the target lesion, adjustments (reinsertion and reorientation) can be performed manually by the clinician. Once the needle is confirmed to be in the target, a biopsy sample is manually procured from each of the two targets sites. Fig. 2.12 shows the segmented actual needle trajectories overlaid on a 3D view showing an MRI image of the prostate gland and defined targets.

Targeting accuracy of the biopsy was evaluated by computing the shortest distance from the desired target to the actual needle trajectory, and summarized in Table 2.3. The accuracy of first insertion attempt was obtained solely by the needle guide, no adjustment was performed. The accuracy of the best insertion attempt

Table 2.2: Imaging Protocols for the Patient Study

Imaging Protocol	Sequence	Flip Angle (deg)	TR (ms)	TE (ms)	Slice Thickness (mm)	Pixel Spacing (mm x mm)
Localizer	T2W-TSE	120	3000	111	2	0.70 x 0.70
Intraoperative	T2W-TSE	150	4800	100	3	0.50 x 0.50
Needle Confirmation	T2W-TSE	120	3000	106	3	0.75 x 0.75

was achieved by adjustment techniques, which represents a realistic accuracy for actual tissue sampling. The accuracy of the best insertion attempt for the two biopsies are  $4.0mm$  and  $3.7mm$ , respectively. This preliminary measure of targeting accuracy is comparable to our previous study on template-based manual ( $6.05mm$ ) and robotic ( $5.42mm$ ) transperineal approach [24]. The total procedure time is  $80min$ , which is significantly reduced compared to our previous study on manual ( $151.29 \pm 37.88min$ ) and robotic needle-guidance template ( $141.67 \pm 19.47min$ ) [24].

Table 2.3: Accuracy Assessment of Preliminary Patient Study

Target	Target Position (mm)			First Attempt Error (mm)				Best Attempt Error (mm)			
	R	A	S	R	A	S	Total	R	A	S	Total
LCGApex	-13.2	8.5	15.6	-5.8	7.7	-1.1	9.7	-0.4	4.0	0.1	4.0
RPZMid	8.8	0.0	33.6	0.0	6.3	0.0	6.3	3.1	2.0	-0.3	3.7

## 2.7 Discussion and Conclusion

This chapter presented development of a fully integrated robotic system for MRI-guided transperineal prostate biopsy, which has been approved by IRB for clinical trials. The clinically oriented robotic system described herein is developed based

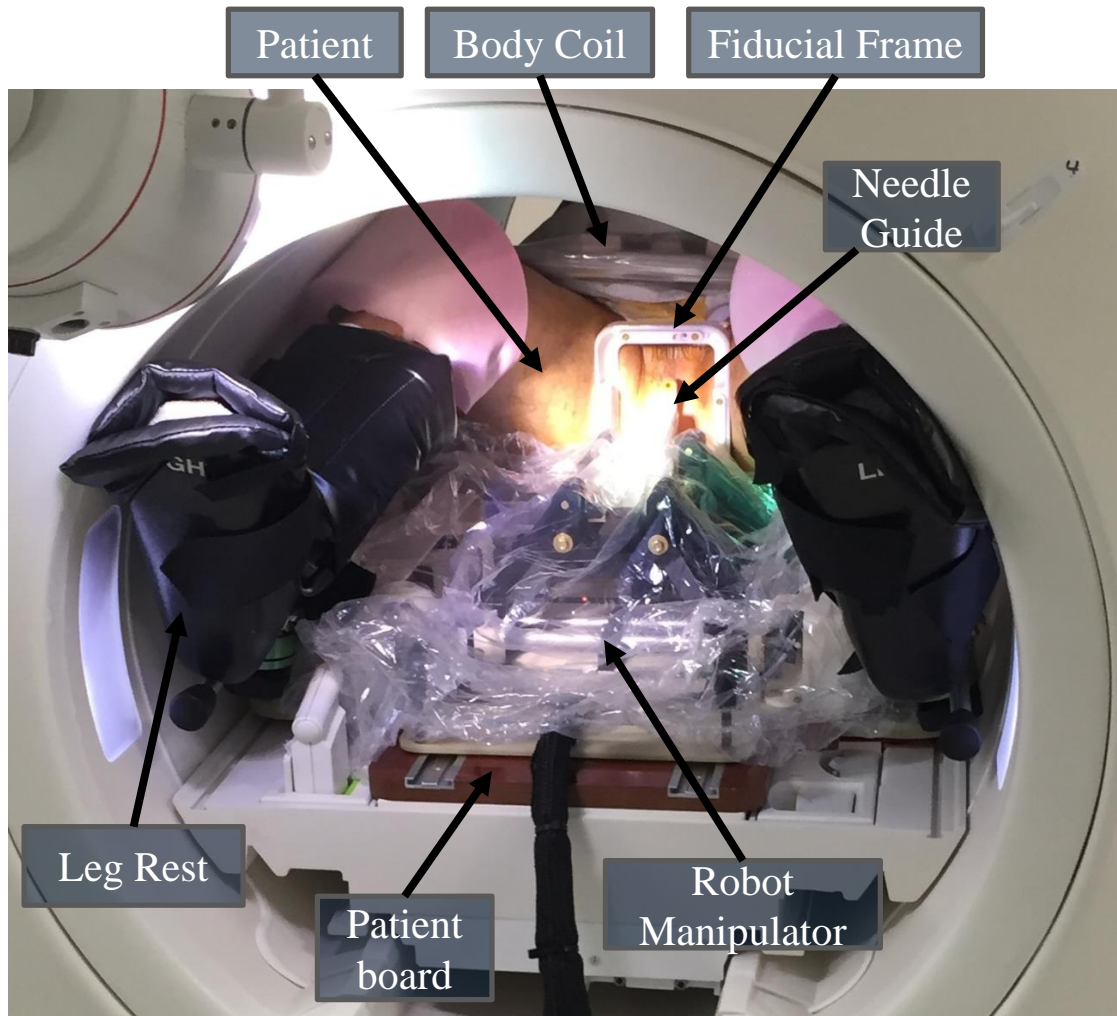


Figure 2.11: System configuration for the patient study. The patient lies in the supine position with legs supported by the leg rest on the patient board. The sterilized fiducial frame is fixed to the patient board between the patient's legs. The robot manipulator is covered by the sterile plastic drape, positioned on the patient board, and locked into place.

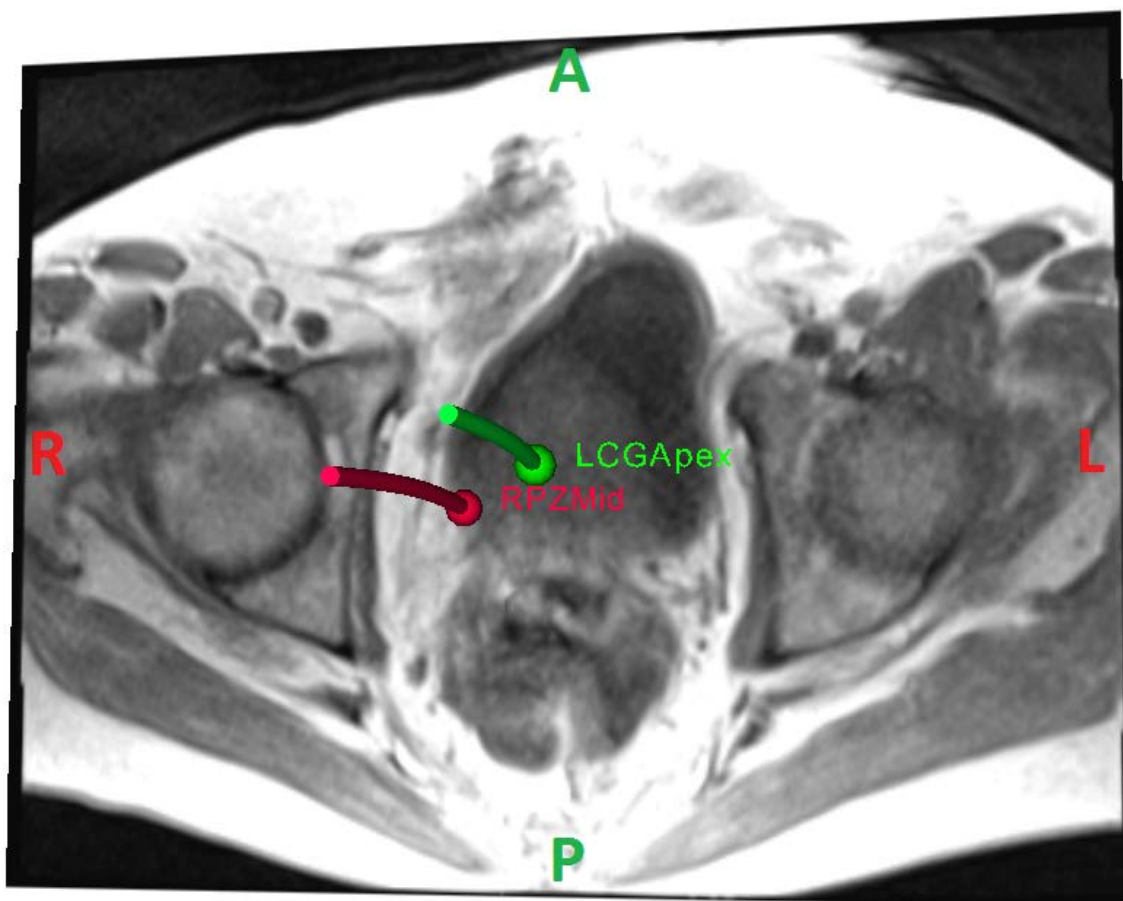


Figure 2.12: 3D view with an MR image of prostate gland showing desired targets (cyan dots) and actual needle trajectories (red lines, segmented from MRI volume images).

on a modular approach, with the modules connected through a network. A major merit of network based modular design approach is that each module can be developed and tested individually, making it readily configured for supporting a specific clinical workflow and extensible to various clinical applications. Safety is a crucial requirement for a clinical system; therefore, even in the case of robot failure, safety mechanisms are considered during the design phases, including motion range limit switches, user controlled foot pedal interlock, independent emergency stop power switch, as well as controller status monitoring with hardware and software. Sterility is a unique and critical requirement for clinical devices; for this reason, the robot manipulator is designed with non-sterilizable and sterilizable components. Non-sterilizable components are covered by a standard disposable pre-sterilized drape and sterilizable components are prepared in a kit and sterilized prior to the procedure.

In our previous study on the mechanism design [70], the system targeting repeatability and accuracy were assessed in free space, demonstrating the errors are less than  $1mm$ . Moreover, compatibility with the MRI environment was evaluated in a 3T MRI scanner with varying robot configurations, showing SNR reduction of less than 16% when controller is powered on. In this work, preclinical phantom studies were performed to evaluate the system targeting accuracy and to rehearse the clinical workflow. The in-plane errors were assessed, demonstrating a RMS error of  $1.5mm$  and maximum error of  $2.1mm$ . The placement accuracy achieved herein is comparable to other preclinical studies of MRI-guided robotic systems; Stoianovici et al. reported an MRI-safe robot for endorectal prostate biopsy with in-vitro targeting accuracy of  $2.1mm$  [18] and Krieger et al. presented in-plane target accuracy of  $2.4mm$  was achieved by an actuated transrectal prostate robot [21]. Also, transperineal approach presented here could be more challenging as typical

distance between the needle entry point and target could be 10-15 cm and needle passes through many tissue layers, which could result in unexpected needle deflection and potentially reduce the targeting accuracy. The targeting accuracy of the proposed system reflects the overall accuracy of the system, which could be classified as registration error (fiducial frame registration and alignment), robot manipulator error (robot mechanism backlash, motion control precision), imager error (imaging resolution), and un-modeled error (needle deflection as inserting into the phantom). Based on the systematic error depicted in Fig. 2.10 for each session, it appears that the dominant error source is most likely registration error. To separate robot accuracy from registration accuracy, the mean error is subtracted for each session, resulting in the in-plane RMS error of  $0.2mm$ .

A preliminary clinical study was described to demonstrate the viability of clinical use of this robotic system. The patient study was performed following the IRB approved clinical workflow. The clinical procedure was performed successfully in about  $80min$ , which is a significant reduction in procedure time as compared to our previous study on manual ( $100.63min$ ) and robotic ( $90.82min$ ) needle-guidance template [24]. Two suspicious sites were targeted and one biopsy tissue core was procured from each target site. The maximum targeting error was  $4.0mm$ , which is acceptable to target a clinically significant tumor foci with a sphere of  $5mm$  radius [73, 74]. More extensive clinical cases are currently ongoing at BWH, and further thorough accuracy analysis in the aspects of organ motion and needle deflection will be considered in future studies.

Manual needle insertion and tissue biopsy sampling along a robotically aligned axis was adopted in this version of the robotic system as an initial goal primarily due to safety and clinical acceptability considerations. However, manual operation inside the tightly constrained scanner bore is still ergonomically awkward and time con-

suming. Also, such manual operation does not allow active compensation of errors resulting from needle deflection and tissue deformation. It is desirable to develop a fully actuated robotic system with teleoperated, cooperative or autonomous needle insertion and rotation, coupled with real-time MRI guided needle tracking leading to a closed-loop biopsy procedure allowing active compensation for needle deflection and tissue deformation. We have reported development of teleoperated [75], fully actuated [76] and recently cooperative [77] needle insertion and rotation devices. Chapter 3 describes a system architecture utilizing such devices for closed-loop interventions, while Chapter 4 describes autonomous needle steering under real-time MRI guidance.



# Chapter 3

## System Architecture for Closed-loop MRI Guided Percutaneous Interventions

### 3.1 Contributions

Intraoperative MRI guided prostate biopsy system, which was lacking actuated needle manipulation and real-time imaging feedback motivated development of an architecture for closed-loop percutaneous intervention under real-time MRI guidance. Closed-loop system architecture presented in this chapter is modular and scalable allowing flexibility to replace various components with another component providing similar functionalities. As shown in Fig. 3.1 various components such as MRI compatible robot, robot controller, scanner control, instrument tracking, surgical planning and navigation applications and therapy monitoring could be replaced with any module providing similar functionalities. Proposed architecture is validated by adapting it to two different percutaneous procedures under real-time MRI

guidance. Also, various modules are developed for each of the procedures validated to confirm proposed architecture. Each of those closed-loop MRI guided procedure are described in chapters 4 and 5 .

## **3.2 Proposed System Architecture**

MRI guided, robot assisted percutaneous interventions involves various system components such as an MRI compatible robotic manipulator, low noise electronics to drive the actuators, therapy delivery instrument and of course an MRI scanner. Integrating all of those components could be a challenging task and would require many communication interfaces between system components. In this section a system architecture for closed-loop, MRI guided, robot assisted percutaneous intervention is presented. Various system components and interface between them along with data flow is described. As shown in Fig. 3.1, such a system consist of MRI scanner, unified imaging interface allowing translation of system to any operating environment, MRI compatible robot and robot controller, real-time image processing module for instrument tracking and therapy progress monitoring, surgical planning and navigation applications and robot control application for high level robot control and surgical workflow management. Each of those modules are described in this chapter with their role and desired capabilities.

## **3.3 Unified Imaging Device Interface**

Translating any surgical device to an operating room is a challenging process. It becomes even more challenging when it is an image guided therapy device due to different imaging interfaces provided by different vendors. In case of MRI, three major vendors include Phillips, Siemens and General Electric. Creating an unified

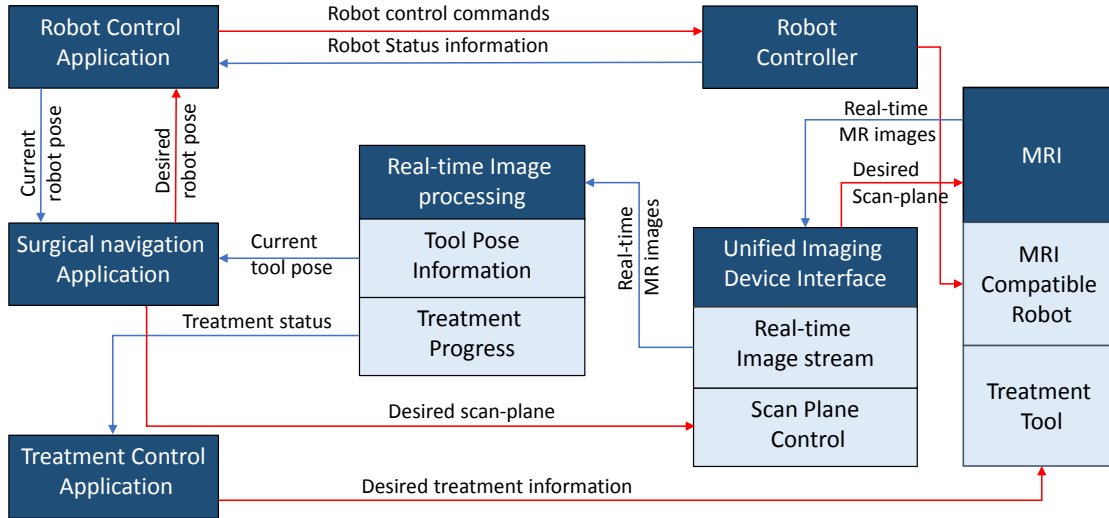


Figure 3.1: Closed-loop system architecture for MRI guided percutaneous interventions showing various system components and their interactions with each other

imaging device interface, which could allow seamless scanner access irrespective of the vendor could make translation process less difficult. I created an unified interface which allows: transfer of images from the MRI scanner to surgical navigation application and scanner control from the surgical navigation application. Fig. 3.2 shows block diagram for unified imaging device interface and dataflow between different modules.

### 3.4 Real-time Image Processing

Intraoperative MRI has been in use for various percutaneous procedures, but potential of real-time MRI has not been well explored. Processing MR images in real-time would allow localization of the therapy delivery instrument or monitor the treatment progress for procedures such as tissue ablation. Most MRI scanners provide real-time imaging capability, this section describes two of the essential real-time MR image processing applications for performing closed-loop intervention and therapy monitoring.

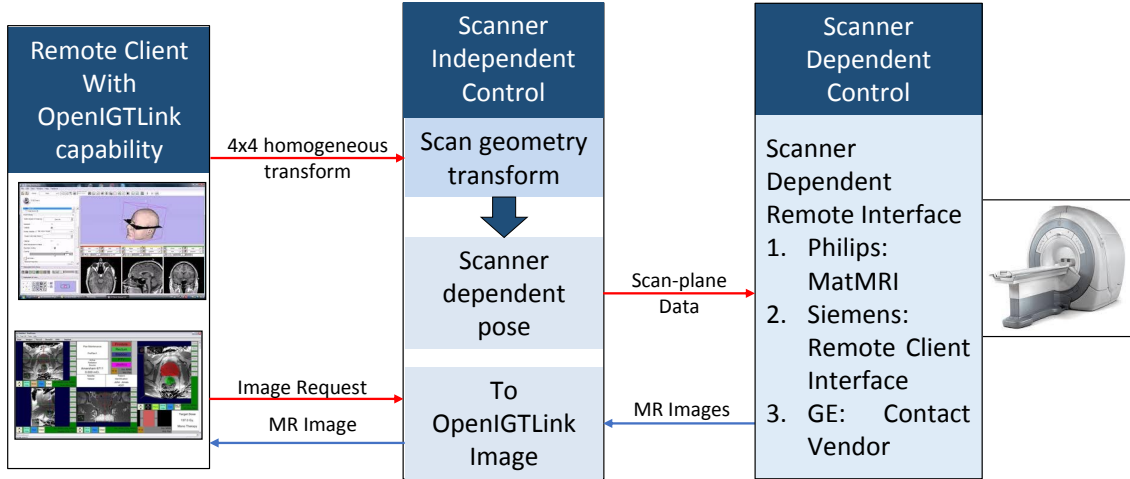


Figure 3.2: Unified Imaging Device interface: showing an interface for vendor independent MRI scanner control

### 3.4.1 Therapy Device Tracking

#### Active Tracking

Active tracking involves development of micro tracking coils embedded within the surgical device/tool. Active tracking coils are tuned for a particular magnetic field strength to get signal only from the regions where the coils are located. This allow accurate localization of the surgical tool. Active tracking coil based localization of ablation probe is discussed in detail in section 5.8.

#### Passive Tracking

Passive tracking involves real-time MRI image processing to track the surgical tool such as a biopsy needle. For some of the percutaneous interventions to keep the tool tip visible, passive tracking might be coupled with scanner control to scan images at the instrument tip locations. Section 4.6 describes real-time MRI based needle tracking used for real-time needle steering.

### **3.4.2 Therapy Monitoring**

Real-time device tracking could help in improved device placement accuracy as well as trajectory correction. But, along with device tracking, real-time imaging can be used for therapy monitoring, such as MRI based temperature monitoring for thermal dose delivery applications such as tumor ablation. Monitoring of tissue ablation using MR-thermometry is described in detail in section 5.9.

## **3.5 Surgical Planning and Navigation**

Surgical planning and navigation are very important aspects of any IGT procedure. Surgical planning involves defining the procedure targets and goals in terms of therapy delivery device placement and then therapy delivery itself. For example, surgical planning for biopsy procedure would involve identifying the lesion and defining the target site for tissue sample collection, while for tumor ablation it would not only involve target site but also the amount of thermal dosage to be delivered to the lesion. Section 2.5.1 described surgical planning and navigation for prostate biopsy procedure while, 5.7 describes surgical planning and navigation for brain tumor ablation procedure.

## **3.6 Robot Control Application**

Robotic device assistance for MRI guided procedure has been the primary focus of this dissertation. Robot control application should not only do closed-loop control of the manipulator but also should ensure safety and manage surgical workflow. Section 2.5.2 described detailed features of a robot control application for prostate biopsy procedure, while the extended feature description in terms of complete workflow

management, user interfaces and safety procedures is described in Appendix A.

## **3.7 Conclusions**

This chapter presented an architecture for closed-loop , robot assisted, MRI guided percutaneous procedure motivated from prostate biopsy procedure. It described various modules of such a system and their role in the complete procedure. Also, it described various features expected from each of the module to integrate such a system for any percutaneous intervention under MRI guidance. Presented architecture is validated by two procedures, Chapter 4 describes fully autonomous needle steering under real-time MRI guidance, while Chapter 5 presents an integrated system for closed-loop monitoring of conformal brain tumor ablation under real-time MR-thermometry.

## Chapter 4

# Closed-loop Needle Steering under MRI Guidance

### 4.1 Contributions

Aim of this research was to demonstrate and validate closed-loop needle steering under real-time MRI guidance. An integrated system consisting of MRI-compatible robot designed by my lab colleague Hao Su [65], real-time scanner control, autonomous needle tracking algorithm and needle steering algorithm was used. My primary contribution in this project was development of real-time, autonomous needle tracking coupled with MRI scanner control and interfacing of it with needle steering robotic platform comprising of 2-DOF (needle rotation and insertion), Application for real-time scanner control, robot control, real-time needle tracking in MR images and needle steering algorithm were developed. Communication interfaces for performing closed-loop operation were developed allowing transfer of MR images to real-time tracking application, needle steering parameters to robot control application and scan geometry updates to real-time scanner control application.

## 4.2 Introduction

Needle-based percutaneous interventions such as biopsies, brachytherapy, and ablation are some of the most common types of minimally invasive procedures. The success rate of these procedures is closely related to the accuracy of the needle tip placement. To perform needle-based procedures using MRI guidance, the surgeon must overcome challenges including a limited workspace, MRI compatibility of instruments, and difficulties of acquiring real-time MR images of the region of interest during the intervention. The use of robotic systems inside the MRI environment can help the surgeon to perform needle-based procedures with MRI guidance [57, 78–81]. Still, most of the procedures proposed so far are still open-loop due to the lack of an effective MRI-based needle tracking method. The development of an autonomous needle tracking system is crucial for the implementation of closed-loop needle insertions. However, MR image acquisition time, difficulties to keep the needle tip in the field of view, and quality of fast and continuous MR images for tracking the needle are issues that make MRI-based needle steering a challenging task. Active needle and catheter tracking techniques were proposed in [82–84], but an RF coil has to be placed on the needle tip to be tracked. Just a few works deal with passive tracking. In [85] needle tracking for two-dimensional (2D) MR images is presented while in [86] a system to track the plane of an active loopless-antenna needle is described. Although these systems were used for needle tracking, feasibility of using these methods for closed-loop needle steering has not been evaluated. Using needle tracking for closed-loop flexible needle steering can improve accuracy of needle-based interventions.

Needle could be steered in a soft tissue using concentric continuum tubes, pre-curved or asymmetric-tip needles. The use of flexible bevel-tipped needles instead



of conventional rigid needles increases the steerability. The enhanced steerability improves accessibility to a lesion which might be obstructed by structures such as nerves, blood vessels or bones on the insertion path. These needles deflect when they are inserted into soft tissue due to the asymmetric interaction forces between the tissue and the bevel tip, which could be used in controlled manner to compensate for undesired needle deflection and tissue movement. Robotic systems used to insert flexible bevel-tipped needles have been presented using video cameras [87], fluoroscopic images [88], ultrasound images [89] and electromagnetic trackers [90] to provide needle tip position feedback. These systems use needle insertion and rotation around the insertion axis to steer the needle towards a target. In [47] duty-cycled rotations were used to provide different needle curvatures, while in [91] only the natural curvature of the needle was used for steering. A feasibility study of manual steering of a flexible needle in the MR environment was presented in [92], where the manual insertions and rotations induced significant errors. Therefore, using an MRI-compatible robotic system to automate insertion and rotation with MRI-based needle tracking system can result in an accurate MRI-guided bevel-tipped needle steering.

In this chapter, a robot-assisted closed-loop flexible needle steering using real-time MR images (in MR imaging context real-time means continuously acquired images at about 1-2 Hz) as feedback is presented. The system consists of an MRI-compatible robot, fast and continuous MR image acquisition, autonomous needle tracking incorporating control of the MRI scan plane geometry, and a needle steering algorithm to insert a flexible bevel-tipped needle towards a pre-defined target as shown in Fig. 4.1. To the best of our knowledge this is the first time that robot-assisted flexible needle steering is performed using real-time MR images for feedback.

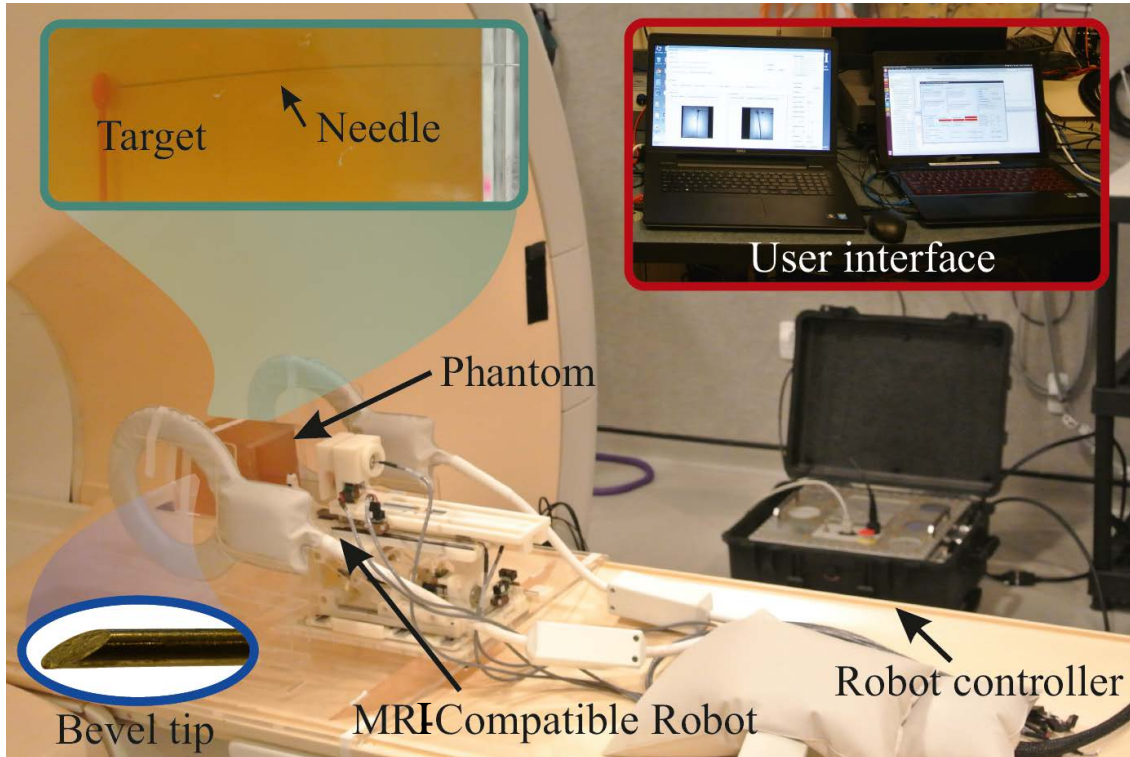


Figure 4.1: Overall system setup showing: user interfaces for robot controller application and needle tracking application (inlay, in console room), MRI compatible robot controller (beside scanner), and the MRI compatible robot which resides on the scanner bed beside the phantom and holds the bevel-tipped needle.

### 4.3 Asymmetric-tip Needle Kinematic Model

A flexible needle with an asymmetric beveled tip bends as it is inserted into the soft tissue due to the asymmetric interaction forces between the bevel tip and the tissue. The position and orientation of the tip could be derived only from two control inputs, needle insertion and rotation at the base of the needle. The needle tip trajectory could be describes by that of a nonholonomic mobile robot as described in [93]. It represents the needle as a bicycle as shown in Fig. 4.2 , with  $\phi$  as the fixed front wheel angle, wheelbase length  $l_1$ , and needle tip at a distance of  $l_2$  along the bicycle path. parameters  $\phi$  and  $l_1$  specifies the needle curvature  $k$ , while  $l_2$  determines needle tip location along the curved needle path. The needle tip is calculated with

these parameters and the control inputs  $u_1$  and  $u_2$ , the needle insertion and rotation speed respectively.

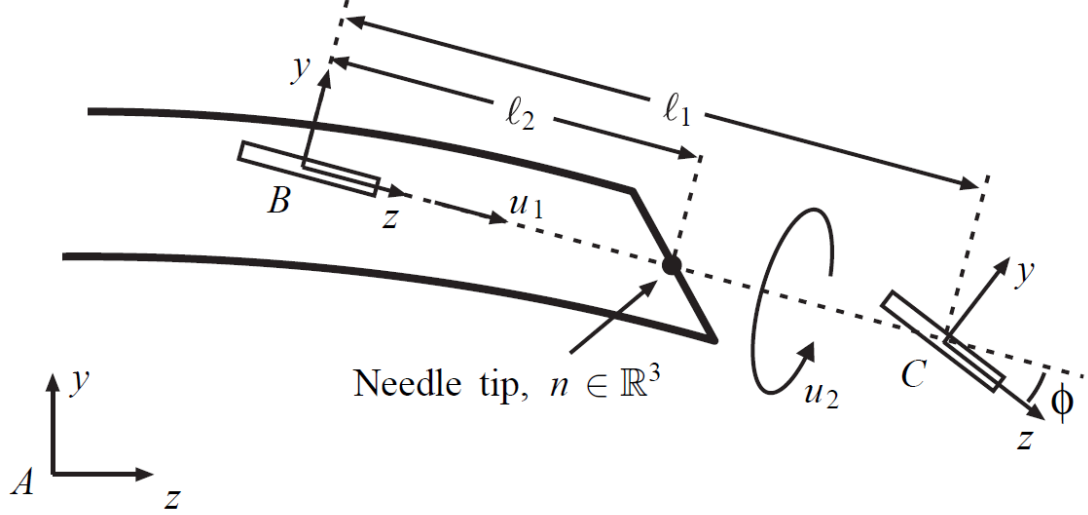


Figure 4.2: Nonholonomic bicycle model of a bevel-tip needle, showing model parameters, homogeneous transforms representing the world frame A, front wheel frame C, back wheel frame B and the needle tip location  $n$  [93] ©2006 SAGE Publications

The discrete model considering the insertion distance and change in rotation angle instead of the speed, could be used for simulations and visualization. Eq. 4.1 shows the discretized bicycle needle model:

$$g_{ab}(k+1) = g_{ab}(k)e^{(u_1(k)\hat{V}_1 + u_2(k)\hat{V}_2)T} \quad (4.1)$$

$$n(k) = R_{ab}(k)l_2e_3 + p_{ab}(k)$$

where,  $g_{ab}$  is the homogeneous transform from world frame A to the rear wheel frame B,  $u_1(k)$  and  $u_2(k)$  are insertion distance and change in rotation respectively at step  $k$ ,  $\hat{V}_1$  and  $\hat{V}_2$  correspond to pure needle insertion and rotation respectively,  $e_3$  is the base vector representing Z axis.

## 4.4 Gaussian-based Continuous Rotation and Variable (CURV) Curvature Steering Model

Kinematic model of the needle can be used to guide the needle tip towards a desired position. However as described in section 4.3 the needle curvature for the entire insertion is considered to be constant which could be determined experimentally. A novel model which could enable variable curvature was presented by my colleague Li Gang. In this model, the insertion speed is an independent control from the needle rotation. Needle is continuously rotated about its primary axis with the rotation velocity following a Gaussian profile. The rotation velocity depends on current rotation angle  $\theta$ , desired rotation angle  $\theta_d$ , Gaussian width  $c$  and steering effort  $\alpha$ . Fig. 4.3 shows model parameters and its effect on the needle rotation velocity profile generated using Eq. 4.2.

$$\hat{\omega}(\theta, \theta_d) = 1 - \alpha e^{-\frac{(\theta - \theta_d)^2}{2c^2}} \quad (4.2)$$

The effect of varying the model parameters, steering effort  $\alpha$  and Gaussian width  $c$  was modeled and studied in detail by Li Gang [94]. By varying the steering effort or the Gaussian width, the needle curvature could be varied and can be used in conjunction with the kinematic model to generate the desired needle trajectory. The relationship between the CURV model parameters, steering effort  $\alpha$ , Gaussian width  $c$  and the kinematic needle model parameters ( $l_1$ ,  $l_2$ ,  $k$  and  $\phi$ ) could be established experimentally. Fig. 4.4 shows simulated needle trajectories by varying the steering effort, while Fig. 4.5 shows the simulated needle trajectories produced by varying the Gaussian width.

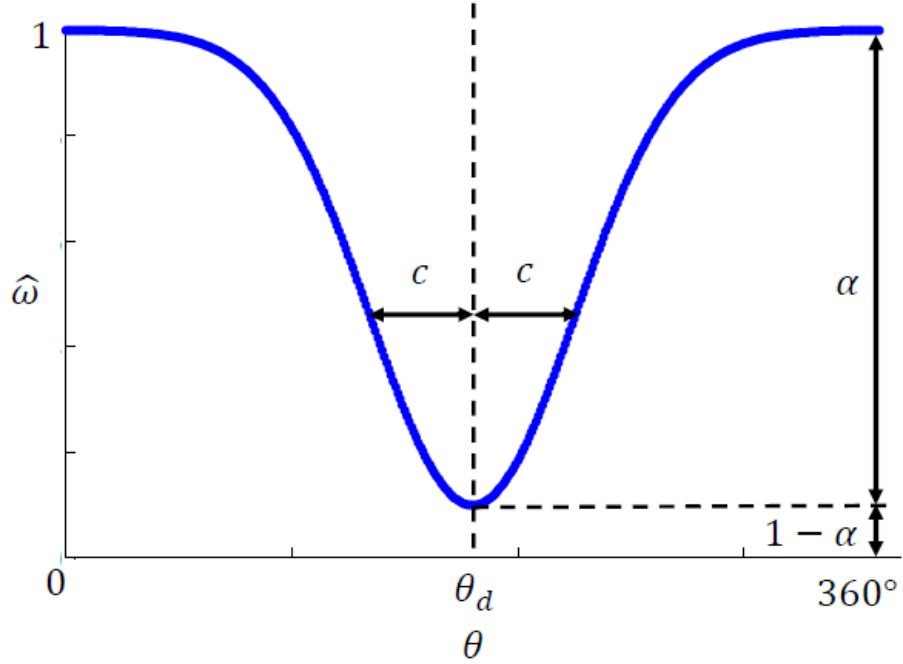


Figure 4.3: CURV needle model showing the model parameters: Gaussian width  $c$ , steering effort  $\alpha$  and resulting rotation velocity profile  $\hat{\omega}$  for a complete  $360^\circ$  rotation given the desired angle  $\theta_d$  ©2016 Li Gang

## 4.5 System Architecture

The system is composed of: (1) hardware subsystem and (2) software subsystem. Components of the hardware subsystem are: (a) MRI compatible robot, (b) MRI compatible robot controller, and (c) MRI scanner. Components of the software subsystem are: (a) autonomous needle tracking and scan plane control application, (b) robot control application, and (c) needle steering algorithm. Fig. 4.6 shows the overall system architecture and components of the system.

The hardware subsystem focuses on continuous intraoperative MR image acquisition and needle steering using the robot placed inside the MRI scanner bore. The flexible needle is driven by the MRI-compatible interventional robot designed to place the needle in the tightly-constrained MRI scanner bore. The robot is driven

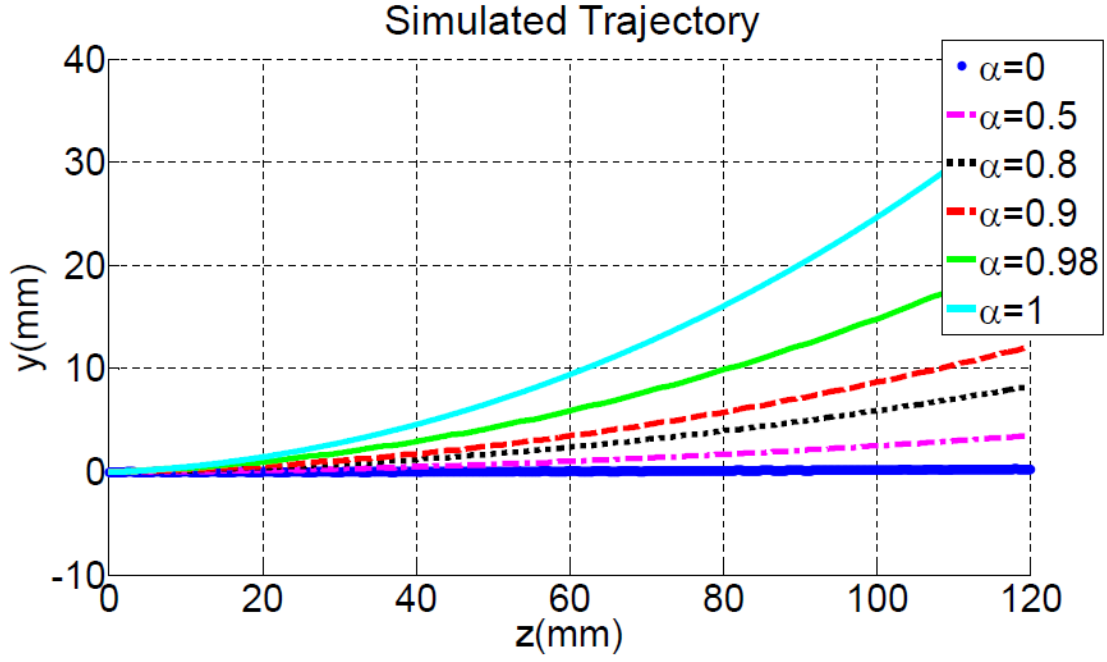


Figure 4.4: Effect of changing steering effort on needle curvature©2016 Li Gang

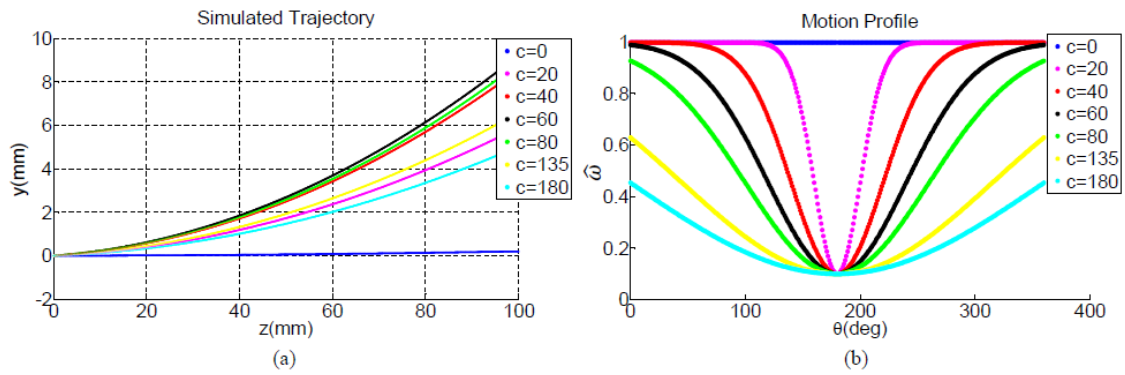


Figure 4.5: Effect of changing Gaussian width on needle curvature©2016 Li Gang

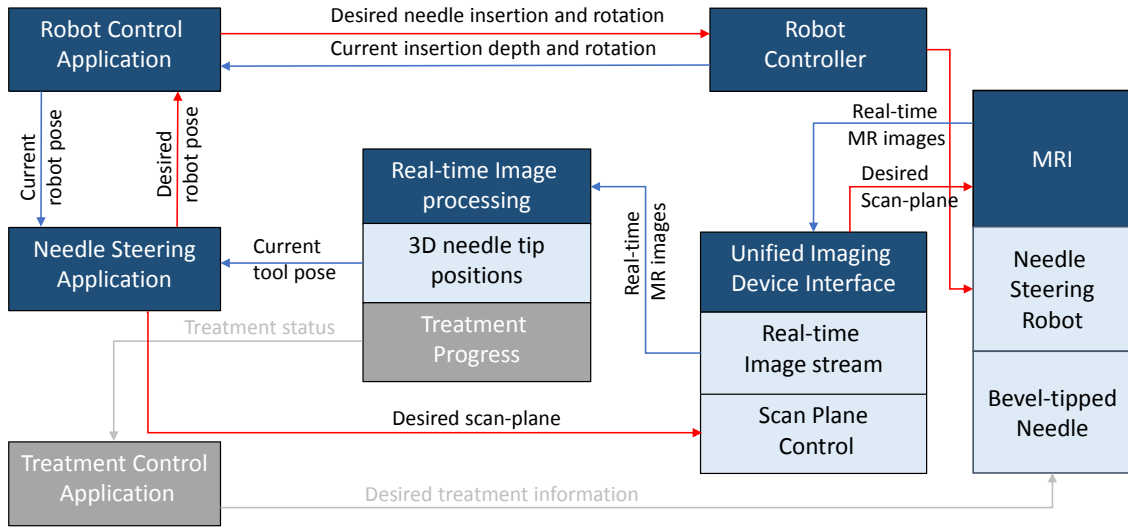


Figure 4.6: Closed-loop needle steering system architecture showing various system components and data flow between them

by non-harmonic piezoelectric motors (PiezoMotor PiezoLegs actuators, Uppsala, Sweden), The robot controller located beside the MRI scanner in Fig. 4.1 is custom developed to be compatible with an MRI environment and provides high-precision closed-loop control of piezoelectric motors, as previously reported in [95].

The software subsystem focuses on autonomously tracking the needle in the most recently acquired MR images, calculating steering parameters, controlling the robot and communication between these components. The connection between the robot controller and the robot control application is established via the fiber optic Ethernet which runs through the patch panel on the wall of the scanner room to eliminate the electrical noise. For the described implementation using a Philips 3T Achieva scanner, the scanner console and the tracking application communicates using the XTC (eXTernal control) [96] Corba Data Dumper to continuously acquire MR images and send the image position and orientation for future scans. Using the most recent images, the needle tracking application calculates the 3D needle position and sends it to the steering algorithm over OpenIGTLink [97] which is an open

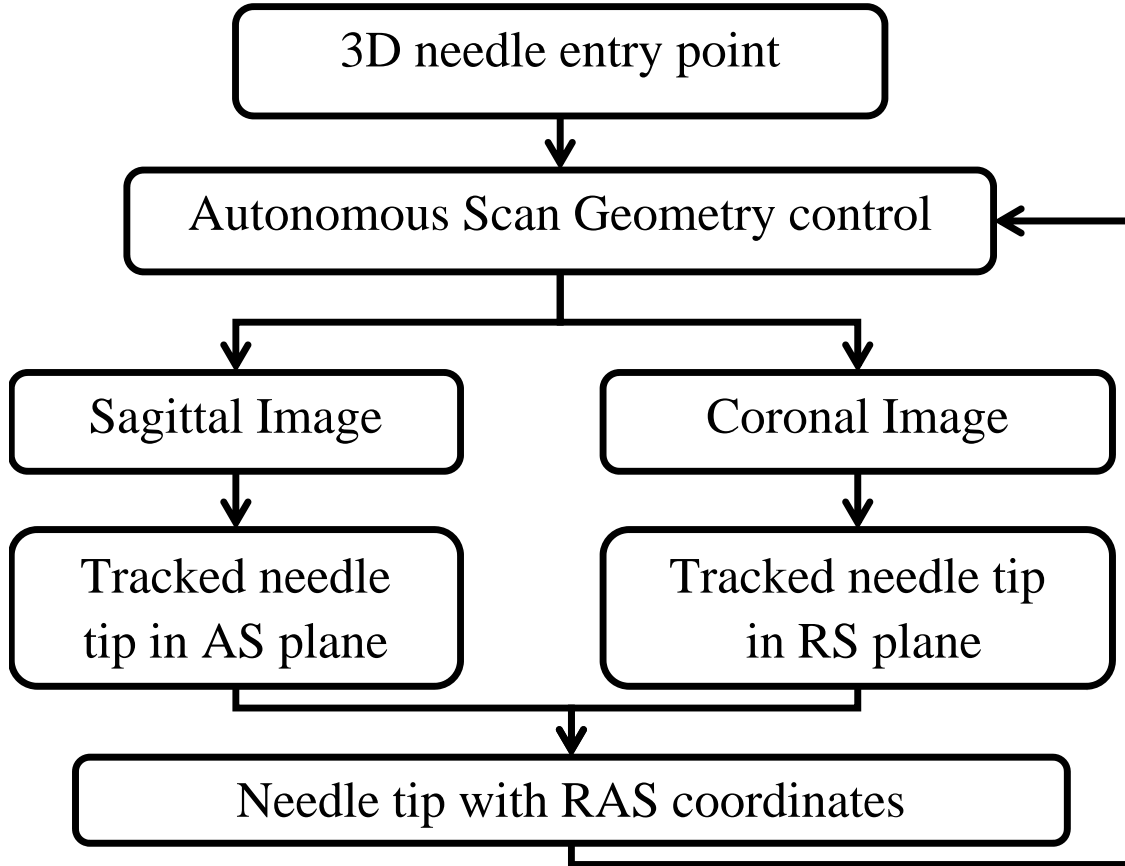


Figure 4.7: Flow chart of the needle tracking application workflow. The application tracks the needle tip in alternating sagittal and coronal images and automatically adjusts the scan plane geometry to maintain the needle tip at their cross-section.

source protocol for communication among image-guided therapy (IGT) applications. The steering algorithm interpolates all past and current needle positions received from the needle tracking application and calculates insertion and rotation values to steer the needle towards the desired target for each increment. The steering parameters calculated by the steering algorithm are sent to the robot controller application over OpenIGTLink, which are passed to the robot controller over the Bowler communication protocol.



## 4.6 Real-time needle tracking with MRI

Autonomous needle tracking in MR images is a challenging task as it requires fast and continuous MR image acquisition, visualization, autonomous scan geometry control, and needle tip tracking. Fig. 4.7 shows the flowchart of the autonomous needle tracking application, where R (right), A (anterior) and S (superior) coordinates are position of the needle tip in scanner coordinates, corresponding with X, Y and Z coordinates, respectively.

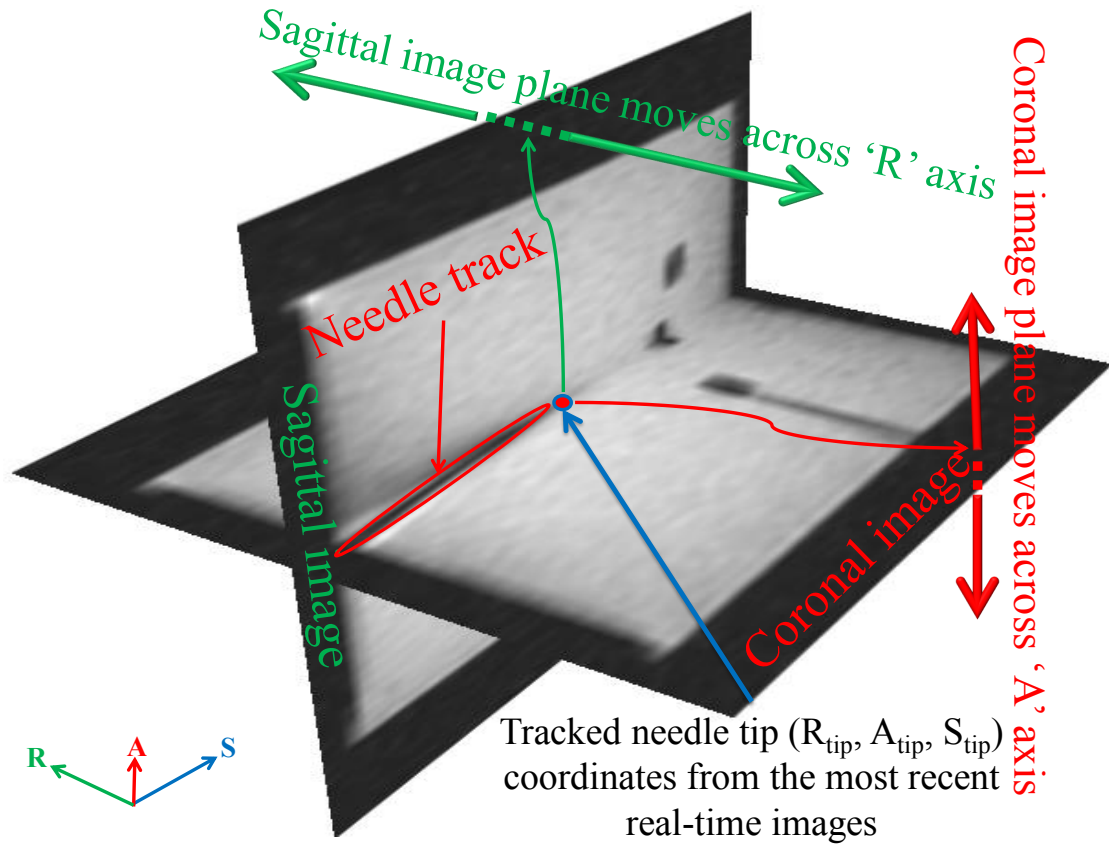


Figure 4.8: Scan geometry control showing how the sagittal image is moved Left/Right ('R' axis) and coronal image is moved Up/Down ('A' axis) autonomously to ensure that the needle tip is always visible in both images. For sagittal image only the 'R' coordinate of the image position changes, while for the coronal image only the 'A' coordinate of the image position changes.

### 4.6.1 Continuous MR Image Acquisition

The MR images should be of sufficient image quality to detect the needle tip, while being fast enough to provide continuous tracking. To reduce the scanning time, one coronal and one sagittal image is acquired with a slice thickness of 10 mm, resulting in two normal projection images of the needle as shown in Fig. 4.8. As described in the subsection 4.6.2, the scan geometry is updated continuously to acquire the sagittal and the coronal images one after the other. The thickness of the slice ensures high SNR while ensuring that the needle is maintained in the field of view.

The MRI sequence used for fast image acquisition is Spoiled Gradient Echo sequence T1-FFE (Fast Field Echo), By using T1-FFE, it is possible to obtain an MR image in either sagittal or coronal plane approximately every 750 ms. The T1-FFE sequence parameters used for all the experiments are: TR: 6.9291 ms, TE: 3.37 ms, Flip angle:  $5^\circ$ , FOV (Field of View) : 120 X 120 mm, acquisition resolution: 1 X 1 mm and reconstruction resolution: 0.42 X 0.42 mm.

### 4.6.2 Autonomous Scan Geometry Control

Scan geometry for the autonomous tracking application used in this paper is defined as a combination of (1) image orientation (transverse/sagittal/coronal) and (2) image position (R, A, S), The needle tip should be visible in both acquired projection images in order to calculate the 3D position of the tip. Since the slices are 10 mm thick, any deflection beyond that causes the needle tip to go out of the acquired projection images. Therefore, the scan geometry is updated using the located tip position in the most recent projection images in order to keep the needle tip visible all the time. As shown in Fig. 4.8 the sagittal image is moved along the R-axis based on the needle tip position determined in the most recent coronal

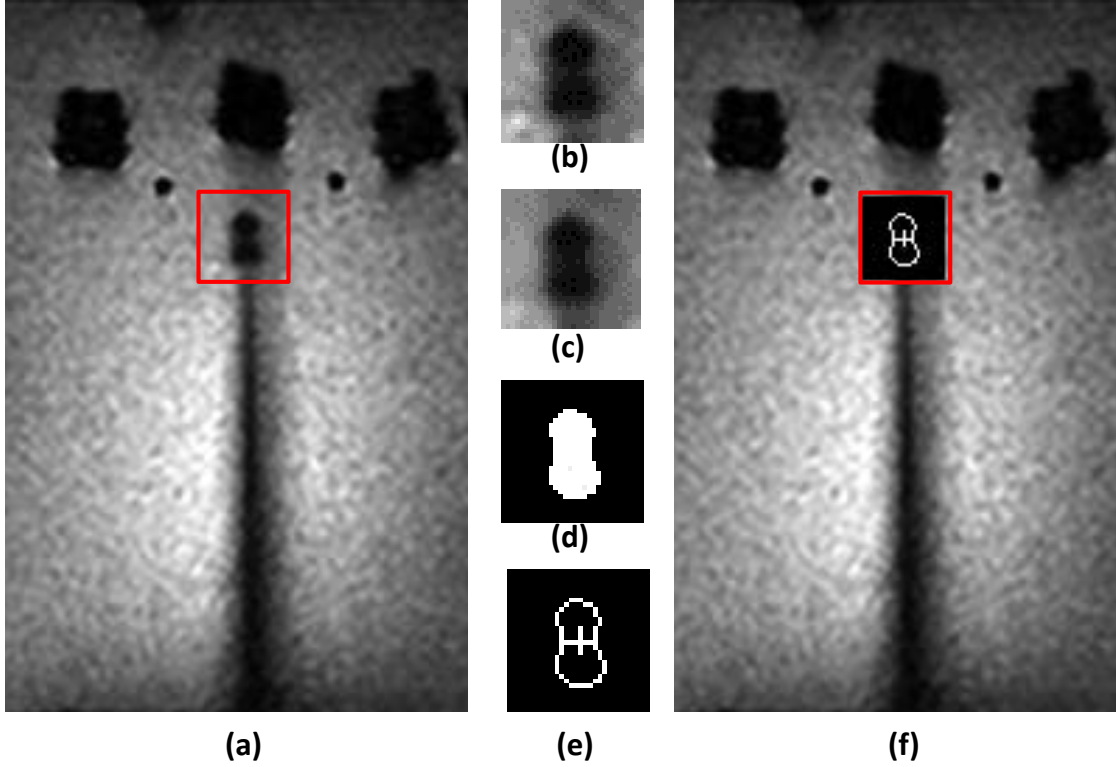


Figure 4.9: Autonomous needle tracking: (a) original image, (b) cropped to region of interest, (c) after median blur, (d) after thresholding, (e) after contour detection and center of contour bounding box, and (f) needle tip overlaid on original image.

image. Likewise, the coronal image is moved along the A-axis based on the needle tip position determined in the most recent sagittal image, maintaining the tip at the cross section.

### 4.6.3 Autonomous Needle Tracking

Tracking the needle tip is a crucial task for closed-loop needle steering. Using the projection images, the tracking problem is reduced from a 3D volume to two 2D images. As shown in Fig. 4.9, most recent images are processed to segment the needle tip using image processing operations including median blurring, thresholding and contour detection over the region of interest and tracked needle tip is overlaid

on the original images. Overlaid images are displayed to visualize the needle tip position and trajectory using the tracking application presented in Fig. 4.10. MR images are being acquired all the time and the needle tip is updated every time new set of images are available. The 3D needle tip coordinates are determined by taking 'R' coordinate from the coronal image and 'A' and 'S' coordinates from the sagittal image with an assumption that the 'S' coordinate is same in both images due to the same value for the 'S' coordinate in scan geometries. Combined needle tip ( $R_{tip}$ ,  $A_{tip}$ ,  $S_{tip}$ ) coordinates are sent to the steering algorithm and the scan geometry is updated.

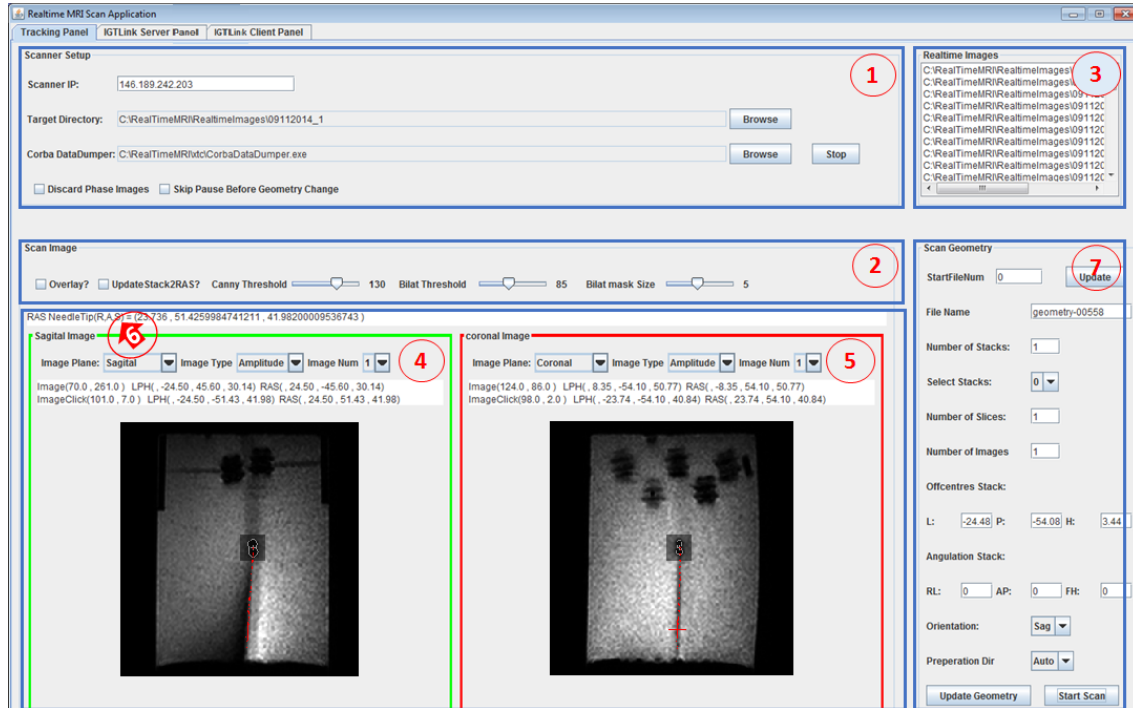


Figure 4.10: Autonomous needle tracking application showing: (1) the scanner control interface for configuring the scanner interface, (2) image processing parameters for autonomous tracking, (3) list of all the images received from XTC, (4) the most recent sagittal image, (5) the most recent coronal image, (6) needle tip coordinates from the autonomous tracking algorithm, and (7) scan geometry update interface to autonomously update the scan geometry based on tracked tip location.

In order to keep the needle tip within the scan region, the insertion speed has to

be limited by real-time scan update rate. Fig. 4.11 shows plot of maximum needle deflection Vs needle curvature, where the insertion depth of 100 mm and step size of 3 mm is assumed. It can be seen that the maximum needle deflection is less than 2.5 mm for needle curvature of 100 mm, this proves that the assumed MR image slice thickness of 10 mm would ensure that the needle tip would always stay within the scan region.

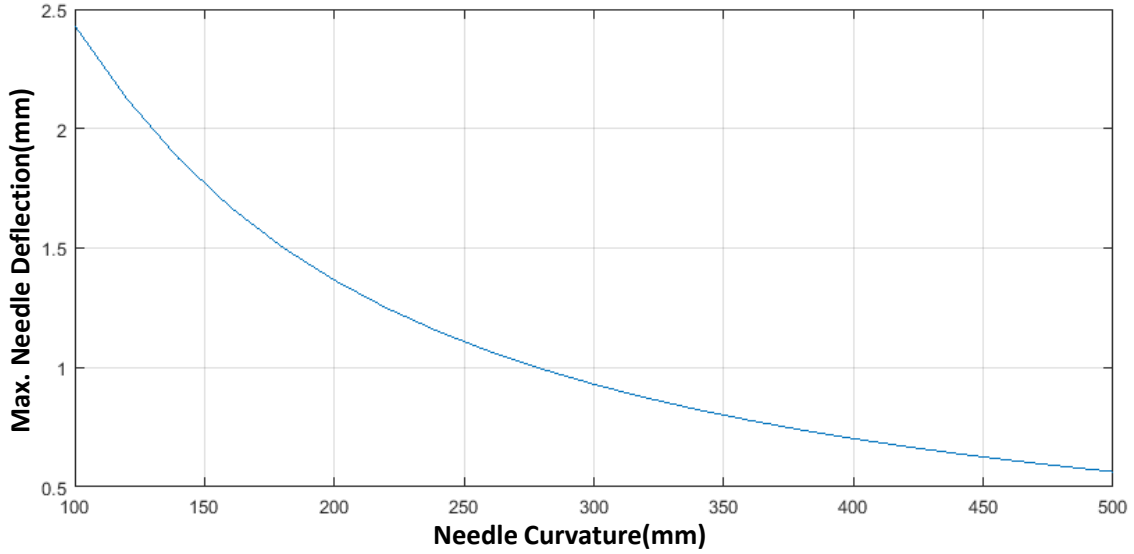


Figure 4.11: Plot showing maximum needle deflection Vs needle curvature, over insertion depth of 100 mm considering 3 mm insertion steps.

## 4.7 Closed-loop Steering Methodology

An asymmetric tip needle is assumed to move along an approximately constant curvature path in the direction corresponding with its bevel tip [98] when it is inserted in a soft tissue. Thus the needle can be steered in the 3D space by axially rotating the needle while it is inserted. The steering algorithm defines the axial rotation angle ( $\alpha$ ) needed to steer towards a target based on the needle and target pose. Also, for autonomous bevel angle controlled steering, the steering algorithm

calculates insertion step depth; while for autonomous and teleoperated insertion using CURV model, the steering algorithm dose not need to define the insertion depth as its continuous insertion at a constant velocity for autonomous steering and user defined insertion speed for teleoperated steering.

First, the needle pose ( $T_{tip}$ ) and target pose ( $T_{tar}$ ) have to be determined in the global frame. The target pose is considered to be a static location without any rotation and can thus be determined manually by using the MRI user interface. The needle pose is defined by:

$$T_{tip} = \begin{bmatrix} R_{tip} & p_{tip} \\ 0 & 1 \end{bmatrix}$$

where  $R_{tip}$  is 3X3 rotation matrix defining the needle tip direction and  $p_{tip}$  is 3x1 needle tip position.

The autonomous needle tracking application provides 3D needle tip positions for each insertion step. Consider that the needle trajectory in last N mm of insertion is given as

$$\begin{bmatrix} X \\ Y \\ Z \end{bmatrix} = \begin{bmatrix} x_1 & x_2 & ..... & x_n \\ y_1 & y_2 & ..... & y_n \\ z_1 & z_2 & ..... & z_n \end{bmatrix}$$

Now to estimate the needle pose, line is fit in YZ and XZ planes from the last N mm trajectory using least square and then those lines are used to determine the angle about X and Y axis respectively. Following equations give slope of the lines as 'a' and 'c' in YZ and XZ planes respectively, which are then used to calculate rotation about X and Y axis respectively.

$$Z = a * Y + b \quad \text{and} \quad Z = c * X + d,$$

$$\theta_X = \arctan(a) \quad \text{and} \quad \theta_Y = \arctan(c)$$

To find rotation about Z, current needle rotation is requested from the robot which is defined as  $\theta_Z$ .

Now needle tip rotation matrix is calculated by combining corresponding rotations about each axis as below,

$$R_{tip} = R_z(\theta_Z) * R_y(\theta_Y) * R_x(\theta_X)$$

The steering algorithm uses the needle and target poses to perform a homogeneous transformation to calculate the axial rotation required to steer the needle towards a predefined target. Fig. 4.12 shows how the relative rotation angle is calculated by first defining the target point within the needle coordinate frame, which is given by

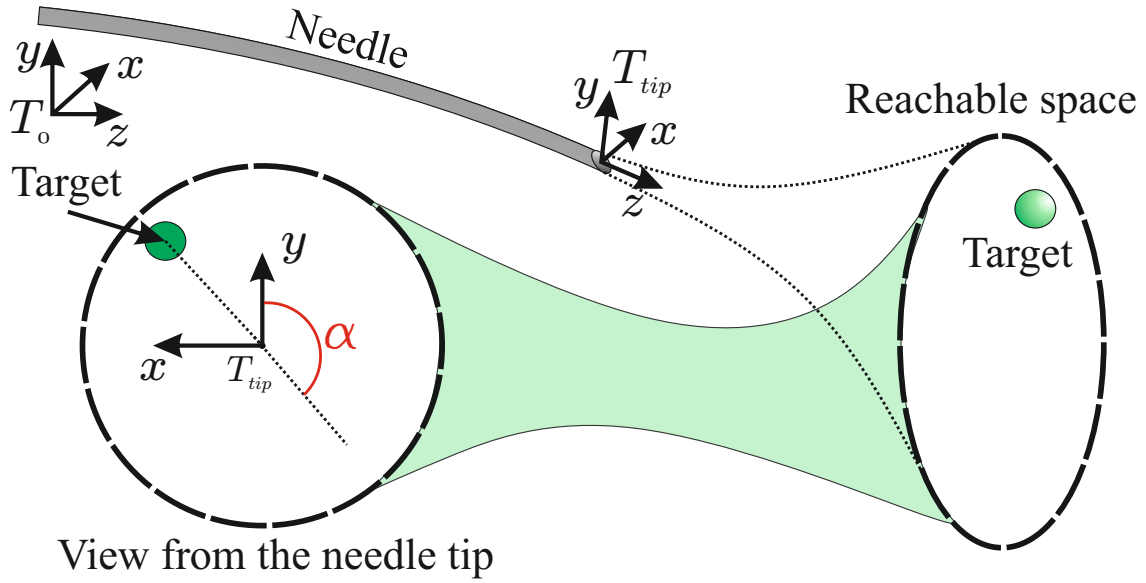


Figure 4.12: Needle steering parameter calculations, where  $\alpha$  is the rotation angle,  $T_{tip}$  is the needle tip frame and  $T_0$  is the global reference frame. [Credit: Pedro Moreira]

$$T_{tip}^{tar} = T_{tip}^{-1}T_{tar},$$

where  $T_{tip}^{tar}$  is the target pose in the needle tip coordinate frame.

The angle  $\alpha$  provides the relative amount of needle rotation needed to align the needle tip z-axis with the target position, which is determined by:

$$\alpha = \arctan(x, y) + \frac{\pi}{2},$$

where  $x$  and  $y$  are the coordinates of the target in the needle tip frame ( $T_{tip}^{tar}$ ), The addition of  $\frac{\pi}{2}$  is due to the definition of the used axis system where 0 degrees is aligned with the negative y-axis. Also, the desired needle curvature to hit the target could be given by Eq. 4.3.

$$k = \frac{1}{R} = \frac{1}{\frac{y}{z} + \frac{z^2}{2y}} \quad (4.3)$$

Estimated rotation angle  $\theta_d$  and curvature  $k$  are used to calculate the control inputs for different steering approaches, discussed in section 4.8.

For bevel angle controlled steering, the insertion step size for each step can be set beforehand. Ideally the insertion depth for each step should be as small as possible so the rotation angle can be determined continuously. However, smaller steps would increase total insertion time. Also, with the current MR image acquisition frame rate of 1.3 fps, faster insertion would result in less needle position feedback to the steering algorithm and consequently the targeting accuracy would be reduced. Thus a trade-off has to be made between the insertion time and the targeting accuracy.

After each insertion step the updated needle track coordinates from the most recent projection images are requested from the autonomous needle tracking appli-



cation. The process of determining the rotation angle is repeated until the target is reached.

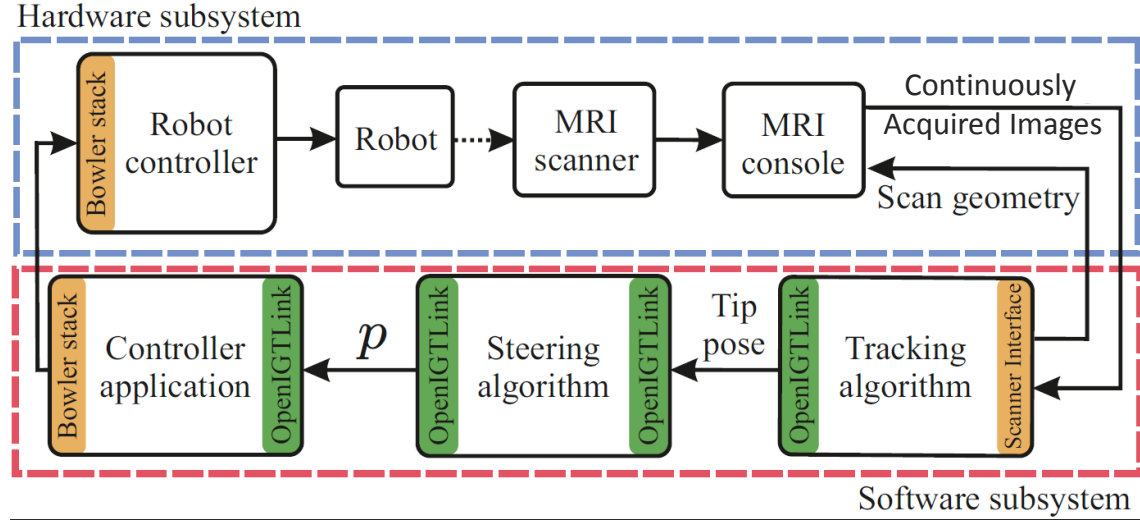


Figure 4.13: Needle steering workflow for control of the robot and the MRI scanner. Communication between the system components uses the OpenIGTLink and Bowler Stack protocols. The parameters ( $p$ ) produced by the steering algorithm depend on the approaches described in this section

## 4.8 Steering Approaches

Needle steering has been performed using three different approaches: (1) bevel angle controlled steering, (2) CURV model based autonomous steering and 3) CURV model based teleoperated insertion and autonomous rotation based steering. This section describes all three approaches and methodology for these approaches. Fig. 4.13 shows complete workflow for the presented needle steering approaches, as shown in figure the steering algorithm could be modified to implement bevel angle controlled, CURV model based or teleoperated insertion based steering.

### **4.8.1 Autonomous Steering with Bevel Angle Control**

The needle steering is performed with constant velocity insertion steps of  $P$  mm, needle pose is determined using the tracked points within the last  $N$  mm as described in section 4.7. Though, needle position is continuously updated by autonomous needle tracking algorithm and sent to the steering algorithm, steering parameters are calculated and sent to the robot controller every 3 mm and insertion is stopped to align the needle to desired steering angle. This process is repeated until the needle tip reaches within  $\epsilon$  mm of the target along the insertion axis.

### **4.8.2 Autonomous Needle Insertion with CURV Steering Model**

The needle steering using CURV model deals with fully autonomous, continuous needle insertion and rotation. The CURV model parameters: desired tip angle  $\theta_d$  and steering effort  $\alpha$  are calculated by the steering algorithm and sent to the low level control algorithm to produce desired rotation velocity profile. The insertion is performed at a constant velocity predefined for each experiment.

### **4.8.3 Teleoperated Needle Insertion with CURV Steering Model**

Teleoperated needle steering using CURV model gives an advantage of user controlled needle insertion, while the needle rotation is autonomously controlled by the steering algorithm. The CURV model parameters: desired tip angle  $\theta_d$  and steering effort  $\alpha$  are calculated by the steering algorithm and sent to the controller to produce desired velocity profile while the insertion is designed to follow the master device being controller by the user.

## 4.9 Experiments and Results

### 4.9.1 Experiment Setup

The feasibility of the system workflow and the accuracy of the closed-loop robot-assisted needle steering are assessed with phantom studies, in a Philips 3T MRI scanner, as shown in Fig. 4.1. A bevel-tipped, solid yet flexible nitinol needle with a diameter of 0.8 mm (21G) and a tip angle of  $30^\circ$  is used in this study. The insertion and rotation of the needle is driven by a 7-DOF MRI-compatible needle placement robot, as described in detail in [65, 78]. The gelatin phantom is made with a mixture of 13% gelatin (Knox, Northfield, USA) and 87% water. Plastic toothpicks are attached on the container wall to serve as target markers. At the beginning of each insertion the needle is inserted 5 mm into the phantom to determine the initial position of needle tip. Target position on the edge of the markers is selected manually in the MR images. Initial tip and target positions are provided to the steering algorithm. During insertions, the needle tip position is autonomously tracked with Spoiled Gradient Echo MR imaging sequence T1-FFE (fast field echo, TR: 6.93 ms, TE: 3.37 ms, Flip angle:  $50^\circ$ ). At the end of the insertion, for better accuracy assessment, the final error is manually determined by comparing the actual tip position collected with a standard diagnostic T2-weighted turbo spin echo (T2W-TSE) image (TR= 3030 ms, TE=115 ms, flip angle= $90^\circ$ , slice thickness = 3 mm, FOV: 120 X 120 X 120 mm, acquisition resolution: 0.5 X 0.5 mm and reconstruction resolution: 0.5 X 0.5 mm) with the desired target position. Phantom is shifted to avoid previous needle tracks and a different entry and target point are determined for each insertion.

### 4.9.2 Results for Bevel Angle Controlled Steering

Five needle steering experiments are performed to validate the bevel angle controlled steering approach. The results of the experiments are summarized in Table 4.1. Based on the selected targets at different locations, the insertion depth varies between 70 mm and 85 mm. The average insertion time is around 12 minutes which includes time for needle alignment and insertion. The final tip positions of the needle correspond with the desired target points with an average total error of 2.5 mm. In most surgical procedures, error along the insertion axis (S) is not considered as significant compared to the errors in RA plane normal to the needle axis. As shown in Table 4.1, average error in the RA plane is 2.09 mm. A study of manual MRI-guided needle biopsy presented in [99] has shown targeting errors of 5.5 mm to 6.3 mm. Without needle steering, considering curving radius of 300 mm and average insertion depth of 80 mm, maximum error for a straight insertion can be as large as 10.08 mm.

Table 4.1: Accuracy Assessment Bevel Angle Controlled Steering to 5 Targets

No	Target Position[mm]			Final Tip Position[mm]			Error[mm]			Total Error[mm]	In-plane(RA) Error[mm]
	R	A	S	R	A	S	R	A	S		
1	4.162	4.59	81.088	6.402	4.69	82.438	2.24	0.1	1.35	2.62	2.24
2	-0.841	-7.09	81.723	0.919	-6.45	82.653	1.76	0.64	0.93	2.09	1.87
3	-1.248	7.92	77.563	0.802	8.55	78.453	2.05	0.63	0.89	2.32	2.14
4	13.176	0	70.474	14.836	0.14	71.904	1.66	0.14	1.43	2.20	1.67
5	9.171	-5.01	81.727	11.651	-4.55	83.787	2.48	0.46	2.06	3.26	2.52
Mean							2.04	0.39	1.33	2.50	2.09
Standard deviation							0.34	0.26	0.47	0.47	0.33

Note: R, A and S are the coordinates of the needle tip, while RA plane corresponds to axial plane in MRI scanner coordinate system.

### 4.9.3 Results from Autonomous CURV steering

The targeting accuracy of autonomous CURV steering is evaluated with a gelatin phantom. 10 random targets are selected around the embedded rubber rings in the gelatin phantom, and different entry points are defined for each insertion to prevent

effects from previous needle tracks. The target accuracy is evaluated using the final confirmation scans and manually segmenting the needle tip and comparing it with the previously defined target. The results from the targeting accuracy are presented in Table 4.2 . The experiment results demonstrate that the RMS error of targeting in 3D space is 0.75 mm. In most clinical procedures, the in-plane error has more significant as the insertion is controlled by the physician and could be adjusted to match with the target plane. The in-plane (RA) RMS error from the performed experiments is 0.73 mm.

Table 4.2: Accuracy assessment of autonomous steering to 10 targets using CURV steering model

Target NO.	Target Position (mm)			Actual Tip Position (mm)			Error (mm)				
	R	A	S	R	A	S	R	A	S	In-plane (RA)	Total
1	18.22	54.58	-25.09	18.8	55.0	-24.9	0.58	0.42	0.19	0.72	0.74
2	13.35	63.20	-25.09	13.6	62.2	-25.0	0.25	1.00	0.09	1.03	1.03
3	10.35	55.33	-26.22	10.6	54.9	-26.3	0.25	0.43	0.08	0.50	0.50
4	14.47	61.95	-19.60	13.6	61.9	-19.6	0.87	0.05	0	0.87	0.87
5	15.47	54.95	-18.00	15.1	56.2	-18.1	0.37	1.25	0.10	1.30	1.31
6	8.50	61.95	-19.00	8.6	62.2	-19.0	0.10	0.25	0	0.27	0.27
7	9.10	53.95	47.00	9.4	54.0	46.5	0.30	0.05	0.50	0.30	0.59
8	17.10	61.58	49.00	17.0	62.0	48.9	0.10	0.42	0.10	0.43	0.44
9	17.73	60.58	50.00	17.9	61.3	49.8	0.17	0.72	0.20	0.74	0.77
10	14.48	51.58	49.00	14.4	51.9	48.9	0.08	0.32	0.10	0.33	0.34
Standard Deviation (mm)							0.24	0.37	0.14	0.33	0.31
Mean Error (mm)							0.31	0.49	0.14	0.65	0.69
RMS Error (mm)										0.73	0.75

#### 4.9.4 Results from Teleoperated Insertion with CURV steering

The needle insertion is controlled by the master device being operated manually, while the rotation is controlled autonomously by the steering algorithm. CURV steering parameters are continuously updated by the steering algorithm and sent over to the robot. For accuracy validation, 10 random targets are selected in the gelatin phantom. The accuracy of needle steering with teleoperated insertion is summarized in Table 4.3.

Table 4.3: Accuracy assessment of steering to 10 targets using teleoperated insertion and CURV steering model

Target NO.	Target Position (mm)			Actual Tip Position (mm)			Error (mm)				
	R	A	S	R	A	S	R	A	S	In-plane (RA)	Total
1	13.05	52.53	46.00	13.1	53.3	46.1	0.05	0.77	0.10	0.77	0.78
2	13.70	62.90	46.00	14.1	62.4	45.9	0.40	0.50	0.10	0.64	0.65
3	16.70	62.03	48.00	16.6	62.0	48.1	0.10	0.03	0.10	0.10	0.14
4	17.90	54.67	49.00	17.6	54.5	49.0	0.30	0.17	0	0.34	0.34
5	10.10	60.95	34.00	10.7	61.0	33.9	0.60	0.05	0.10	0.60	0.61
6	14.48	62.95	38.00	15.2	63.0	37.9	0.72	0.05	0.10	0.72	0.73
7	16.48	53.95	38.00	15.9	53.0	37.9	0.58	0.95	0.10	1.11	1.12
8	17.73	57.95	36.00	18.1	58.0	36.1	0.37	0.05	0.10	0.37	0.39
9	6.73	57.95	36.00	7.6	59.0	36.1	0.87	1.05	0.10	1.36	1.37
10	15.35	53.95	38.00	14.5	54.0	37.9	0.85	0.05	0.10	0.85	0.86
Standard Deviation (mm)							0.27	0.39	0.03	0.35	0.35
Mean Error (mm)							0.48	0.37	0.09	0.69	0.70
RMS Error (mm)										0.77	0.78

## 4.10 Discussion and Conclusions

This chapter presents a closed-loop steering approach for bevel-tipped needles using an MRI-compatible robot and an autonomous needle tracking system. Three different steering approaches: (1) autonomous bevel angle controlled steering, (2) autonomous CURV model based steering and (3) steering using teleoperated insertion utilizing CURV model are presented. The needle tracking problem is reduced from a 3D volume to a 2D image processing by using the projected images in coronal and sagittal planes. The MRI scan-plane geometry is continuously adjusted to keep the needle tip visible during the insertion, which is essential for tracking the needle tip. This approach provides closed-loop steering of the needle to autonomously reach a target. It is the first time that the closed-loop needle steering using autonomous needle tracking is performed under real-time MRI-guidance. Though targeting errors of less than 1 mm with closed-loop control could potentially improve treatment quality for various needle based percutaneous interventions such as prostate biopsy, the non-homogeneous tissue properties and patient movement could potentially affect the system accuracy. Also, it can be seen that the continuous insertion and

rotation using CURV approach providing variable curvature has proven to provide better accuracy compared to constant curvature based bevel angle controlled steering. Though, the experiments are performed in a homogeneous gelatin phantoms, only limiting factor for performing such experiments in ex-vivo tissues would come from developing more robust needle tracking algorithm, faster scan sequence with optimized Field Of View (FOV) and improved image contrast highlighting tissue boundaries along with the needle tip. The presented results have proven that various percutaneous interventions could be performed under real-time MR image guidance.

# Chapter 5

## Closed-loop Conformal Brain Tumor Ablation under Real-time MRI Guidance

### 5.1 Contributions

Stereotactic neurosurgery has been a research focus in the AIMLab since its inception. I worked on development and integration of an MRI compatible robotic system for conformal brain tumor ablation under real-time MRI guidance. Two generation of robot and robot controllers are developed, mechanical system is designed by my lab colleagues Gang Li [64], Christopher Nycz and Radian Gondokaryono, while electronics system is designed and developed by Alex Camilo and Paulo Carvalho. The latest version of system comprises of MRI compatible robot, real-time Linux based motion control hardware and firmware, high level robot control and clinical user interface, surgical planning application (TheraVision, Acoustic MedSystems Inc.), High Intensity Focused Ultrasound applicator and ablation



system controller (Acoustic MedSystem Inc.), All the system components communicate over OpenIGTLink to deliver closed-loop thermal dose delivery to an arbitrary shaped tumor. My role has been to integrate the complete system to deliver desired thermal dosage under real-time MR-thermometry monitoring, which required development of precise ultrasonic motor control, surgical workflow management, ablation probe localization using active MR-tracking coils, real-time MR-thermometry and real-time MRI scanner control. Also, I developed OpenIGTLink interface for communication between robot control application, TheraVision, 3DSlicer and real-time scanner controller. The integrated system has been successfully used for cadaver and animal trials producing promising results.

## 5.2 Introduction

Stereotactic neurosurgical procedures are among the most common minimally invasive procedures performed under image guidance. Minimally invasive procedures such as DBS electrode placement and tumor ablation are often performed under image guidance, but using a mechanical stereotactic frames such as Leksell Stereotactic System<sup>®</sup> (Elekta AB) and AXiiiS Stereotactic Miniframe (Monteris Medical Inc) as shown in Fig. 5.1 . Use of such a mechanical frame induces human and systematic errors, while the image guidance still remains uncoupled to the surgical device. In a typical procedure, preoperative MRI is acquired a few days before the surgery, while during the surgical procedure interventional CT images are fused with MR images to guide the surgical device [100], which is adjusted manually by setting entry angles and insertion depth. As the image guidance is not directly coupled with the surgical device, it potentially could induce human error and limited precision of the mechanical system could results in non-optimal outcome. Introducing a robotic

device coupled with image guidance could potentially improve the surgical workflow, improve the tool placement accuracy and potentially reduce human induced errors.

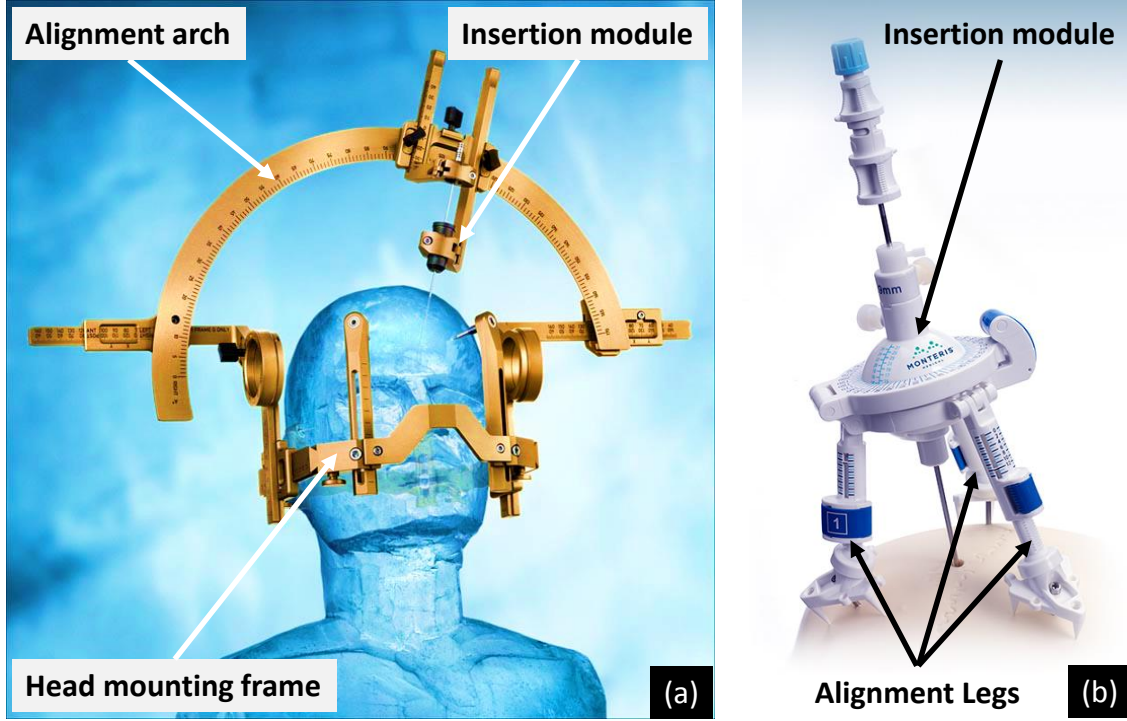


Figure 5.1: Stereotactic neurosurgery frames: (1) Leksell Stereotactic System<sup>®</sup> (©Elekta AB) and (b) AXiiiS Stereotactic Miniframe (©Monteris Medical Inc)

Brain metastases are among the most common neurological complications with incidence of 9%-17% , of which primary cancers such as the lung cancer, breast cancer, and melanoma account for 67%-80% of all cancers [101]. In recent year, interventional MRI guided neurosurgery systems [59] and laser interstitial thermal therapy for treatment of brain tumors [58] have shown promising results. With intraoperative MRI guidance the tool placement accuracy has improved while the laser ablation could deliver conformal ablation to desired tumor regions. Fig. 5.2 shows a smart frame device (ClearPoint, MRI interventions) and an ablation system (NeuroBlate, Monteris Inc.), Though, MRI guided robotic systems has been explored for various minimally invasive procedures such as prostate biopsy [21–24],

there aren't any fully actuated robotic systems for minimally invasive neurosurgical procedures under MRI guidance. A fully actuated robotic system for stereotactic neurosurgery procedure could allow more accurate placement of the surgical device under MR image guidance. Our research group developed fully actuated, MRI compatible system for DBS electrode placement [64, 102]. This motivated development of an MRI guided robotic system for conformal brain tumor ablation using focused ultrasound interstitial ablation device. In this chapter an integrated system comprising of an 7-DOF MRI compatible robot, robot controller, ablation system, precise active tracking coil based ablation probe localization, and real-time MRI guided thermal dosage monitoring is presented.

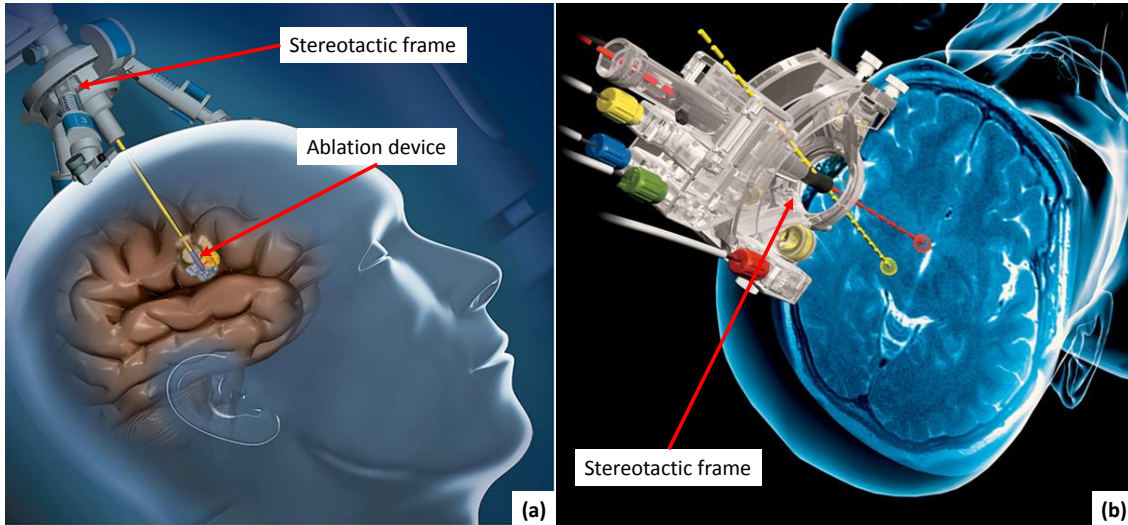


Figure 5.2: (a) NeuroBlate system (©Monteris Inc.) and (b) smart frame device (ClearPoint from ©MRI interventions)

### 5.3 System Architecture

This system is developed to deliver real-time MRI guided thermal dosage to targeted brain tumor. The robotic manipulator augments the traditional stereotactic frame

and provides additional degrees of freedom to precisely place the ablation device at the target location. The system implements the presented closed-loop system architecture and have following modules specific to this application: (1) MRI compatible robotic manipulator, (2) real-time Linux based embedded robot controller, (3) robot control application, (4) surgical planning and navigation applications: TheraVision and 3D Slicer, (5) real-time scanner control and thermometry module and (5) active tracking coil based ablation device localization module. Fig. 5.3 depicts the adopted system architecture and data flow between various components, while Fig. 5.4 shows typical system setup for a tumor ablation procedure.

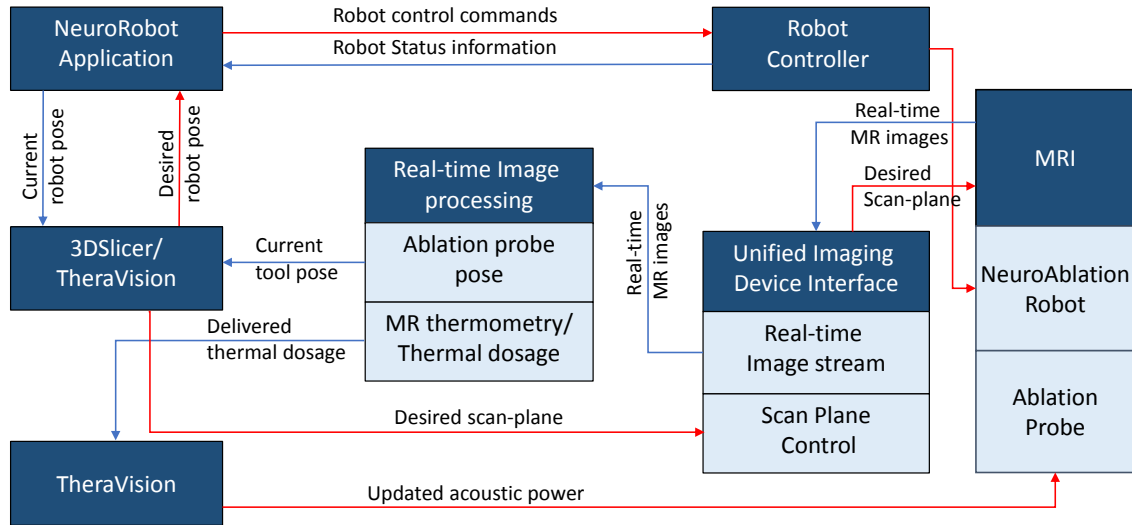


Figure 5.3: Closed-loop system architecture adopted to neurosurgery application showing various modules of the system and data flow between them

The surgical plan is prepared on the planning application 3DSlicer using intra-operative MR images. The plan includes desired target and entry locations for the ablation device. The robotic manipulator is registered to the scanner coordinate system using a rigidly attached localization frame (Z-Frame) to the robot platform. The surgical navigation application, TheraVision computes the registration transform, which is sent to the robot control application over OpenIGTLink. After robot

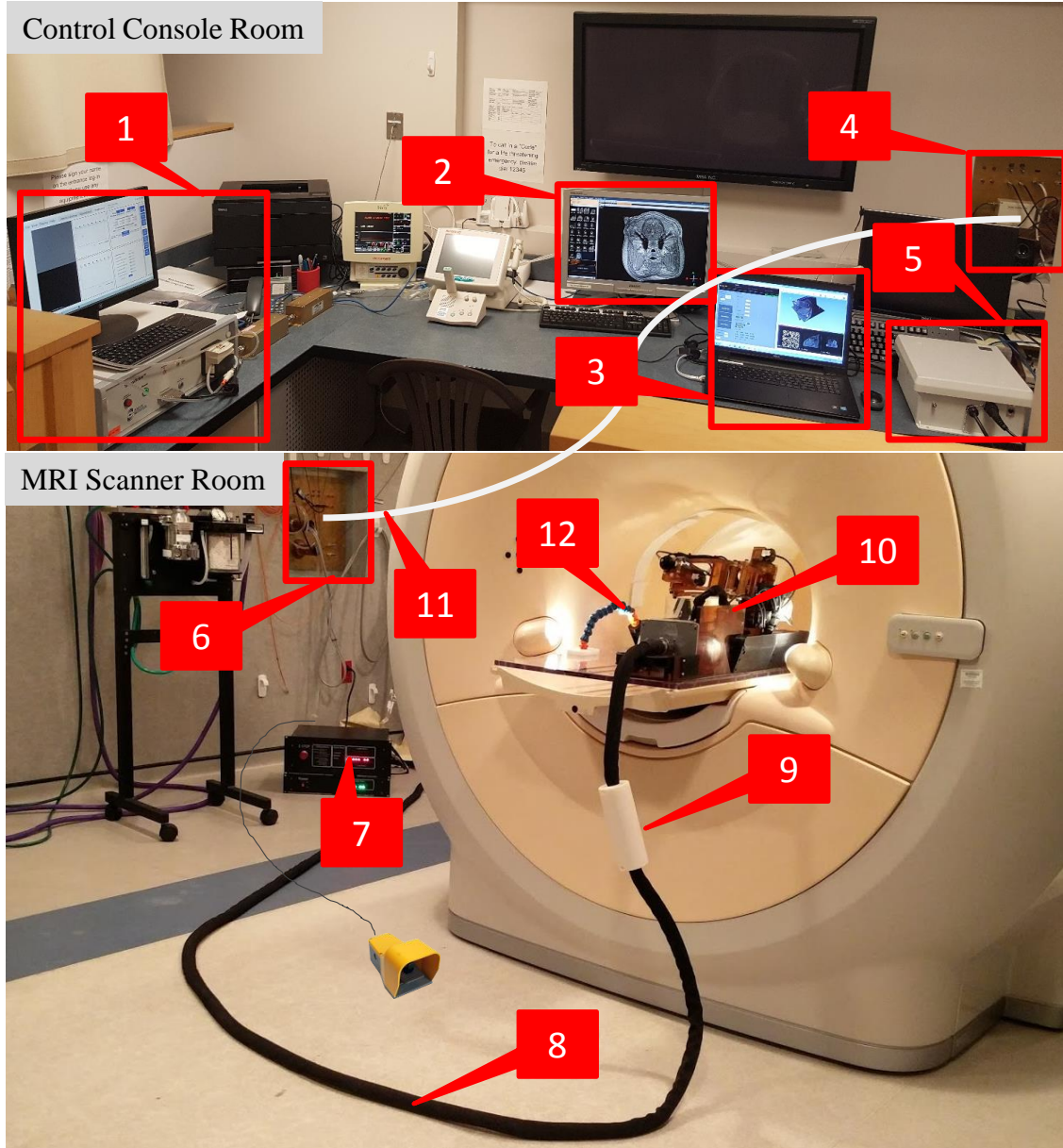


Figure 5.4: Integrated system setup: In the control console room: (1) Ablation system, (2) MRI control console, (3) surgical navigation user interface, and robot control application, (4) patch panel, and (5) network interface box with fiber optic connector. Inside the scanner room: (6) patch pane through which scanner console and components inside the MR room are connected, (7) MRI compatible robot controller, (8) custom cable carrying motor and encoder connections, (9) ballen for reducing EMI, (10) robotic manipulator inside the scanner bore, (11) fiber optic cable for communication between robot control application and the embedded robot controller, and (12) custom MR imaging coil

is registered to the scanner coordinate system, the TheraVision receives the target and entry points and visualizes them on the intraoperative MR images on the day of surgical procedure, and then computes the target pose (4x4 homogeneous transform) and sends it to the robot control application. Robot control application performs the inverse kinematics and sends the joint level commands to the embedded robot controller. The physician engages the foot-pedal to activate the robot motion and robot aligns to desired target pose, except that the probe insertion is performed after the ablation probe is attached to the robot maintaining the sterile field. Once the probe is inserted to the desired depth, confirmation MR image are acquired along with the tracking coil images and a scan plane perpendicular to the probe path and passing through the ablation elements is set through the robot control application. After the scan plane is set at desired position and orientation, the ablation device is powered ON and the MR-thermometry module starts temperature and thermal dosage monitoring and displays it in real-time. Once the desired thermal dosage is delivered, the ablation device is manually powered OFF and the probe is pulled out and detached from the robot.

## 5.4 MRI Compatible Neurosurgery Robot

Two generations of robotic manipulators are developed. Though both systems are mechanically different, their kinematics model is somewhat similar. Both the manipulators have 3-DOF for positioning, while 3-DOF to align the ablation device and 1-DOF for ablation device insertion. Fig. 5.5(a) shows CAD model of previous generation of the robot [94], while Fig. 5.5(b) shows CAD model of the latest manipulator. Previous generation of the robotic manipulators was designed by Gang Li, while the current generation is designed and developed by Christopher Nycz and



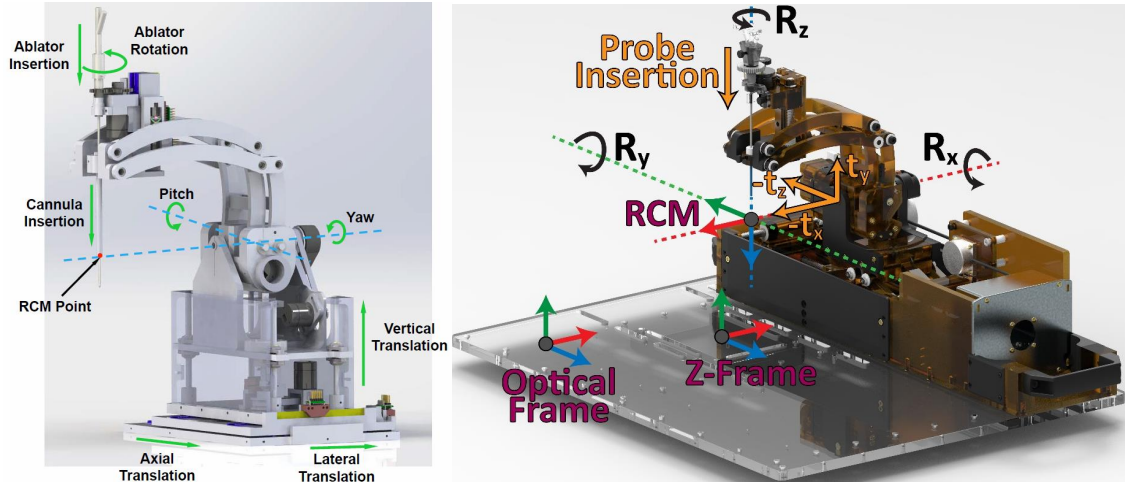


Figure 5.5: (a) First generation NeuroAblation robot CAD model showing all the joints and their motion directions [94]©2016 Li Gang, (b) Latest manipulator with machined parts

Radian Gondokaryono. My role in this design process was to provide needed inputs regarding robot workspace and development of needed electronic interfaces to the robot controller. Fig. 5.6 shows custom developed encoder interfaces and Fig. 5.7 shows the custom made cable being used for the current version of the robot.

## 5.5 Embedded Robot Controller

Two generations of robot controller are also developed. Both version of the controller implements closed-loop control of piezoelectric motors, safety mechanisms and communication interfaces to the robot control application. Previous generation controller was described in detail in Section 2.4.3, while Fig. 5.8 shows current generation controller component layout. The current generation controller uses National Instruments' System on Module (SOM) running real-time Linux, while its FPGA core runs high speed reliable SPI communication to each of the motor control modules. The electronics components are developed by my lab colleagues Alex

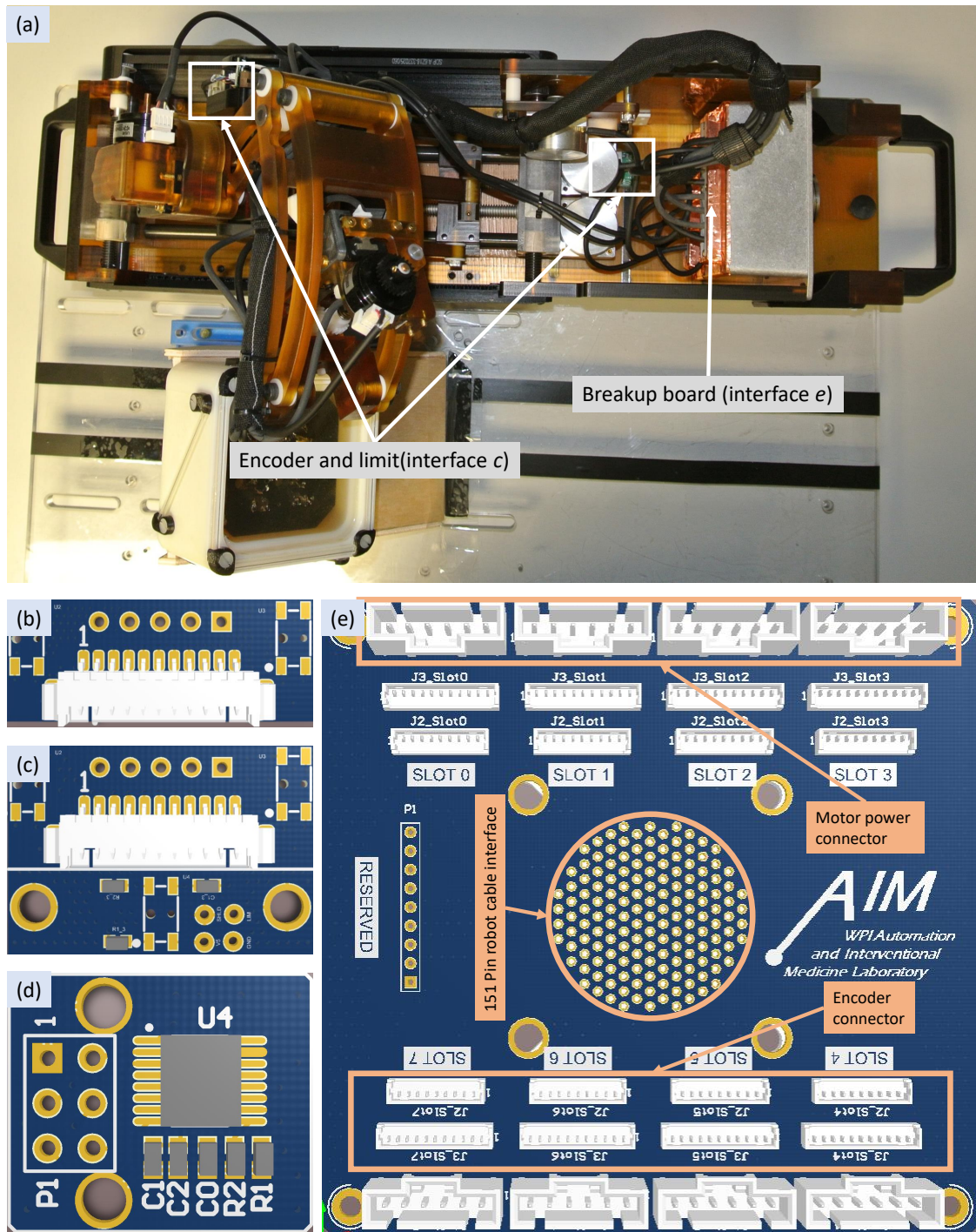


Figure 5.6: Custom developed encoder and cable interfaces: (a) showing location of interfaces (c) and (e) on the robot, (b, c, and d) three versions of encoder and limit interfaces and (e) the breakup board for all the robot axis





Figure 5.7: Custom cable design: left showing layout of 151 conductors color coded pin-out to identify each encoder and motor power cable clusters and on the right showing the final assembled cable

and Paulo.

## 5.6 Robot Control Application

The robot control application is adapted from the prostate robot control application described in section 2.5.2. The CUI is adopted to the neurosurgery robot and the robot pose visualization is advanced through display of 3D robot poses as shown in Fig. 5.9. An additional interface for communication between robot control application and 3DSlicer is developed, which allows sending registration transform and current robot pose over OpenIGTLink. Also, an advanced planning interface based on entry-point definition is developed, which allows planning with given entry point. This interface generates workspace of the robot by assuming given entry point as a virtual Remote Center Motion (RCM) point for the manipulator, this potentially

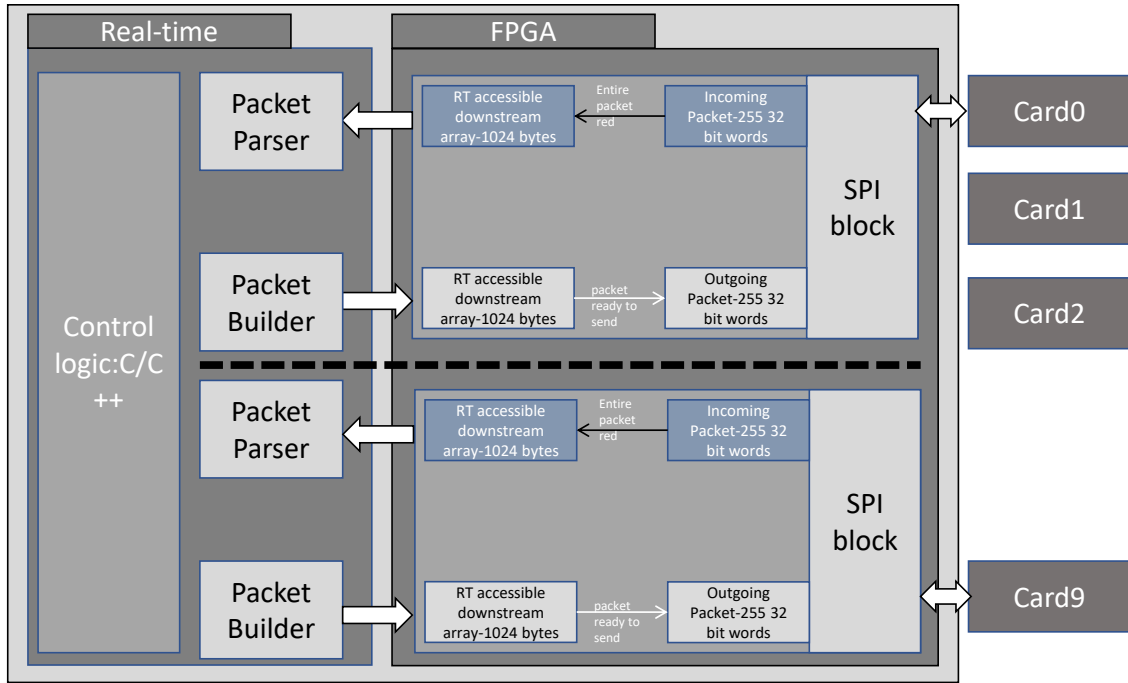


Figure 5.8: Current generation Controller block diagram

could allow better planning and ensure reachability of the robot given an entry point. Fig. 5.10 shows this slicer communication and workspace planning interface.

## 5.7 Surgical Navigation System

Surgical navigation plays an important role in IGT procedures. Preoperative planning and visualization are essential components of any IGT system. As described in Chapter 2, surgical navigation based on preoperative or intraoperative images allows dynamic changes in surgical plan and navigation during the procedure. Two surgical planning and navigation application are integrated for the brain tumor ablation system: (1) TheraVision: primary application for the ablation system planning and control and (2) 3DSlicer: primary application for surgical planning and navigation. Both the application interfaces are described in detail in this section. Fig. 5.11 shows typical workflow used for the surgical procedure.

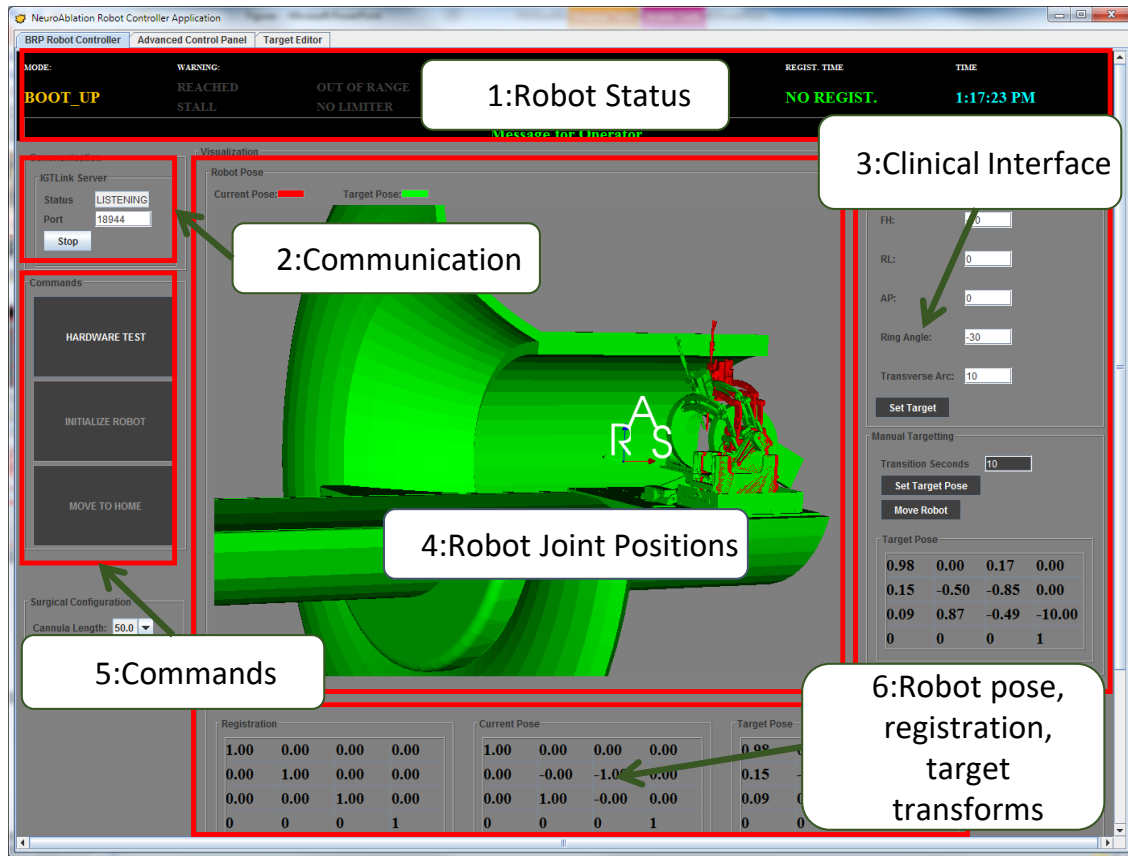


Figure 5.9: Clinical robot control application (CUI) showing: (1) robot status, (2) communication interface, (3) clinical interface mimicking stereotactic frame parameters, (4) current and target robot poses visualized with 3D models, (5) robot commands, (5) robot current pose, registration and target transforms

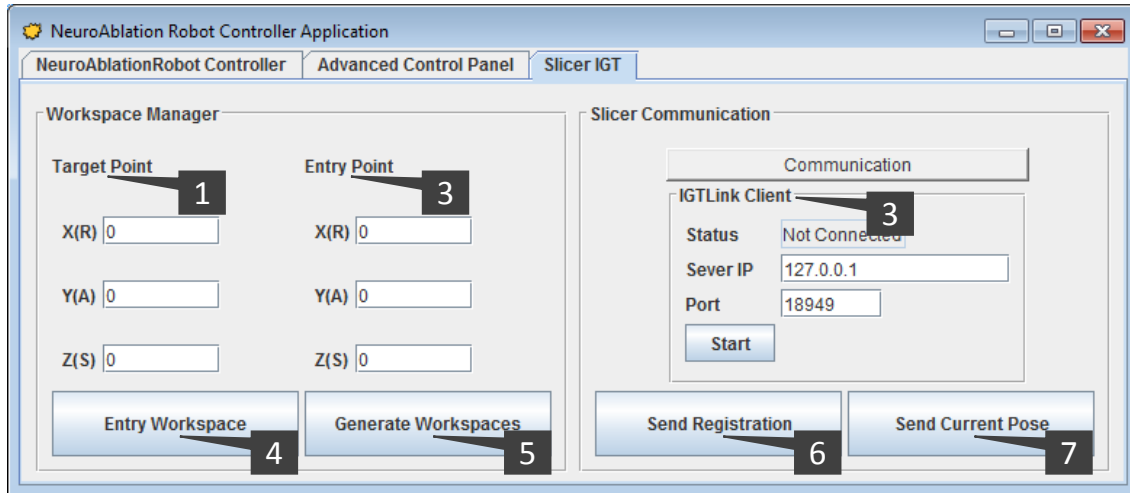


Figure 5.10: Slicer communication and entry point based surgical planning interface showing: (1) defining target point, (2) defining entry point, (3) OpenIGTLink client for communication with slicer, (4) command to generate workspace given the entry point, (5) command to generate robot workspace from its XML specifications, (6) command to send the robot registration transform to 3DSlicer and (7) command to send current robot pose to 3DSlicer

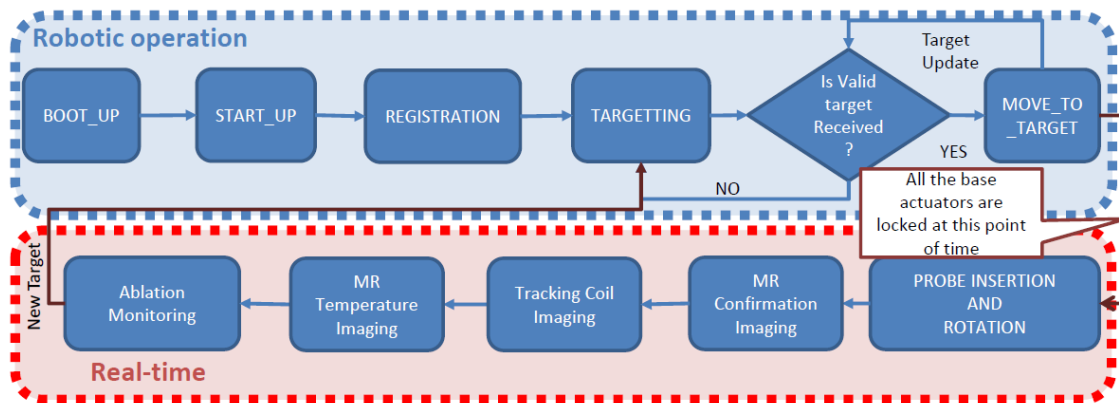


Figure 5.11: TheraVision workflow for brain tumor ablation showing robotic and real-time image guided operations during the procedure, also shows only valid system state transitions

### 5.7.1 Robot Workspace Analysis

Overlay of the robot workspace on the intraoperative MR images helps in determining the reachability of the robot. Based on the robot configuration specified by XML file, the robot control application has a workspace generation module, which generates both target and entry point workspaces considering all the joint limits. Fig. 5.14 shows generated workspace with robot at its home position, overlaid on top of the acquired intraoperative MR images. Also, during the surgical planning phase, as the entry points is specified first, it is essential to know the reachable target regions given an entry point. In order to generate such dynamic workspace, a module as shown in Fig. 5.10 takes entry point as input and generates reachable workspace assuming the entry point as virtual RCM point. Fig. 5.12 shows one of such workspace generated given an entry point. As it can be seen that the reachable workspace is significantly reduced once the entry point is specified, overlay of such a workspace helps in determining the reachable target points from the defined entry point.

### 5.7.2 TheraVision

TheraVision is a FDA approved surgical planning and navigation application developed by Acoustic MedSystems Inc. and has been in use at various research sites. TheraVision has mainly four modules related to the brain tumor ablation system. (1) HIFU Ablation Probe controller hardware, (2) ablation control application, (3) surgical planning and navigation module and (4) OpenIGTLink based robot control module. Fig. 5.13 shows various modules of the TheraVision application for surgical planning and navigation.

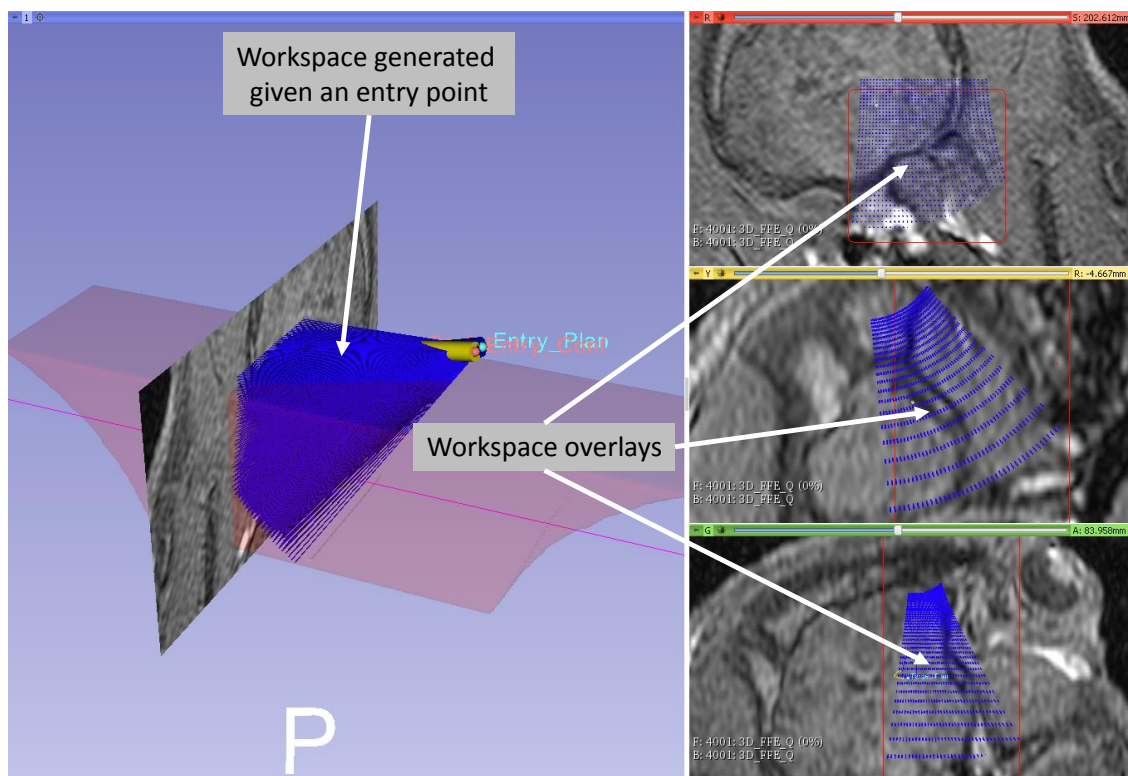


Figure 5.12: Slicer user interface showing dynamic workspace calculated based on a given entry point

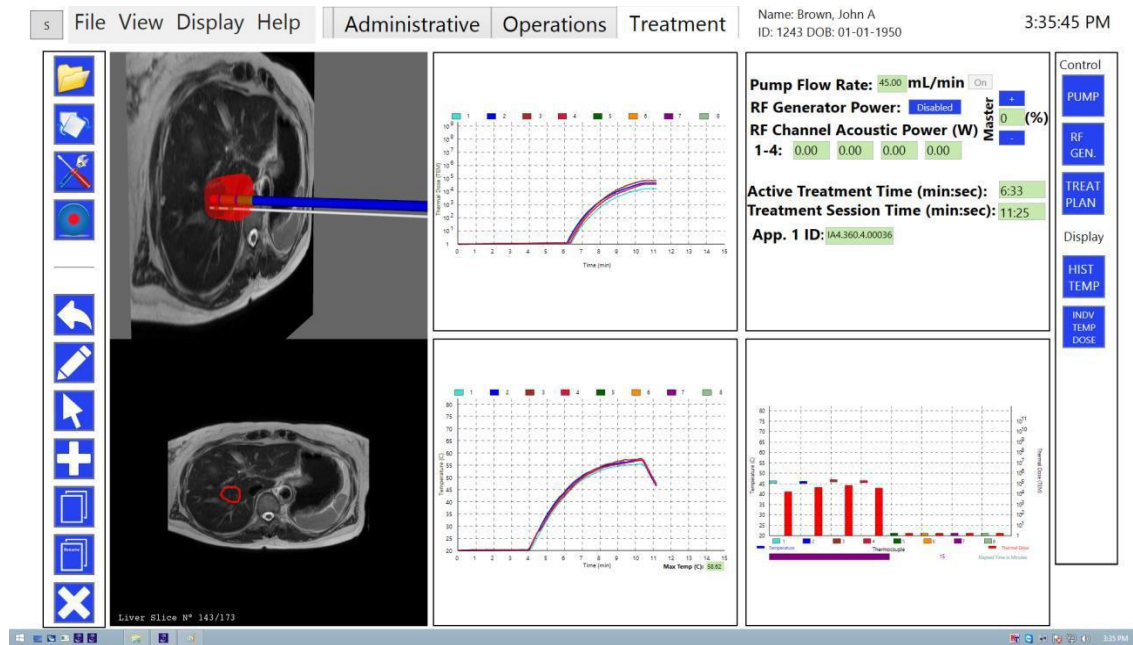


Figure 5.13: TheraVision modules for brain tumor ablation: (1) image and thermal dosage visualization, (2) acoustic power Vs time graph, (3) treatment control module and (4) fluid circulation control module

### 5.7.3 3DSlicer

3DSlicer is a commonly used surgical planning and navigation application for various IGT procedures. 3DSlicer based surgical planning and navigation workflow is created for preoperative planning and visualization. 3D slicer visualizes robot workspace, overlaid on top of intraoperative images to convey reachability of the robot. The surgeon selects the desired target and entry points using 3 views as displayed in Fig. 5.14. Once the desired target and entry points are defined, they are transferred to the TheraVision, which then sends a desired target pose to the robot control application.

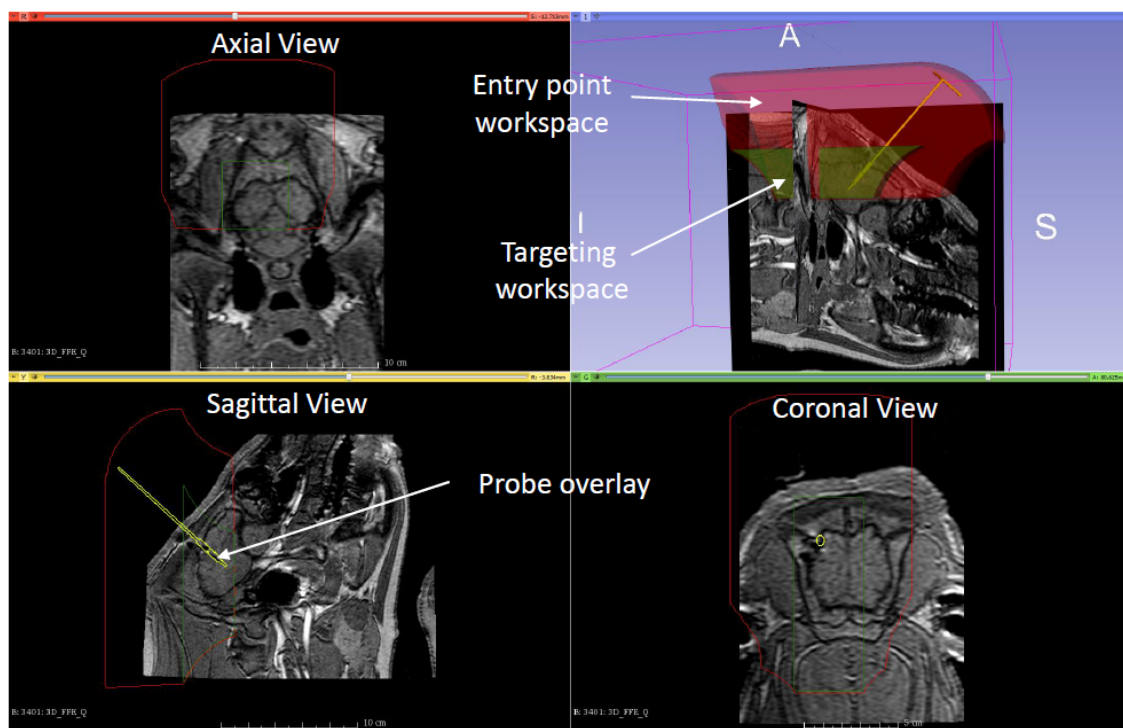


Figure 5.14: Slicer User Interface for brain tumor ablation planning showing intra-operative MR images, overlay of robot workspaces, and ablation probe.



## 5.8 Ablation Probe Tracking Using Active Coils

Passive tracking has an advantage of minimum hardware dependency and can work on any MRI scanner or in-fact for any imaging modality, but accuracy of tracking is compromised by the image quality. Damoulin. et .el [103] presented real-time position monitoring of invasive device using micro tracking coils, while real-time bi-planar needle tracking using micro coil embedded in a polyetheretherketone needle tip was demonstrated by Leung et.el [104], Hillenbrand et.el [105] presented active device tracking and high-resolution intra-vascular MRI using a catheter-based, opposed-solenoid phased array coil. It is possible to integrate multiple micro tracking coils in a needle like medical devices [106] to get not only position but also orientation information. Wang et.el [107] demonstrated tracking of metallic stylet for brachytherapy using 3 embedded micro tracking coils. Localization of minimally invasive devices such as an ablation probe is critical to the success of not only the surgical procedures but also for the precise localization of the ablation zone. For an ablation probe, its position as well as orientation both are important to overlay it over the intraoperatively acquired MR images and define the scan geometry for MR thermometry images which are supposed to be perpendicular to the probe axis. In this section, the construction of the ablation probe and tracking coils localization algorithm are described.

### 5.8.1 Probe Construction

ACOUSTx<sup>TM</sup> (Acoustic MedSystems Inc.) ultrasound ablation applicator consists of one or more directional ultrasound based ablation elements and two tracking coils. One tracking coil is located near the tip of the probe while the other one at the other end of ablation elements, giving precise localization of each ablation elements. The

probe could have up to 4 ablation elements, each with different characteristics such as angle of ablation zone and length. Fig. 5.15 shows some of the probes that has been explored. Embedded tracking coils are placed such that the ablation probe position and orientation along with precise positions of the ablation elements also could be derived. Fig. 5.16 shows detailed picture of one of the probes with ablation elements and tracking coil locations.

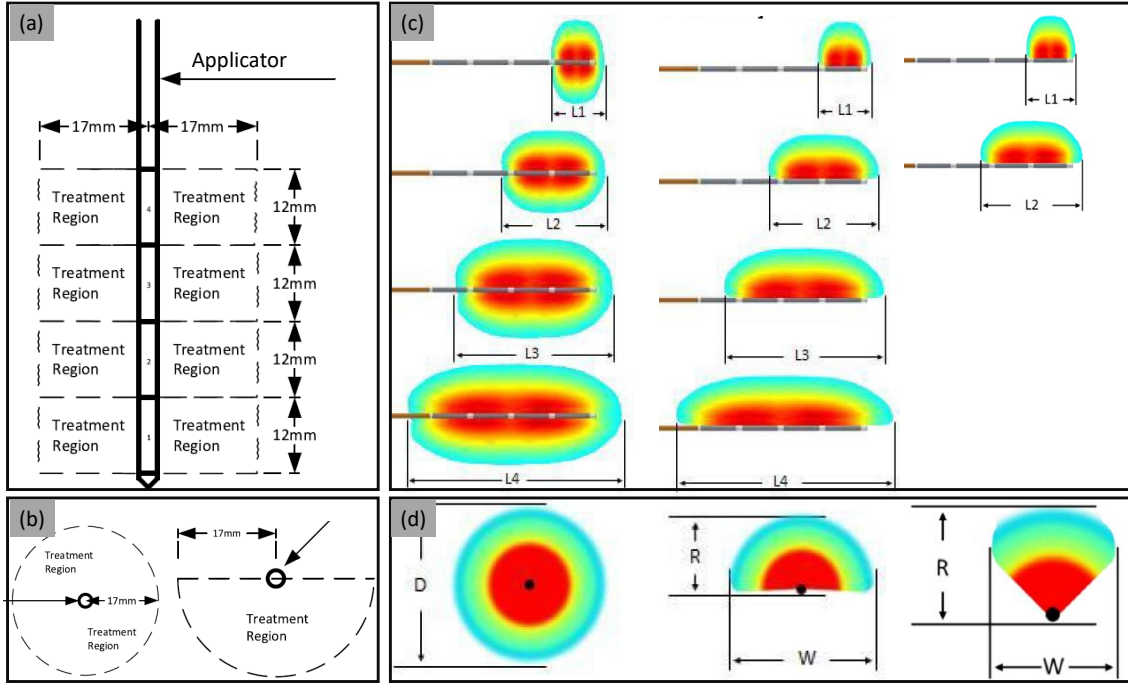


Figure 5.15: Ablation patterns for ACOUSTx<sup>TM</sup> ultrasound applicators: (a) Front and side views: longitudinal ablation pattern, (b) top view: radial ablation patterns for 360° and 180° applicators, (c) side view of longitudinal ablation patterns for 360°, 180° and 90° probes and (d) top view radial ablation patterns for 360°, 180° and 90° probes (©Acoustic MedSystems Inc.)

### 5.8.2 Probe Localization Algorithm

Localization of the ablation probe is an important part of the surgical workflow, not only to ensure that the probe is at the right position and orientation but also to setup the scan plane geometry for MR thermometry, which has to be a perpendicular

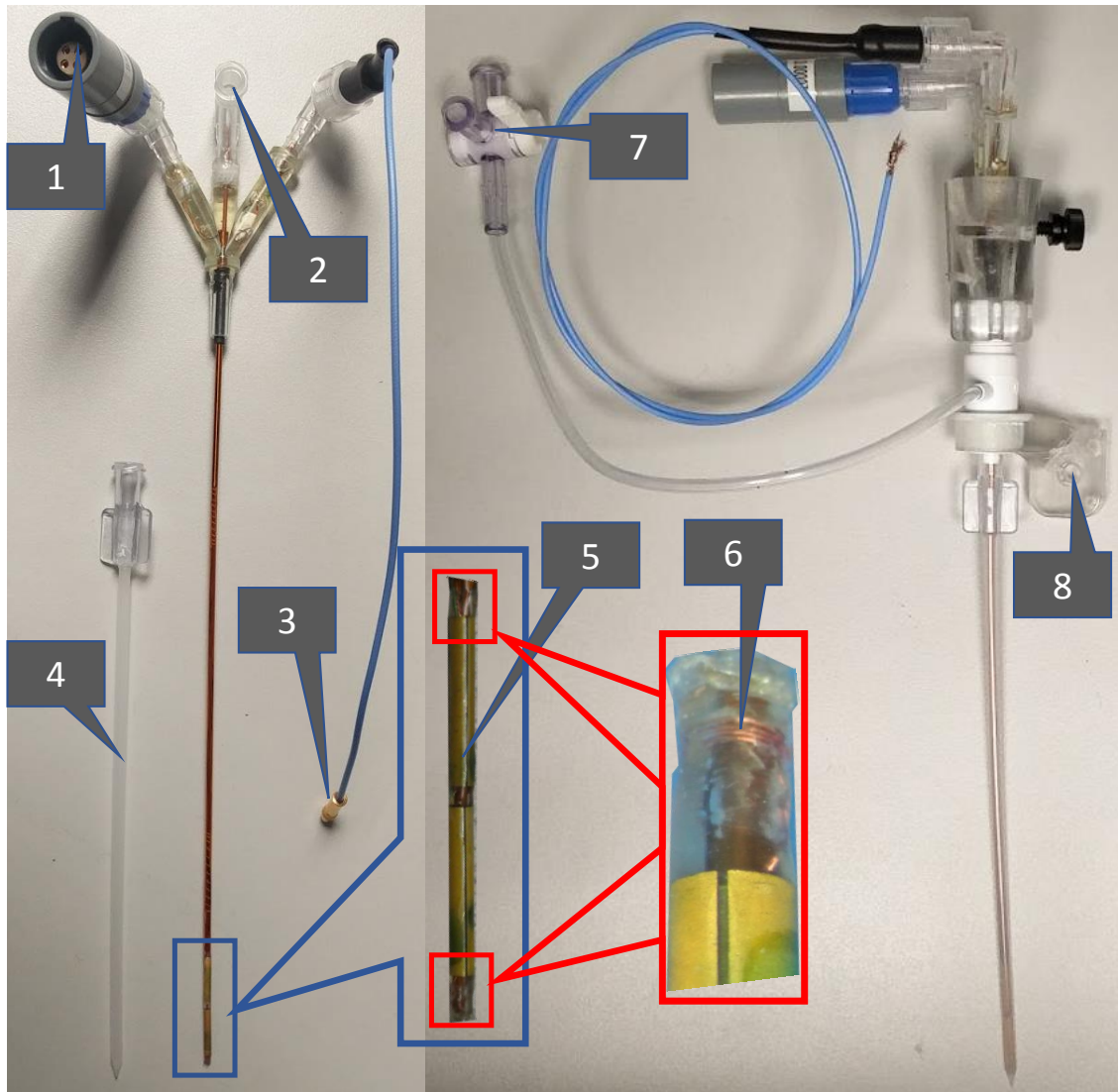


Figure 5.16: Ablation probe construction showing: (1) connector for the ablation elements, (2) water flow inlet, (3) connector for tracking coil interface, (4) outer sleeve for water flow, (5) two high intensity ultrasound ablation elements, (6) micro tracking coils embedded at the tip and along the probe axis, (7) outlet for water flow, and (8) fixture for attaching the probe to robot

plane intersecting with the ablation element. Micro tracking coils can be localized by a scan sequence with 1D projections giving X, Y and Z coordinates of the coils. Embedding more than 1 coil would allow to calculate not only position but also orientation of the device such as ablation probe or catheter. Though, 1D projections could be fast, the localization accuracy is compromised by 1 dimensional signal intensities. We devised a 2D projection sequence and image processing algorithm which utilizes image intensities around the coil to precisely localize it. The scan sequence is created such that in each of the X, Y and Z directions, there are two echoes recorded with opposite reading directions. The simple most algorithm is to find peaks and take average of their positions in both echoes, but to improve the accuracy, an algorithm which utilizes image intensities around the tracking coil to better estimate the center of the coils is developed. Fig. 5.17 shows one of the image and subsequent image processing steps performed to localize the coils. While Fig. 5.18 shows how information from all 6 slices is combined to give precise position of each of the coils, which is used to calculate probe orientation.

## 5.9 MRI Based Thermal Dose Monitoring

Minimally invasive tumor ablation using method such as laser interstitial thermal therapy and high-intensity ultrasound therapy have received increasing interest in recent years. But, in order to use such technologies, it is essential to be able to safely and efficiently measure the tissue temperature throughout the ablation procedure. MR imaging could be used for noninvasive temperature monitoring by monitoring change in temperature sensitive MR parameters such as the Proton Resonance Frequency (PRF). Due to the linear relationship between temperature change and PRF shift as well as less dependence on tissue type itself, PRF based thermometry is one

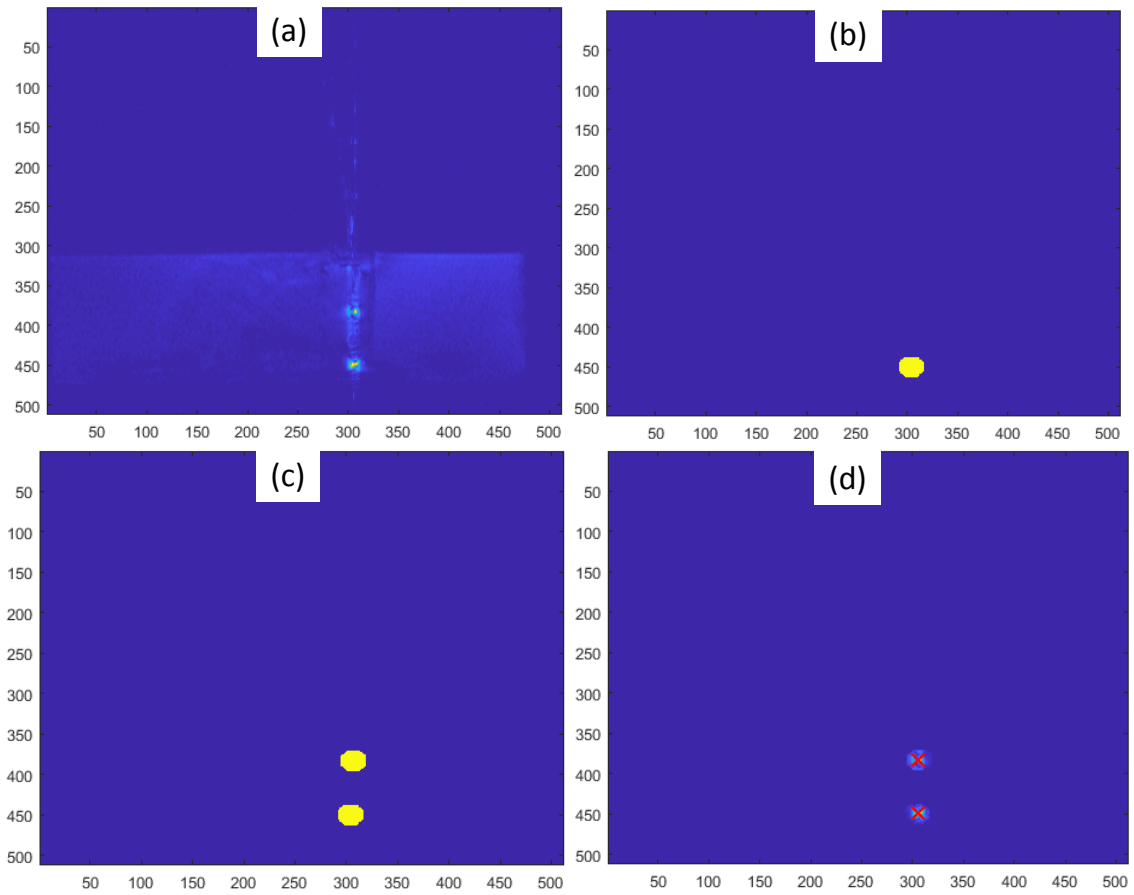


Figure 5.17: Image processing steps for tracking coil localization (a) original image, (b) mask for first tracking coil, (c) mask containing both the tracking coils and (d) calculated coil locations overlaid with red cross marks

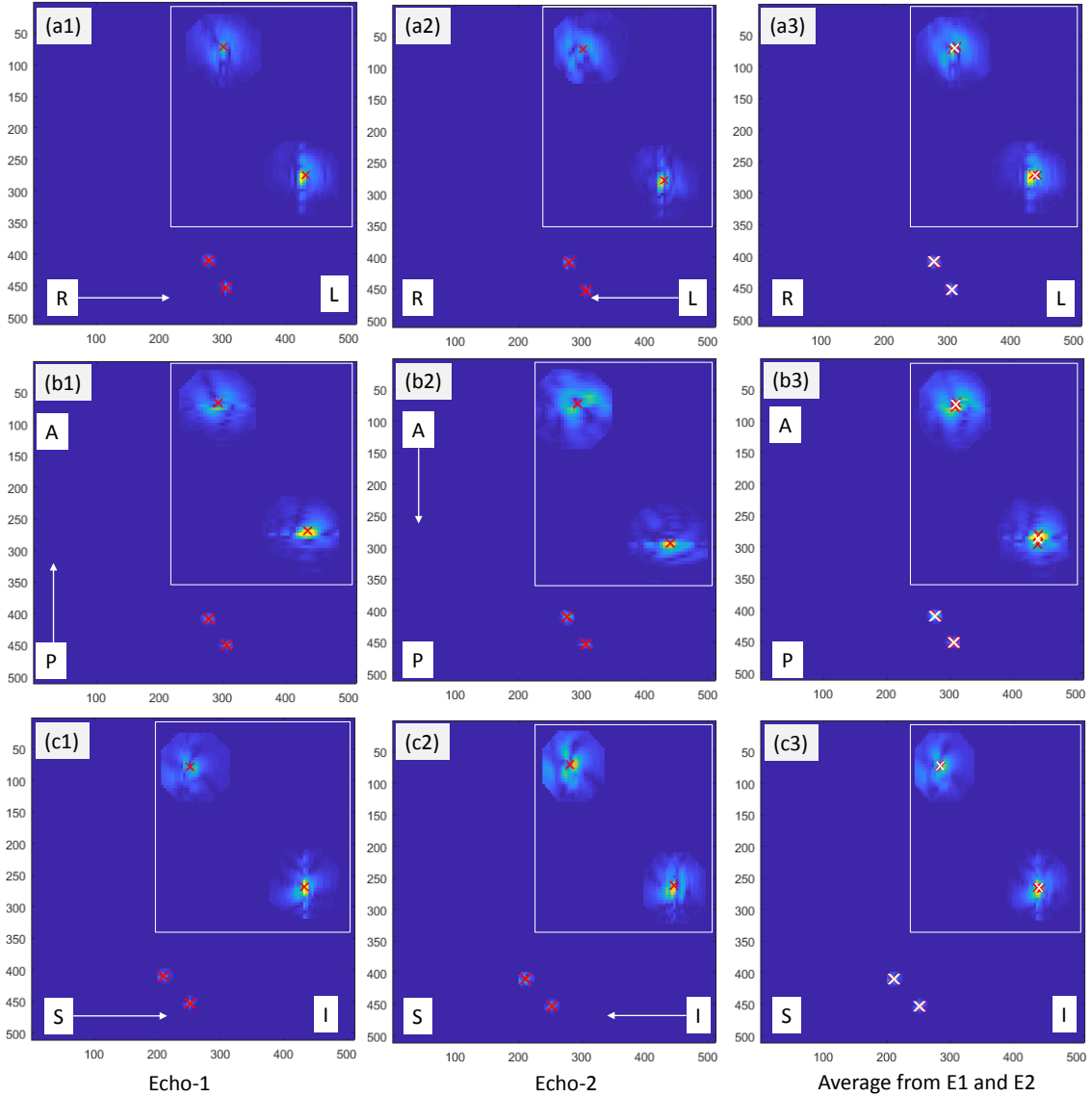


Figure 5.18: Ablation probe localization using 6 projections: 2 projections in transverse plane with reading directions RL (a1) and LR (a2), 2 projections in transverse plane with reading directions PA (b1) and AP (b2) and 2 projections in sagittal plane with reading directions SI (c1) and IS (c2), (a3) shows calculated center position of the coils from (a1) and (a2), (b3) shows calculated center position of the coils from (b1) and (b2) and (c3) shows calculated center position of the coils from (c1) and (c2), The red cross marks are coil locations in individual slices while the white cross marks are average positions calculated from the 2 echoes: LR: Left-Right, AP: Anterior-Posterior and SI: Superior-Inferior

of the most preferred choice for many in vivo procedures.

The relationship between temperature and the PRF was first reported by Hindman [108]. Ishihara et al. [109] developed a precise and fast temperature mapping in MR imaging using the PRF shift phenomena and De Porter et al. [110] validated it with in vivo tissue experiments.

MR phase images can be used to deduce change in PRF [111], which can be used to calculate the temperature change. Temperature change between two consecutive phase images could be calculated by multiplying the phase difference by a scaling factor, as shown in Eq. 5.1.

$$\Delta T = \frac{\Delta\phi}{\gamma\alpha B_0 T_E} \text{ where,} \quad (5.1)$$

$\Delta\phi$  = the phase difference between two consecutive images,

$\Delta T$  = scaled temperature difference,

$\alpha$  = temperature dependent water resonance chemical shift  $- 0.0094\text{ppm}/^\circ\text{C}$ ,

$\gamma$  = gyromagnetic ratio  $- 42.58 \text{ MHz/T}$ ,

$B_0$  = magnetic field strength and

$T_E$  = echo time

In order to calculate cumulative temperature change, temperature difference between two consecutive images could be accumulated over the period of ablation procedure. Absolute temperature is not the only important factor for ablation of biological tissue, but the accumulated temperature over time determines cell survival. Sapereto and Dewey developed the concept of Thermal Dose (TD) and demonstrated that a temperature of  $43^\circ\text{C}$  caused a clearly observable tissue necrosis after

240 minutes [112]. Therefore, the TD at which the tissue necrosis is defined as 240 equivalent minutes. Using this method any time-temperature data could be converted to an equivalent minutes of heating at 43 °C. In Eq. 5.2, the resulting CEM43 °C value represents the effect of the time-temperature history on cell necrosis.

$$CEM43^{\circ}C = \sum_{i=1}^n t_i \cdot R^{43-T_i} \text{ where,} \quad (5.2)$$

*CEM°C is the cumulative number of equivalent minutes at 43°C,*

*t<sub>i</sub> is the i – th time interval,*

*T<sub>i</sub> is the average temperature during time interval t<sub>i</sub> and*

*(R(T < 43°C) = 0.25, R(T > 43°C) = 0.5)*

### 5.9.1 MatMR-TD Monitor Application

Monitoring of temperature changes based on PRF could provide valuable feedback to the physician about ongoing ablation procedure. A MATLAB<sup>TM</sup> (Mathworks Inc) application (MatMR-TD Monitor) is developed to perform real-time temperature monitoring and thermal dose calculation. MATLAB interface for Philips scanner, MatMRI [113] is used to communicate with the scanner and retrieve real-time MR images. Fig.5.19 shows the MatMR-TD Monitor application interface with various GUI elements: (1) Scanner communication interface, (2) OpenIGTLink interface for transmitting MR thermal dosage images to surgical navigation applications (Ther-aVision and 3DSlicer), (3) probe tracking interface to calculate and display probe pose information, (4) command to update the scan geometry from the probe pose, (5) command to start/stop acquiring the temperature mapping data, commands



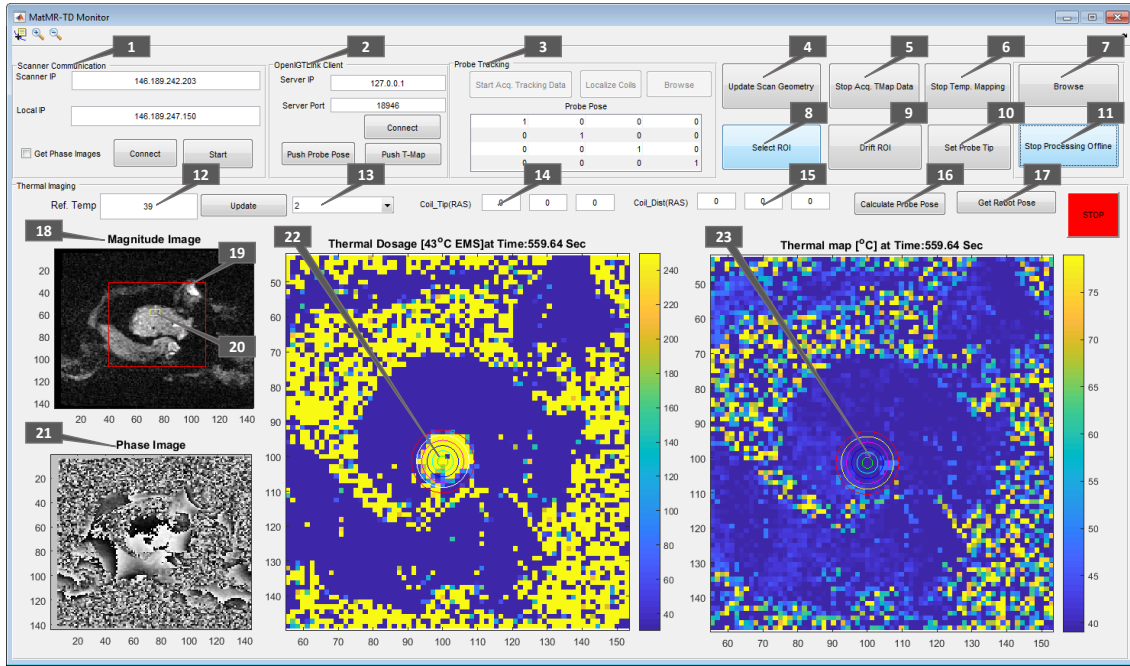


Figure 5.19: MatMR-TD Monitor Application showing various modules for scanner control, probe tracking, offline image processing and MR thermometry along with thermal dosage visualization

to (6) start/stop temperature mapping, (7) load offline time temperature data, (8) specify Region of Interest for temperature monitoring, (9) specify a phase reference region to compensate for phase drift, (10) to specify the probe tip location for the ablation region overlay, (11) start/stop processing the data offline, (12) specify tissue reference temperature, (13) select desired image view, (14) specify location of the tracking coil at the probe tip, (15) specify the location of the tracking coil along the probe axis, (16) calculate probe pose from the specified tracking coil locations, (17) request current robot pose from the robot control application, (18) image overlay of real-time magnitude image with (19) region of interest rectangle(red), (20) phase drift rectangle(yellow), (21) real-time phase image, (22) calculated thermal dosage, and (23) real-time temperature change.

## 5.10 Experiments and Results

Experiments are performed in gelatin phantom to evaluate the robot mechanism accuracy in MRI. For accuracy assessment in MRI, along with gelatin phantom experiments, preliminary animal study is also presented. Also, active tracking coil based probe localization experiments are performed to evaluate the accuracy of image based localization algorithm. At the end, results from ablation experiments in animal studies are presented. Different imaging protocol used for these experiments are listed in Table. 5.1.

Table 5.1: NeuroAblation Robot Imaging Protocols for MRI Phantom Studies and an Animal Study

Imaging Protocol	Sequence	Flip Angle (deg)	TR (ms)	TE (ms)	Slice Thickness (mm)	Slice Spacing (mm)	Pixel Spacing (mm x mm)
Localizer	T2W-TSE/MS	90	3000	90	3	3	0.47 x 0.47
Plan/Confirmation	T1-FFE/3D	15	10	2	2	1	0.44 x 0.44
Tracking Coil	T1-FFE/Multi Echo	10	30	8	200	0	0.39 x 0.39
MR Thermometry	FE-EPI	20	39	15	7	0	1.39 x 1.39
Post Ablation	DWI-SE	90	3700	76	4	0	0.90 x 0.90

### 5.10.1 Accuracy Assessment in MRI

Phantom studies were performed under live MRI guidance to evaluate the targeting accuracy of the system inside a 3T Philips Achieva scanner (Philips, The Netherlands), The phantom used in this study is a mixture of 2.5 ounce gelatin and 12 ounce water. An ablation probe is robotically aligned and then inserted into the phantom and imaged with diagnostic 3D-FFE imaging protocol: Confirmation (Table. 5.1) . The experiment was conducted with 5 target defined from the acquired planning image set, at each of the 5 target location probe was inserted in 5 differ-

ent orientations. In the beginning of the experiment, robot was registered to the scanner coordinate system by acquiring calibration frame images and performing Z-Frame registration. With 5 target location and 5 orientation at each locations, 25 targets in total were collected to assess the system accuracy. The experimental setup was designed as a mock up of typical clinical procedures, which commonly include 1-5 target with 1-5 possible orientations and require only one registration for each patient.

Table 5.2: Experimental Results of NeuroAblation Robot MRI Phantom Study

<b>Target \ RMS Error</b>	<b>R (mm)</b>	<b>A (mm)</b>	<b>S (mm)</b>	<b>Yaw (degrees)</b>	<b>Pitch (degrees)</b>
Target 1	0.23	0.60	0.63	1.35	1.41
Target 2	1.40	0.36	0.80	1.97	1.35
Target 3	2.09	0.41	0.28	1.27	1.12
Target 4	1.83	1.03	0.72	1.48	0.81
Target 5	1.36	0.44	0.72	0.27	0.30
Total	1.38	0.57	0.63	1.27	1.00

The desired target positions defined in 3DSlicer were compared with actual probe tip positions (manually segmented from MRI volume images) to assess targeting accuracy. The experiments results are summarized for each of the five targets in Table 5.2, with maximum tip RMS error of  $1.38mm$  in R direction and maximum orientation RMS errors of 1.27 degrees in Yaw axis.

### 5.10.2 Active Tracking Based Probe Localization

Experiments are performed with a 3D printed template, allowing ablation probe to be inserted at various angles. The template is designed such that all the insertions intersect at a common point, mimicking the typical RCM mechanism similar to the

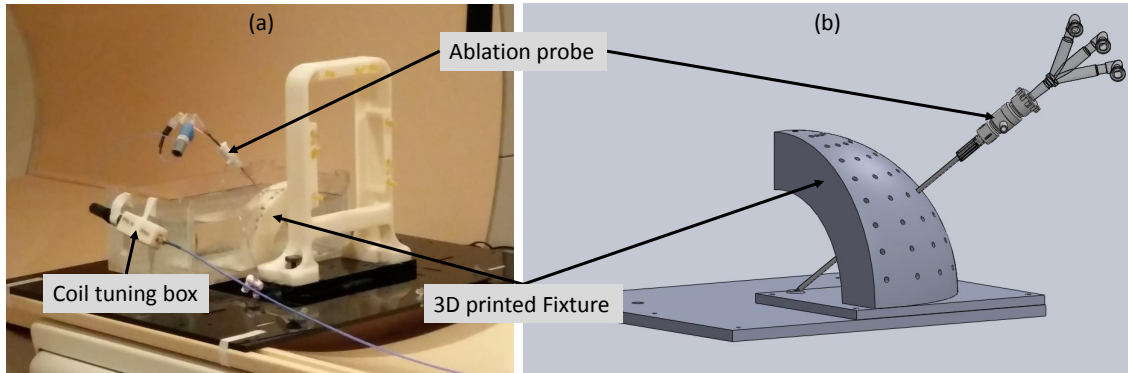


Figure 5.20: Probe localization experiment setup showing 3D printed fixture, probe inserted through one of the guiding holes and the coil tuning box



Figure 5.21: Probe localization results showing errors in R, A and S coordinates and two of the insertion angles.

robot presented in this chapter. As shown in Fig. 5.20, ablation probe is inserted in to the guiding hole and a coil tuning box is connected to the probe to acquire signal from the micro tracking coils. To evaluate the accuracy of the probe localization algorithm, all insertions are performed in air avoiding any possible deflection due to probe bending. Tracking coil sequence described in Table. 5.1 is used to acquire 2 echoes in 3 projection images, giving locations of the tracking coils in R, A and S coordinates. Image processing algorithm described in section 5.8.2 is used to localize the tracking coils and calculate probe position and orientation. Fig. 5.21 shows plot of tip errors in R, A and S coordinates with RMS error of less than 1.1 mm and orientation errors with RMS error of less than  $2.3^\circ$ .

### 5.10.3 Results from a Preliminary Animal Study

Table 5.3: Accuracy Assessment for One of The Animal Studies

	Target			Entry		
	R	A	S	R	A	S
Planned	6.32	83.96	212.00	4.23	94.17	244.70
Achieved	8.92	85.39	211.90	1.47	94.29	244.22
Error	2.60	1.43	-0.10	-2.75	0.12	-0.48
RMS Error	1.71			1.61		

Animal studies are performed to evaluate integrated system accuracy. Accuracy is evaluated in terms of probe placement accuracy and ablation regions size. In this section the probe placement accuracy and comparison of planned versus achieved

ablation zone is presented. Before the animal is brought in the MR room, the robot base platform with embedded registration frame is firmly attached to the scanner bed, and a calibration frame localization is performed to register the robot coordinate system to scanner coordinate system. Once the animal is prepared with planned burr hole, it is laid on the scanner bed in head first prone orientation and appropriate life support systems are setup. Robot is attached to the robot base and robot workspace is visually confirmed, then a planning image (3D FFE, 1x1x1mm voxel resolution) set is acquired, which is used to prepare the surgical plan and define the target location, overlaid robot workspace helps determine that the desired target is within the reachable region. Defined target and entry point are used to calculate desired robot pose and sent over to the robot controller, robot aligns when the foot switch is engaged by the physician. Once robot is at the desired orientation and position, a sterile cannula is inserted to guide the sterile probe attached to the robot, which is then inserted robotically to desired insertion depth. Confirmation scan is acquired to validate that the probe was inserted to desired target location, scan plane for MR thermometry is set to a plane perpendicular to the probe axis. Ablation element is powered ON and real-time temperature change is observed using MR thermometry, when a desired ablation region is created in displayed MR thermal dosage image, the ablation element is powered OFF. At the end, ablation probe is pulled out and incision is stitched. Accuracy of probe placement for one of the animal studies is 1.71 mm at the tip and 1.61 mm at the entry point, planned and achieved target and entry points are shown in Table 5.3. Fig. 5.22 shows planned versus achieved probe pose, while Fig. 5.23 shows comparison of MR thermal dosage map and histology of the brain, it could be seen that the size of the ablation zone calculated by MR thermometry confirms with the histology data.

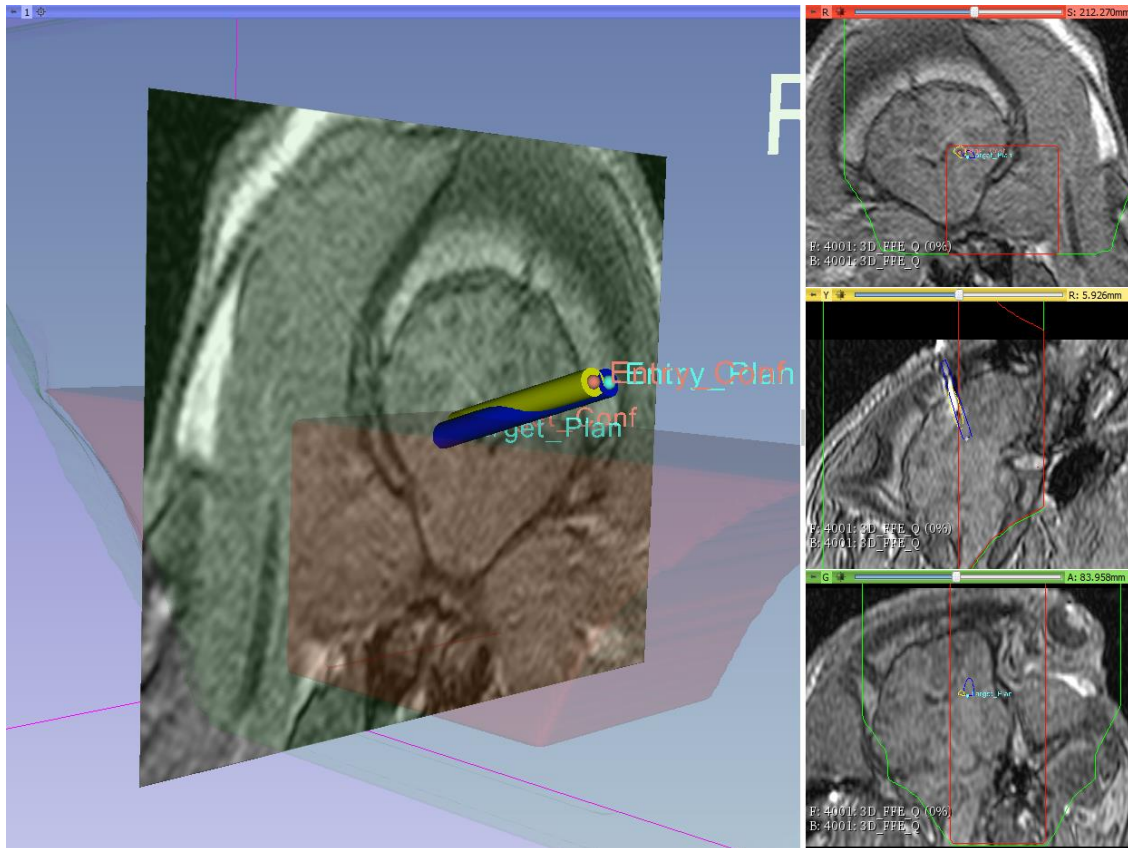


Figure 5.22: Slicer scene showing planned trajectory in blue and achieved trajectory in yellow, along with overlay of robot workspace and its intersection with each of the slice views

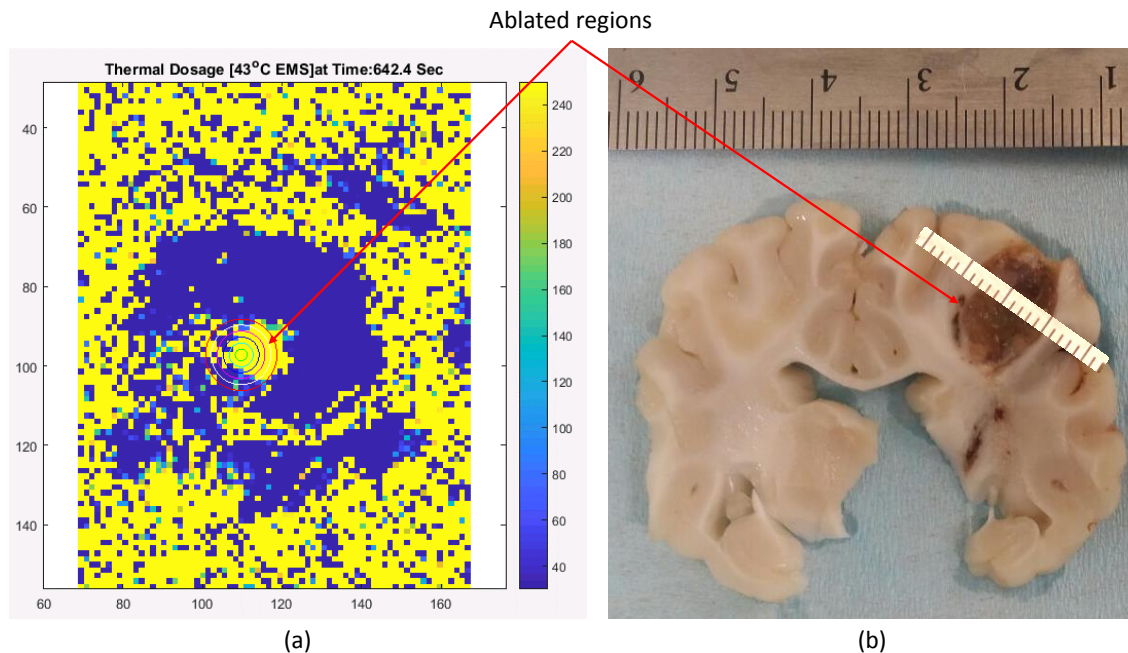


Figure 5.23: Comparison of (a) MR thermometry based thermal dosage and (b) histology data, confirming the size of the ablation region being in range of 9-10 mm diameter in both the data sets

## 5.11 Discussion and Conclusion

This chapter presented development of a fully integrated robotic system for MRI-guided conformal brain tumor ablation, which has been approved by IACUC for animal studies. The clinically optimized system presented in this chapter is designed with considerations that it could be used for any stereotactic neurosurgery procedure such as DBS or tumor ablation. Throughout the design and validation procedure, sterility, safety and interference with the MR imaging device are considered. The surgical planning and navigation along with the ablation system are integrated to produce conformal ablation zone at a desired target location and orientation.

Multiple generation of the robotic manipulators have been developed by our group [64, 102], the current generation is developed to be precise and more rigid with all machined parts. With current manipulator, compatibility with the MRI



environment was evaluated in a 3T MRI scanner with varying robot configurations, showing SNR reduction of less than 16% when controller is powered on. Also, phantom studies were performed to evaluate the system targeting accuracy and MR based thermometry. Accuracy of  $1.6 \pm 0.7$  reported in MR phantom studies using the presented robotic system are better than the manual stereotactic frame based DBS electrode placement procedure which has reported accuracy of  $2.8 \pm 1.3$  for Nexframe and  $2.5 \pm 1.2$  for the Leksell frame [114]. The errors reported with the robotic system here, could potentially come from robot mechanism issues such as backlash, robot registration error and other unmodeled errors during the probe artifact segmentation.

A preliminary animal study was described to demonstrate the viability of clinical use of this robotic system. The animal study was performed following the IACUC approved clinical workflow. A preliminary animal studies are performed to evaluate the system accuracy and viability of using such a system for tumor ablation. For each of the animal study, various acoustic power settings were evaluated to understand effect of it on shape and size of the ablation zone in live brain tissue. During each of the animal studies, real-time MR thermometry was used to calculate and visualize thermal dosage delivered to the brain tissue around the ablation probe. At most two sites were targeted and ablation was performed with various acoustic power settings. Results are presented comparing calculate thermal dosage using real-time MR images and histology data. Further survivable animal trials are under progress and would eventually lead towards a clinically viable system for use in humans.

The presented work in this chapter, development of an integrated system for MRI guided conformal brain tumor ablation addresses some of the current challenges posed by existing manual and semi-actuated stereotactic neurosurgery frames. Compare to existing stereotactic neurosurgery frames, a fully actuated robotic de-

vice could improve procedure accuracy and surgical workflow while reduce procedure time leading to improved quality of treatment. However, presented system is not yet ready for human trials and would require more validation of system accuracy in animal studies and eventually human cadaver studies. Also, this system could be extended for other stereotactic neurosurgery by replacing the ablation device with an appropriate therapy delivery tool.

# Chapter 6

## Conclusions

This dissertation presented an intraoperative MRI guided system for prostate biopsy and a framework for performing closed-loop, robot assisted percutaneous interventions under real-time MRI guidance. The presented framework is modular and easily adoptable to various surgical procedures. Each of the system module could be swapped by another module providing similar functionalities desired for a particular surgical procedure. Two of the applications adopting the presented system architecture are presented and system accuracy and validation results are described.

### 6.1 Dissertation Contributions

#### 6.1.1 Intraoperative MRI guided Prostate Biopsy

An integrated system for intraoperative MRI guided prostate biopsy was presented. Our collaborators at Johns Hopkins University developed the robotic manipulator, while me and my lab colleagues developed and improved some of the existing robot control components to provide better accuracy, safety and reliability. Various communication interfaces between robot controller and, surgical planning applications

were developed. Accuracy of the robotic manipulator was evaluated in bench-top as well as gelatin phantom studies in MRI. After obtaining IRB approval, the integrated system was translated to an operating room for human trials. Sterilization and surgical workflow were optimized for the prostate biopsy procedure and had been used for 30 patient trials at Brigham and Womens' Hospital.

### **6.1.2 Closed-loop Needle Steering under MRI Guidance**

Real-time MRI guided needle steering system comprising of 2-DOF (needle insertion and rotation) robotic manipulator, MRI compatible robot controller, scanner control module , real-time needle tracking application and steering algorithm was presented in Chapter 4. System components were developed to track the needle in real-time, control the MRI scanner to image at desired scan location. Also, various communication interfaces were developed to perform closed-loop steering: an OpenIGTLink interface between robot control application and steering algorithm to send steering parameters and, an interface between real-time needle tracking application and scanner control application to send updated scan geometry based on tracked needle tip. The presented system was validated with 3 different steering methodologies: autonomous steering using bevel angle control, autonomous and teleoperated insertion with CURV steering model.

### **6.1.3 Closed-loop Brain Tumor Ablation under Real-time MRI Guidance**

An MRI compatible robot, integrated with an ablation system utilizing image guidance for conformal brain tumor ablation was presented in Chapter 5. Two version of the robotic manipulator was designed and validated in both bench-top and MRI

phantom studies. Precise localization of the ablation device was achieved by integrating micro tracking coils along the probe axis. An image processing algorithm was developed to precisely localized the embedded tracking coils. A MATLAB application was developed to perform real-time MR thermometry and calculate delivered thermal dosage using the high intensity ultrasound ablation device. A surgical planning and navigation workflow was devised using 3DSlicer and TheraVision, which displayed overlay of robot workspace and targets on MR images. The integrated system has been used in preliminary acute animal studies, further survivable trials are in progress.

## **6.2 Impact of Presented Work**

closed-loop control of a robotic device using imaging feedback is a needed step for advancing MRI guided, robot assisted percutaneous interventions towards shared or full autonomy. The frame work presented in this dissertation, considered various desired system components needed for performing closed-loop percutaneous interventions under real-time MRI guidance. The presented architecture is modular and flexible so that it could be adapted for a wide range of surgical procedures. System components such as MRI compatible robot, embedded robot controller, robot control application, surgical planning and navigation applications, surgical device localization using active and passive tracking methods, unified imaging interface for MRI scanner control and therapy monitoring, could be adopted to requirements of a surgical procedure of interest.

Two of the systems presented in this dissertation: intraoperative MRI guided, robot assisted prostate biopsy and real-time MRI guided conformal brain tumor ablation has been successfully translated to operating room for human and animal

studies respectively. It is not very often that a robotic systems under MRI guidance reach to human and animal studies stage, as it requires accurate and reliable robotic manipulator, safe robot control system, optimized surgical workflow and well established sterilization process.

## 6.3 Future Work

The intraoperative MRI guided prostate biopsy system presented in this dissertation has manual needle insertion procedure, which is still less accurate and does not utilize real-time MR images as feedback for needle trajectory correction. One of the goals for future systems is to fully actuated needle insertion and rotation mechanism, coupled with real-time MRI guidance. Also, haptic force feedback is being considered for cooperative and teleoperated needle insertions. Eventually a robotic system with shared or full autonomy, coupled with real-time needle tracking and scanner control is the ultimate goal.

Regarding the needle steering work presented in this dissertation, the future work will focus on ex-vivo tissue experiments, online needle model estimation and motion planning. Eventually, the needle steering system will be integrated with the clinical grade prostate biopsy system presented in chapter 2, to deliver an integrated system for fully autonomous prostate biopsy under real-time MRI guidance.

The conformal brain tumor ablation system under real-time MRI guidance system has reached to animal studies stage, but it is yet not ready for human trials. Next step would to evaluate the probe placement accuracy in human cadavers and characterization of ablation size and shape in animal trials. Also, streamlined surgical workflow, optimized sterilization procedure and improved surgical planning and navigation for the entire surgical procedure would be important before proceeding

for human trials.

# Appendix A

## Prostate Robot Work-flow and User Manual



# BRP Robot System Setup and Workflow Execution Instructions

Nirav Patel, Weijian Shang and Gregory Fischer  
WPI

## Contents

0. GENERAL WORKFLOW_ROBOT SETUP	125
0.1. Patient Board Setup	125
0.2. Robot Controller Setup	126
0.3. Robot Initialization	126
0.4. Patient Move-In	127
0.5. Patient Board Setup with Patient	127
0.6. Robot Draping	128
0.7. Robot in Position	128
1. SET UP_PHYSICAL HARDWARE	130
1.1. Assumptions and Hardware List	130
1.1.1. Assumptions	130
1.1.2. Hardware List	130
1.2. Robot Interface Box	130
1.3. Robot Controller Box	131
2. SET UP_NETWORK	132
2.1. Computer Connections	132
2.2. Finding the Robot Controller's IP Address	132
2.3. Port Forwarding for DICOM Push	132

2.4. RadVision Assist Device IP Change	133
3. START UP_ROBOT CONTROL APPLICATION	138
3.1. Downloading Robot Control Application	138
3.2. Running Robot Control Application	138
3.3. 45-second Countdown Timer	139
3.4. Establish Connection	139
3.5. Hardware Test	140
3.6. Homing Procedure	142
3.7. Robot Ready	144
4. START UP_RADVISION	145
5. SETTING UP DICOM PUSH_RADVISION	148
5.1. Setting Up IP Address	148
5.2. Starting DICOM Push Receiving	148
5.3. Saving the Received Image Set	150
5.4. Loading the Received Image Set	150
6. Z-FRAME CALIBRATION_PART 1	151
7. Z-FRAME CALIBRATION_PART 2	156
8. TARGETING	159
8.1. Loading the Image Set	159
8.2. Three Approaches to Send Target to the Robot Controller	160
8.2.1. Manually Typed Target	160
8.2.2. Picking Targets by Markers	166
8.2.3. Import Targets from File	170
9. HARDWARE ERRORS AND RESOLUTIONS	172
9.1. Color of LEDs for motor drivers and their meaning	172
9.2. Limit Error	172
9.3. Stall Error	174
10. ADVANCED CONTROL PANEL	178
11. LIST OF FIGURES	180

## 0. GENERAL WORKFLOW\_ROBOT SETUP

Section 0 is a general workflow should be followed during the procedure especially for setting up the robot. For each step in section 0, the technical details could be found in following sections.

- Refer to section 1 for setting up physical hardware connections.
- Refer to section 2 for setting up networks.
- Refer to section 3 and 4 for starting the robot control application and RadVision software.
- Refer to section 5 for setting up DICOM push.
- Refer to section 6 and 7 for Z-Frame registration.
- Refer to section 8 for targeting.
- Refer to section 9 for hardware errors and their resolutions.
- Refer to section 10 for an instruction of the advanced control panel.

### 0.1. Patient Board Setup

- Red bag → patient board → bedding/foam → tape



Figure 0.1 Put red bag before patient board



Figure 0.2 Put patient board over red bag



Figure 0.3 Put bedding on patient board



Figure 0.4 Tape the patient board

## 0.2. Robot Controller Setup

- Refer to section 1.3 to connect all the electric cables to the controller.
- Connect cooling air hose to the cooler.
- Connect the other end of the air hose to the medical air supply.
- Set the air flow rate to 15 (turning it higher and lowering it to around 15).



Figure 0.5 General Controller setup. Please refer to Figure 0.6 and Figure 1.2 for more details.



Figure 0.6 Medical air connection

## 0.3. Robot Initialization

- Connect robot to the controller, then power up the controller.
- Refer to section 3 until the robot is successfully homed and ready to run.
- Refer to section 4 for establishing connection between RadVision and robot application.
- No draping and sterilized parts is attached to the robot during this procedure.
- In the meantime, refer to section 0.4 and 0.5 to get the patient ready in the scanner room.



Figure 0.7 Get the robot connected to the controller



Figure 0.8 Initialize the robot without draping and sterilized parts



#### 0.4. Patient Move-In

- Move in the patient while engineers are preparing/homing the robot.
- Get the patient ready in bed comfortably.



Figure 0.9 Move in patient while homing the robot



Figure 0.10 Patient ready in bed

#### 0.5. Patient Board Setup with Patient

- Attach knee and elbow bumpers.
- Attach imaging coils.
- After the patient is ready in bed, push the bed all the way through the scanner to the other side.
- Attach Z-Frame.



Figure 0.11 Push the patient through the scanner to the other side

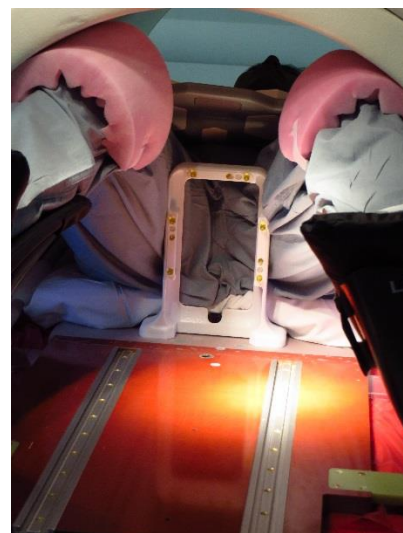


Figure 0.12 Z-Frame in position

## 0.6. Robot Draping

- Move the robot in the room and tape the wire down carefully on the ground.
- Drape the robot and push the front piece/ needle guide in. Leave enough drape on both side so that the robot could reach extreme positions without pulling the drape.
- Tape both side of the drape to keep it well organized.
- Lock the front piece in the end.



Figure 0.13 Move the robot in the room and tape the wire down.



Figure 0.14 Drape the robot and push the front piece in



Figure 0.15 Tape both side of the drape to keep it organized



Figure 0.16 Lock the front piece

## 0.7. Robot in Position

- Move the cart with the robot close to the scanner.
- Push the robot in position until it hit the stop which is the Z-Frame.
- Lock the robot in place with two screws near the back handles.



- Finally, the robot is ready.



Figure 0.17 Move the cart close to the scanner



Figure 0.18 Push the robot in position until it hit the Z-Frame



Figure 0.19 Lock the robot in place with two screws

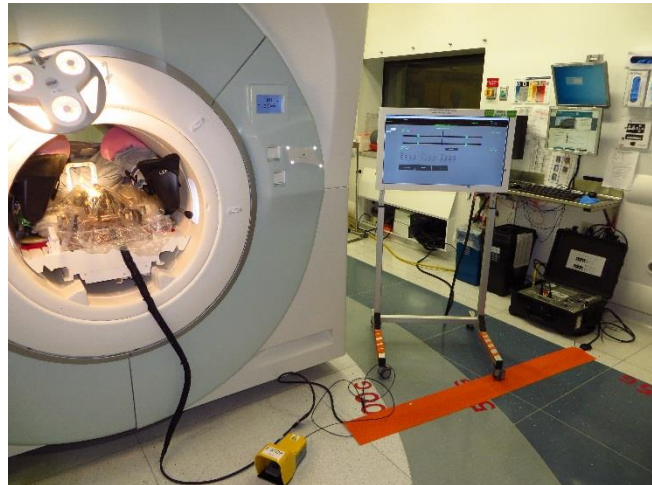


Figure 0.20 Robot Ready

- Until this point, section 1~4 should be all set.
- Refer to section 5 for setting up DICOM push.
- Refer to section 6 and 7 for Z-Frame registration.
- Refer to section 8 for targeting.

## 1. SET UP\_PHYSICAL HARDWARE

### 1.1. Assumptions and Hardware List

#### 1.1.1. Assumptions

- RadVision is already installed and set up.
- Java Version 6 or higher is installed and system path is set up accordingly so that JAVA.EXE is visible and accessible from terminal/command window.

#### 1.1.2. Hardware List

- Robot interface box;
- Robot controller box;
- Windows Laptop running robot control software and RadVision;
- Several Ethernet cables and one fiber optic cable.

### 1.2. Robot Interface Box

- Connect one Ethernet cable to computer running robot control software and RadVision using LAN port.
- Connect the other Ethernet cable to MRI Console using WAN port.
- Connect one end of the fiber optic cable to its connector shown in Figure 1.1.
- The interface box doesn't need to be open during normal running.



*Figure 1.1 Robot interface box*

*1) Power cord and switch; 2) Fiber optic cable to robot controller box; 3) Two LAN ports*



4) WAN port

5) Media converter

6) Router

### 1.3. Robot Controller Box

- Connect the other end of the fiber optic cable to its connector on the surface of the robot controller box. Connect foot pedal connector and main power cord.
- Before turn the power on, make sure E-stop is ON (pressed).
- To power the controller up, turn on the main power switch first, following by logic power switch. Boot Status LEDs should be blinking now.
- When booting is done, all Boot Status LEDs and Motion Status LEDs should be **BLUE**.

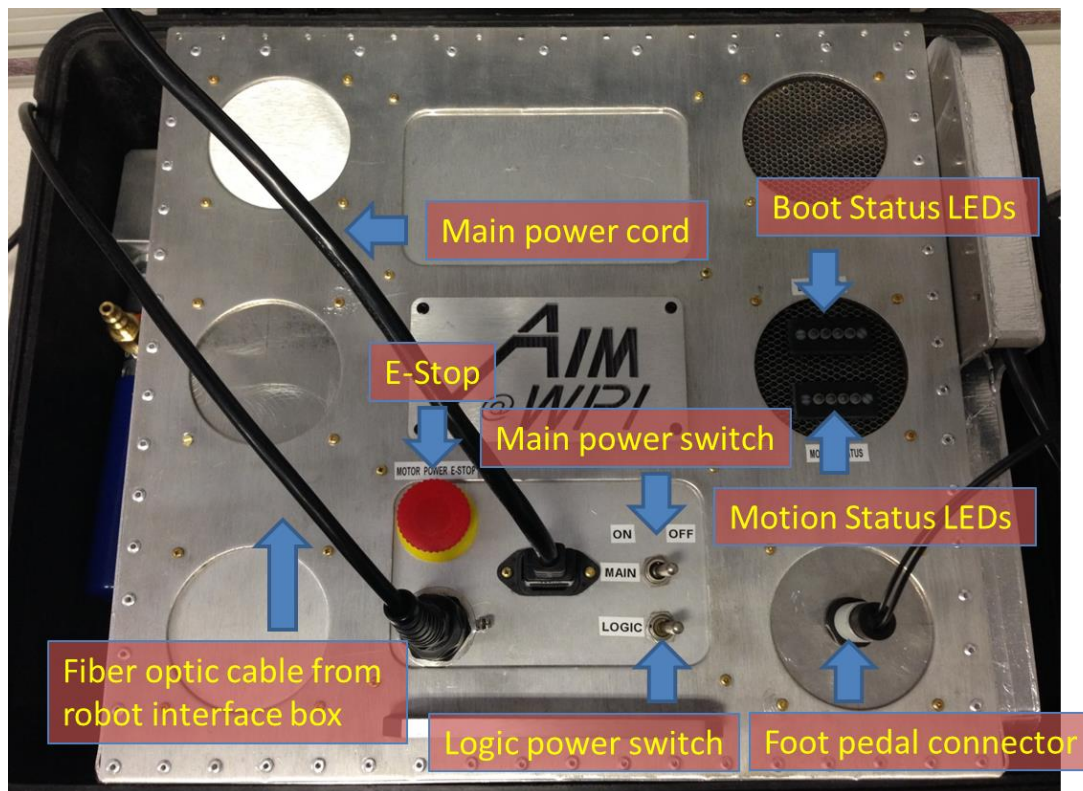


Figure 1.2 Robot controller box

## 2. SET UP\_NETWORK

### 2.1. Computer Connections

- As shown in Figure 1.1 Robot interface box, there is one LAN cable connected to the interface box. Connect it to the Windows PC running robot controller application and RadVision.
- If you are using two laptops to run robot controller application and RadVision separately, user need to follow RadVision instruction manual to change the IP address of Assist device to point to Windows PC in order to make those two computers connected over network.

### 2.2. Finding the Robot Controller's IP Address

Usually, this step is not required since the router is set up with static IP for both Windows PC and robot controller.

- Windows PC: 192.168.0.103
- Robot Controller: 192.168.0.2

### 2.3. Port Forwarding for DICOM Push

Open web browser and go to <http://192.168.0.1>. It will ask for username: Admin and password: brp.

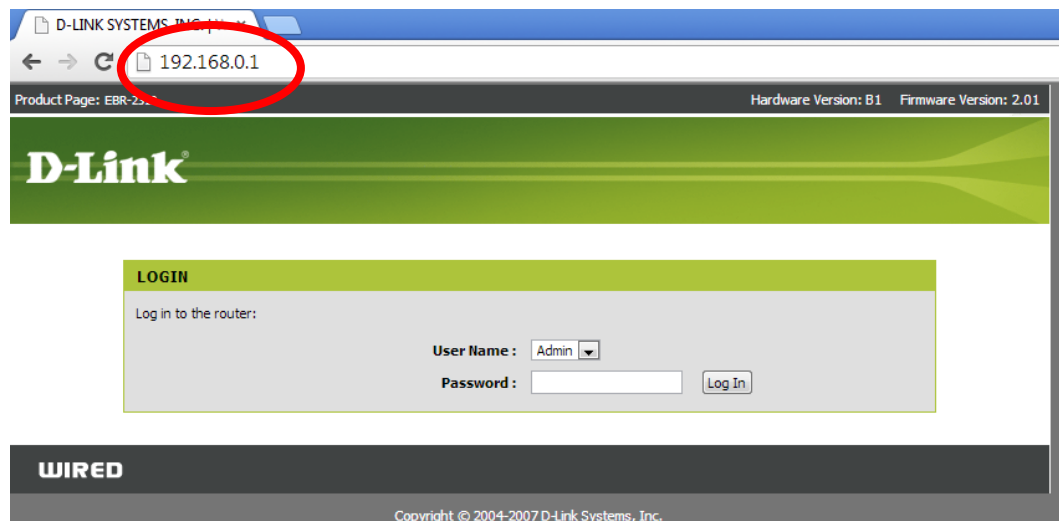


*Figure 2.1 User authentication page for Router*

Navigate to “ADVANCED” page on router configuration and then click on “PORT FORWARDING” which should load Figure 2.2 Port forwarding for DICOM push. Make sure the IP Address for DICOM is the IP address of RadVision computer. By default, it is 192.168.0.110.

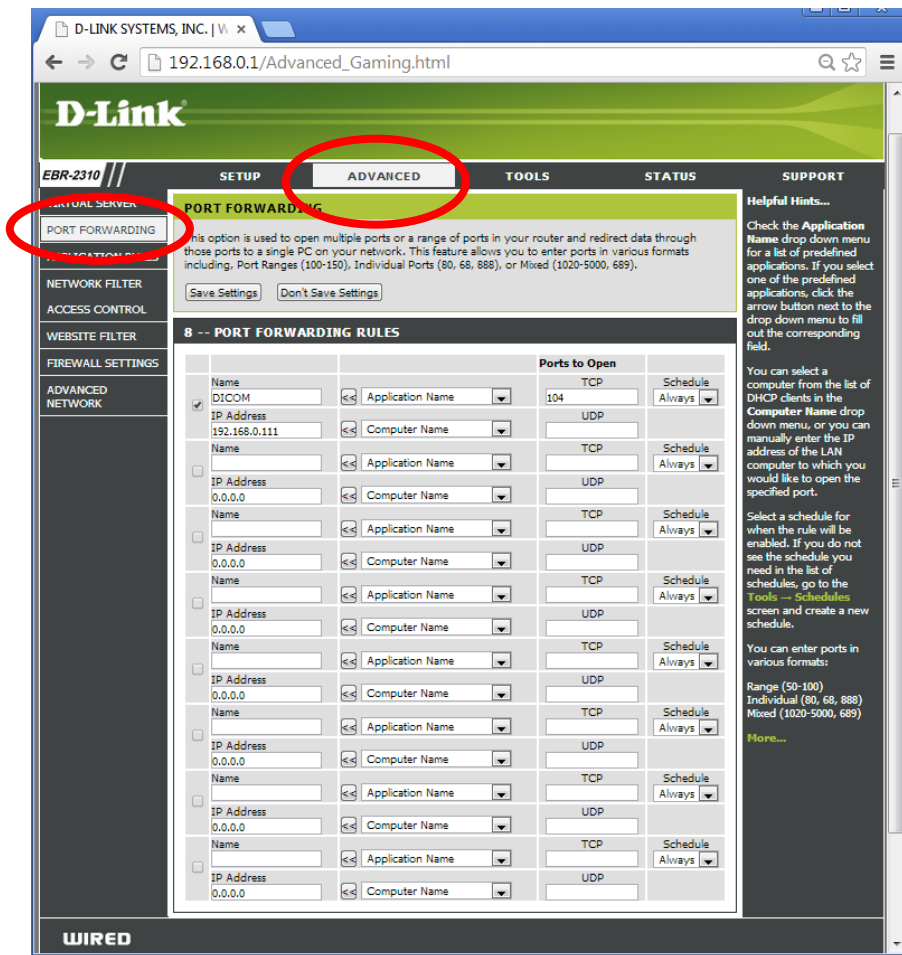


Figure 2.2 Port forwarding for DICOM push

## 2.4. RadVision Assist Device IP Change

- 2.4.1. Open Admin applicationn from Desktop. And enter password: **RadVisionAdmin**

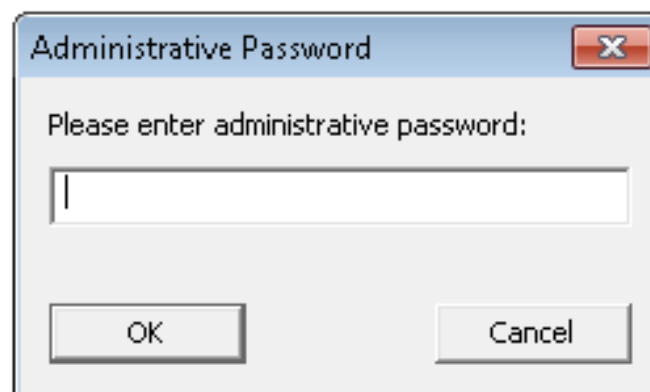
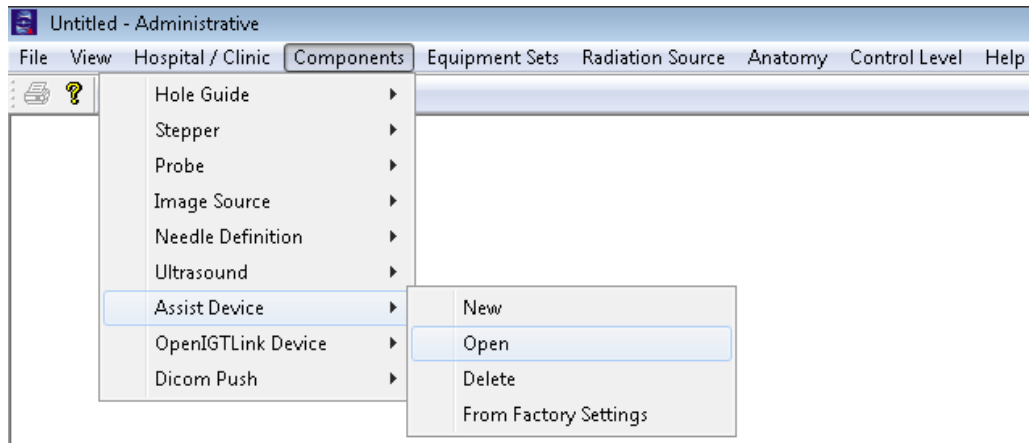


Figure 2.3 Rad Vision Admin Login

2.4.2. Open **Assist device** as shown in the snapshot below



*Figure 2.4 Open Assist Device*

2.4.3. It should show popup as shown below. Select **BRPBot** and click OK

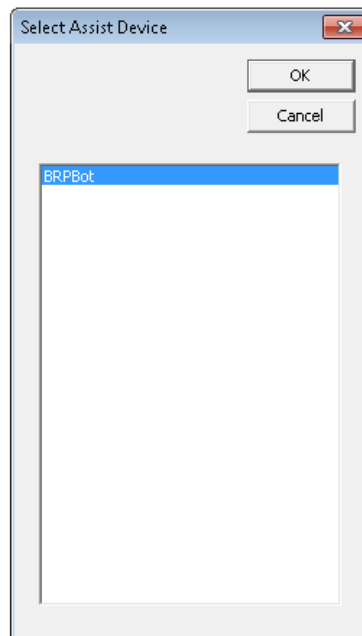


*Figure 2.5 Selet BRPBot*

2.4.4. See the “**Network IP**” field should be showing **192.168.0.103**, this would work only if LAN cable is connected and it can assign IP of the computer to **192.168.0.103**. But as you might be using it without network connection you should change that field to **localhost OR 127.0.0.1** so that it does not fail. After changing the IP address hit OK.

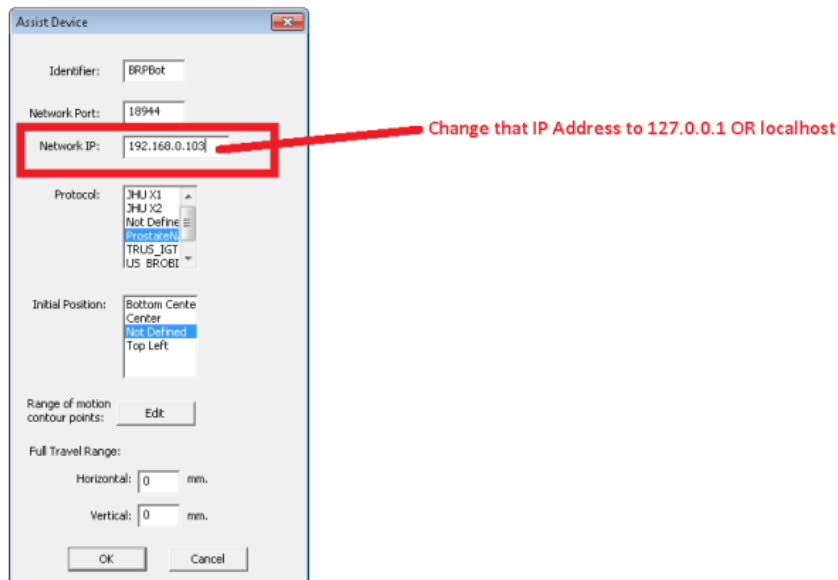


*Figure 2.6 Change IP address*

2.4.5. Open Generic device setting as shown in below screen.

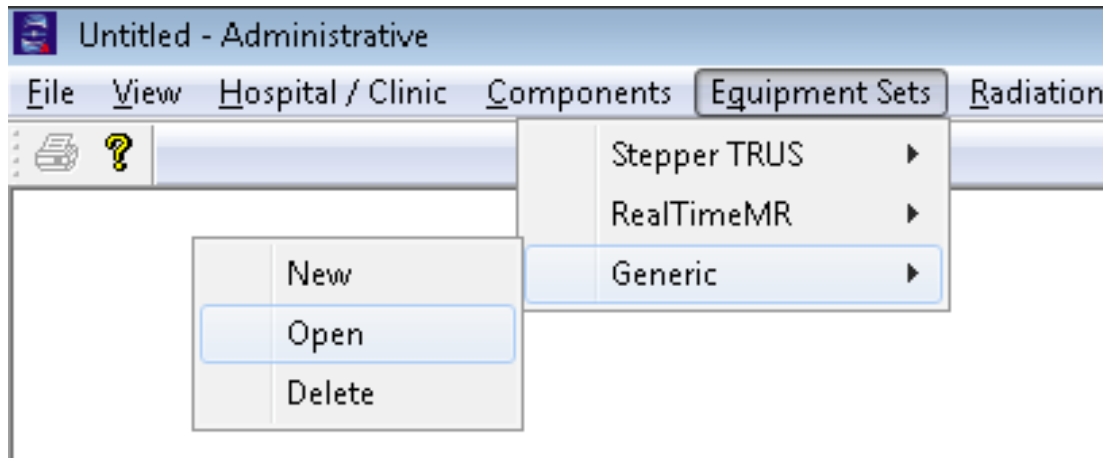


*Figure 2.7 Open generic device*

2.4.6. That should open following dialog. Select **BRP\_Bot** and hit OK.

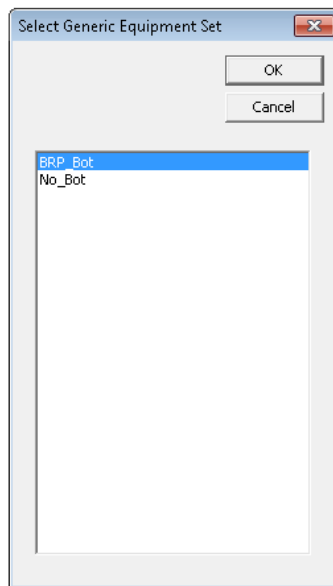


*Figure 2.8 Select BRP\_Bot*

2.4.7. As shown in below figure just click on **BRPBot** drop down menu once and reselect **BRPBot**, and then hit OK.

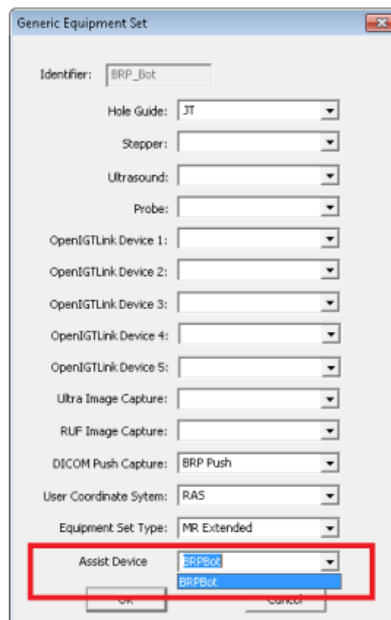


*Figure 2.9 Reselect BRPBot*

2.4.8. As shown in below figure update hospital data.

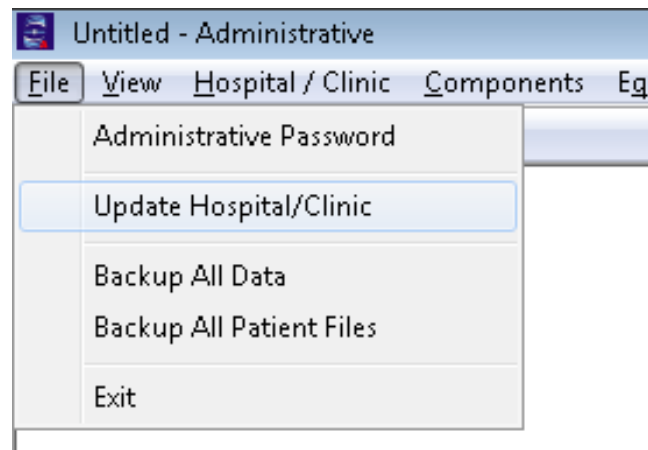


*Figure 2.10 Update hospital data*

2.4.9. As shown in message in below figure please close RadVision if it was Open and reopen it to use updated settings.

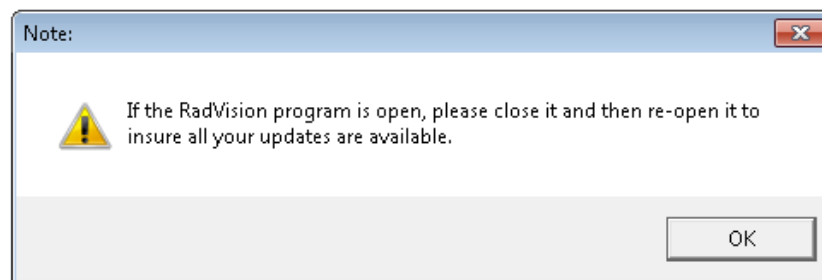


*Figure 2.11 Close and Reopen RadVision software*

2.4.10. Exit from Admin as shown in below figure.

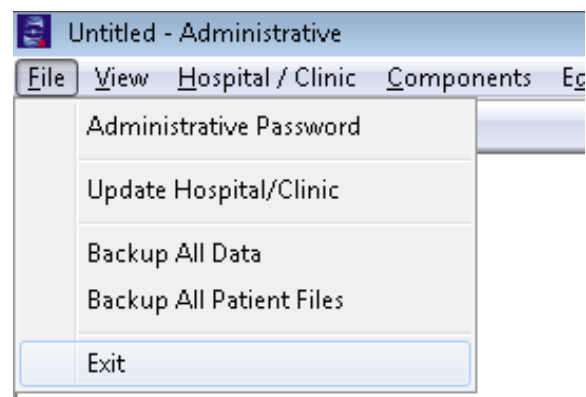


*Figure 2.12 Exit from Admin software*

### 3. START UP\_ROBOT CONTROL APPLICATION

#### 3.1. Downloading Robot Control Application

Until permanent file sharing place is decided, user can download ZIP file containing JAR, .BAT and .SH files from following Dropbox link:

<https://www.dropbox.com/sh/eolmehmcdi9vn0k/Az9fWM5Aoa>

#### 3.2. Running Robot Control Application

3.2.1. Windows: Launch JAVA application by opening .BAT file supplied with JAR file. Make sure JAR file and .BAT file are in the same folder. Both of these files are supplied by WPI. When running .BAT file, you should see the dialog box shown in Figure 3.2.

3.2.2. Linux: After unzipping the file, please right-click on the directory which contains JAR, .BAT and .SH files and open properties dialog. Navigate to "Permissions" tab and enable the directory content to be executable by clicking on checkbox next to "Execute" option and make it display tick mark and then click on "Apply Permissions to Enclosed Files" button. This makes SH file to be executable by double clicking on it.

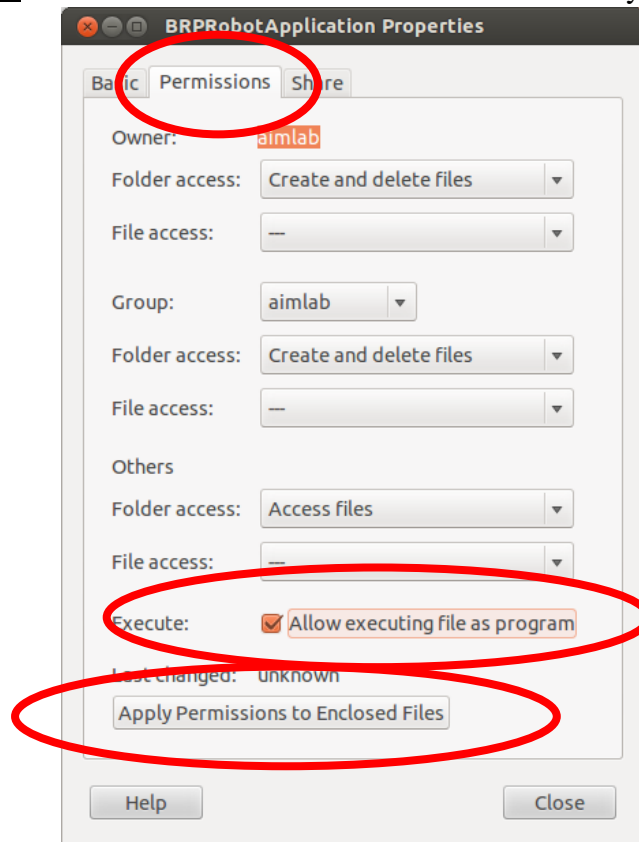
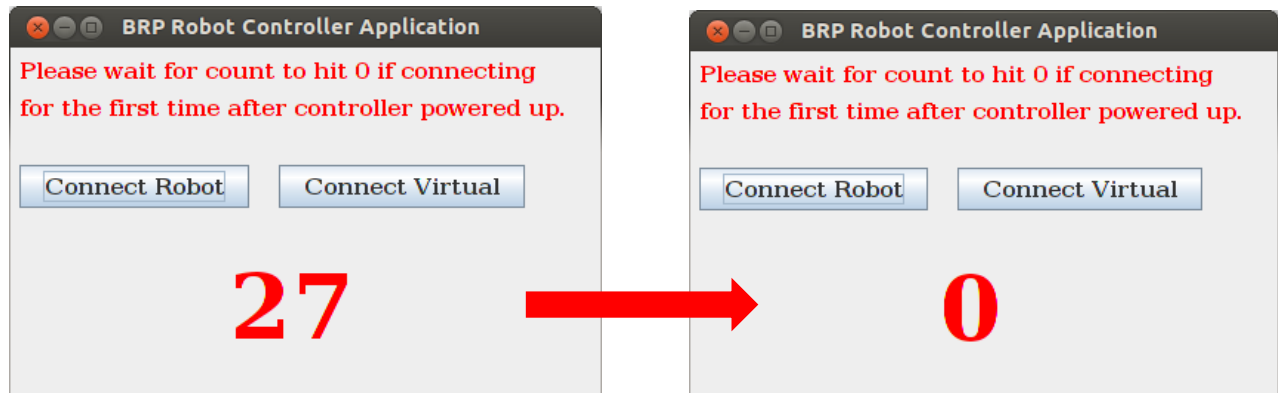


Figure 3.1 Dialog to change file permissions to make directory content executable on Linux

After all, by running either BRPRobotApplication.BAT on Windows or



BRPRobotApplication.sh on Linux, user should see Figure 3.2.



*Figure 3.2 JAVA application start up dialog with countdown timer*

### 3.3. 45-second Countdown Timer

- Wait it until hit zero (0): First connection after starting the robot controller;
- Connect robot any time you want: Not the first connection.

### 3.4. Establish Connection

- If you want to work with the real robot, click on “Connect Robot”.
- If you are not connected to the real robot but just want to test the system WITHOUT robot, click on “Connect Virtual”. It is a simulator.
- There will not be any more dialog asking for IP address since it is static.

In both cases of virtual controller or real robot controller, you should wait for UI to load. Once either virtual controller or real robot is connected and ready to run, you should see Figure 3.3. You can see that the robot is shown to be in BOOT\_UP mode in upper left corner which means homing procedure is not yet executed.



Figure 3.3 BOOT\_UP mode, homing procedure is not yet executed

### 3.5. Hardware Test

This is a safety feature that is required only once at the first connection to test the robot hardware.

- Clicking on HARDWARE TEST will show the confirmation dialog. Click Yes to run it. In the meantime, the HARDWARE TEST button turns to TESTING... and disabled.

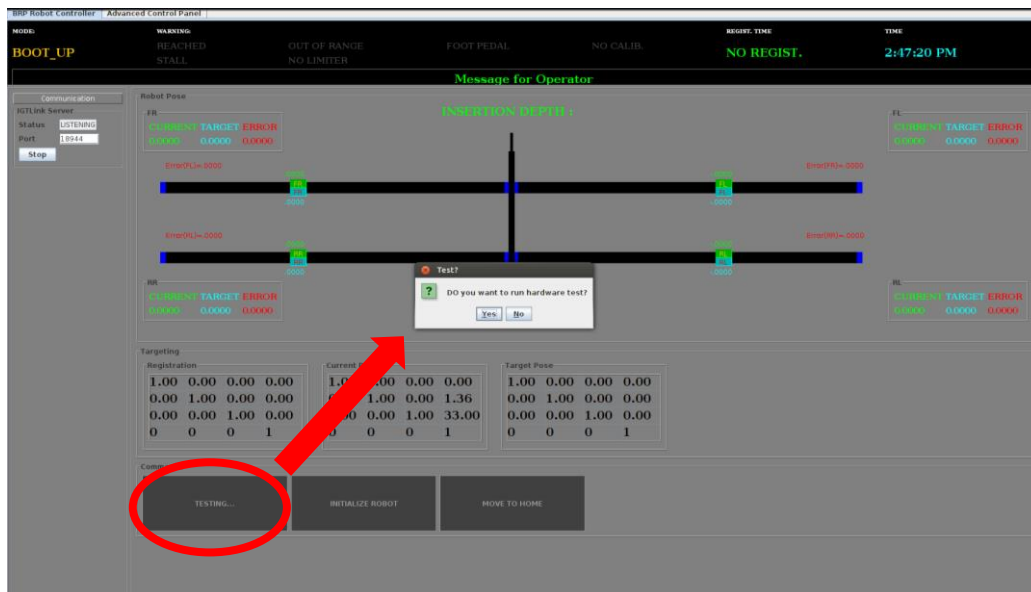
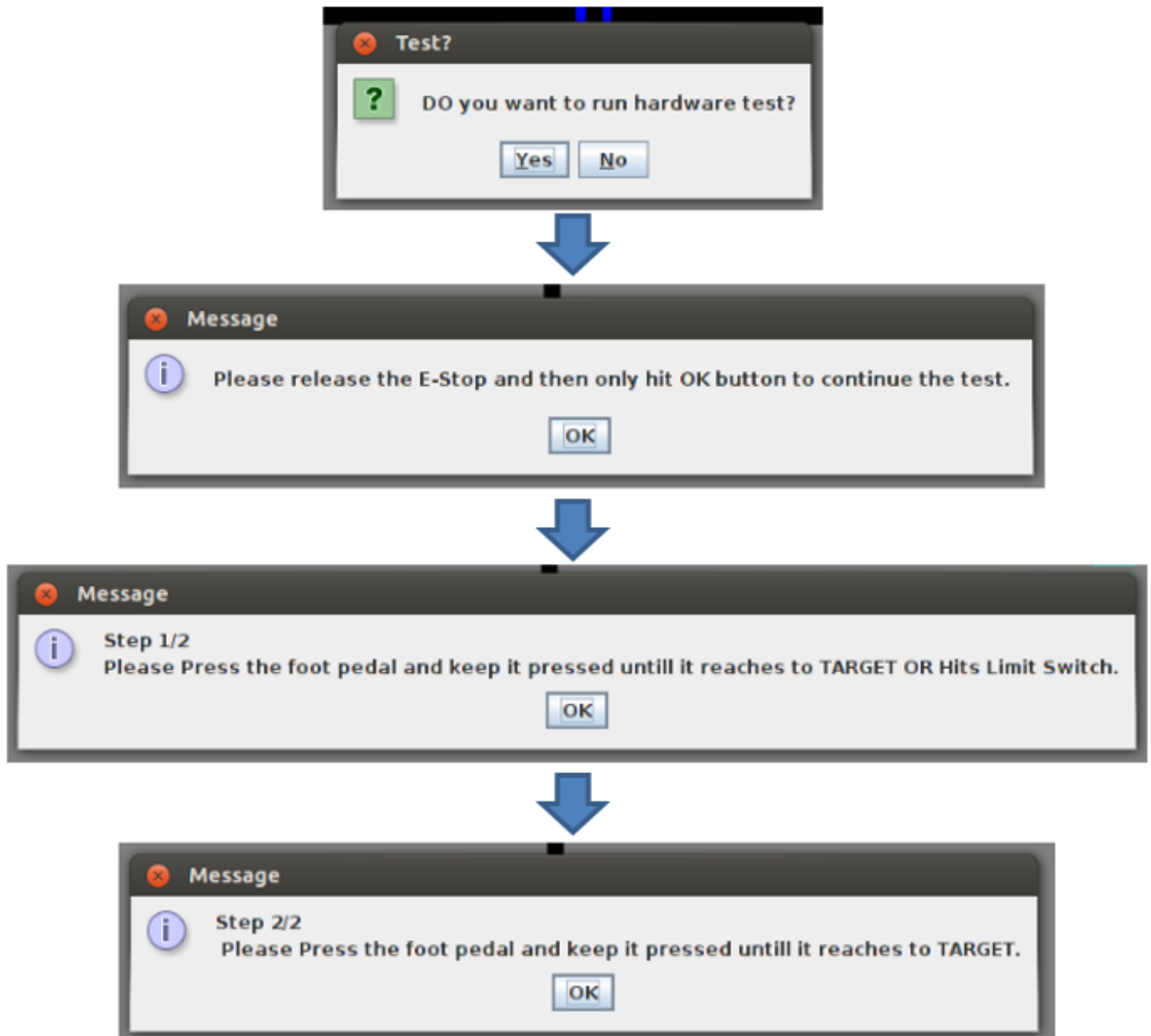


Figure 3.4 Hardware Test

- The foot pedal is enabled during the whole procedure.

- Please follow the messages to finish the two-step test as shown in Figure 3.5:



*Figure 3.5 Hardware Test Messages*

- After the hardware test is done, the Commands area should look like Figure 3.6. The HARDWARE TEST button turns to HARDWARE READY, and INITIALIZE ROBOT button is enabled.

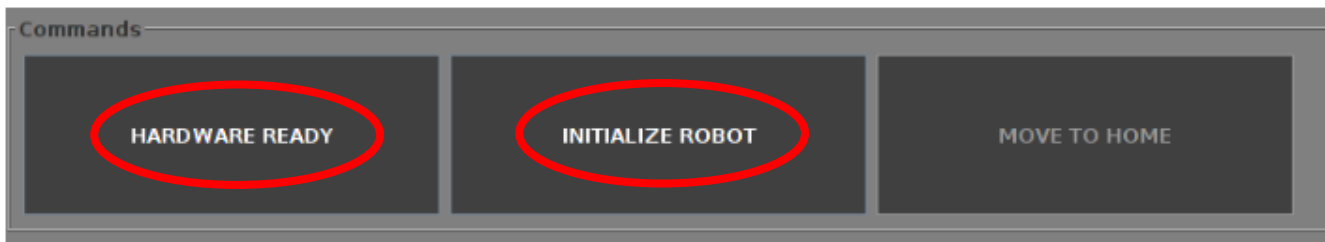


Figure 3.6 Done with Hardware Test

### 3.6. Homing Procedure

- To run homing procedure, click on “INITIALIZE ROBOT” button and you should see Figure 3.7.

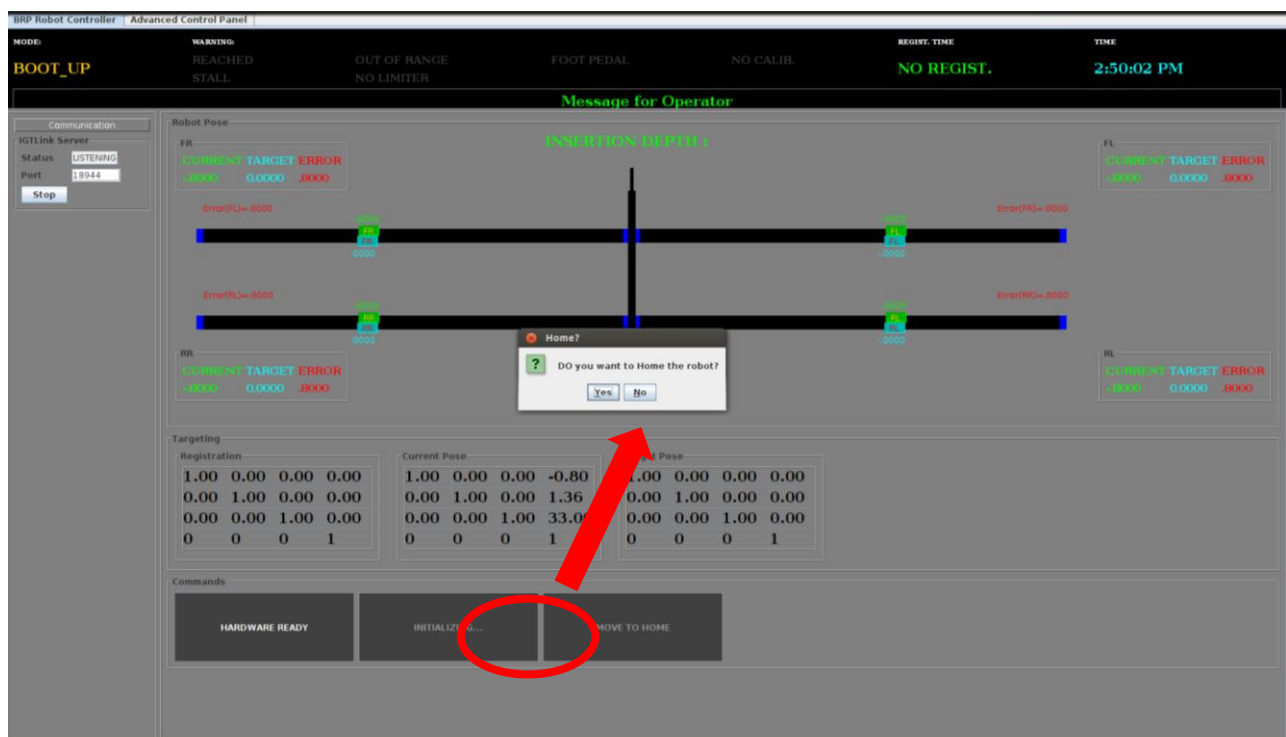


Figure 3.7 Robot homing confirmation dialog

- Here you get a choice to confirm that if you want to run homing procedure or not.
- If you click on YES, robot will start running homing procedure which is basically moving all links to LEFT most end and then to positions which make needle to be at center of the platform and at predefined height.
- Similar to Hardware Test, you also need to follow the messages to finish this two-step homing procedure as shown in Figure 3.8.

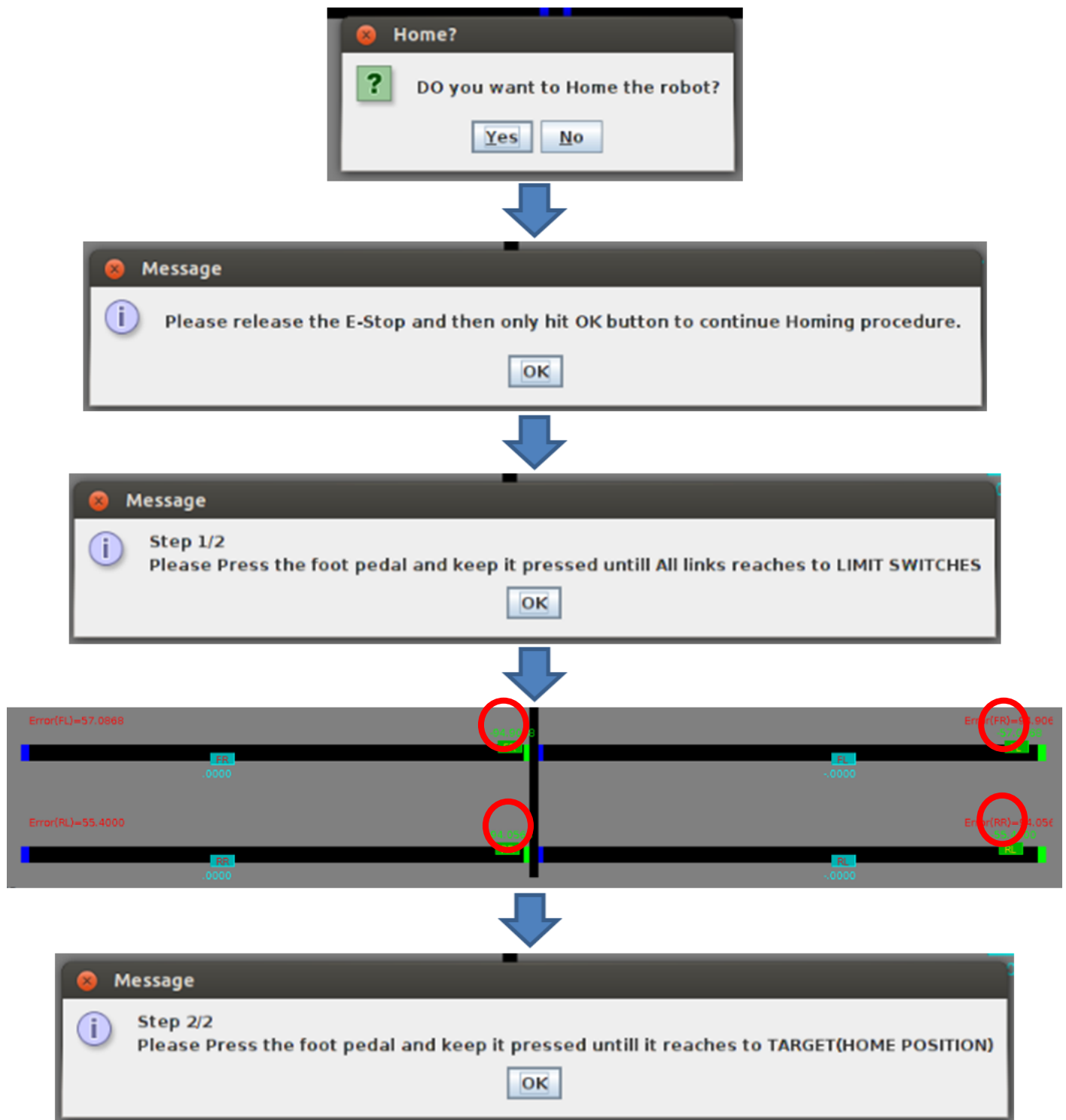


Figure 3.8 Homing procedure key steps

- If homing procedure finished successfully you should see *Figure 3.9* which shows robot mode as STAR\_UP.



*Figure 3.9 STAR\_UP mode, homing finished successfully*

### 3.7. Robot Ready

At this point, the robot is ready to connect to RadVision and run.

## 4. START UP\_RADVISION

4.1.Run RadVision from desktop shortcut and you should be able to see Figure 4.1.

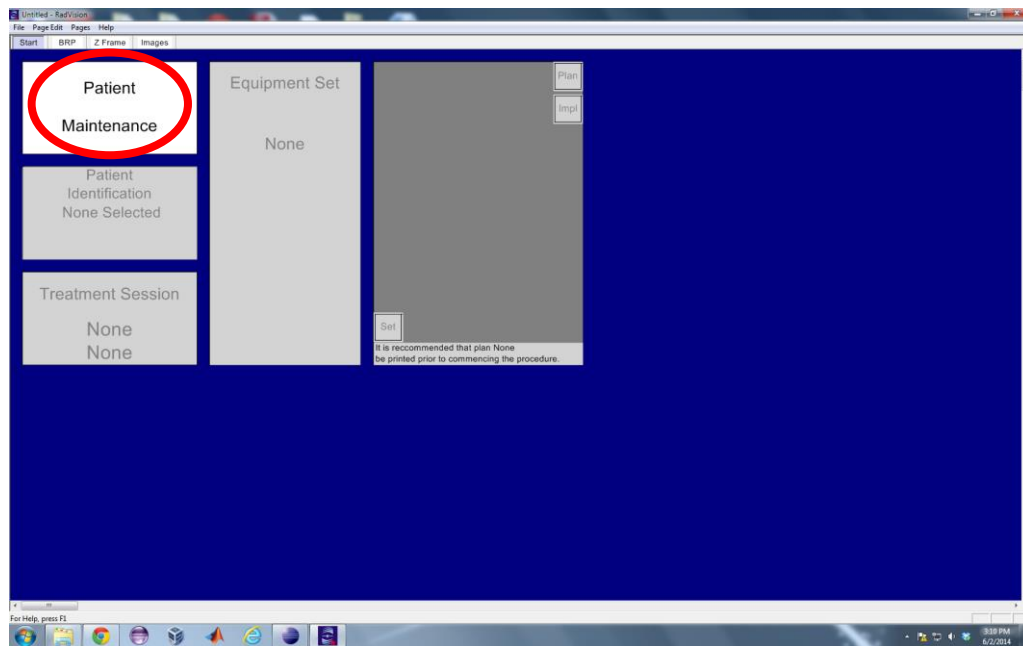


Figure 4.1 RadVision start-up screen

4.2.Click on “Patient Maintenance” panel, and three options would show up. Click on “Open” option and you should see Figure 4.2.

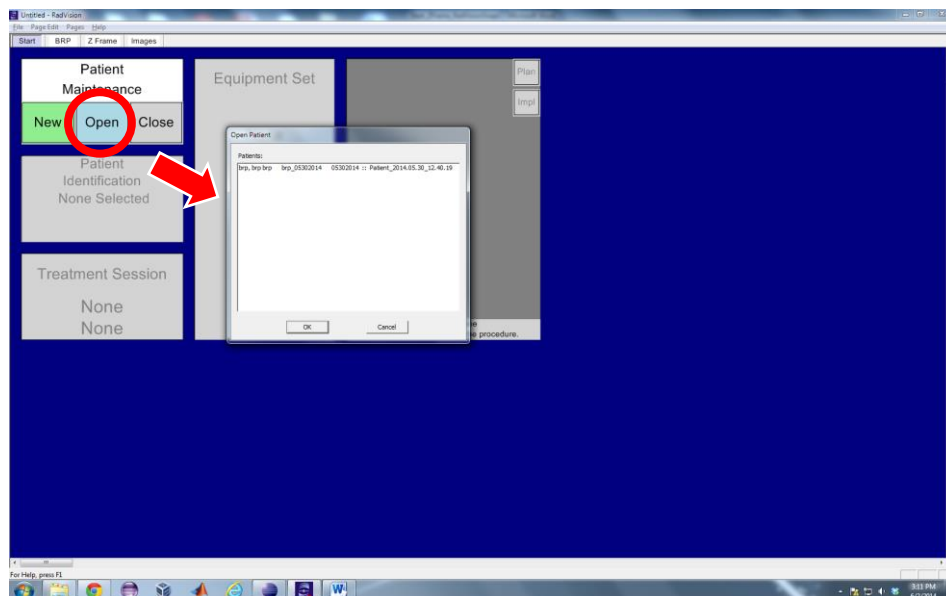


Figure 4.2 RadVision on click of Open Patient option

4.3. Select the patient you want to work on and click OK. You should see Figure 4.3.

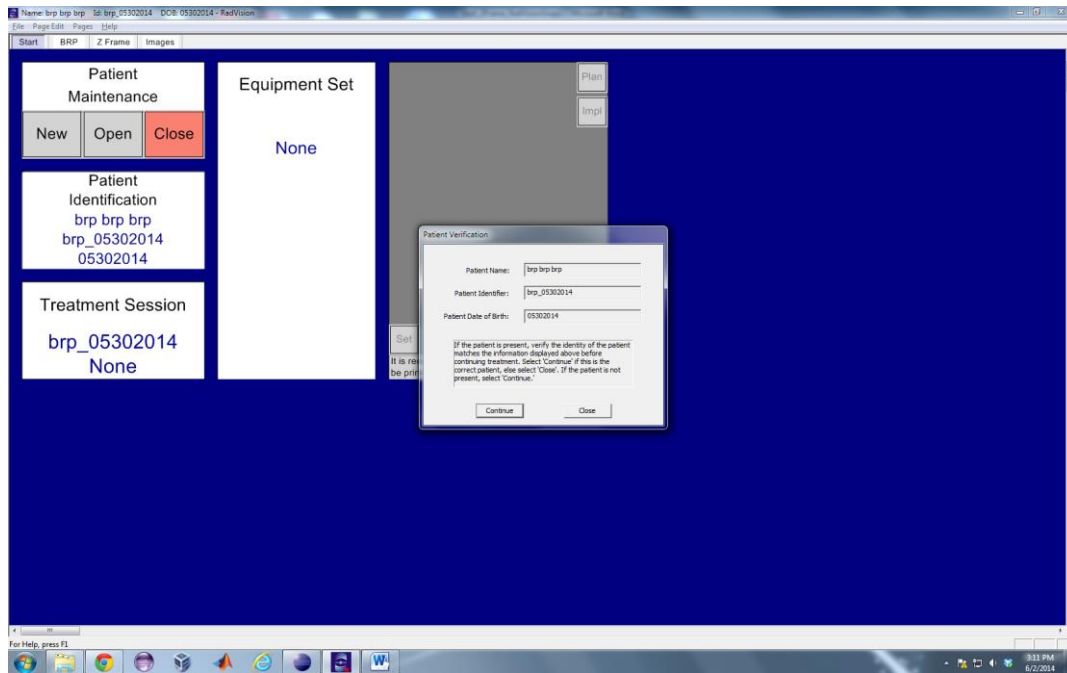


Figure 4.3 Patient confirmation dialog on RadVision window

4.4. Click on “Continue” and you should see that RadVision tries to connect with robot controller JAVA application. If it is able to connect successfully and you do not see any error dialog, click on BRP tab on top of the window and you should see Figure 4.4.

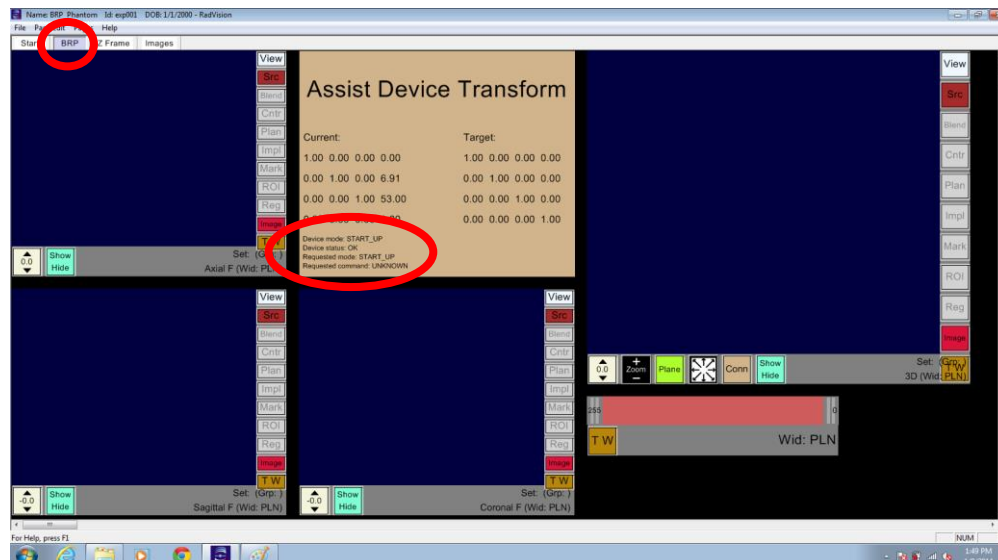


Figure 4.4 After loading the patient and successful connection to robot controller application



If some network error occurred while connecting to Assist Device (robot controller application), you should see Figure 4.5.

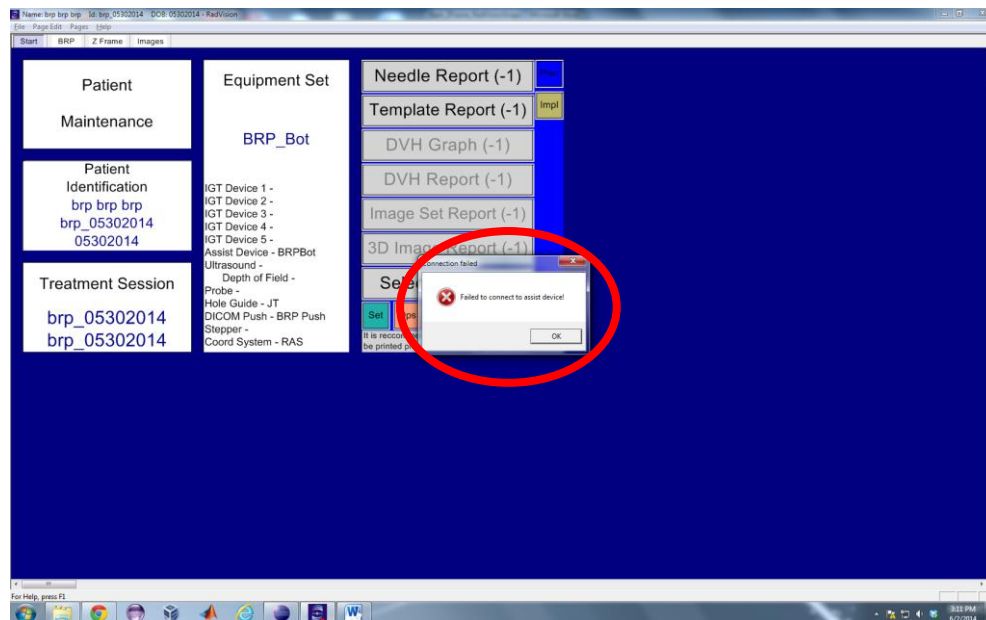


Figure 4.5 Error Dialog when connection error while connecting to robot control application

4.5. You can see that in Figure 4.4, in Assist Device Transform frame, current Device Mode is START\_UP and current robot position is also displayed. At this point you should see following status update in JAVA application in Figure 4.6. Status has changed to CONNECTED in communication panel (Left panel).



Figure 4.6 IGTLServer status changed to CONNECTED on RadVision connection

## 5. SETTING UP DICOM PUSH\_RADVISION

### 5.1. Setting Up IP Address

Usually, this step is not required as long as the Windows PC running RadVision has the same IP address as before. It has been set up as static IP: 192.168.0.103. Please refer to **section 2.4** or RadVision Manual to use the RadVision Admin application (different application from RadVision) to change the IP for DICOM Push if needed.

### 5.2. Starting DICOM Push Receiving

DICOM push receiving should be started every time you want to have a new MRI scan. Without starting it, the just scanned images could not be received by RadVision.

Usually it is needed for receiving Z-Frame images and every intra-operative image set you want to get from MRI.

- Run “DICOM Store” application (different application from RadVision) to listen to scanner DICOM push images. Leave it always on.
- In RadVision, navigate to Images tab on top of the window and click on “Src” on the middle panel and select “Pushed Dicom” and click “OK”, like in Figure 5.1.

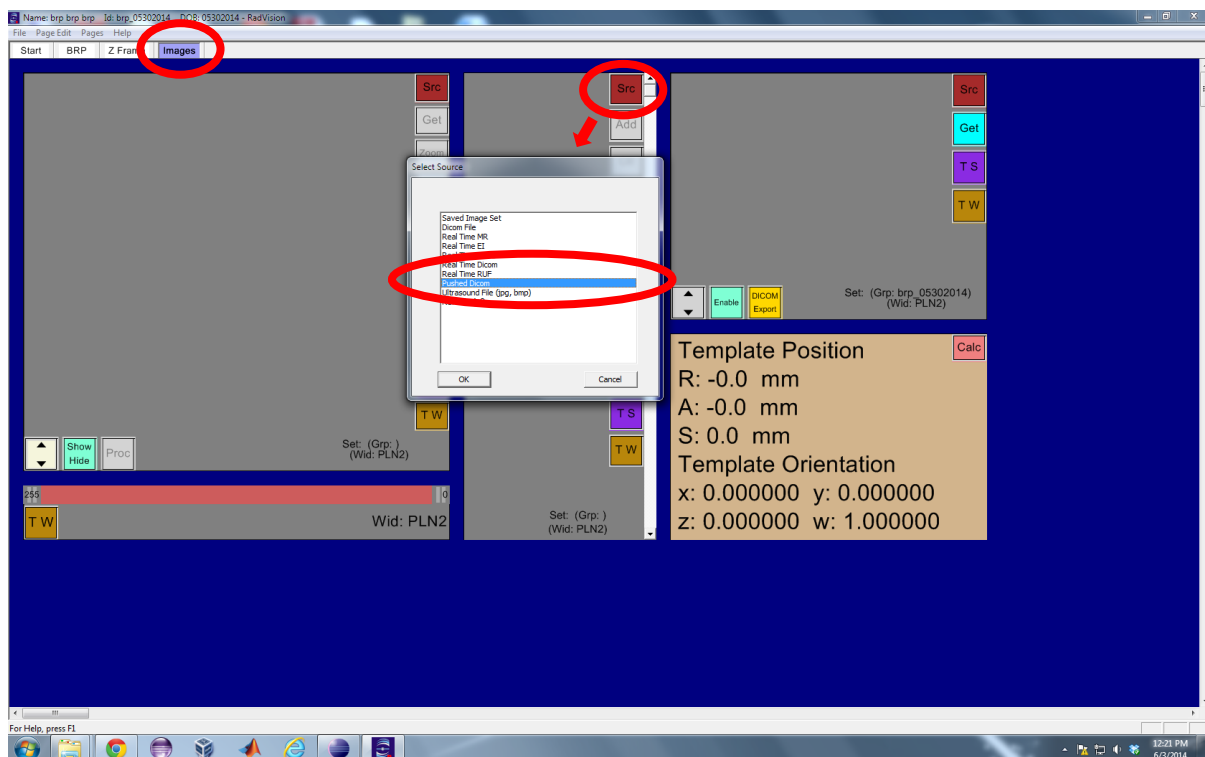


Figure 5.1 Starting listening to pushed dicom in RadVision

- If treatment session is not selected, select it, like in Figure 5.2.

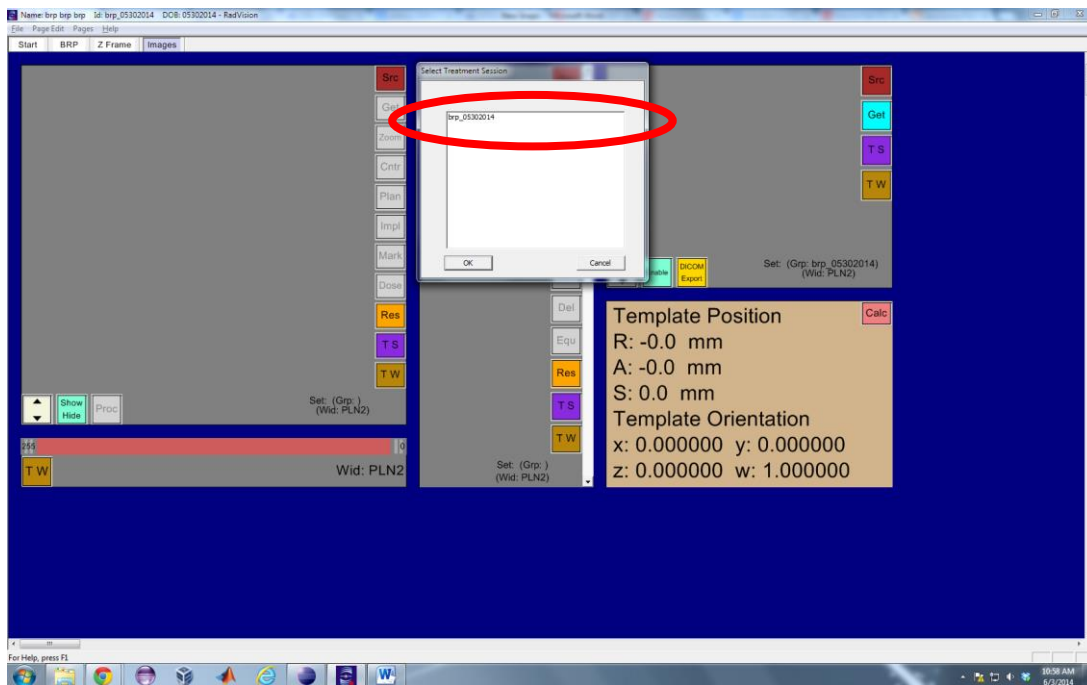


Figure 5.2 Select the treatment session if it is not selected beforehand

- Choose the checkbox for “Use DICOM series number and series description as image set name” and click on “OK”, like in Figure 5.3.

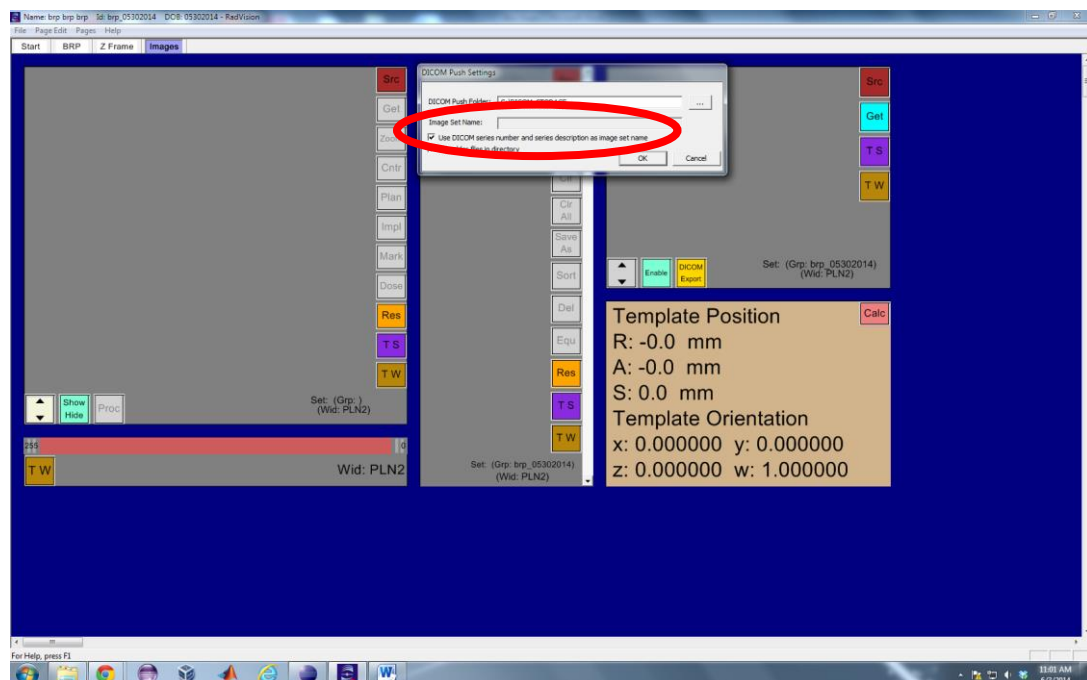


Figure 5.3 Check the "Use DICOM series Number and series description as image set name"

- Until here you should be all set for receiving the images from MRI.

### 5.3. [Saving the Received Image Set](#)

- Once a set of images is received by RadVision, it is automatically saved with its series name.
- There is also other way to re-save the image set with a different name, but it is not suggested.

### 5.4. [Loading the Received Image Set](#)

- Please refer to section 6.1 and section 8.1 about how to load saved image sets.

## 6. Z-FRAME CALIBRATION\_PART 1

This step involved both RadVision and robot controller. Z-FRAME CALIBRATION\_PART 1 describes RadVision procedure and then Z-FRAME CALIBRATION\_PART 2 describes how CALIBRATION transform is provided to robot controller application.

6.1. Click on Z-Frame tab on top of the window and click on “Src” button and you should see Figure 6.1.

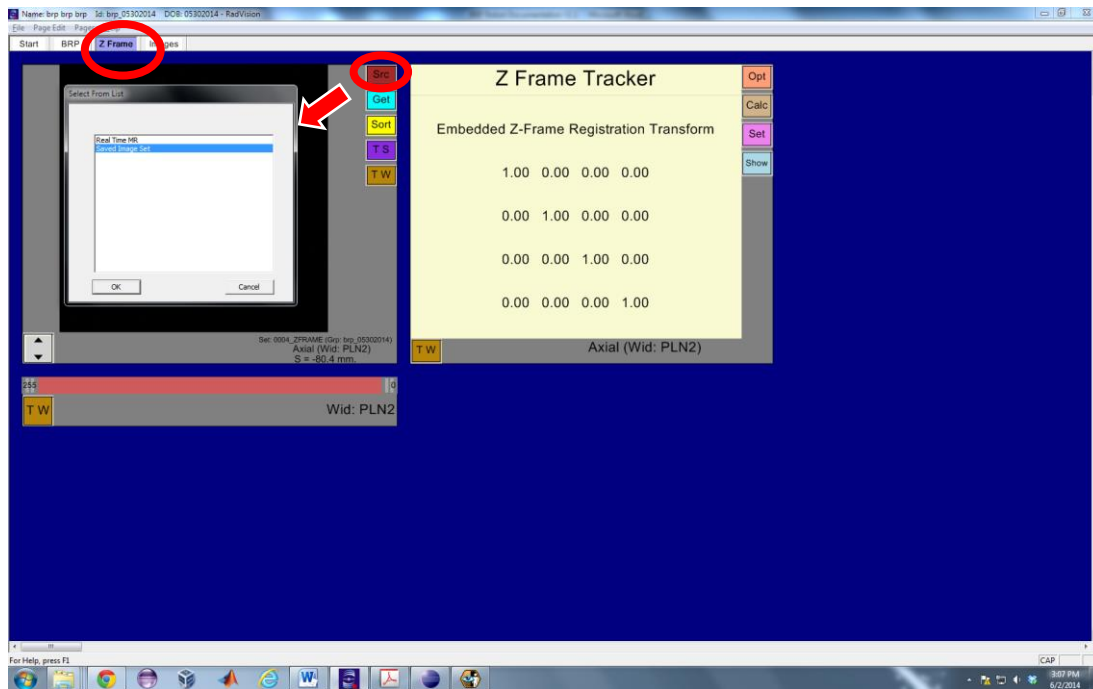


Figure 6.1 Z-Frame calculation window with Image Source selection pop-up

6.2. If you are going to use saved images (which is usually the case) click on Saved Image set and then click OK. On clicking OK you should see Figure 6.2.

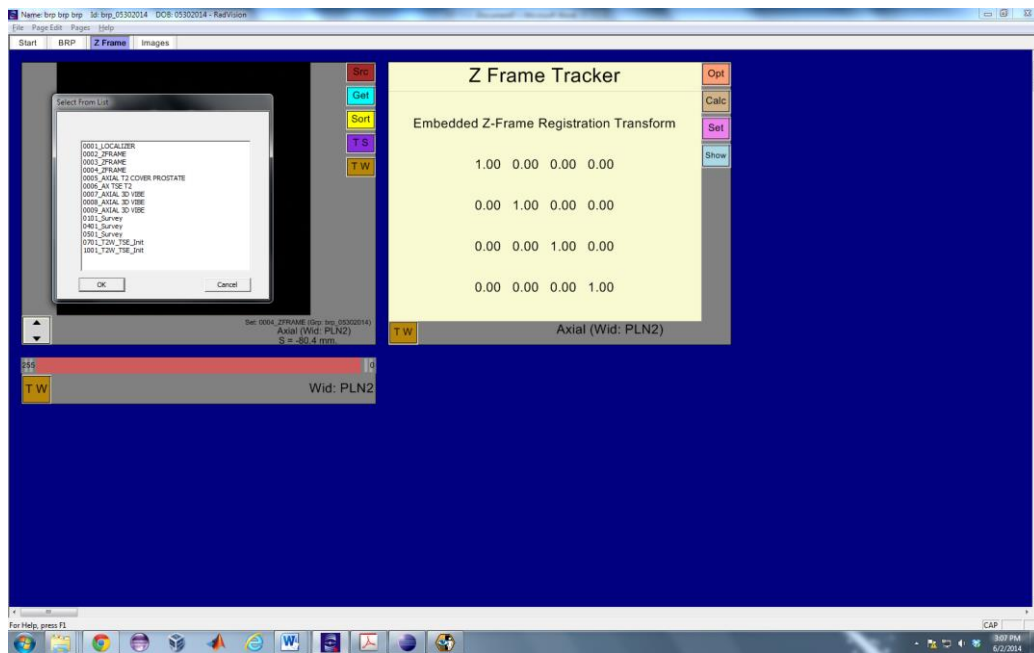


Figure 6.2 Z-Frame window with image list

6.3. In Figure 6.2, you should see a list of saved Image Sets, select the desired one and click OK. Clicking on OK should load Figure 6.3.

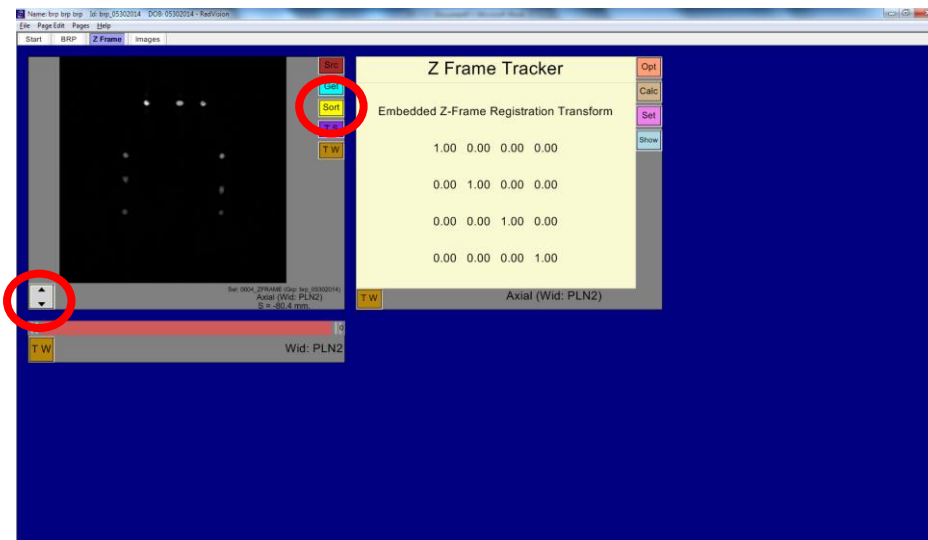


Figure 6.3 Z-Frame window with loaded image

6.4. Before calculating the calibration transformation matrix, the images should be sorted by “S” direction. Click on yellow “Sort” button and choose “Sort by S” in Figure 6.4.

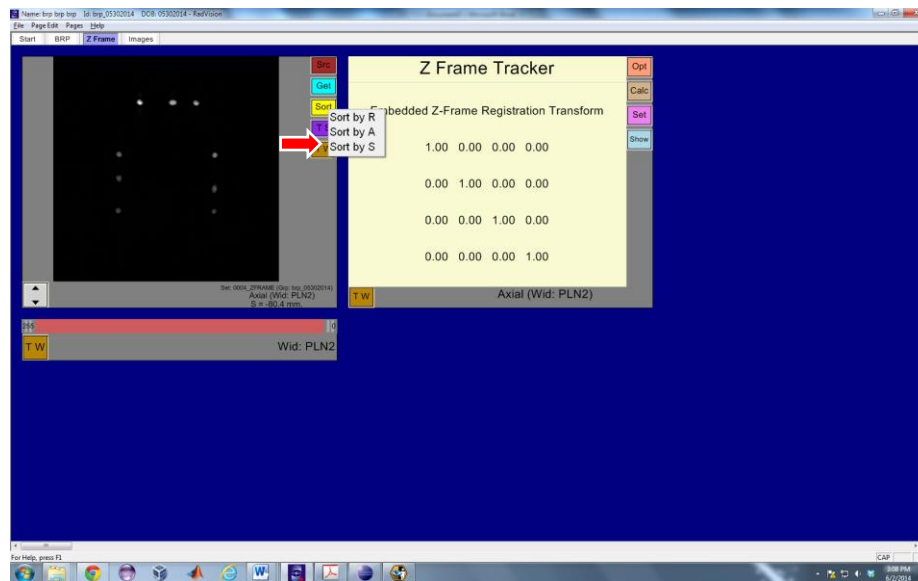


Figure 6.4 Sort z-frame images by S direction

6.5. To calculate new calibration transform, click on “Calc” button in “Z Frame Tracker” panel. You should see Figure 6.5 where you get option to calculate calibration transform for Assist Device.

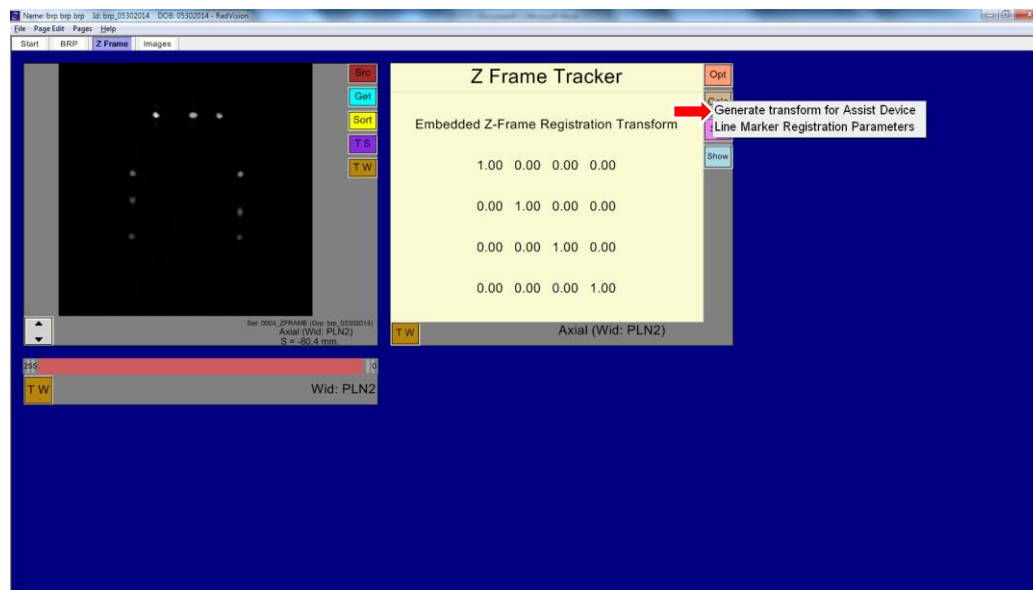


Figure 6.5 Z-Frame window with menu options for calculating the registration matrix

6.6. Click on “Generate result for Assisted Device” and you should see where “Embedded Z-Frame Registration Transform” is updated in Figure 6.6.

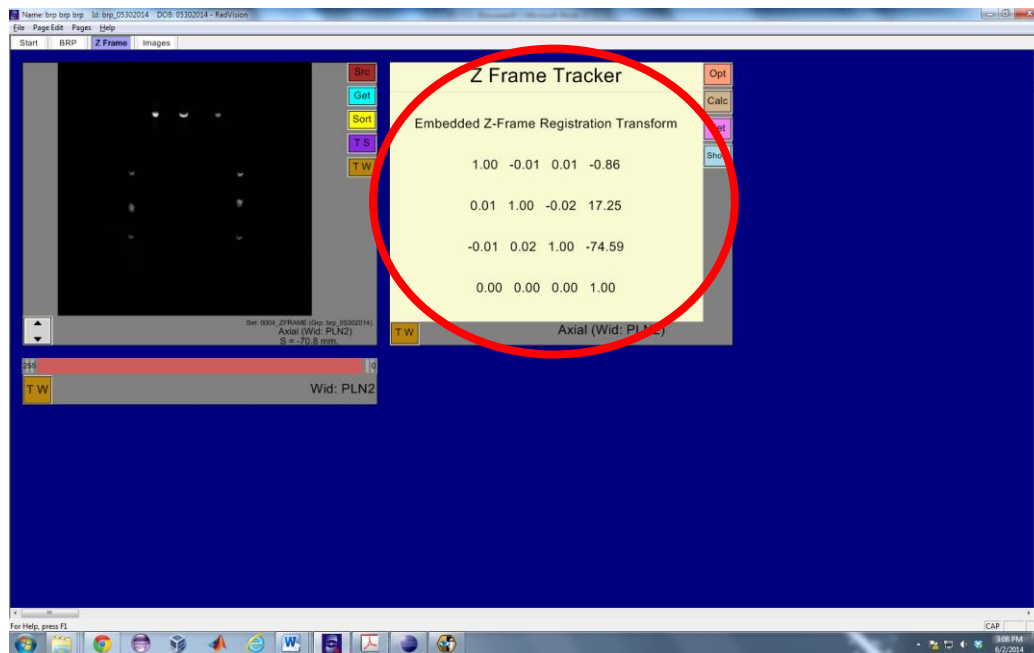


Figure 6.6 Calculated calibration transform

6.7. If algorithm is not able to calculate the results from images, background of the “Z Frame Tracker” frame will turn to **RED** color with all the values assigned to 0.0000 as shown in Figure 6..

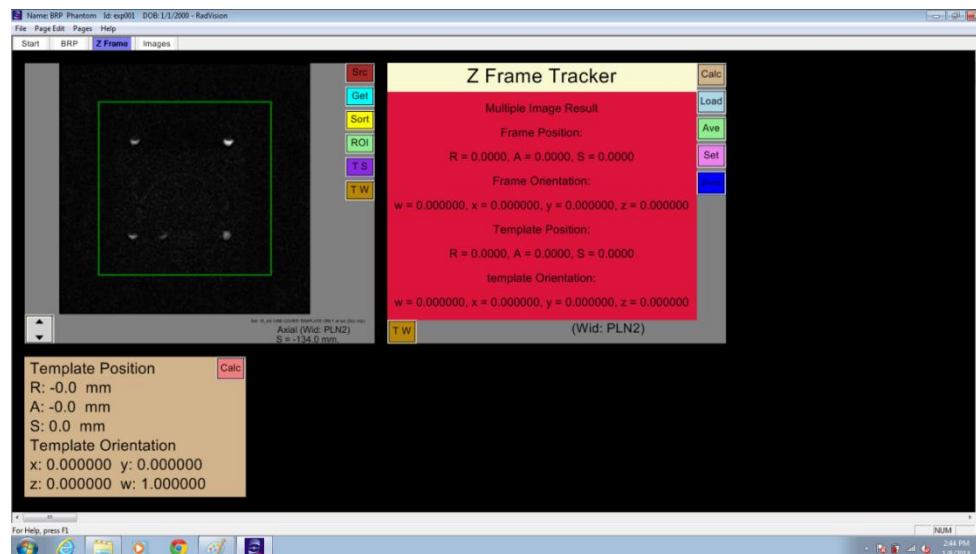
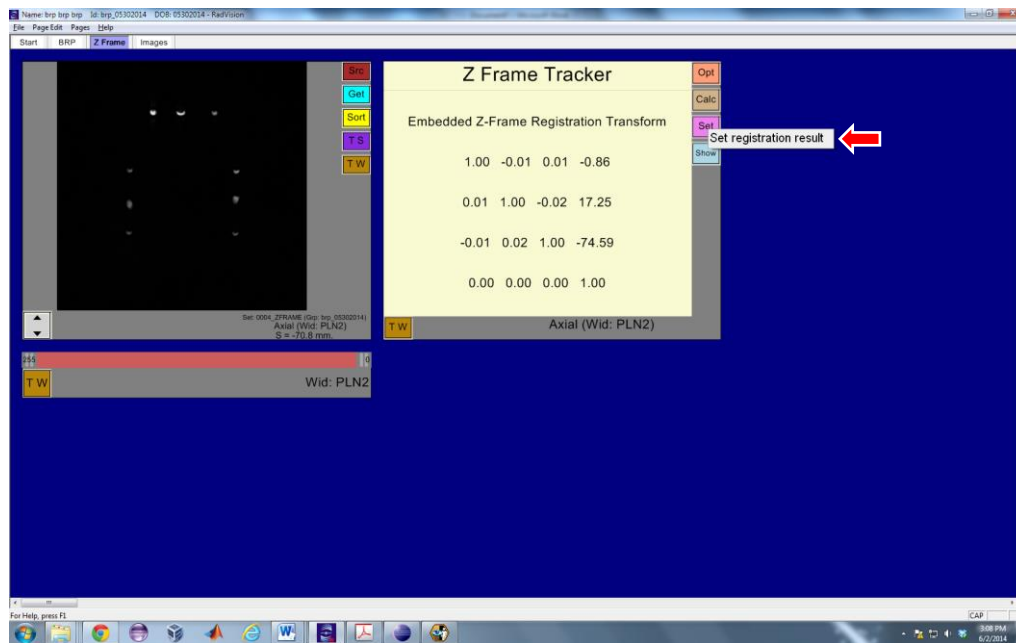


Figure 6.7 Error when algorithm fails to calculate z-frame transform

6.8. Now if result is calculated successfully, it can be sent to robot controller. In order to do so user should click on “Set” button which displays pop-up menu options as displayed in Figure 6..



Click on “Set registration result” to move forward.



*Figure 6.8 Menu options to set calculated result to be sent to robot controller*

6.9. Once result is set, user should follow Z-FRAME CALIBRATION\_PART 2 work phase procedure for sending it to robot controller.

## 7. Z-FRAME CALIBRATION\_PART 2

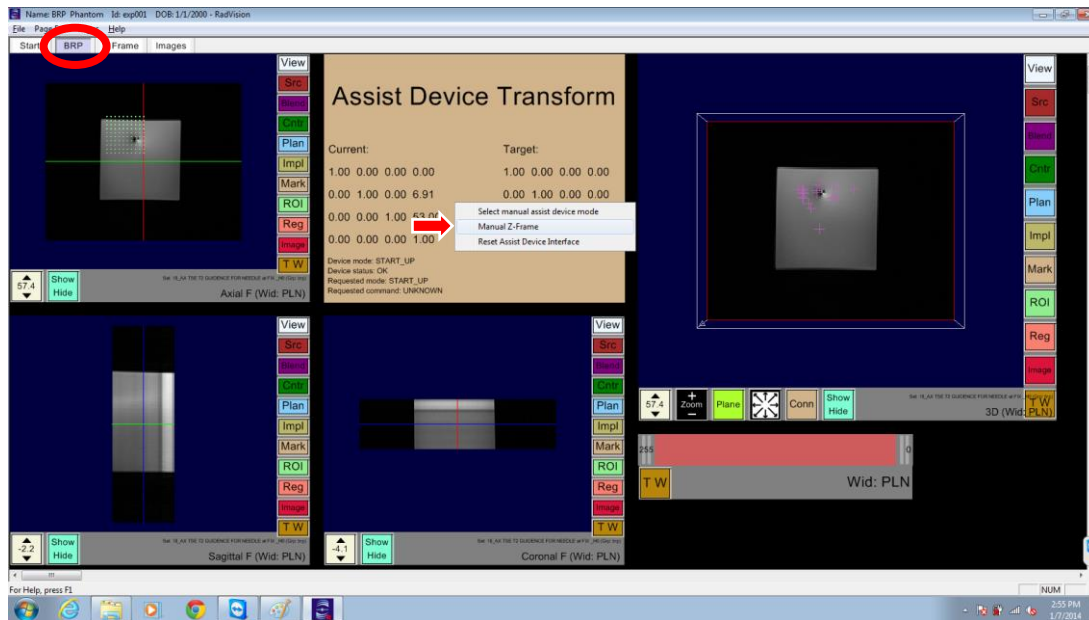


Figure 7.1 Menu options to send manual z-frame from BRP window

7.1. In RadVision click on BRP menu on top of the window and then right click in Assist Device Transform frame which should display pop-up menu as displayed in Figure 7.1. Click on Manual Z-Frame menu item and it should display Figure 7.2.

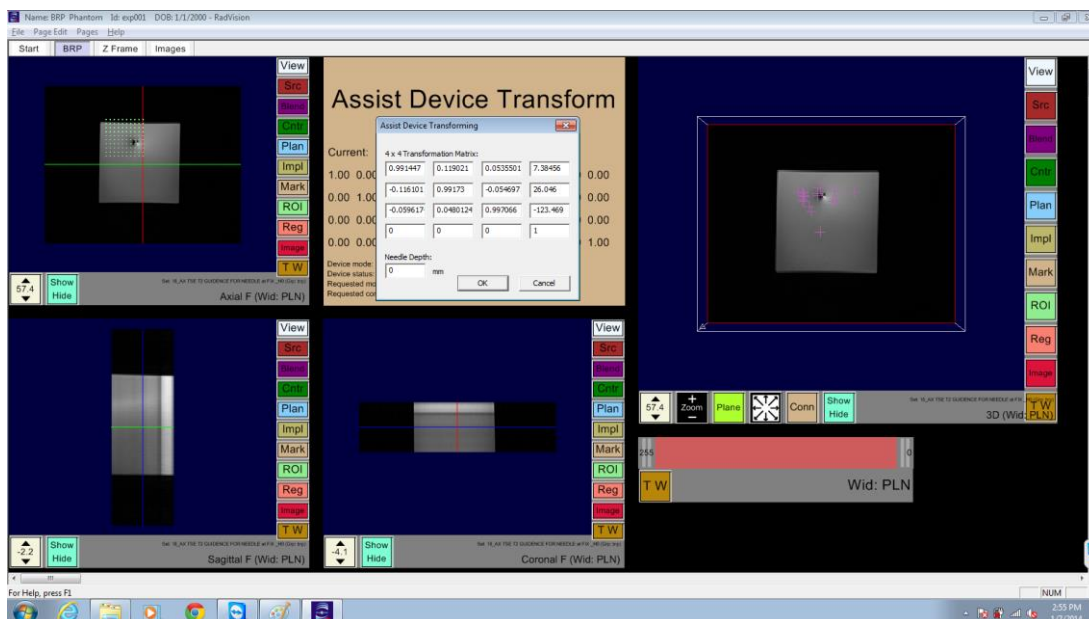
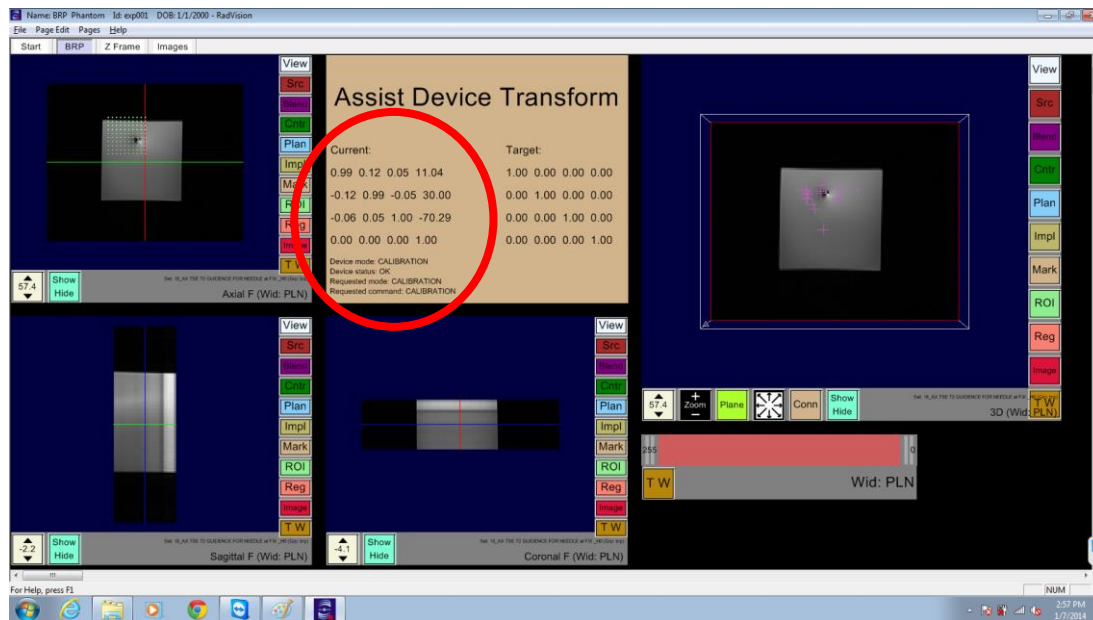


Figure 7.2 Z-frame transform matrix to be sent to robot controller

7.2.. Click on OK and that should send the transform to robot controller. If sending was successful, RadVision should look like Figure 7.3.



*Figure 7.3 RadVision after successfully sending CALIBRATION transform*

7.3. User can observe that Current Device Mode changes to CALIBRATION and Current position transform is also updated.

If transform was valid (orthogonal), robot controller should look like Figure 7.4.



Figure 7.4 Robot Control application after receiving valid CALIBRATION transform

- 7.4. User can see that current Mode should have changed to CALIBRATION and current position also should have been updated. At this point of time robot is ready for targeting and user should follow TARGETING work phase instructions.

## 8. TARGETING

### 8.1. Loading the Image Set

Before user can start targeting, he/she should set up and load images in the BRP tab. To load images user should click on Src button as shown in below figure and then click on “Select Image Set” which should load Figure 8.1 and Figure 8.2.

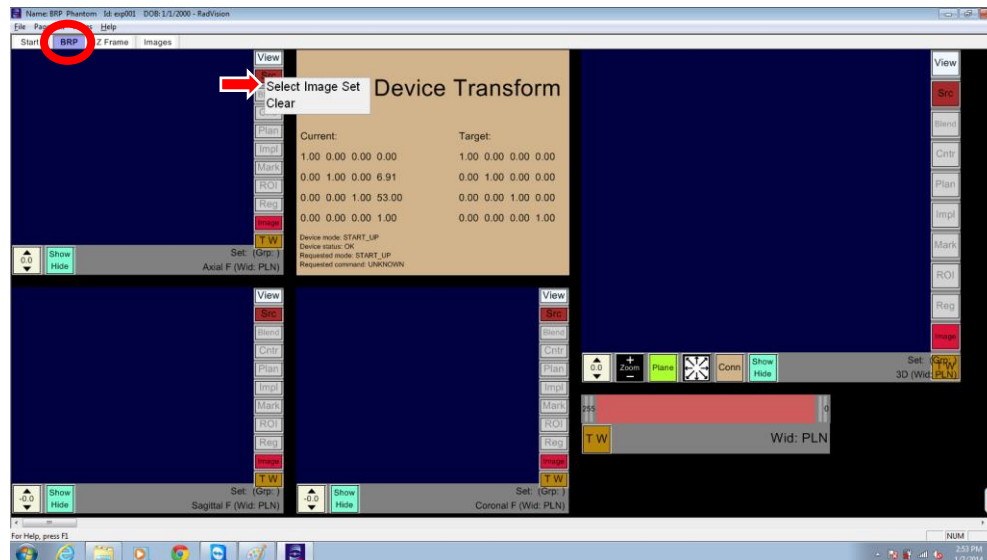


Figure 8.1 Menu to select images for TARGETING

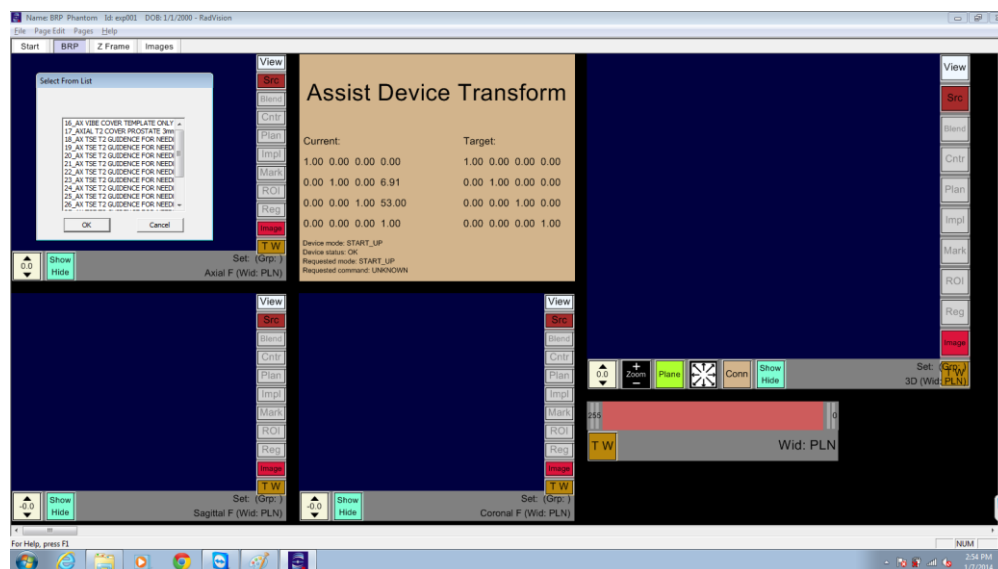


Figure 8.2 List of saved image sets

- Now user should select appropriate Image set and Click on OK which will load Figure 8.3 where Current Mode would be CALIBRATION and images should have been loaded to

various R-A-S image panels.

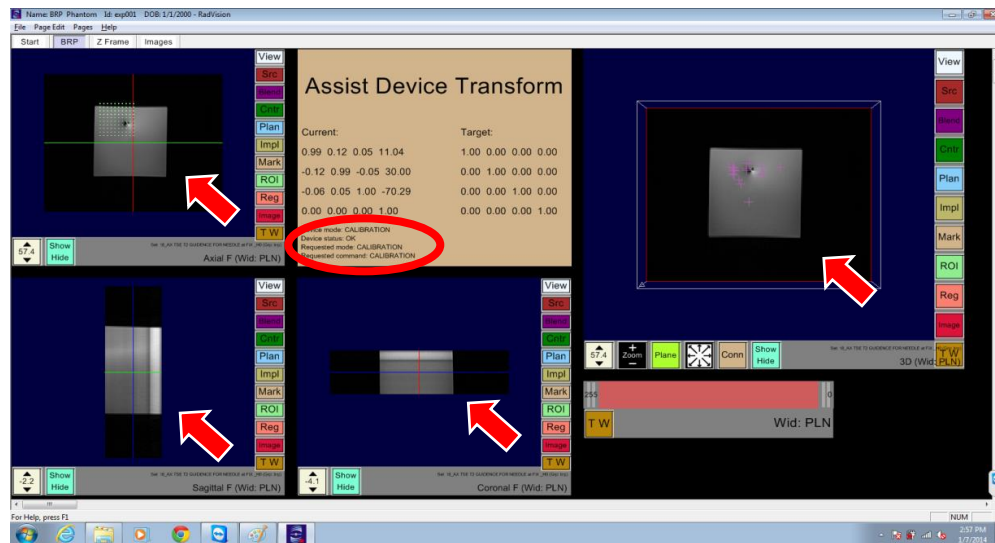


Figure 8.3 After loading desired image set

## 8.2. Three Approaches to Send Target to the Robot Controller

### 8.2.1. Manually Typed Target

- Left click on Assist Device Transform panel and that will load Figure 8.5 where a 4X4 matrix will be displayed and user can manually edit it and send it. If this is not the FIRST target being sent then user will get a Po-Up window saying to retract the needle as shown in Figure 8.4.

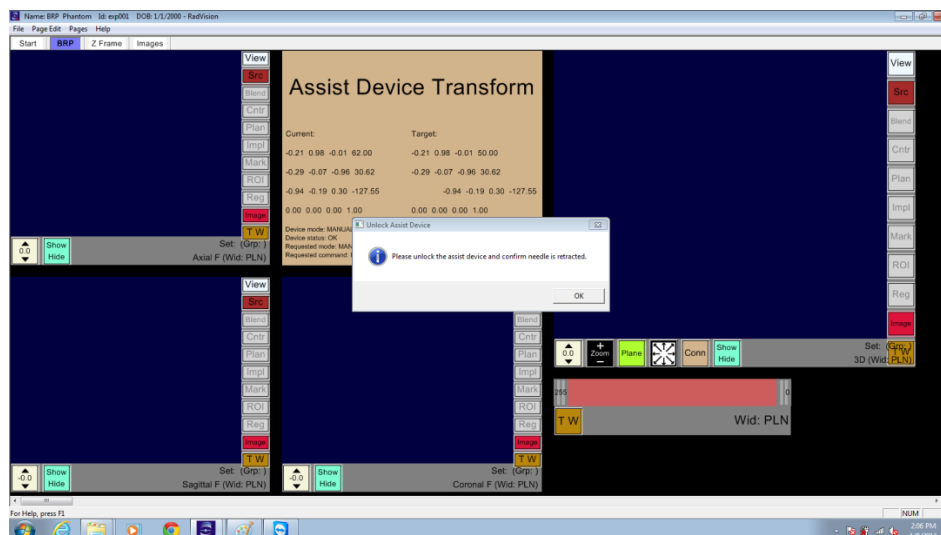


Figure 8.4 User confirmation to retract needle before sending new Target

- User should retract the needle if it is still inserted and then only click on OK. System will

NOT be able to detect whether the needle has already been retracted or not, so it's user's responsibility to make sure that needle is retracted before he/she press OK button. On pressing OK button user should see Figure 8.5.

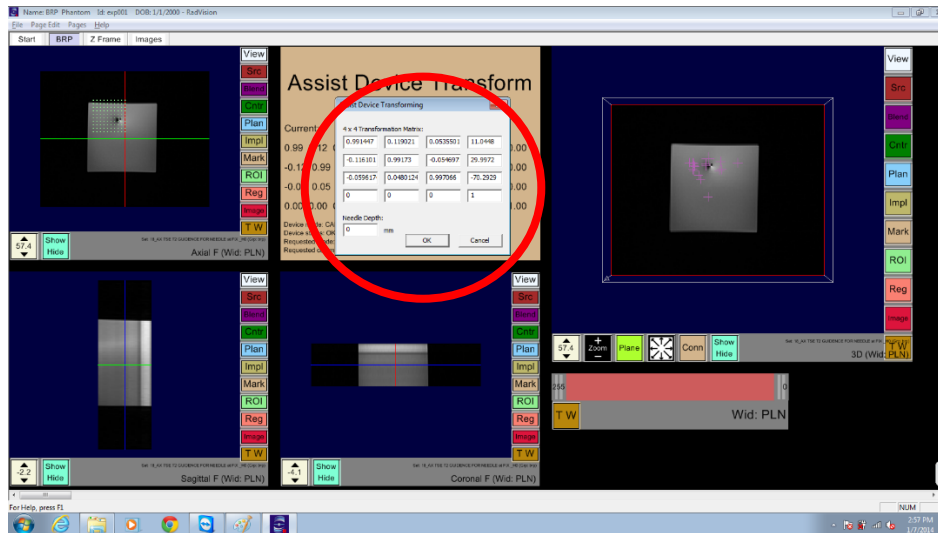


Figure 8.5 Sending Target transform manually

- After editing the target matrix, user should click on OK which will send the target to the robot controller over IGT Link. If target was valid, the robot controller application should look like Figure 8.6. If this was first target then it shows “Received VALID Target” message and if this was an updated target then operator message should be “Updated Target received, aborting current target”.



Figure 8.6 After Robot Control Application received valid target

- In Figure 8.6, user can observe that Current Mode should have changed to TARGETING and current and desired joint positions should have been updated. The BLUE bar indicating target joint positions should have moved to desired positions and a message is displayed on top of the panel “Received Valid Target”. If received target was valid then RadVision screen should look like Figure 8.7.

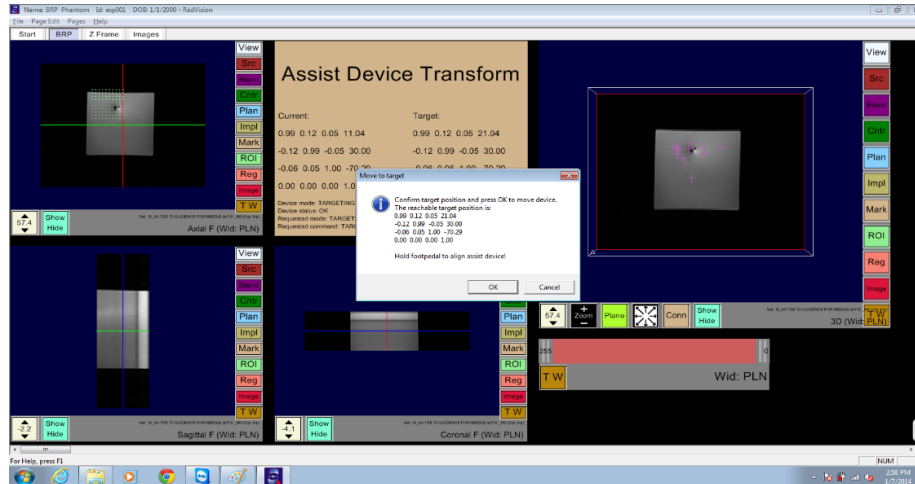


Figure 8.7 For sending MOVE\_TO\_TARGET request to robot control application

- Here user has an option to either move the robot to target or cancel the target. If user clicks on **OK**, MOVE\_TO\_TARGET command is sent to robot controller. Also operator message “Please Release the E-Stop and press the Foot Pedal to move the Robot” is displayed and current mode changes to MOVE\_TO\_TARGET as shown in Figure 8.8.





Figure 8.8 After receiving MOVE\_TO\_TARGET request from RadVision

**NOTE:** BEFORE pressing the foot pedal, operator should wait for all LEDs on Controller Panel to turn to **Yellow** and wait for approximately 10 seconds. Please refer **Error! Reference source not found.** or reference figures.

- If user clicks on Cancel, MOVE\_TO\_TARGET will not be sent and nothing happens on robot controller application. At this point of time, if user decides to send an updated target, he/she should follow TARGETING work phase from section 8.2 and upon sending updated target, robot controller shows Operator message “Updated Target received, aborting current target” and screen should look like in Figure 8.9. This is an EXCEPTION case when operator decides to send updated target before robot reached to target sent previously.



Figure 8.9 On Receiving Updated Target while moving to previous target

- On pressing foot pedal, robot controller moves the robot to target position. When foot pedal is pressed, “Foot Pedal” indicator turns **green** as shown in Figure 8.10 and robot starts moving.



Figure 8.10 While waiting for foot pedal to be pressed to move the Robot

- If robot has moved to desired position, robot controller screen should look like Figure 8.11 where “Reached” indicator turns **Green**. Current robot mode changes to **MANUAL** and a message is displayed saying “Robot has reached to the target position”. At the same time, RadVision screen looks like Figure 8.12. Current mode has changed to **MANUAL** and current position is the same as target position.



Figure 8.11 On successfully reaching to the target position

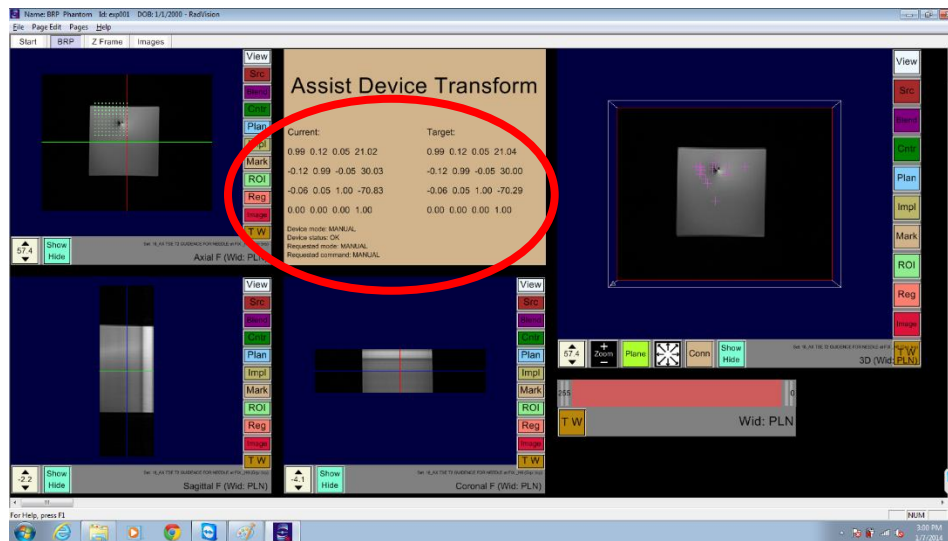


Figure 8.12 RadVision window when robot reaches to target position

### 8.2.2. Picking Targets by Markers

- In order to select a target by clicking on the image user should follow these instructions.
- Adding new marker: To add a new marker, click on “Mark” button and then click on “Ops” button which should load Figure 8.13.

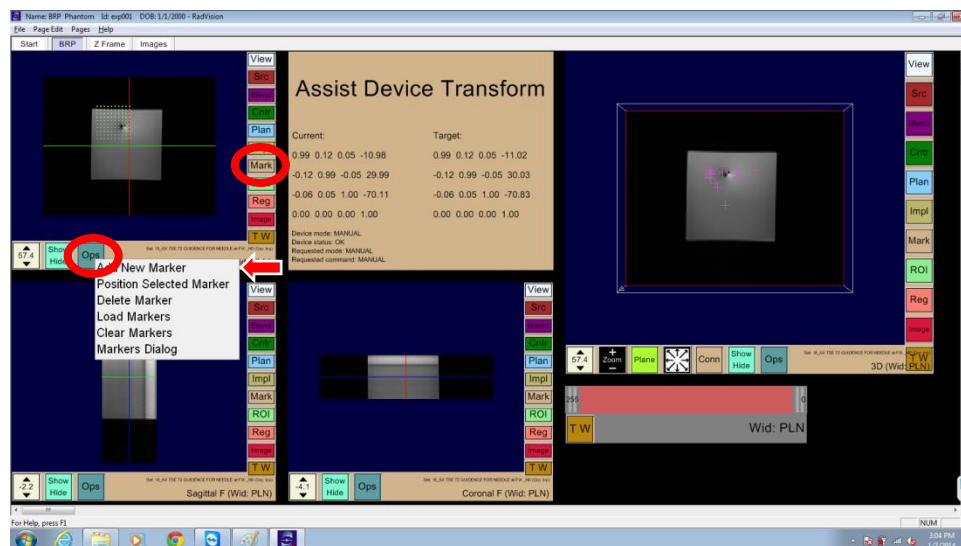


Figure 8.13 Menu options to add new marker

- Click on Add New Marker and right click on image where you want to add a new marker which will show Figure 8.14 to enter marker name along with current RAS position of the marker.

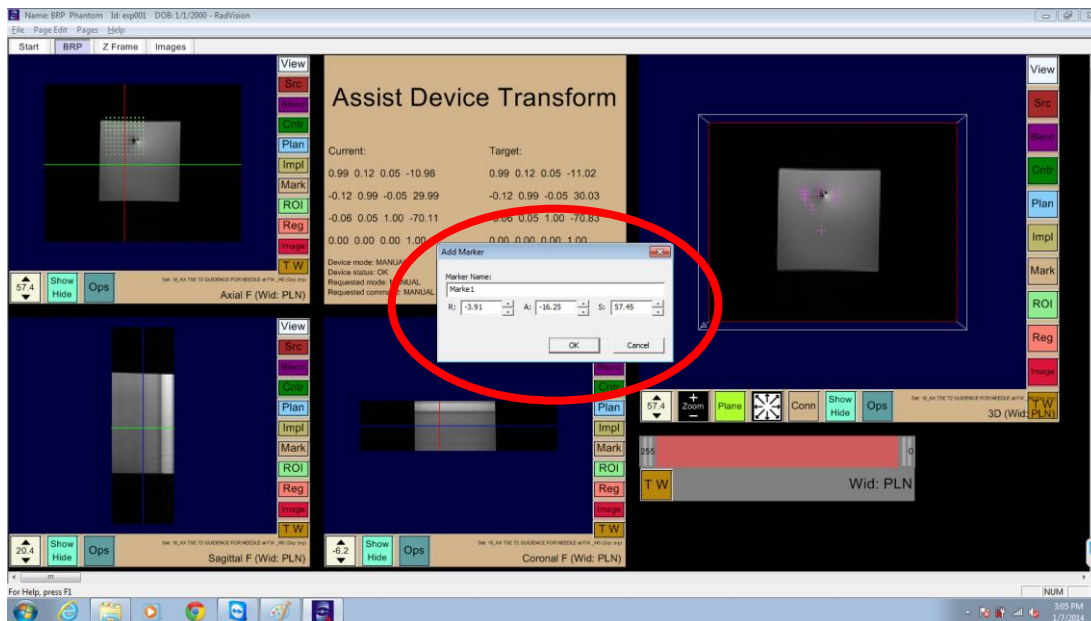


Figure 8.14 Pop-up to enter new Marker name and adjust RAS values

Enter the name and press OK. Then click on “Ops” button and it should show Figure 8.15.

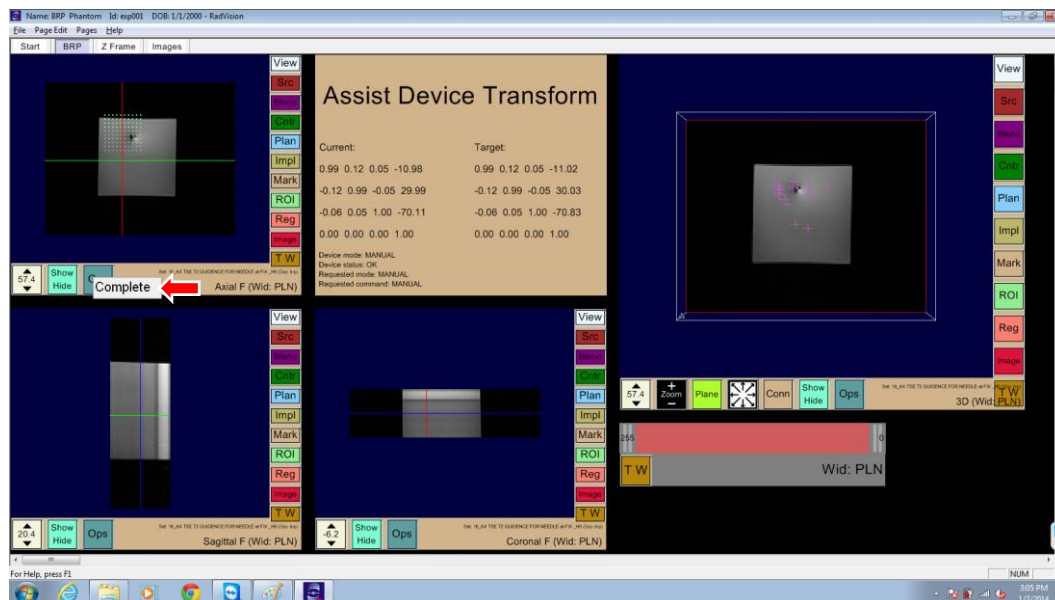


Figure 8.15 Menu option to complete new marker creation procedure

Click on Complete and that should add a new marker (target).

- Sending already existing marker as target to Assist Device: Again click on “Ops” button which should display Figure 8.16.

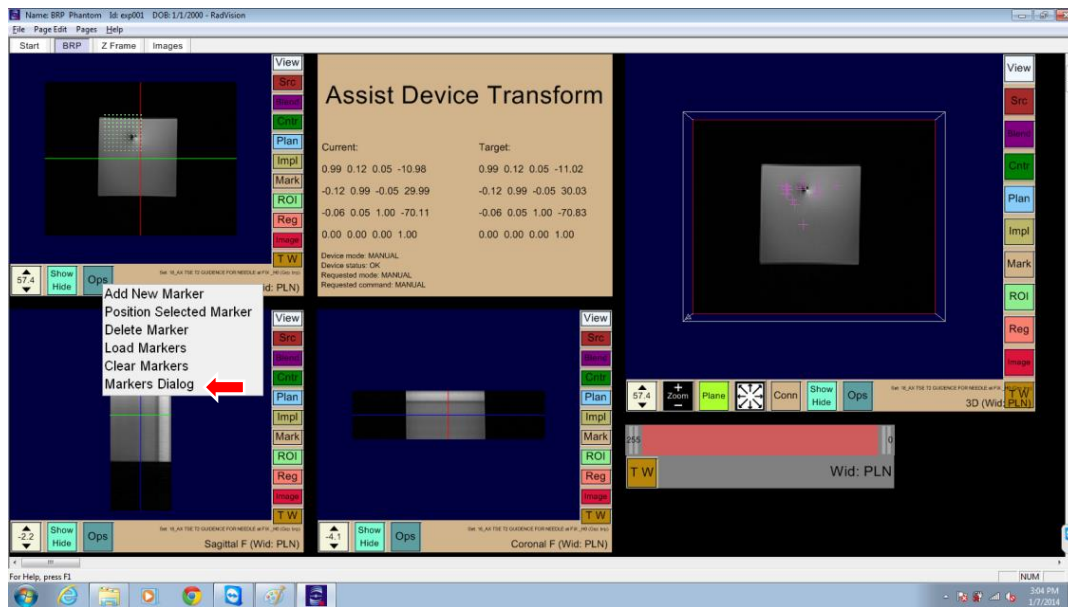


Figure 8.16 Menu option to load markers dialog

- Click on “Marker Dialog” menu item and that should load Figure 8.17 where all the existing markers are displayed. Select the marker you want to send to the robot controller.

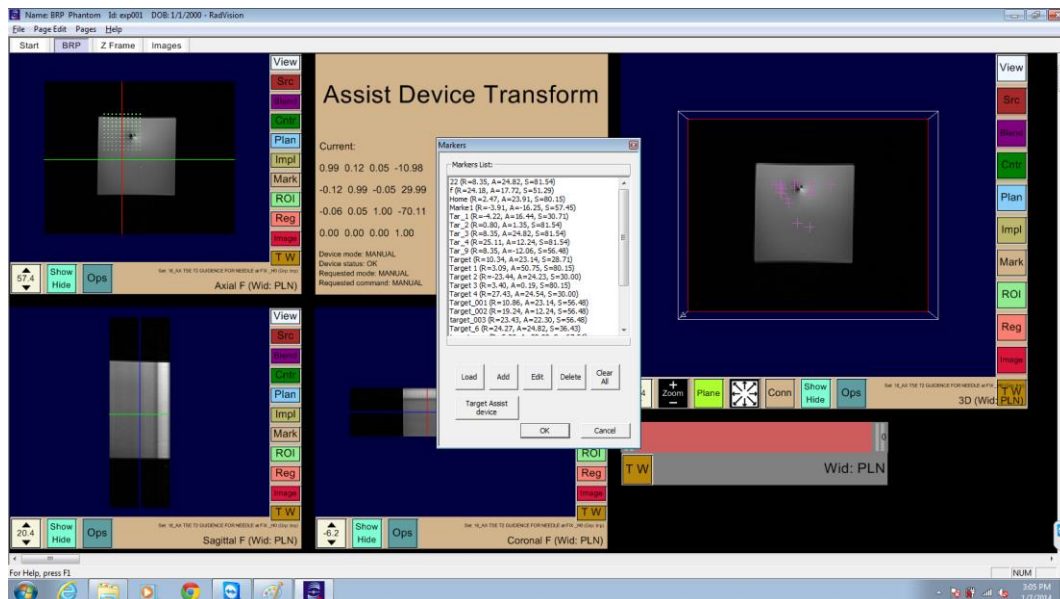


Figure 8.17 Pop-up displaying list of existing markers and command button to send target to robot control application

- Once you have selected the marker, click on “Target Assist Device” button which should load Figure 8.18.

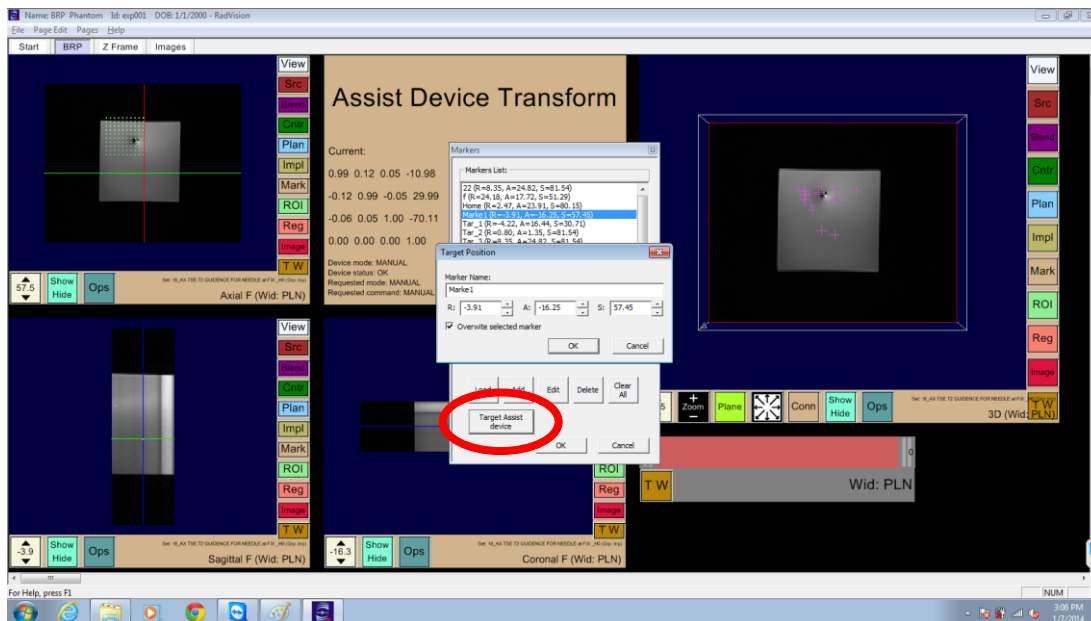


Figure 8.18 Marker edit window before sending the target to robot control application

- If you are sure about RAS values for the marker, press OK and that should send the target to the robot controller and robot controller should look like what is shown in Figure 8.6 in section 8.2.1 if target was valid. And RadVision should show Figure 8.19 if this was not the first target. User should retract the needle and click OK.

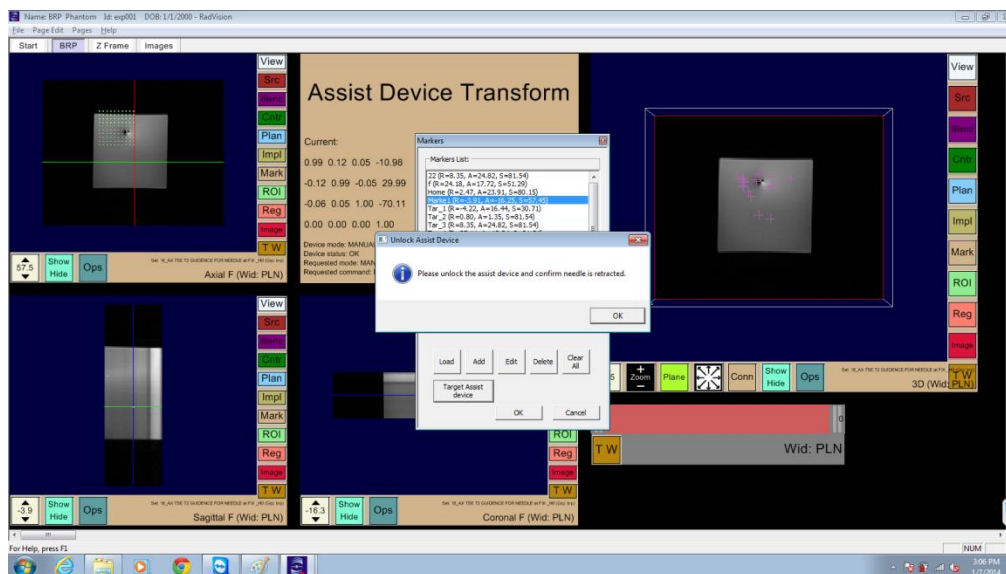


Figure 8.19 User confirmation pop-up to confirm needle retraction

- User should click on OK to move forward, it should load the Figure 8.20.



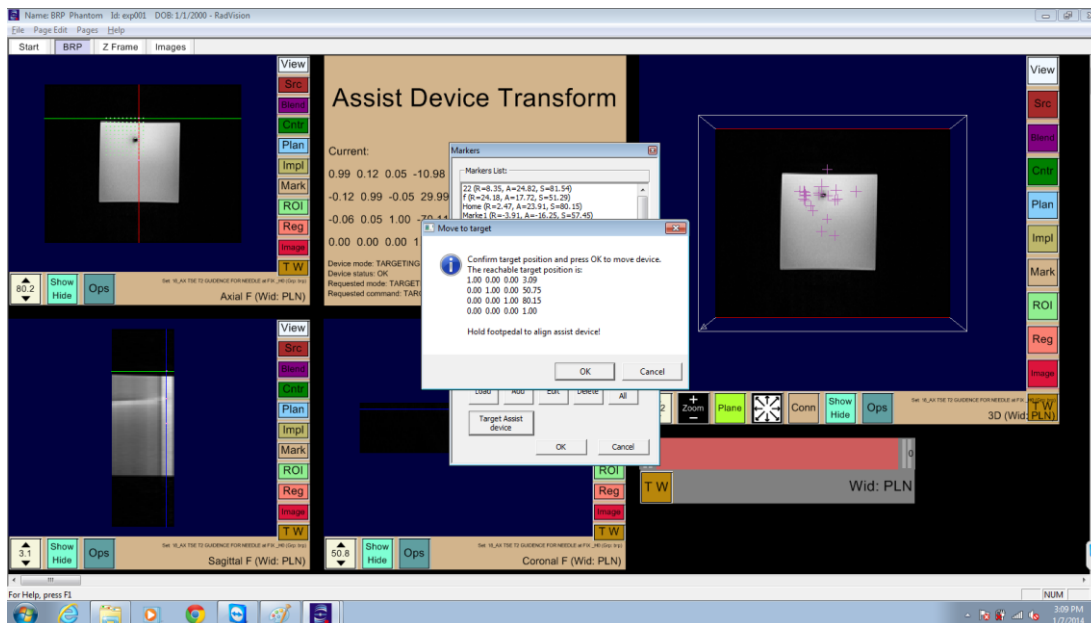


Figure 8.20 After sending valid marker to the robot control application

- Clicking OK will send MOVE\_TO\_TARGET command to the robot controller and that will follow same workflow as from Figure 8.6 in section 8.2.1.

### 8.2.3. Import Targets from File

This is usually the case when using RadVision with 3D Slicer next to each other.

- A target list is created and exported by 3D Slicer.
- In RadVision, on BRP tab, click on “Mark”, then “Ops” button which should display Figure 8.21.



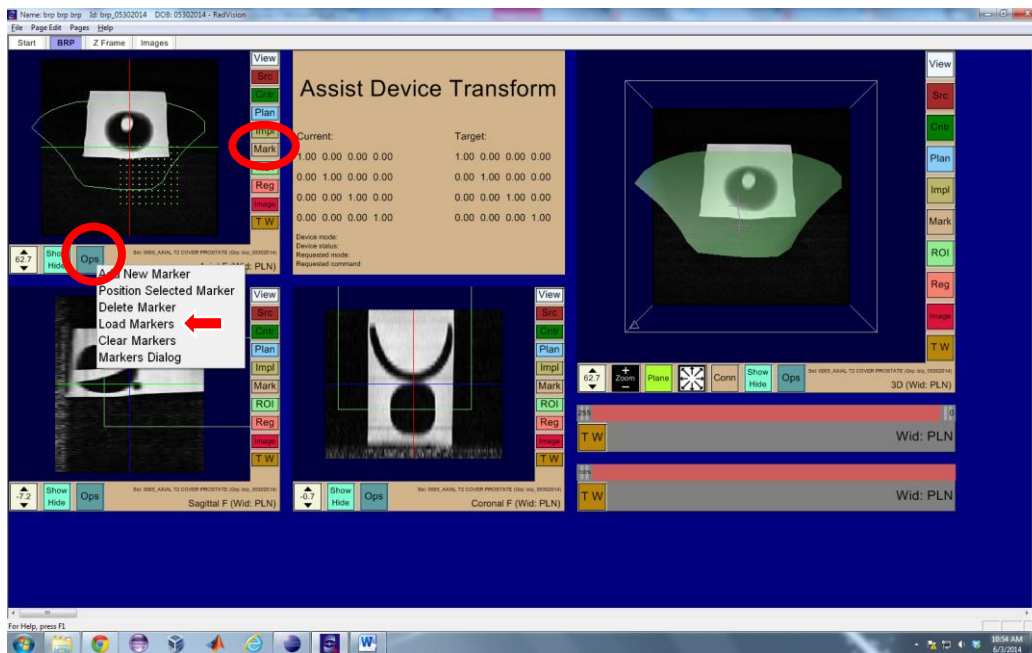


Figure 8.21 Load Markers

- Click on Load Markers to import the target from the exported file, like shown in Figure 8.22.

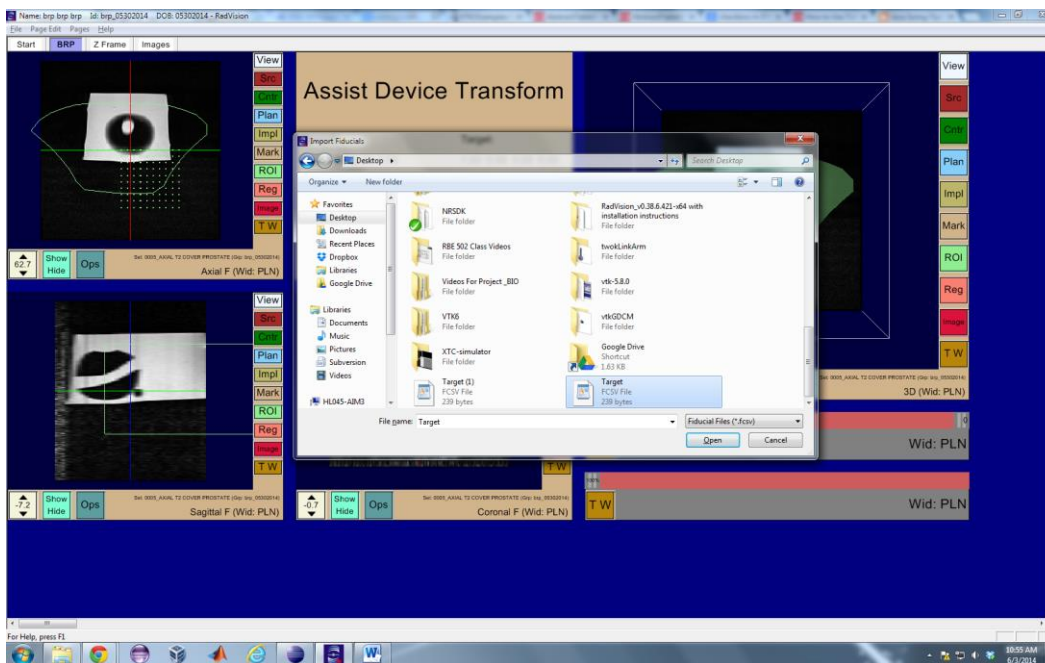


Figure 8.22 Choose desired marker file to load

- The rest of the work is similar to section 8.2.2 from Figure 8.17.

## 9. HARDWARE ERRORS AND RESOLUTIONS

### 9.1. Color of LEDs for motor drivers and their meaning

- BLUE:** Axis is at Target Position.
- YELLOW:** Axis has received Target position and is waiting for Foot Pedal to be pressed to move the Robot.
- GREEN:** Motor is running and encoder position is changing.
- RED:** Hardware Error. (Limit Switch or Stall Error)

### 9.2. Limit Error

While robot controller is ON and robot controller application is running, if any of the Limit Switches is unplugged accidentally or cable is broken, there is a limit error.

#### 9.2.1. Visualization

- Robot controller application will pop-up a message as shown in Figure 9.1.
- Motion Status LED on the robot controller turn to **RED** indicating hardware error as shown in Figure 9.2.

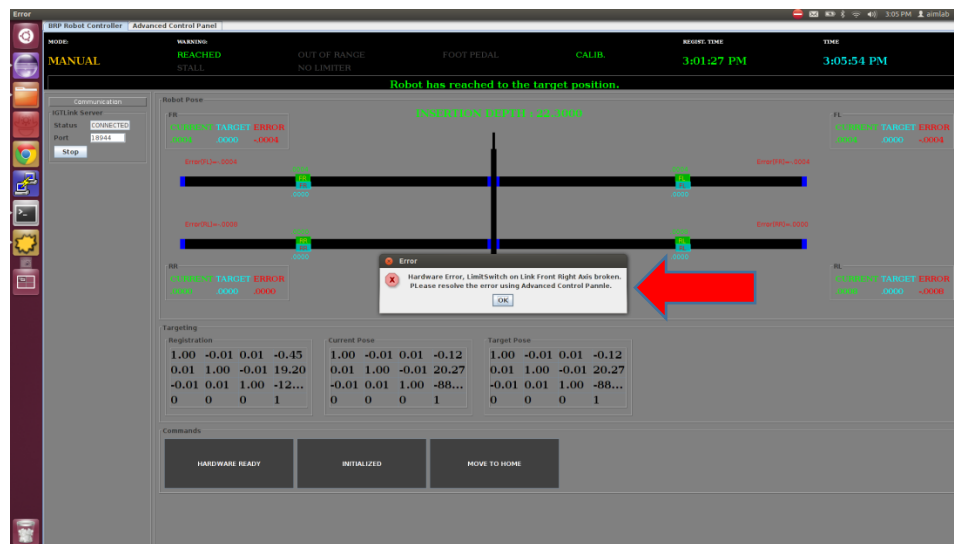


Figure 9.1 Pop-up showing Limit Switch Error

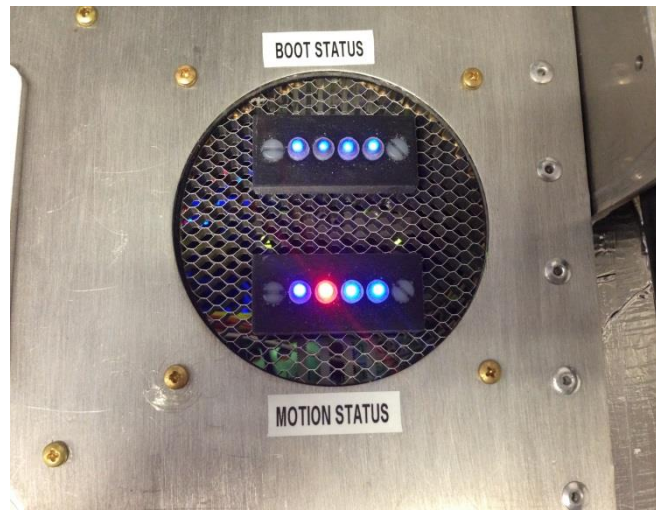


Figure 9.2 Motion Status LED Turns to **RED** on Limit Error

### 9.2.2. Resolving the limit error

- On clicking **OK** button, user interface will show visual indicator for the error as shown in Figure 9.3.



Figure 9.3 Indication of Limit Switch Error (**Orange** link bar with limit indicators turned to **Red**)

- Limit error can be cleared using Advanced Control Panel (refer to section 10).
- Once operator checks all the Limit switch connections and cables and finds that all connections look good, he/she should click on Clear Limit Error button and wait until error is cleared on the user interface and it appears as shown in Figure 9.4.

- Motion Status LEDs on the robot controller should turn to **BLUE** as shown in Figure 9.5.



Figure 9.4 After clearing the Limit Switch Error

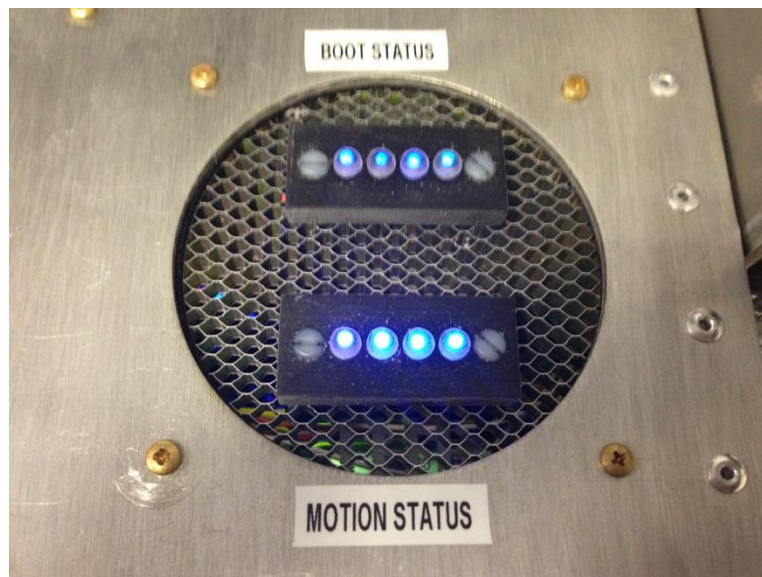


Figure 9.5 Motion Status LED Turns to **BLUE** on clearing Limit Error

### 9.3. Stall Error

While robot controller is ON and robot controller application is running, if any of the Encoder/Motor-Power connector is unplugged accidentally or cable is broken, there is a stall error.

#### 9.3.1. Visualization

- Robot controller application will pop-up a message as shown in Figure 9.6.
- On Stall error robot goes to BOOT\_UP mode as encoder positions are lost and without re-running the Homing procedure robot cannot be used for TARGETTING.
- Motion Status LED on the controller turns to **RED** as shown in Figure 9.7.

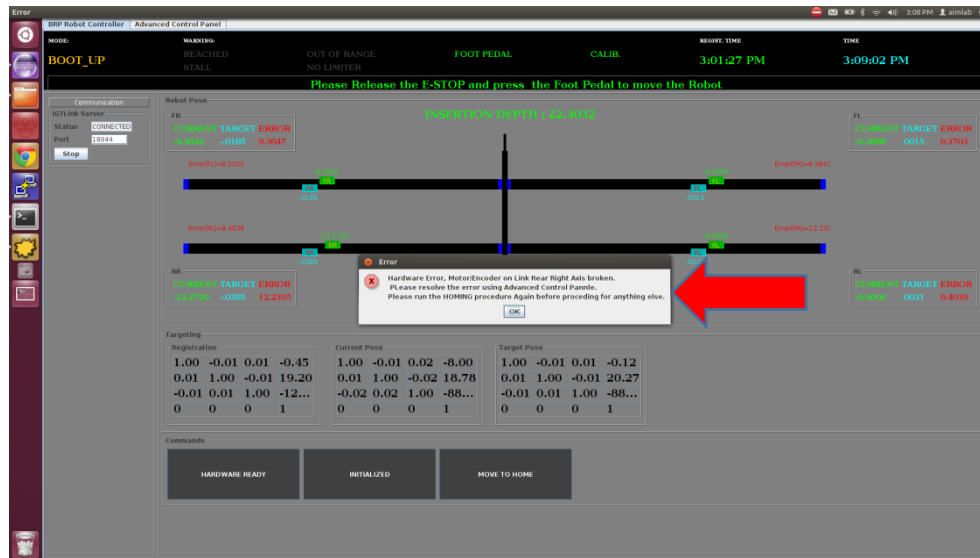


Figure 9.6 Pop-up showing Stall Error (Disconnected Encoder/Motor-Power cable)



Figure 9.7 Motion Status LED Turns to **RED** on Stall Error

- On clicking OK button, user interface will show visual indicator for the error as

shown in Figure 9.8.



Figure 9.8 Indication of Stall Switch Error (*Red link bar*)

### 9.3.2. Resolving the stall error

- Stall error can be cleared using Advanced Control Panel (refer to section 10).
- After operator has checked all the hardware connections and robot is ready, operator should click on “clear STALL Error” button and wait for user interface to update and the visual indicator turn to normal (BLACK color for the link bar) as shown in Figure 9.9.
- It can be seen that robot is in BOOT\_UP Mode so operator must run Homing procedure before proceeding for anything else.
- On clearing the Stall Error, Motion Status LEDs should turn to **BLUE** as shown in Figure 9.10.





Figure 9.9 After clearing the Stall Error

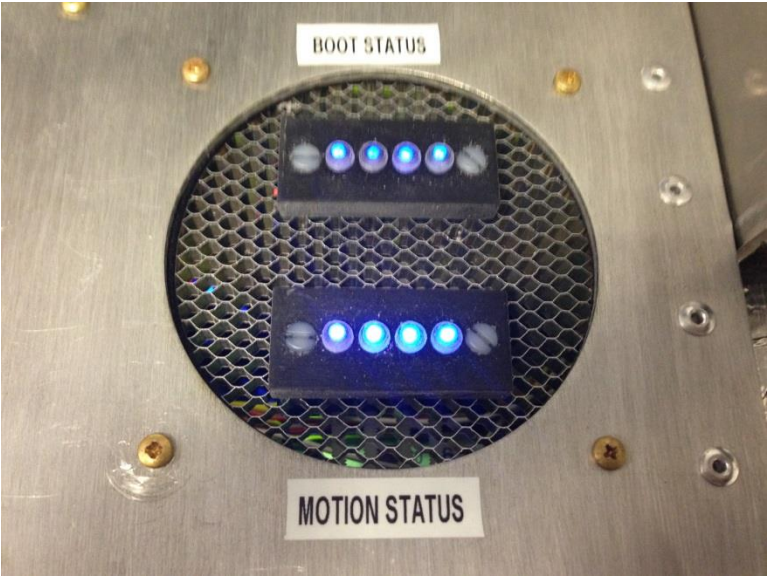


Figure 9.10 Motion Status LED Turns to **BLUE** on clearing Stall Error

## 10. ADVANCED CONTROL PANEL

Use password brp to get into the advanced control panel.

Figure 10.1 shows advanced Controller Panel and various functions which can be used in case of hardware error. Table 10.1 Button/Checkbox captions and functions they perform lists button captions and functions they perform.

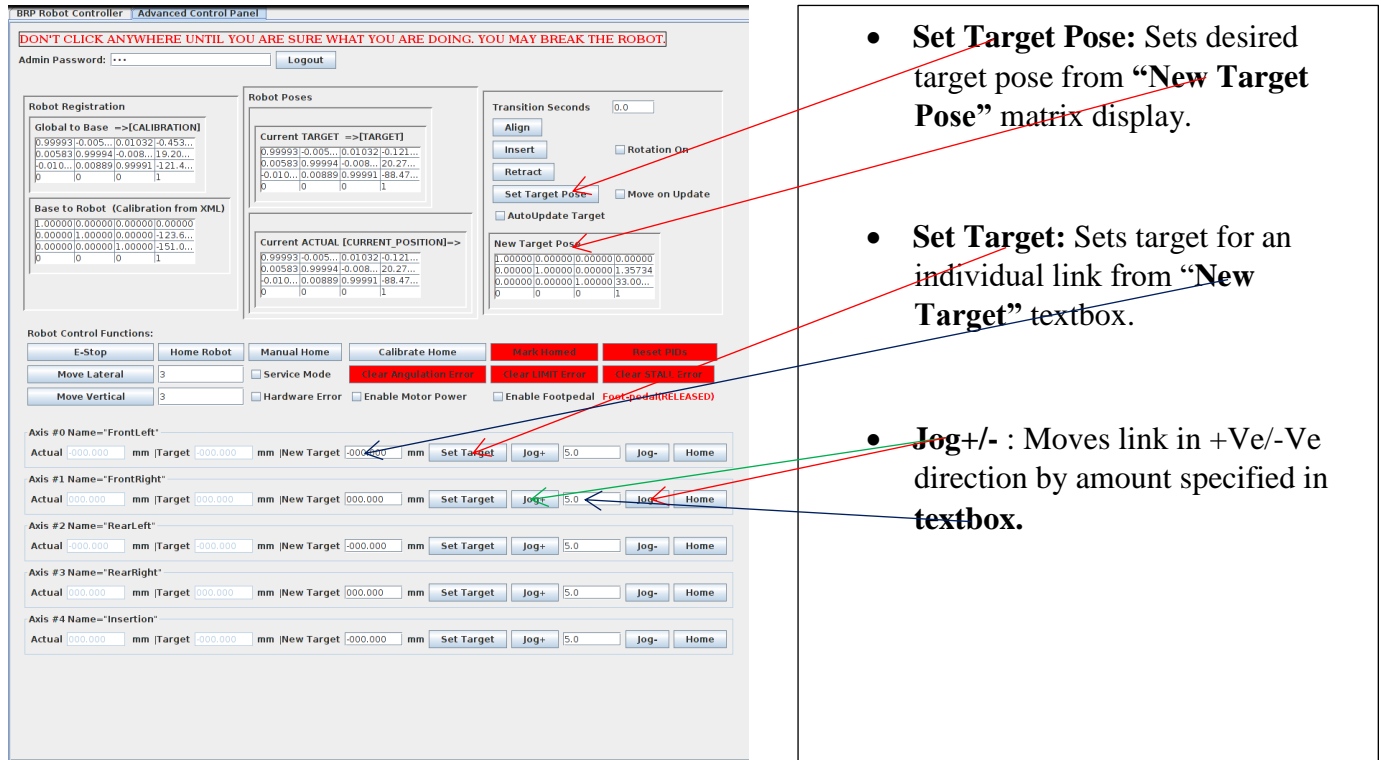


Figure 10.1 Advanced Controller User Interface

Table 10.1 Button/Checkbox captions and functions they perform

Button/Checkbox Caption	Functionality
E-Stop	Sends Kill-PID command, loses its effect on pressing foot-pedal. Not advised for use.
Home Robot	Same as “Initialize robot” on HUI, not advised to use from here.
Manual Home	Resets PIDs to Zero(0), not advised until one knows what it will do to controller.
Calibrate Home	Old procedure for precise homing procedure, no more required but left for future use if required, not advised for use.
Mark Homed	Marks robot Initialized, should never be used as this updates the controller state and can result in completely undesirable behavior.



Reset PIDs	Resets PID controllers to Zero(0)
Move Lateral	Undefined behavior, not advised for use.
Service Mode	Ignores RadVision workflow, not advised for any clinical case.
Clear Angulation Error	Just allows pop-up of angulation error if there was an angulation error and is yet not cleared. This should never be required until one of the axis went to wrong position due to electrical noise. After clearing this homing procedure should be run again. Caution: Robot does not go to BOOT_UP mode on this kind of error but operator should make sure that robot homing procedure is re-run.
Clear Limit Error	Clears Limit Error if it happened. Also, enables future pop-ups for the limit errors.
Clear Stall Error	Clears Stall error if it happened. Also, enables future pop-ups for the stall errors.
Move Vertical	Undefined functionality, not advised for use.
Hardware Error	Sets controller to be in hardware error (Limit Error). Not advised for use.
Enable Motor Power	Turns ON/OFF motor power. Not to be used until absolutely necessary.
Enable Footpedal	Enables/Disables foot pedal. Should never disable foot pedal as that would be a safety hazard.

## 11. LIST OF FIGURES

Figure 0.1 Put red bag before patient board .....	125
Figure 0.2 Put patient board over red bag .....	125
Figure 0.3 Put bedding on patient board .....	125
Figure 0.4 Tape the patient board .....	125
Figure 0.5 General Controller setup. Please refer to Figure 0.6 and Figure 1.2 for more details. ....	126
Figure 0.6 Medical air connection .....	126
Figure 0.7 Get the robot connected to the controller .....	126
Figure 0.8 Initialize the robot without draping and sterilized parts .....	126
Figure 0.9 Move in patient while homing the robot .....	127
Figure 0.10 Patient ready in bed .....	127
Figure 0.11 Push the patient through the scanner to the other side .....	127
Figure 0.12 Z-Frame in position .....	127
Figure 0.13 Move the robot in the room and tape the wire down.....	128
Figure 0.14 Drape the robot and push the front piece in.....	128
Figure 0.15 Tape both side of the drape to keep it organized.....	128
Figure 0.16 Lock the front piece.....	128
Figure 0.17 Move the cart close to the scanner.....	129
Figure 0.18 Push the robot in position until it hit the Z-Frame .....	129
Figure 0.19 Lock the robot in place with two screws .....	129
Figure 0.20 Robot Ready .....	129
Figure 1.1 Robot interface box .....	130
Figure 1.2 Robot controller box .....	131
Figure 2.1 User authentication page for Router .....	132
Figure 2.2 Port forwarding for DICOM push .....	133
Figure 2.3 Rad Vision Admin Login .....	133
Figure 2.4 Open Assist Device .....	134
Figure 2.5 Selet BRPBot.....	134
Figure 2.6 Change IP address .....	135
Figure 2.7 Open generic device .....	135
Figure 2.8 Select BRP_Bot .....	136
Figure 2.9 Reselect BRPBot .....	136
Figure 2.10 Update hospital data .....	137
Figure 2.11 Close and Reopen RadVision software .....	137
Figure 2.12 Exit from Admin software.....	137
Figure 3.1 Dialog to change file permissions to make directory content executable on Linux.....	138
Figure 3.2 JAVA application start up dialog with countdown timer .....	139
Figure 3.3 BOOT_UP mode, homing procedure is not yet executed .....	140
Figure 3.4 Hardware Test.....	140
Figure 3.5 Hardware Test Messages .....	141

Figure 3.6 Done with Hardware Test.....	142
Figure 3.7 Robot homing confirmation dialog.....	142
Figure 3.8 Homing procedure key steps .....	143
<i>Figure 3.9 START_UP mode, homing finished successfully.....</i>	<i>144</i>
Figure 4.1 RadVision start-up screen.....	145
Figure 4.2 RadVision on click of Open Patient option .....	145
Figure 4.3 Patient confirmation dialog on RadVision window .....	146
Figure 4.4 After loading the patient and successful connection to robot controller application .....	146
Figure 4.5 Error Dialog when connection error while connecting to robot control application.....	147
Figure 4.6 IGTLServer status changed to CONNECTED on RadVision connection .....	147
Figure 5.1 Starting listening to pushed dicom in RadVision .....	148
Figure 5.2 Select the treatment session if it is not selected beforehand.....	149
Figure 5.3 Check the "Use DICOM series Number and series description as image set name" .....	149
Figure 6.1 Z-Frame calculation window with Image Source selection pop-up .....	151
Figure 6.2 Z-Frame window with image list.....	152
Figure 6.3 Z-Frame window with loaded image.....	152
Figure 6.4 Sort z-frame images by S direction .....	153
Figure 6.5 Z-Frame window with menu options for calculating the registration matrix.....	153
Figure 6.6 Calculated calibration transform .....	154
Figure 7.1 Menu options to send manual z-frame from BRP window .....	156
Figure 7.2 Z-frame transform matrix to be sent to robot controller.....	156
Figure 7.3 RadVision after successfully sending CALIBRATION transform .....	157
Figure 7.4 Robot Control application after receiving valid CALIBRATION transform.....	158
Figure 8.1 Menu to select images for TARGETING.....	159
Figure 8.2 List of saved image sets.....	159
Figure 8.3 After loading desired image set .....	160
Figure 8.4 User confirmation to retract needle before sending new Target .....	160
Figure 8.5 Sending Target transform manually .....	161
Figure 8.6 After Robot Control Application received valid target .....	161
Figure 8.7 For sending MOVE_TO_TARGET request to robot control application .....	162
Figure 8.8 After receiving MOVE_TO_TARGET request from RadVision.....	163
Figure 8.9 On Receiving Updated Target while moving to previous target .....	164
Figure 8.10 While waiting for foot pedal to be pressed to move the Robot .....	165
Figure 8.11 On successfully reaching to the target position .....	165
Figure 8.12 RadVision window when robot reaches to target position .....	166
Figure 8.13 Menu options to add new marker .....	166
Figure 8.14 Pop-up to enter new Marker name and adjust RAS values .....	167
Figure 8.15 Menu option to complete new marker creation procedure .....	167
Figure 8.16 Menu option to load markers dialog.....	168
Figure 8.17 Pop-up displaying list of existing markers and command button to send target to robot	

control application.....	168
Figure 8.18 Marker edit window before sending the target to robot control application .....	169
Figure 8.19 User confirmation pop-up to confirm needle retraction .....	169
Figure 8.20 After sending valid marker to the robot control application .....	170
Figure 8.21 Load Markers.....	171
Figure 8.22 Choose desired marker file to load .....	171
Figure 9.1 Pop-up showing Limit Switch Error.....	172
Figure 9.2 Motion Status LED Turns to RED on Limit Error .....	173
Figure 9.3 Indication of Limit Switch Error (Orange link bar with limit indicators turned to Red) ....	173
Figure 9.4 After clearing the Limit Switch Error.....	174
Figure 9.5 Motion Status LED Turns to BLUE on clearing Limit Error.....	174
Figure 9.6 Pop-up showing Stall Error (Disconnected Encoder/Motor-Power cable) .....	175
Figure 9.7 Motion Status LED Turns to RED on Stall Error.....	175
Figure 9.8 Indication of Stall Switch Error (Red link bar) .....	176
Figure 9.9 After clearing the Stall Error .....	177
Figure 9.10 Motion Status LED Turns to BLUE on clearing Stall Error .....	177
Figure 10.1 Advanced Controller User Interface.....	178

This is the End of the Document

# Bibliography

- [1] Andriy Fedorov, Reinhard Beichel, Jayashree Kalpathy-Cramer, Julien Finet, Jean-Christophe Fillion-Robin, Sonia Pujol, Christian Bauer, Dominique Jennings, Fiona Fennessy, Milan Sonka, et al. 3d slicer as an image computing platform for the quantitative imaging network. *Magnetic resonance imaging*, 30(9):1323–1341, 2012.
- [2] Rahmi Onur, Peter J Littrup, J Edson Pontes, and Fernando J Bianco. Contemporary impact of transrectal ultrasound lesions for prostate cancer detection. *The Journal of urology*, 172(2):512–514, 2004.
- [3] Kiarash Shahlaie, Paul S Larson, and Philip A Starr. Intraoperative computed tomography for deep brain stimulation surgery: technique and accuracy assessment. *Operative Neurosurgery*, 68:ons114–ons124, 2011.
- [4] Helen Xu, Andras Lasso, Siddharth Vikal, Peter Guion, Axel Krieger, Aradhana Kaushal, Louis Whitcomb, and Gabor Fichtinger. Mri-guided robotic prostate biopsy: a clinical accuracy validation. *Medical Image Computing and Computer-Assisted Intervention–MICCAI 2010*, pages 383–391, 2010.
- [5] Garnette R Sutherland, Isabelle Latour, and Alexander D Greer. Integrating an image-guided robot with intraoperative mri. *IEEE engineering in medicine and biology magazine*, 27(3):59–65, 2008.
- [6] Roberto Blanco Sequeiros, Risto Ojala, Juho Kariniemi, Jukka Perälä, Jaakko Niinimäki, Heli Reinikainen, and Osmo Tervonen. Mr-guided interventional procedures: a review. *Acta Radiologica*, 46(6):576–586, 2005.
- [7] Nikolaos V Tsekos, Azadeh Khanicheh, Eftychios Christoforou, and Constantinos Mavroidis. Magnetic resonance-compatible robotic and mechatronics systems for image-guided interventions and rehabilitation: a review study. *Annu. Rev. Biomed. Eng.*, 9:351–387, 2007.
- [8] Osamu Ukimura. Image-guided surgery in minimally invasive urology. *Current opinion in urology*, 20(2):136–140, 2010.
- [9] American cancer society: key statistics about prostate cancer.

- [10] Gary J Kelloff, Peter Choyke, and Donald S Coffey. Challenges in clinical prostate cancer: role of imaging. *AJR. American journal of roentgenology*, 192(6):1455, 2009.
- [11] Misop Han, Doyoung Chang, Chunwoo Kim, Brian J Lee, Yihe Zuo, Hyung-Joo Kim, Doru Petrisor, Bruce Trock, Alan W Partin, Ronald Rodriguez, et al. Geometric evaluation of systematic transrectal ultrasound guided prostate biopsy. *The Journal of urology*, 188(6):2404–2409, 2012.
- [12] Hedvig Hricak, Peter L Choyke, Steven C Eberhardt, Steven A Leibel, and Peter T Scardino. Imaging prostate cancer: A multidisciplinary perspective 1. *Radiology*, 243(1):28–53, 2007.
- [13] Russell H Taylor, Arianna Menciassi, Gabor Fichtinger, and Paolo Dario. Medical robotics and computer-integrated surgery. In *Springer handbook of robotics*, pages 1199–1222. Springer, 2008.
- [14] Kyle B Reed, Ann Majewicz, Vinutha Kallem, Ron Alterovitz, Ken Goldberg, Noah J Cowan, and Allison M Okamura. Robot-assisted needle steering. *IEEE robotics & automation magazine*, 18(4):35–46, 2011.
- [15] Johnathan A Engh, G Podnar, D Kondziolka, and Cameron N Riviere. Toward effective needle steering in brain tissue. In *Engineering in Medicine and Biology Society, 2006. EMBS’06. 28th Annual International Conference of the IEEE*, pages 559–562. IEEE, 2006.
- [16] Ken Masamune, Etsuko Kobayashi, Yoshitaka Masutani, Makoto Suzuki, Takeyoshi Dohi, Hiroshi Iseki, and Kintomo Takakura. Development of an mri-compatible needle insertion manipulator for stereotactic neurosurgery. *Journal of Image Guided Surgery*, 1(4):242–248, 1995.
- [17] Gregory S Fischer, Iulian Iordachita, Csaba Csoma, Junichi Tokuda, Simon P DiMaio, Clare M Tempany, Noby Hata, and Gabor Fichtinger. MRI-compatible pneumatic robot for transperineal prostate needle placement. *IEEE/ASME Transactions on Mechatronics*, 13(3), 2008.
- [18] Dan Stoianovici, Chunwoo Kim, Govindarajan Srimathveeravalli, Peter Sebrecht, Doru Petrisor, Jonathan Coleman, Stephen B Solomon, and Hedvig Hricak. MRI-safe robot for endorectal prostate biopsy. *IEEE/ASME Transactions on Mechatronics*, (99):1–11, 2013.
- [19] Dan Stoianovici, Danny Song, Doru Petrisor, Daniel Ursu, Dumitru Mazilu, Michael Muntener, Michael Mutener, Michael Schar, and Alexandru Patriciu. MRI Stealth robot for prostate interventions. *Minim Invasive Ther Allied Technol*, 16(4):241–248, 2007.

- [20] Sang-Eun Song, Nobuhiko Hata, Iulian Iordachita, Gabor Fichtinger, Clare Tempany, and Junichi Tokuda. A workspace-orientated needle-guiding robot for 3t mri-guided transperineal prostate intervention: evaluation of in-bore workspace and mri compatibility. *The International Journal of Medical Robotics and Computer Assisted Surgery*, 9(1):67–74, 2013.
- [21] Alexandra Krieger, Sang-Eun Song, N Bongjoon Cho, Iulian I Iordachita, Peter Guion, Gabor Fichtinger, and Louis L Whitcomb. Development and evaluation of an actuated mri-compatible robotic system for mri-guided prostate intervention. *Mechatronics, IEEE/ASME Transactions on*, 18(1):273–284, 2013.
- [22] Derya Yakar, Martijn G. Schouten, Dennis G. H. Bosboom, Jelle O. Barentsz, Tom W. J. Scheenen, and Jurgen J. Futterer. Feasibility of a pneumatically actuated MR-compatible robot for transrectal prostate biopsy guidance. *Radiology*, 260(1):241–247, 2011.
- [23] Stephan Zangos, Andreas Melzer, Katrin Eichler, Cyrus Sadighi, Axel Thallhammer, Boris Bodelle, Renate Wolf, Tatjana Gruber-Rouh, Dirk Proschek, Renate Hammerstingl, et al. Mr-compatible assistance system for biopsy in a high-field-strength system: initial results in patients with suspicious prostate lesions. *Radiology*, 259(3):903–910, 2011.
- [24] Gaurie Tilak, Kemal Tuncali, Sang-Eun Song, Junichi Tokuda, Olutayo Olu-biyi, Fiona Fennessy, Andriy Fedorov, Tobias Penzkofer, Clare Tempany, and Nobuhiko Hata. 3t mr-guided in-bore transperineal prostate biopsy: A comparison of robotic and manual needle-guidance templates. *Journal of Magnetic Resonance Imaging*, 2014.
- [25] Roger Gassert, Roland Moser, Etienne Burdet, and Hannes Bleuler. Mri/fmri-compatible robotic system with force feedback for interaction with human motion. *Mechatronics, IEEE/ASME Transactions on*, 11(2):216–224, 2006.
- [26] Michiel R Van den Bosch, Maaïke R Moman, Marco Van Vulpen, Jan J Battermann, Ed Duiveman, Leonard J van Schelven, Hendrik de Leeuw, Jan JW Lagendijk, and Marinus A Moerland. Mri-guided robotic system for transperineal prostate interventions: proof of principle. *Physics in medicine and biology*, 55(5):N133, 2010.
- [27] Yue Chen, Christopher D Mershon, and Zion Tsz Ho Tse. A 10-mm mr-conditional unidirectional pneumatic stepper motor. *IEEE/ASME Transactions on Mechatronics*, 20(2):782–788, 2015.
- [28] Dan Stoianovici, Alexandru Patriciu, Doru Petrisor, Dumitru Mazilu, and Louis Kavoussi. A new type of motor: Pneumatic step motor. *Mechatronics, IEEE/ASME Transactions on*, 12(1):98–106, 2007.

- [29] Martijn G Schouten, Janneke Ansems, W Klaas Jan Renema, Dennis Bosboom, Tom WJ Scheenen, and Jurgen J Fütterer. The accuracy and safety aspects of a novel robotic needle guide manipulator to perform transrectal prostate biopsies. *Medical physics*, 37(9):4744–4750, 2010.
- [30] Stephan Zangos, Christopher Herzog, Katrin Eichler, Renate Hammerstingl, Andreas Lukoschek, Stefanie Guthmann, Bernd Gutmann, Uwe Joseph Schoepf, Phillip Costello, and Thomas J Vogl. Mr-compatible assistance system for punction in a high-field system: device and feasibility of transgluteal biopsies of the prostate gland. *Eur Radiol*, 17(4):1118–1124, Apr 2007.
- [31] Sang-Eun Song, Junichi Tokuda, Kemal Tuncali, Clare M Tempany, Enxia Zhang, and Nobuhiko Hata. Development and preliminary evaluation of a motorized needle guide template for mri-guided targeted prostate biopsy. *Biomedical Engineering, IEEE Transactions on*, 60(11):3019–3027, 2013.
- [32] Robert C Susil, Cynthia Mard, Axel Krieger, Jonathan A Coleman, Kevin Camphausen, Peter Choyke, Gabor Fichtinger, Louis L Whitcomb, C. Norman Coleman, and Ergin Atalar. Transrectal prostate biopsy and fiducial marker placement in a standard 1.5t magnetic resonance imaging scanner. *J Urol*, 175(1):113–120, Jan 2006.
- [33] Derya Yakar, Martijn G Schouten, Dennis GH Bosboom, Jelle O Barentsz, Tom WJ Scheenen, and Jurgen J Fütterer. Feasibility of a pneumatically actuated mr-compatible robot for transrectal prostate biopsy guidance. *Radiology*, 260(1):241–247, 2011.
- [34] Haytham Elhawary, Zion Tsz Ho Tse, Abbi Hamed, Marc Rea, Brian L Davies, and Michael U Lamperth. The case for MR-compatible robotics: a review of the state of the art. *The international journal of medical robotics and computer assisted surgery*, 4(2):105–113, 2008.
- [35] Jurgen J Fütterer, Sarthak Misra, and Katarzyna J Macura. MRI of the prostate: potential role of robots. *Imaging*, 2(5):583–592, 2010.
- [36] Roger Gassert, Akio Yamamoto, Dominique Chapuis, Ludovic Dovat, Hannes Bleuler, and Etienne Burdet. Actuation methods for applications in mr environments. *Concepts in Magnetic Resonance Part B: Magnetic Resonance Engineering*, 29(4):191, 2006.
- [37] Ann Majewicz, Joshua J Siegel, Andrew A Stanley, and Allison M Okamura. Design and evaluation of duty-cycling steering algorithms for robotically-driven steerable needles. In *Robotics and Automation (ICRA), 2014 IEEE International Conference on*, pages 5883–5888. IEEE, 2014.



- [38] Kyle B Reed, Vinutha Kallem, Ron Alterovitz, Ken Goldbergxz, Allison M Okamura, and Noah J Cowan. Integrated planning and image-guided control for planar needle steering. In *Biomedical Robotics and Biomechatronics, 2008. BioRob 2008. 2nd IEEE RAS & EMBS International Conference on*, pages 819–824. IEEE, 2008.
- [39] Daniel Glozman and Moshe Shoham. Image-guided robotic flexible needle steering. *IEEE Transactions on Robotics*, 23(3):459–467, 2007.
- [40] Momen Abayazid, Pedro Moreira, Navid Shahriari, Sachin Patil, Ron Alterovitz, and Sarthak Misra. Ultrasound-guided three-dimensional needle steering in biological tissue with curved surfaces. *Medical engineering & physics*, 37(1):145–150, 2015.
- [41] Pedro Moreira, Gert van de Steeg, Ferdi van der Heijden, Jurgen J Fütterer, and Sarthak Misra. A preliminary evaluation of a flexible needle steering algorithm using magnetic resonance images as feedback. In *Biomedical Robotics and Biomechatronics (2014 5th IEEE RAS & EMBS International Conference on*, pages 314–319. IEEE, 2014.
- [42] Pierre E Dupont, Jesse Lock, Brandon Itkowitz, and Evan Butler. Design and control of concentric-tube robots. *IEEE Transactions on Robotics*, 26(2):209–225, 2010.
- [43] Hao Su, Diana C Cardona, Weijian Shang, Alexander Camilo, Gregory A Cole, D Caleb Rucker, Robert J Webster, and Gregory S Fischer. A mri-guided concentric tube continuum robot with piezoelectric actuation: a feasibility study. In *Robotics and Automation (ICRA), 2012 IEEE International Conference on*, pages 1939–1945. IEEE, 2012.
- [44] Robert J Webster III, Joseph M Romano, and Noah J Cowan. Mechanics of precurved-tube continuum robots. *IEEE Transactions on Robotics*, 25(1):67–78, 2009.
- [45] Thomas R Wedlick and Allison M Okamura. Characterization of pre-curved needles for steering in tissue. In *Engineering in Medicine and Biology Society, 2009. EMBC 2009. Annual International Conference of the IEEE*, pages 1200–1203. IEEE, 2009.
- [46] Sarthak Misra, Kyle B Reed, Benjamin W Schafer, KT Ramesh, and Allison M Okamura. Mechanics of flexible needles robotically steered through soft tissue. *The International journal of robotics research*, 2010.
- [47] Davneet S Minhas, Johnathan A Engh, Michele M Fenske, and Cameron N Riviere. Modeling of needle steering via duty-cycled spinning. In *Engineering*

*in Medicine and Biology Society, 2007. EMBS 2007. 29th Annual International Conference of the IEEE*, pages 2756–2759. IEEE, 2007.

- [48] Ron Alterovitz, Michael Branicky, and Ken Goldberg. Motion planning under uncertainty for image-guided medical needle steering. *The International journal of robotics research*, 27(11-12):1361–1374, 2008.
- [49] Simon P DiMaio and Septimiu E Salcudean. Needle steering and motion planning in soft tissues. *IEEE Transactions on Biomedical Engineering*, 52(6):965–974, 2005.
- [50] Zipi Neubach and Moshe Shoham. Ultrasound-guided robot for flexible needle steering. *IEEE Transactions on Biomedical Engineering*, 57(4):799–805, 2010.
- [51] Momen Abayazid, Gustaaf J Vrooijink, Sachin Patil, Ron Alterovitz, and Sarthak Misra. Experimental evaluation of ultrasound-guided 3d needle steering in biological tissue. *International journal of computer assisted radiology and surgery*, 9(6):931–939, 2014.
- [52] Troy K Adebar, Ashley E Fletcher, and Allison M Okamura. 3-d ultrasound-guided robotic needle steering in biological tissue. *IEEE Transactions on Biomedical Engineering*, 61(12):2899–2910, 2014.
- [53] Gustaaf J Vrooijink, Momen Abayazid, Sachin Patil, Ron Alterovitz, and Sarthak Misra. Needle path planning and steering in a three-dimensional non-static environment using two-dimensional ultrasound images. *The International journal of robotics research*, 33(10):1361–1374, 2014.
- [54] Pedro Moreira, Sachin Patil, Ron Alterovitz, and Sarthak Misra. Needle steering in biological tissue using ultrasound-based online curvature estimation. In *Robotics and Automation (ICRA), 2014 IEEE International Conference on*, pages 4368–4373. IEEE, 2014.
- [55] Pedro Moreira, Momen Abayazid, and Sarthak Misra. Towards physiological motion compensation for flexible needle interventions. In *Intelligent Robots and Systems (IROS), 2015 IEEE/RSJ International Conference on*, pages 831–836. IEEE, 2015.
- [56] Hao Su, Weijian Shang, Gregory A Cole, Kevin Harrington, and Gregory S Fischer. Haptic system design for mri-guided needle based prostate brachytherapy. In *Haptics Symposium, 2010 IEEE*, pages 483–488. IEEE, 2010.
- [57] R. Seifabadi, I Iordachita, and G. Fichtinger. Design of a teleoperated needle steering system for MRI-guided prostate interventions. In *IEEE International Conference on Biomedical Robotics and Biomechatronics (BioRob)*, pages 793–798, Rome, Italy, June 2012.

- [58] Alireza M Mohammadi and Jason L Schroeder. Laser interstitial thermal therapy in treatment of brain tumors—the neuroplate system. *Expert review of medical devices*, 11(2):109–119, 2014.
- [59] Paul S Larson, Philip A Starr, Geoffrey Bates, Lisa Tansey, R Mark Richardson, and Alastair J Martin. An optimized system for interventional mri guided stereotactic surgery: preliminary evaluation of targeting accuracy. *Neurosurgery*, 70(OPERATIVE):ons95, 2012.
- [60] David B Comber, Diana Cardona, RJ Webster III, and Eric J Barth. Precision pneumatic robot for mri-guided neurosurgery. *ASME J. Med. Dev*, 6(1):017587, 2012.
- [61] Mingyen Ho, Alan B McMillan, J Marc Simard, Rao Gullapalli, and Jaydev P Desai. Toward a meso-scale sma-actuated mri-compatible neurosurgical robot. *IEEE Transactions on Robotics*, 28(1):213–222, 2012.
- [62] Cyrus Raoufi, Andrew A Goldenberg, and Walter Kucharczyk. A new hydraulically/pneumatically actuated mr-compatible robot for mri-guided neurosurgery. In *Bioinformatics and Biomedical Engineering, 2008. ICBBE 2008. The 2nd International Conference on*, pages 2232–2235. IEEE, 2008.
- [63] Gregory S. Fischer, Axel Krieger, Iulian Iordachita, Csaba Csoma, Louis L. Whitcomb, and Gabor Fichtinger. MRI compatibility of robot actuation techniques - a comparative study. *Int Conf Med Image Comput Comput Assist Interv*, Sept. 2008.
- [64] Gang Li, Hao Su, Gregory A Cole, Weijian Shang, Kevin Harrington, Alex Camilo, Julie G Pilitsis, and Gregory S Fischer. Robotic system for mri-guided stereotactic neurosurgery. *IEEE Transactions on Biomedical Engineering*, 62(4):1077–1088, 2015.
- [65] Hao Su, Weijian Shang, Gregory Cole, Gang Li, Kevin Harrington, Alexander Camilo, Junichi Tokuda, Clare M Tempany, Nobuhiko Hata, and Gregory S Fischer. Piezoelectrically actuated robotic system for MRI-guided prostate percutaneous therapy. *Mechatronics, IEEE/ASME Transactions (In Press)*, 2014.
- [66] Gang Li, Hao Su, Weijian Shang, Junichi Tokuda, Nobuhiko Hata, Clare M Tempany, and Gregory S Fischer. A fully actuated robotic assistant for mri-guided prostate biopsy and brachytherapy. In *SPIE Medical Imaging*, pages 867117–867117. International Society for Optics and Photonics, 2013.
- [67] Andriy Fedorov, Kemal Tuncali, Fiona M Fennessy, Junichi Tokuda, Nobuhiko Hata, William M Wells, Ron Kikinis, and Clare M Tempany. Image registration for targeted mri-guided transperineal prostate biopsy. *Journal of Magnetic Resonance Imaging*, 36(4):987–992, 2012.

- [68] Junichi Tokuda, Gregory S Fischer, Xenophon Papademetris, Ziv Yaniv, Luis Ibanez, Patrick Cheng, Haiying Liu, Jack Blevins, Jumpei Arata, Alexandra J Golby, et al. Openigtlink: an open network protocol for image-guided therapy environment. *The International Journal of Medical Robotics and Computer Assisted Surgery*, 5(4):423–434, 2009.
- [69] Junichi Tokuda, Kemal Tuncali, Iulian Iordachita, Sang-Eun Song, Andriy Fedorov, Sota Oguro, Andras Lasso, Fiona M Fennessy, Clare M Tempany, and Nobuhiko Hata. In-bore setup and software for 3t mri-guided transperineal prostate biopsy. *Physics in medicine and biology*, 57(18):5823, 2012.
- [70] Sohrab Eslami, Weijian Shang, Gang Li, Nirav Patel, Gregory S Fischer, Junichi Tokuda, Nobuhiko Hata, Clare M Tempany, and Iulian Iordachita. In-bore prostate transperineal interventions with an mri-guided parallel manipulator: system development and preliminary evaluation. *The International Journal of Medical Robotics and Computer Assisted Surgery*, 2015.
- [71] Junichi Tokuda, Sang-Eun Song, Kemal Tuncali, Clare Tempany, and Nobuhiko Hata. Configurable automatic detection and registration of fiducial frames for device-to-image registration in mri-guided prostate interventions. In *Medical Image Computing and Computer-Assisted Intervention–MICCAI 2013*, pages 355–362. Springer, 2013.
- [72] Neuron robotics: Bolwer protocol.
- [73] Guillaume Ploussard, Jonathan I Epstein, Rodolfo Montironi, Peter R Carroll, Manfred Wirth, Marc-Oliver Grimm, Anders S Bjartell, Francesco Montorsi, Stephen J Freedland, Andreas Erbersdobler, et al. The contemporary concept of significant versus insignificant prostate cancer. *European urology*, 60(2):291–303, 2011.
- [74] Thomas A Stamey, FS Freiha, JE McNeal, EA Redwine, AS Whittemore, and HP Schmid. Localized prostate cancer. *Cancer*, 71(S3):933–38, 1993.
- [75] Weijian Shang, Hao Su, Gang Li, and Gregory S Fischer. Teleoperation system with hybrid pneumatic-piezoelectric actuation for mri-guided needle insertion with haptic feedback. In *Intelligent Robots and Systems (IROS), 2013 IEEE/RSJ International Conference on*, pages 4092–4098. IEEE, 2013.
- [76] Meng Li, Berk Gonenc, Kiyoun Kim, Weijian Shang, and Iulian Iordachita. Development of an mri-compatible needle driver for in-bore prostate biopsy. In *17th International Conference on Advanced Robotics, ICAR*, 2015.
- [77] Marek Wartenberg, Niravkumar Patel, Gang Li, and Gregory S Fischer. Towards synergistic control of hands-on needle insertion with automated needle steering for mri-guided prostate interventions. In *Engineering in Medicine and*

*Biology Society (EMBC), 2016 IEEE 38th Annual International Conference of the*, pages 5116–5119. IEEE, 2016.

- [78] Gang Li, Hao Su, Weijian Shang, Junichi Tokuda, Nobuhiko Hata, Clare M Tempny, and Gregory S Fischer. A fully actuated robotic assistant for MRI-guided prostate biopsy and brachytherapy. In *SPIE Medical Imaging: Image-Guided Procedures, Robotic Interventions, and Modeling*, page 8671:867117, 2013.
- [79] D. Stoianovici, Chunwoo Kim, G. Srimathveeravalli, P. Sebrecht, D. Petrisor, J. Coleman, S.B. Solomon, and H. Hricak. MRI-safe robot for endorectal prostate biopsy. *IEEE/ASME Transactions on Mechatronics*, 19(4):1289–1299, 2014.
- [80] MartijnG. Schouten, JoyceG.R. Bomers, Derya Yakar, Henkjan Huisman, Eva Rothgang, Dennis Bosboom, TomW.J. Scheenen, Sarthak Misra, and JürgenJ. Fütterer. Evaluation of a robotic technique for transrectal MRI-guided prostate biopsies. *European Radiology*, 22(2):476–483, 2012.
- [81] S. Abdelaziz, L. Esteveny, L. Barbé, P. Renaud, B. Bayle, and M. de Mathelin. Development of a MR-compatible cable-driven manipulator: Design and technological issues. In *IEEE International Conference on Robotics and Automation (ICRA)*, pages 1488–1494, St. Paul, USA, 2012.
- [82] Jochen Krücker, Sheng Xu, Neil Glossop, Anand Viswanathan, Jörn Borgert, Heinrich Schulz, and Bradford J Wood. Electromagnetic tracking for thermal ablation and biopsy guidance: clinical evaluation of spatial accuracy. *Journal of Vascular and Interventional Radiology*, 18(9):1141–1150, 2007.
- [83] Daniel A Leung, Jorg F Debatin, Simon Wildermuth, Norbert Heske, Charles L Dumoulin, Robert D Darrow, Markus Hauser, Clarence P Davis, and Gustav K von Schulthess. Real-time biplanar needle tracking for interventional MR imaging procedures. *Radiology*, 197(2):485–488, 1995.
- [84] Sheng Xu, Jochen Kruecker, Baris Turkbey, Neil Glossop, Anurag K Singh, Peter Choyke, Peter Pinto, and Bradford J Wood. Real-time MRI-TRUS fusion for guidance of targeted prostate biopsies. *Computer Aided Surgery*, 13(5):255–264, 2008.
- [85] Eyal Kochavi, Dorith Goldsher, and Haim Azhari. Method for rapid MRI needle tracking. *Magnetic Resonance in Medicine*, 51(5):1083–1087, 2004.
- [86] Shashank Sathyanarayana, Pelin Aksit, Aravind Arepally, Parag V. Karmarkar, Meiyappan Solaiyappan, and Ergin Atalar. Tracking planar orientations of active MRI needles. *Journal of Magnetic Resonance Imaging*, 26(2):386–391, 2007.

- [87] MC Bernardes, Bruno Vilhena Adorno, Philippe Poignet, and GA Borges. Robot-assisted automatic insertion of steerable needles with closed-loop imaging feedback and intraoperative trajectory replanning. *Mechatronics*, 23(6):630–645, 2013.
- [88] A Majewicz, T.R. Wedlick, K.B. Reed, and AM. Okamura. Evaluation of robotic needle steering in ex vivo tissue. In *IEEE International Conference on Robotics and Automation (ICRA)*, pages 2068–2073, Anchorage, USA, 2010.
- [89] Gustaaf J Vrooijink, Momen Abayazid, Sachin Patil, Ron Alterovitz, and Sarthak Misra. Needle path planning and steering in a three-dimensional non-static environment using two-dimensional ultrasound images. *International Journal of Robotics Research (In Proof)*, 33(10):1361–1374, 2014.
- [90] S. Patil, J. Burgner, R.J. Webster, and R. Alterovitz. Needle steering in 3-d via rapid replanning. *IEEE Transactions on Robotics*, 30(4):853–864, Aug 2014.
- [91] M. Abayazid, R. J. Roesthuis, R. Reilink, and S. Misra. Integrating deflection models and image feedback for real-time flexible needle steering. *IEEE Transactions on Robotics*, 29(2):542 – 553, 2013.
- [92] Pedro Moreira, Gert van de Steeg, Ferdi van der Heijden, Jurgen J Fütterer, and Sarthak Misra. A preliminary evaluation of a flexible needle steering algorithm using magnetic resonance images as feedback. In *IEEE International Conference on Biomedical Robotics and Biomechatronics (BioRob)*, pages 314–319, São Paulo, Brazil, 2014.
- [93] Robert J Webster III, Jin Seob Kim, Noah J Cowan, Gregory S Chirikjian, and Allison M Okamura. Nonholonomic modeling of needle steering. *The International Journal of Robotics Research*, 25(5-6):509–525, 2006.
- [94] Gang Li. *Robotic System Development for Precision MRI-Guided Needle-Based Interventions*. PhD thesis, Worcester Polytechnic Institute, 2016.
- [95] Hao Su, Diana C Cardona, Weijian Shang, Alexander Camilo, Gregory A Cole, D Caleb Rucker, Robert J Webster, and Gregory S Fischer. A MRI-guided concentric tube continuum robot with piezoelectric actuation: a feasibility study. In *IEEE International Conference on Robotics and Automation (ICRA)*, pages 1939–1945, St. Paul, USA, 2012.
- [96] J Smink, M Häkkinen, R Holthuizen, S Krueger, M Ries, Y Berber, C Moonen, M Köhler, and E Vahala. external control (xtc): a flexible, real-time, low-latency, bi-directional scanner interface. In *Proceedings of the International Society of Magnetic Resonance Medicine*, page 1755, 2011.

- [97] Junichi Tokuda, Gregory S Fischer, Xenophon Papademetris, Ziv Yaniv, Luis Ibanez, Patrick Cheng, Haiying Liu, Jack Blevins, Jumpei Arata, Alexandra J Golby, et al. Openigtlink: an open network protocol for image-guided therapy environment. *The International Journal of Medical Robotics and Computer Assisted Surgery*, 5(4):423–434, 2009.
- [98] R. J. Webster III, J. S. Kim, N. J. Cowan, G. S. Chirikjian, and A. M. Okamura. Nonholonomic modeling of needle steering. *The International Journal of Robotics Research*, 25(5-6):509–525, 2006.
- [99] Philip Blumenfeld, Nobuhiko Hata, Simon DiMaio, Kelly Zou, Steven Haker, Gabor Fichtinger, and Clare Tempany. Transperineal prostate biopsy under magnetic resonance image guidance: a needle placement accuracy study. *Journal of Magnetic Resonance Imaging*, 26(3):688–694, 2007.
- [100] Zaman Mirzadeh, Kristina Chapple, Meg Lambert, Rohit Dhall, and Francisco A Ponce. Validation of ct-mri fusion for intraoperative assessment of stereotactic accuracy in dbs surgery. *Movement Disorders*, 29(14):1788–1795, 2014.
- [101] Lakshmi Nayak, Eudocia Quant Lee, and Patrick Y Wen. Epidemiology of brain metastases. *Current oncology reports*, 14(1):48–54, 2012.
- [102] Gregory Cole, Julie Pilitsis, and Gregory S Fischer. Design of a robotic system for mri-guided deep brain stimulation electrode placement. In *Robotics and Automation, 2009. ICRA '09. IEEE International Conference on*, pages 4450–4456. IEEE, 2009.
- [103] CL Dumoulin, SP Souza, and RD Darrow. Real-time position monitoring of invasive devices using magnetic resonance. *Magnetic resonance in medicine*, 29(3):411–415, 1993.
- [104] Daniel A Leung, Jorg F Debatin, Simon Wildermuth, Norbert Heske, Charles L Dumoulin, Robert D Darrow, Markus Hauser, Clarence P Davis, and Gustav K von Schulthess. Real-time biplanar needle tracking for interventional mr imaging procedures. *Radiology*, 197(2):485–488, 1995.
- [105] Claudia M Hillenbrand, Daniel R Elgort, Eddy Y Wong, Arne Reykowski, Frank K Wacker, Jonathan S Lewin, and Jeffrey L Duerk. Active device tracking and high-resolution intravascular mri using a novel catheter-based, opposed-solenoid phased array coil. *Magnetic resonance in medicine*, 51(4):668–675, 2004.
- [106] Qiang Zhang, Michael Wendt, Andrik J Aschoff, Jonathan S Lewin, and Jeffrey L Duerk. A multielement rf coil for mri guidance of interventional devices. *Journal of Magnetic Resonance Imaging*, 14(1):56–62, 2001.

- [107] Wei Wang, Charles L Dumoulin, Akila N Viswanathan, Zion TH Tse, Alireza Mehrtash, Wolfgang Loew, Isaiah Norton, Junichi Tokuda, Ravi T Seethamraju, Tina Kapur, et al. Real-time active mr-tracking of metallic stylets in mr-guided radiation therapy. *Magnetic resonance in medicine*, 73(5):1803–1811, 2015.
- [108] JC Hindman. Proton resonance shift of water in the gas and liquid states. *The Journal of Chemical Physics*, 44(12):4582–4592, 1966.
- [109] Yasutoshi Ishihara, Arturo Calderon, Hidehiro Watanabe, Kazuya Okamoto, Yoshinori Suzuki, Kagayaki Kuroda, and Yutaka Suzuki. A precise and fast temperature mapping using water proton chemical shift. *Magnetic Resonance in Medicine*, 34(6):814–823, 1995.
- [110] John De Poorter, Carlos De Wagter, Yves De Deene, Carsten Thomsen, Freddy Ståhlberg, and Eric Achten. Noninvasive mri thermometry with the proton resonance frequency (prf) method: in vivo results in human muscle. *Magnetic resonance in medicine*, 33(1):74–81, 1995.
- [111] Dennis L Parker, Vernon Smith, Philip Sheldon, Lawrence E Crooks, and Lauren Fussell. Temperature distribution measurements in two-dimensional nmr imaging. *Medical physics*, 10(3):321–325, 1983.
- [112] Stephen A Sapareto and William C Dewey. Thermal dose determination in cancer therapy. *International Journal of Radiation Oncology\* Biology\* Physics*, 10(6):787–800, 1984.
- [113] Benjamin Zaporzan, Adam C Waspe, Thomas Looi, Charles Mougenot, Ari Partanen, and Samuel Pichardo. Matmri and mathifu: software toolboxes for real-time monitoring and control of mr-guided hifu. *Journal of therapeutic ultrasound*, 1(1):7, 2013.
- [114] Maarten Bot, Pepijn Van Den Munckhof, Roy Bakay, Diane Sierens, Glenn Stebbins, and Leo Verhagen Metman. Analysis of stereotactic accuracy in patients undergoing deep brain stimulation using nexframe and the leksell frame. *Stereotactic and functional neurosurgery*, 93(5):316–325, 2015.